NASA Technical Memorandum 100732

Geodetic Measurement of Deformation in California

Jeanne Sauber
Geodynamics Branch
Laboratory for Terrestrial Physics
NASA/Goddard Space Flight Center
Greenbelt, Maryland

National Aeronautics and
Space Administration

Goddard Space Flight Center
Greenbelt, Maryland

1989

Acknowledgements

This work was completed under the supervision of my two advisors at M.I.T. Sean C. Solomon and Thomas H. Jordan.

This research was supported by the National Aeronautics and Space Administration through a Graduate Student Research Fellowship (NGT-50103) and through the Crustal Dynamics Project under grant NAG 5-814 and NAG 5-459. Support for part of this research was provided by the U.S. Geological Survey while I worked in Menlo Park.

Table of Contents

Chapter 1. Introduction

Historically geodetic measurements, although imprecise by today's standards, have been utilized to address fundamental scientific questions. The founder of scientific geodesy, Eratosthenes, deduced the radius of the Earth on the basis of the measurement of the baseline between Alexandria and Aswan made with a camel whose walking speed was well-calibrated. The value he obtained departs from the radius of a mean spherical Earth (6371 km) by -2% [*Torge*, 1980]. Early in this century two scientists, H.F. Reid and A. Wegener, proposed models central to modern crustal deformation studies. Geodetic surveys made before and after the 1906 earthquake have provided considerable information on the crustal deformation that accompanied the great San Francisco earthquake. These data led *Reid* [1910] to postulate that strain accumulated elastically by continuous slow motions at great distances from the San Andreas fault and that such strain is released by sudden slip on the fault surface at the time of an earthquake. *Wegener* [1929] tested his hypothesis of continental drift by the direct measurement of drift rates through repeated observations of astronomical positions. In his words "... only recently this method furnished the first real proof of the present-day displacement of Greenland predicted by drift theory ... ." Unfortunately, Wegener had to rely on inaccurate data, and the calculated rates of separation between North America and Europe were two orders of magnitude larger than current estimates.

High-precision space geodetic data from very long baseline interferometry (VLBI), satellite laser ranging (SLR) and the U.S. global positioning system (GPS), along with trilateration and spirit leveling measurements, are providing present-day rates of deformation at intercontinental, regional, and local spatial scales. In some situations where an extended measurement period yields an improved estimate of rates of strain, historical triangulation and leveling data can also be utilized in concert with the more precise modern

measurements. The recent influx of high-resolution data has the potential to influence significantly the way we formulate studies of tectonic deformation.

In the western U.S., VLBI measurements have been made since 1979 as part of the National Aeronautics and Space Administration (NASA) Crustal Dynamics Project. These measurements provide discrete sampling of the temporal and spatial deformation field. The proper interpretation of the VLBI-derived rates of deformation requires an examination of geologic and more densely sampled ground-based geodetic data. At the spatial scales spanned by a local geodetic network, auxiliary geologic and geophysical data can be utilized to examine the relation between measured incremental strain and the accommodation of strain seen in local geological structures, strain release in earthquakes, and principal stress directions inferred from *in situ* measurements. Integration of the results from local areas to the regional spatial scale provides a framework for developing kinematic models testable by VLBI measurements.

In this thesis I examine the rates of deformation across the Pacific - North American plate boundary zone in California. In the first two studies I process triangulation and trilateration data measured on two regional networks, one in the central Mojave Desert and one in the Coast Ranges east of the San Andreas fault (Figure 1). In the third study I process VLBI data from stations distributed across the Pacific - North American plate boundary zone in the western United States. Several common themes are pursued in each study: (1) the relation of the measured incremental strain to long-term deformation (2) the integration of diverse data that provide estimates of the rate and orientation of deformation, and (3) spatial scales of deformation and the relation of deformation in subregions to the overall accommodation of deformation across the plate boundary.

The Mojave Desert block is a major structural element in southern California which lies to the northeast of the 'big-bend' region and contains active right-lateral strike-slip faults oriented nearly parallel to the direction of Pacific - North American relative motion. This portion of the plate boundary represents a transition from primarily simple right-lateral

slip on the faults in southernmost California to extension in the Great Basin and transcurrent motion on the San Andreas fault in central California. In Chapter 2 I estimate the present-day rate of deformation across the northwest striking faults of the central Mojave Desert. To relate the measured incremental strain to long-term deformation, focal mechanisms are determined for recent earthquakes and the relative contribution of earthquakes to the measured strain is evaluated. The tectonic implications of these geodetic and seismological results, together with other regional geodetic and geologic data, are then explored.

The May 1983 Coalinga earthquake ($M_L = 6.7$), which involved slip on a thrust or reverse fault beneath a young fold, has focused attention on the importance of understanding the mode and rate of deformation east of the San Andreas fault in central California. In Chapter 3, I determine rates of crustal strain in the Diablo Range north of Coalinga from a triangulation and trilateration network and from line-length changes determined by means of trilateration measurements within 10 km of the San Andreas fault. To distinguish between models relating the formation of fold structures in the southern Coast Ranges to motion along the San Andreas fault, the principal directions determined geodetically for the rate of strain within the Diablo Range are compared with the orientations of the maximum principal stress (σ_1) estimated from wellbore breakouts, the azimuths of P axes determined from earthquake focal mechanisms, and the trends of major fold structures. The distribution of strike-slip and compressive displacements within the Coast Ranges is constrained by a comparison of the predictions from plate kinematic models and from the findings of regional geologic and geodetic studies.

VLBI measurements of changes in vector baselines that both span and are distributed within the Pacific - North American plate boundary zone over the last six years provide a unique geodetic data set . In Chapter 4 I process VLBI data to obtain estimates of the rate of change of tangential station position in a North-America-fixed reference frame. These data are used as constraints on the integrated rate of deformation across portions of the

continental plate boundary in California and provide a framework to interpret regional geodetic and geologic studies. On the basis of geologic data the rates of deformation have been estimated in southern and central California over time scales of approximately 10^2 - 10^6 years, while with triangulation, trilateration, and VLBI data the rates of deformation over the last 10^0 - 10^2 years may be determined. For three regions, across southern California just north of the Imperial fault, in the 'big-bend' region, and in central California, I compare the rates of deformation derived from VLBI and ground-based geodetic data, and I examine the relationship between the rates of deformation determined from geological data and those estimated from geodetic data.

In Chapter 5, I summarize the principal conclusions of this thesis and suggest several topics for future research.

Figure Captions

Figure 1. Locations of VLBI sites (triangles with station codes) and geodetic networks utilized in this thesis. CMN = Central Mojave Network and SBN = San Benito Network. Quaternary fault traces are from *Jennings* [1975]. Mercator projection of California, Nevada, and western Arizona.

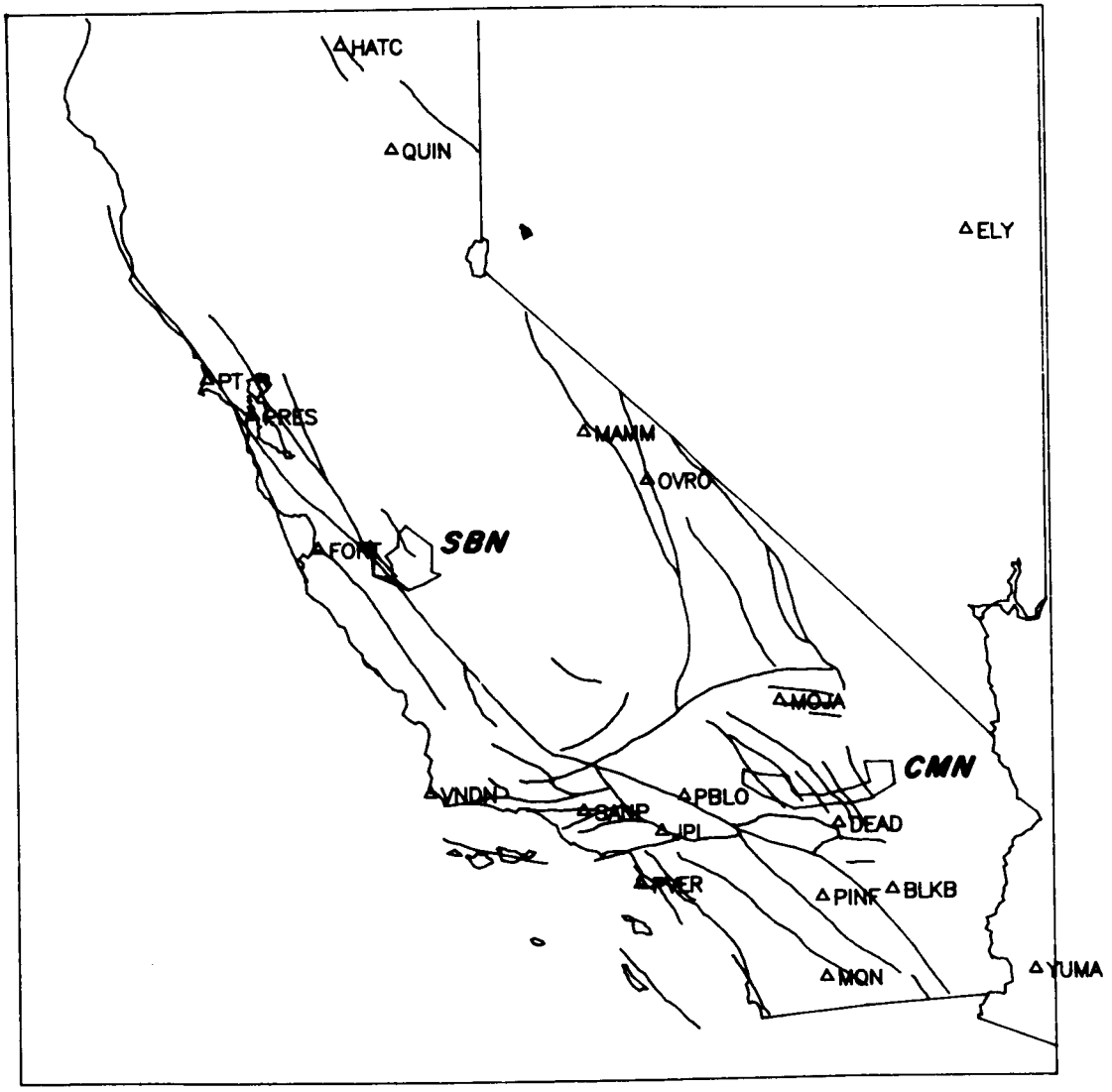

Figure 1. Locations of VLBI sites (triangles with station codes) and geodetic networks utilized in this thesis. CMN = Central Mojave Network and SBN = San Benito Network. Quaternary fault traces are from *Jennings* [1975]. Mercator projection of California, Nevada, and western Arizona.

Chapter 2. Geodetic Measurement of Deformation in the Central Mojave Desert, California

Introduction

The boundary between the Pacific and North American plates in California is characterized by active deformation over a broad region (Figure 1). Quaternary fault slip rates [*Sieh and Jahns*, 1984; *Weldon and Sieh*, 1985], as well as geodetic estimates of slip rate from trilateration data [*Prescott et al.*, 1985] and very long baseline interferometry (VLBI) [*Lyzenga et al.*, 1986], indicate that in central and southern California the San Andreas fault system has accommodated approximately 68% of the relative plate motion of 50mm/yr predicted from the NUVEL-1 global plate velocity model [*DeMets et al.*, 1987]. Where the remaining fraction of the relative plate motion is accommodated is uncertain; high angle strike-slip faults subparallel to the San Andreas system may take up a significant proportion of this "missing" plate motion.

The strike of the San Andreas fault system is approximately parallel to the slip direction of relative plate motion, N35°W, along most parts of the plate boundary. However, in the 'big-bend' section the San Andreas fault locally changes its trend by 20°-30° along a 190-km-long segment between San Gorgonio Pass and Tejon Pass. An essential structural element at this portion of the plate boundary is the Mojave Desert block, which lies to the northeast of the big-bend region and contains active right-lateral strike-slip faults oriented nearly parallel to the direction of Pacific-North American relative motion. The rate and mode of deformation in this block is thus important to an understanding of the character and distribution of deformation at the plate boundary and to earthquake risk assessment in southern California.

In this chapter, data from triangulation and trilateration surveys conducted between 1934 and 1982 are used to determine rates of shear strain in the central Mojave Desert (Figure 2). On the assumption that these strain rates represent a long-term average rate, they permit an improvement to the estimates of slip rate obtained from geological observations. In addition, focal mechanisms determined for six recent earthquakes, in combination with three previously determined focal mechanisms [*Kanamori and Fuis*,

1976], are used to examine the relationships among seismicity, strain data, and local geology. Finally, the data from this study, along with other geologic and geodetic data, are used as a basis for exploring the tectonic implications for southern California.

General Setting of the Mojave Desert Block

The dominant active structural elements of the Mojave Desert block are right-lateral, strike-slip faults trending approximately N35°W - N42°W. The surface traces of these faults are 8-80 km long and are spaced approximately 8-30 km apart (Figure 2). *Dokka* [1983] has documented cumulative right-lateral displacement on the major northwest-striking faults of 27-38 km in the last 20 m.y. The time of initiation of fault slip is poorly constrained, however, because of the lack of mappable offsets of rock units along the faults. From field observations, *Dokka* [1983] has suggested that strike-slip faulting may have started as late as Pliocene or Quaternary. According to this view, the northwest-striking faults of the central Mojave may be in an early stage of development. If most of the strike-slip motion began ~5 m.y. ago, when major spreading initiated in the Gulf of California and acceleration of slip occurred on the San Andreas fault [*Moore and Curray,* 1982; *Page and Engebretson*, 1984; *Winker and Kidwell*, 1985], the average rate of slip along the northwest-trending faults may be as much as ~7 mm/yr. If slip instead initiated 20 m.y. ago, the slip rate could be as low as 1 mm/yr. All the faults from Helendale to Ludlow show some Quaternary displacement [*Dokka*, 1983], with no one fault appearing to dominate. This is further corroborated by field observations (B.C. Burchfiel and J.D. Walker, personal communication, 1985) indicating that any long-term deformation occurring on the northwest-striking faults is probably not confined to a single active fault. Geologic field observations [*Dokka and Glazner*, 1982; B.C. Burchfiel and J.D. Walker, personal communication, 1985] further suggest that compressional and extensional features are small and erratic in the central Mojave and are due to local irregularities in fault geometry.

Left-lateral faults of approximately east-west strike are also common, especially in the northeast corner of the Mojave block(Figure 2). The Garlock and Pinto Mountain faults that bound the Mojave block show this type of motion. The surface expressions of northwest-trending strike-slip faults of the central Mojave terminate, to the south, at the Pinto Mountain fault; at the northern boundary of the Mojave block such faults do not cross the Garlock fault. Left-lateral displacements of at least 48 to 65 km have been documented on the central and western portions of the Garlock fault [*Davis and Burchfiel*, 1973]. An average displacement rate of about 11 mm/yr on the central part of the Garlock fault has been estimated from a match of displaced Pleistocene alluvial fan gravels by *Carter* [1980]. A lower rate of 7 mm/yr during the Holocene period has been suggested by *Astiz and Allen* [1983] from a compilation of alignment array data and offset of primarily Holocene strata.

The Mojave block is bounded on the west by the big-bend portion of the San Andreas fault. The long term slip rate on this portion of the fault is estimated to be 35 mm/yr [*Weldon and Sieh*, 1985]. The average strike is N65°W. The maximum shear strain rate measured between 1973 and 1983 across the San Andreas fault on the Palmdale network is 0.37 ± 0.02 μstrain/yr oriented N65°W [*King and Savage*, 1984]. Between the San Andreas fault and the most western fault of the central Mojave, the Helendale fault, there are a few small reverse faults. Focal mechanisms in this transition region are mostly thrust-type events [*Sauber et al.* , 1983]. On the southwestern boundary, north-south crustal shortening of the San Bernardino block occurs at a step in the San Andreas fault [*Meisling*, 1984].

Historically, the Mojave block has been characterized by small to moderate-size earthquakes. In the area of the central Mojave examined in this study (Figure 3), five earthquakes with local magnitude $M_L \geq 5.0$ have occurred since 1932 (Figure 4). North of the study area a M_L=6.2 earthquake occurred in 1947 on the Manix fault near Barstow. No additional earthquakes of $M_L \geq 6.0$ have occurred in the Mojave block since 1860 [*Moths*

and Ellsworth, 1980; B.M. Sheffels, personal communication, 1985]. Just south of the study area the Homestead Valley sequence (M_L= 4.9, 5.2, 4.5, 4.8) occurred in 1979 [*Stein and Lisowski*, 1983]. Active seismicity terminates eastward along a line given approximately by an extension southward of the Death Valley fault [*Hileman et al.,* 1973].

Geodetic Strain Rates

Method

Triangulation surveys were conducted by the National Geodetic Survey (N.G.S.) throughout much of the Mojave Desert between 1934 and 1940 and again in 1965. To examine deformation in the central Mojave, the United States Geological Survey (U.S.G.S.) performed a trilateration survey in 1982 of the area shown in Figure 3. This geodetic network extends ~110 km east-west and spans the area from west of the Helendale fault to east of the Ludlow fault. The stations are distributed such that most angle observations cross one of the major faults. For comparison with the earlier surveys the distances measured using trilateration were reduced to angles between different geodetic stations. The standard deviation for angles derived from triangulation is approximately 0.8" and for the angles derived from trilateration measurements is approximately 0.1" [*Federal Geodetic Control Committee*, 1984].

An equation is formed relating the observation Φ_{ijk} of the k th angle at the i th station during the j th survey at a given time t_{ij} to the engineering shear strain rate components $\dot{\gamma}_1$ and $\dot{\gamma}_2$ and the initial angle $\Phi_{ik}{}^0$ for each angle observation [*Frank*, 1966; *Prescott*, 1976]:

$$\phi_{ijk} = t_{ij} (A_{ik}{}^1\dot{\gamma}_1 + A_{ik}{}^2\dot{\gamma}_2) + \phi_{ik}{}^0 \qquad (1)$$

where

$$A_{ik}{}^1 = (\sin 2\theta_{ik}{}^2 - \sin 2\theta_{ik}{}^1)/2$$
$$A_{ik}{}^2 = (\cos 2\theta_{ik}{}^2 - \cos 2\theta_{ik}{}^1)/2 \qquad (2)$$

are coefficients which depend on the azimuths θ^1_{ik} and θ^2_{ik} of sides 1 and 2 of the k th angle at the i th station. The quantities $\gamma_1 = \varepsilon_{11} - \varepsilon_{22}$ and $\gamma_2 = \varepsilon_{12} - \varepsilon_{21}$, where ε_{ij} are elements of the strain tensor, are the shear components in a geographic coordinate system in which the 1-axis points to the east and the 2-axis points north; γ_1 measures right-lateral shear across a vertical plane striking N45°W (or left-lateral shear across a vertical plane striking N45°E); γ_2 measures right-lateral shear across a vertical plane striking eastward (or left-lateral shear across a vertical plane striking northward). The total engineering shear strain rate $\dot{\gamma}$ and the azimuth of maximum right-lateral shear Ψ are related to $\dot{\gamma}_1$ and $\dot{\gamma}_2$ by:

$$\dot{\gamma} = (\dot{\gamma}_2^{\,2} + \dot{\gamma}_2^{\,2})^{1/2} \tag{3}$$

$$\psi = 1/2 \arctan (\dot{\gamma}_1/\dot{\gamma}_2)$$

To estimate strain rates, angle changes between successive surveys were fit to a strain rate field assumed to be spatially and temporally uniform. By using both the older triangulation data and the recent trilateration data, the shear strain rate could be determined over a 48 year period. The two shear strain rate components $\dot{\gamma}_1$ and $\dot{\gamma}_2$ were derived by weighted least squares. Since the angles determined using trilateration are more accurate it is desirable to include a weighting matrix in the least squares inversion. The inverse of the data variance-covariance matrix was therefore used for the weight matrix [*Prescott*, 1976]; thus angle changes determined from triangulation measurements alone (1934/40 - 1965) were downweighted relative to angle changes obtained from trilateration and triangulation together (1934/40 - 1982, 1965 - 1982).

The full three dimensional strain tensor includes dilatation, horizontal and vertical shear components, and vector rotation [*Ramsay*, 1967]. By examining only angle changes between successive surveys we can estimate only the horizontal distortion of the region. Even in two dimensions rotation about a vertical axis, $\omega = (\varepsilon_{12} - \varepsilon_{21})/2$, cannot be derived

without a reliable external, or a conventionally adopted internal, reference direction. Likewise surface dilatation, $\Delta = (\varepsilon_{11} + \varepsilon_{22})/2$, cannot be derived from angle measurements without an accurate reference length [*Frank*, 1966]. Dilatation and rotation affect the determination of shear strain only if such modes of deformation occur within the network in a non-uniform manner.

Results

Strain fields were determined for a number of different spatial subnets using a moving window approach. In addition, we searched for strong spatial strain gradients by examining and comparing the observed angle changes with those predicted by least squares analysis assuming a uniform strain field. The predicted angle changes were obtained from the estimates of $\dot{\gamma}_1$ and $\dot{\gamma}_2$ determined from the entire data set. Standard deviations reflect both misfit and data uncertainties due to measurement imprecision.

The most western subnet included stations that crossed the Helendale and Lenwood faults (Figure 3). For this subnet we found $\dot{\gamma} = 0.17 \pm 0.05$ μrad/yr and Ψ = N41°W ± 11°. Moving eastward across the network, in a subnet that spans the Lenwood fault, Johnson Valley fault, and part of the Camp Rock fault (Figure 3), we found $\dot{\gamma} = 0.15 \pm 0.04$ μrad/yr and Ψ = N38°W ± 7°. In the next subnetwork, which spans only the Johnson Valley and Camp Rock faults, we found $\dot{\gamma} = 0.15 \pm 0.05$ μrad/yr and Ψ = N40°W ± 8°. Thus, for the region between the Helendale and Camp Rock faults, in the western half of the network, the strain rate was nearly constant. Because there are not enough stations located between potentially active faults, it is uncertain whether there is strain accumulation associated with the Helendale and Camp Rock faults or if all the observed strain is associated with the Lenwood and Johnson Valley faults. The average strain rate parameters for this western region are given in Table 1. Significant strain is indicated for the $\dot{\gamma}_1$ component in this region. Since the geologic data indicate large right-lateral displacements along northwest-trending faults, $\dot{\gamma}_1$ is most simply interpreted as

representing right-lateral shear strain accumulation across a vertical plane striking N45°W. The maximum rate of right-lateral shear strain occurs on a plane oriented N41°W ± 5° and is equal to 0.16 ± 0.03 μrad/yr. Angle changes at individual station combinations are well predicted by this strain field. If we assume that the measured deformation is due to right-lateral motions across the local faults, this rate of average shear strain corresponds to a net displacement rate of 6.7 ± 1.3 mm/yr across this portion of the survey area. This region of active deformation is measured on the central Mojave network at a distance of 40 to 90 km from the big-bend segment of the San Andreas fault. The orientation of the maximum right-lateral shear strain is N41°W ± 5°, significantly different from the orientation of maximum shear strain, N65°W, near the San Andreas fault [*King and Savage*, 1984].

From Camp Rock fault eastward across the net there is a transition from significant strain rates to very low strain rates; i.e., rates that are less than the errors in the shear strain components $\dot{\gamma}_1$ and $\dot{\gamma}_2$ (eastern region, Table 1). In the eastern portion of the network the density of throughgoing northwest-oriented faults decreases (Figure 3) and one of the few major faults, the Ludlow fault, shows little Quaternary displacement [*Dokka*, 1983].

The spatial pattern and orientation of the observed strain field suggest a relation to the northwest-trending faults of the central Mojave and argue against an influence from the more distant San Andreas fault. First, the direction of maximum right-lateral shear strain is parallel to the trends of local faults and differs significantly from the San Andreas strike and the orientation of contemporary shear straining across it. Furthermore, the active deformation measured on the central Mojave network is located 40 to 90 km from the nearest adjacent portions of the San Andreas. While some observations [*Thatcher*, 1979b] and deformation models [*Thatcher*, 1983] suggest that interseismic straining may be broadly distributed across the southern San Andreas, neither the shear strain orientation nor the sharp decline in its magnitude across the Mojave network support the existence of a San Andreas strain field sufficiently widespread to account for the deformation reported here.

The average rate estimate of ~7 mm/yr for the western region is similar to the geologic slip rate determined from the cumulative fault offset across all the northwest faults, assuming slip initiated on the major faults about 5 m.y. ago. Since *Dokka* [1983] and previous workers such as *Garfunkel* [1974] report Quaternary fault movement on all the faults from Helendale fault east to the Ludlow fault, the results of this study may suggest a change in the distribution of faults which accommodate motion. This change may represent an evolution within the Quaternary or it may reflect a fluctuation which occurs on the shorter time scales of a plate boundary seismic cycle.

In an effort to search for temporal variations in the strain data, we examined the angle residuals (predicted angle changes minus observed angle changes) when the entire data set (1934/40 - 1965, 1934/40 - 1982, 1965 - 1982) was used to determine the strain parameters, and we calculated separately the strain parameters for the time periods 1934/40 - 1965 and 1965 - 1982. Since strain accumulation is insignificant in the eastern portion of the network, only the results from the western region are discussed. No systematic temporal trends were found in the angle residuals. Unfortunately not as many stations were used in the 1965 survey, so the number of angles for the two time periods 1934/40 - 1965 and 1965 - 1982 are quite small. Additionally, for the two early surveys only the less accurate triangulation method was used. Thus, the strain rate and orientation for the early time period is poorly resolved. For 1934/40 - 1965, $\dot{\gamma} = 0\ .09 \pm 0.07$ μrad/yr and $\Psi =$ N58°E ± 28°, not a statistically meaningful result. For 1965 - 1982, $\dot{\gamma} = 0.20 \pm 0.08$ μrad/yr and Ψ=N28°W ± 14°. The two values for $\dot{\gamma}$ are not significantly different.

Other Geodetic Studies in the Mojave Block

Two other recent geodetic studies in the Mojave block show strain rates similar to those documented here. The orientation of the plane of maximum shear strain, however, differs among the studies. *Timmerman et al.* [1985] estimated horizontal strain within a large area adjacent to and including the big-bend portion of the San Andreas fault; their area

includes the northern two thirds of the Mojave block. They used mostly triangulation data, but they also considered astronomic azimuth and trilateration data. The triangulation data used for our study (1934/40, 1965) are a subset of the triangulation data used by *Timmerman et al.* [1985]. None of the U.S.G.S. trilateration data obtained after 1979, however, was used in their work. For a zone which includes our region of active deformation (Table 1, western region) and extends from the central Mojave northward to the Garlock fault (their District VI), *Timmerman et al.* [1985] found $\dot{\gamma} = 0.13 \pm .04$ μrad/yr and $\Psi = N75°W \pm 8°$. This orientation is closer to the trend of the San Andreas fault than to the strike of the local faults in the Mojave block.

King [1985] examined trilateration measurements taken between 1979 and 1983 from a network that spans the Calico and Camp Rock faults near Barstow (Figure 2). The maximum shear strain rate from the Barstow network data was found to be 0.08 ± 0.05 μrad/yr with $\Psi = N21°W \pm 17°$. This network spans only two of the northwest-striking faults and falls within the transition region between active deformation to the west and low strain rates to the east observed on the central Mojave network (Table 1). The strain rate for data from a subnet of our central Mojave network extending from the Calico fault to just west of the Camp Rock fault (Figure 3) was determined to be 0.03 ± 0.05 μrad/yr, a result not significantly different from that of *King* [1985].

Earthquake Focal Mechanisms

It is of interest to compare the derived strain field with the directions of principal stresses inferred from fault plane solutions of earthquakes within the Mojave block (Figure 4). We have determined the focal mechanisms for six earthquakes that occurred in the central Mojave Desert between May 1976 and February 1984. These mechanisms supplement the focal mechanisms of the June 1, 1975, Galway Lake and the November-December 1975 Goat Mountain earthquakes previously determined by *Kanamori and Fuis* [1976] and G. Fuis (personal communication, 1985).

Method and Results

Earthquakes for which we have determined fault plane solutions are listed in Table 3. The arrival time and first motion data are from the Southern California Seismic Network and were obtained with the assistance of U.S.G.S. and Caltech staff. A version of HYPO71 [*Lee and Lahr*, 1975] was used to locate these events. The adopted crustal structure is taken from the refraction study of *Fuis* [1980] and is given in Table 2. Station polarities were checked against a list with polarity data from teleseisms, local quarry blasts, and Nevada Test Site blasts (courtesy of T. Webb). The P-wave first motion data and focal mechanisms for these events are given in Figure 5.

As shown in map view in Figure 6, the focal mechanisms of earthquakes in the region of the Mojave network are primarily strike-slip. Some normal faulting events also occur. Since two completely different mechanisms are consistent with the data for event 4, both solutions are considered in the analysis; the strike-slip solution is referred to as event 4*. A preferred nodal plane for each event, based on surface rupture, aftershock patterns and local geology [*Kanamori and Fuis*, 1976 ; *Hill and Beeby*, 1977], is also indicated in Table 3.

The strikes of the fault planes for some of these events (4*, 8 and 9, Table 3) are similar to the orientation of the major faults in the area and to the direction of relative slip between the North American and Pacific plates. For a second group the preferred fault planes have strikes that are more northerly by 5-20° (1,3,5 and 7, Table 3). Events 2 and 4 are normal faulting earthquakes that accommodate east-west extension. The preferred nodal plane for event 6 is consistent with the more northerly orientation of some of the surface faults observed nearer to the San Bernardino mountains and the Pinto Mountain fault (Figure 2). There does not seem to be a correlation between mechanism type and focal depth (Table 3). There is an apparent discrepancy between the orientation of rupture for recent large events (Goat Mountain, Galway Lake, and Homestead Valley earthquakes)

and the orientation of the major faults in the area. Understanding this discrepancy is important for the determination of the state of stress in the region. For example, in their estimate of the principal stress orientation in the Mojave Desert, *Zoback and Zoback* [1980] relied on first motion data, the distribution of aftershocks, and ground breakage data from the 1975 Galway Lake earthquake. They estimated the least principal horizontal stress to be oriented N75°W, with a maximum horizontal stress thus directed at N15°E. A more northerly direction for the maximum stress would have been estimated if the orientation of the main faults in the area had instead been used. As the field data suggest that the strike-slip faulting may be in an early stage of development [*Dokka and Glazner*, 1982; *Dokka,* 1983], we compare below the focal mechanism results to experimental simulations of simple shear. From the relation between the focal mechanism results, the strain data, and the local geology, we then make tentative conclusions on the long-term slip behavior of this region.

Comparison of Principal Stress Directions Estimated from Earthquake Focal Mechanisms with Geodetic Strain Directions

We first compare principal stress directions inferred from the fault plane solutions in Table 3 with the direction of the most compressive strain determined geodetically. Following the suggestion of *Celerier and Brace* [1984] and B. Celerier (personal communication, 1985), the orientation of principal stresses may be estimated by testing the alternative assumptions that (1) slip occurred on the plane of maximum resolved shear stress, (2) the fault planes are determined by a Coulomb-Anderson failure criterion, and (3) slip occurred on a pre-existing plane of weakness.

The most common method for relating focal mechanisms to the stress field is to equate the P, B, and T axes to the directions of the principal stresses σ_1, σ_2 and σ_3, respectively. The nodal planes in this case are assumed to coincide with the planes of maximum shear stress. The P and T axes for the nine events of Table 3 are given in Figure

7a. The inferred orientation of σ_1(taken to equal the P axis) is approximately north-northeast and that of σ_3 (T axis) is east-southeast for most events. The P axis for many of the events is more easterly than the direction of maximum shortening (nearly north-south) determined from the strain data. For a homogeneous, isotropic medium the principal stress and strain directions should be the same. The difference seen in Figure 7a may be due to (1) a heterogeneous stress field or heterogeneous medium properties, (2) an orientation of measured incremental strain that differs from the orientation of the absolute strain field, or (3) slip occurring at an orientation other than that corresponding to the maximum shear stress. The assumption that the axes of measured incremental strain and regional stress commonly coincide is supported by the result of *Prescott et al.* [1979] that the direction of maximum shear strain agrees very well with the surface strike of nearby faults in several regions of California. Therefore, we examine the effect of assuming that slip occurs on faults with an orientation other than that of the plane of maximum shear stress.

If slip on the fault planes is controlled by a Coulomb-Anderson criterion instead of the maximum-shear-stress criterion , the angle α between the fault normal and σ_1 will be:

$$\alpha = \phi/2 + \pi/4$$

where ϕ is the angle of internal friction. When faults have no strength ϕ becomes zero and slip will occur on the maximum shear plane, as assumed above. Since a preferred fault plane has been chosen for each earthquake (see Table 3), α is measured from the auxiliary plane. We denote the resulting estimate of the direction of σ_1 by P_f. For a fault strength approximately equal to the average strength of crustal material, that is $\phi = 30°$ (coefficient of internal friction $\mu = 0.6$), P_f is as given in Figure 7b. For events 1,3,5 and 7 P_f is nearly aligned with the orientation of the most compressive principal strain given by the geodetic data. The occurrence of normal faulting events (2,4) and event 6 are still unexplained.

For a region where pre-existing zones of weakness occur, slip may occur on such planes before the formation of Coulomb-Anderson failure planes. In this case a fault plane may bear no simple geometric relation to the stress directions. *McKenzie* [1969] has shown that the maximum compressive stress may have an orientation anywhere within the dilatational quadrant. For a variety of focal mechanisms from a region of uniform stress, the maximum principal stress direction may be approximated by the dilatational region common to all events [*Sbar*, 1982]. This region of acceptable orientations for σ_1 includes the orientation of the axes of the most compressive strain (Figure 7b).

Comparison of Results to Models of a Region under Simple Shear

Experimental simulatations of simple shear indicate an evolution in the formation of a shear zone [*Tchalenko*, 1970; *Freund*, 1974; and *Wilcox et al.*, 1973] that may be compared with existing structures in the field [*Tchalenko and Ambraseys*, 1970; *Freund*, 1974; and *Aydin and Page*, 1984]. In the initial stages of shear the net displacement is accommodated on faults with orientations that differ from that of the maximum shear stress by $\phi/2$ and $90°-\phi/2$, where ϕ is the angle of internal friction. Failure at these orientations is consistent with a Coulomb-Anderson failure condition. In the central Mojave, events 1,3,5 and 7 occur on faults oriented approximately $\phi/2$ from the maximum shear direction. In later stages of development in the shear experiments, additional shears at other orientations form; finally, continuous horizontal shears develop ('D shears'). The D shears are at an orientation parallel to the direction of applied shear and are the major structures that accommodate motion. Events 4*, 8, and 9 have fault planes similar to the major faults of the Mojave region and are probably displacement controlled.

In summary, the strike of the major faults of the region are at the orientation of maximum strain accumulation and thus, are the faults along which long term displacement will preferentially occur. Secondary faulting controlled by a Coulomb-Anderson type

failure mechanism or by slip on pre-existing faults can account for slip on faults of other orientations.

Contribution of Earthquakes to Measured Strain

The measured strain could be due to one or more of several different mechanisms: (1) earthquakes, (2) fault creep, or (3) elastic and anelastic strain accumulation. An estimate of the strain due to earthquakes from January 1932 - June 1984 was determined using the method of *Molnar* [1983]. All earthquakes with $M_L \geq 3.0$ that occurred within the region between 34.33 and 34.92°N and between 115.60 and 117.33°W were included in the calculation (Figure 4). The maximum depths of well located events fall between 10-15 km [*Corbett and Hearn*, 1983]. Most events, however, occur at depths of less than 6 km. Assuming a thickness of 10 km for the seismic zone gives a volume V of the region of 8.2×10^{19} cm^3. The empirical relation between M_L and seismic moment M_o derived for southern California earthquakes by *Thatcher and Hanks* [1973] was used to estimate the moment for individual events. Without detailed information on the mechanism of these earthquakes we calculate a moment sum assuming the same mode of release for all earthquakes, that is, right-lateral strike-slip on a vertical plane oriented N41°W. A moment sum (ΣM_o) of 6.8×10^{24} dyn-cm was determined. Given a shear modulus appropriate for granite (3.0×10^{11} dyn/cm^2), a seismic strain release value of $\gamma = 0.6$ μstrain over a time period of 52.5 years was determined. This is equivalent to less than four years of strain accumulation in the western region of the Mojave survey area.

While this simple calculation is, of course, only a rough estimate because of uncertainities in the completeness of the catalog and because of the exclusion of events with $M_L < 3.0$, it is safe to conclude that slip due to earthquakes accounts for only an insignificant portion of the deformation measured in the region between Helendale and Camp Rock faults. All five of the $M_L \geq 5.0$ events in fact occur east of the Camp Rock fault. Some combination of fault creep and elastic or anelastic deformation of the

lithosphere must therefore be responsible for the measured strain. Seven millimeters per year of creep along some combination of the northwest-striking faults from Helendale to Camp Rock could account for the rate and orientation of the measured strain. Possible creep on the Lenwood/Lockhart fault is reported near Barstow [*Jennings*, 1975]. Alternatively, if most of the deformation is stored as elastic strain energy, larger earthquakes would be expected to occur in the future in the Mojave region.

Tectonic Implications of Deformation in the Mojave Desert

Previous models of the kinematic behavior of the Mojave block [*Garfunkel*, 1974; *Bird and Rosenstock*, 1984; *Weldon and Humphreys*, 1986] differ significantly. This is at least in part due to uncertainties in the slip rate across the northwest-striking faults of the central Mojave. Provided that the strain rates over the 50-year time period of this study represent the long-term average rate across the northwest-trending faults, the rate of ~7 mm/yr represents an important additional constraint on kinematic models for the region. This constraint on the slip rate, along with other geologic and geodetic data, serve as a basis for exploring the tectonic implications and examining previous kinematic models of deformation for the Mojave block.

In the geometric model of *Garfunkel* [1974] the Mojave block is crossed diagonally by many right-lateral faults. The San Andreas and Garlock faults are the southwestern and northern boundaries of the model. Assuming that the northern boundary of the Mojave block remained adjacent to the southern part of the rigid Sierra Nevada block, the cumulative right-lateral slip estimated by *Dokka* [1983] would require approximately 10-12° of counterclockwise rotation in such a model. The internal deformation of the Mojave block would be accompanied by an increase in the magnitude of the bend of the San Andreas fault. Such counterclockwise rotation of the Mojave block might eventually act to rotate the northwest-striking faults out of an orientation favorable to accommodate relative plate motion [*Garfunkel and Ron*, 1985].

In contrast, in the kinematic model of *Bird and Rosenstock* [1984], the northwest-trending right-lateral shear zone of the Mojave Desert is represented as a single fault with an overall slip rate of 6.8 mm/yr. Bird and Rosenstock predict that as a result of the ~7 mm/yr of relative motion across the central Mojave, either crustal shortening occurs on the western portion of the Garlock fault or crustal extension takes place on the eastern portion of this fault. Thrusting in the Tehachapi Mountains (Figure 2) is their preferred interpretation. Alternatively, the distributed deformation on the northwest-striking faults of the Mojave may instead be kinematically related to strike-slip motion on the right-lateral faults north of the Garlock fault (Figure 2) that bound the region of extensional tectonics in the Great Basin. *Walker* [1985] combined the offsets documented by *Dokka* [1983] and the predicted counterclockwise rotation of 10-12° to construct a model connecting these displacements to movements on the Furnace Creek fault.

One of the geologic constraints on kinematic models of the Mojave block is the slip rate on the Garlock fault. The observed left-lateral displacement on the Garlock fault has generally been considered to be due to the westward displacement of the Sierra Nevada block relative to stable North America [*Davis and Burchfiel*, 1973; *Weldon and Humphreys*, 1985]. Thus, the Garlock fault would accommodate the difference in motion between east-west extension in the Great Basin and a more stable Mojave block. In contrast, if the Mojave block moves northeast relative to North America, less extension is required in the Great Basin to acccount for Garlock motions [*Bird and Rosenstock*, 1984]. Such a motion would result in significant compression across the Avawatz Mountains (Figure 2). *Minster and Jordan* [1985] have estimated the rate of spreading in the direction ~N71°W in the Basin and Range to be 7.1 ± 1.5 mm/yr on the basis of VLBI observations constrained by orientation information. Thus, assuming that the slip rate of about 11mm/yr given by *Carter* [1980] for the Garlock fault is representative, the Mojave block is required to move to the northeast relative to North America. However, for the lower slip rate of 7

mm/yr on the Garlock fault given by *Astiz and Allen* [1983] this additional northeastern motion of the Mojave Block may not be necessary.

Within the Mojave block there are actually two domains of transcurrent faults that show Quaternary movement, right-lateral faults of the central Mojave and left-lateral faults in the northeast corner of the block (Figure 2). Paleomagnetic data could provide some constraint on the amount of rotation in the two domains of the Mojave block. However, paleomagnetic directions derived from rocks of Miocene or younger age give contrasting results. Miocene volcanic rocks collected near Barstow suggest counterclockwise rotations of up to 30° [*Burke et al.*, 1982], and *MacFadden et al.* [1987] indicate that the 13-18 Ma Barstow Formation was rotated about 15° counterclockwise. Paleomagnetic results from the western Mojave Desert suggest that the region may have been rotated 35° - 45° clockwise between 20 and 16 Ma and then subsequently rotated 10° - 20° counterclockwise [*Golombek and Brown*, 1988]. *Weldon et al.* [1984] found paleomagnetic evidence indicating that the southwestern Mojave has rotated less than 4° since mid-Miocene time. Adjacent to the domain of left-lateral faults, the eastern portion of the Garlock fault is bent (Figure 2). This geometry is suggestive of clockwise rotation [*Luyendyk et al.*, 1980]. Horizontal strain accumulation across the eastern 150 km of the Garlock fault estimated from trilateration measurements between 1972 and 1984 indicate a maximum shear strain rate of 0.18 ± 0.01 μrad/yr across a vertical plane oriented N59°E ± 2° for left-lateral shear or N31°W for right-lateral shear [*King and Lisowski*, 1985; M. Lisowski, personal communication, 1985]. The local strike of the eastern section of the Garlock fault is, however, approximately east-west. The clockwise rotation of this domain may thus be rotating the Garlock out of its original orientation.

The relation of slip on the northwest-trending faults of the central Mojave to the tectonics of surrounding region will require additional data to resolve the outstanding questions. Regardless, the deformation measured across the western portion of the central Mojave network accounts for 14% of the predicted 50 mm/yr of relative motion between

the North American and Pacific plates or appoximately one-third of the 'missing' plate motion not accommodated by the San Andreas system. With significant deformation occurring east of the San Andreas fault in the central Mojave Desert less deformation is needed west of the San Andreas to account for the total predicted plate motion [e.g., *Weldon and Humphreys,* 1986].

Summary

We have examined triangulation/trilateration data from a geodetic network that spans the northwest-striking faults of the central Mojave Desert of California. For the region between the Helendale and Camp Rock faults the shear strain rate was determined to be 0.16 ± 0.03 μrad/yr, with maximum right-lateral shear strain occurring on a plane oriented N41°W ± 5°. If we assume that this deformation is due to right-lateral displacement across the local faults, the average shear straining corresponds to a relative displacement of 6.7 ± 1.3 mm/yr across this portion of the network. This slip estimate is similar to the geologic slip rates given by *Dokka* [1983], on the assumption that slip began ~5 m.y. ago when major spreading initiated in the Gulf of California and acceleration of slip occurred on the San Andreas fault. From the Camp Rock fault eastward across the network there is a transition from significant to very low strain rates.

From an examination of nine focal mechanisms and their relation to the local geology and the strain data, our results suggest that most of the long term displacement (or at least the strain accumulation) occurs parallel to the orientation of the local northwest-trending faults. This orientation is nearly along the direction of relative motion between the North American and Pacific plates. Secondary faulting controlled by a Coulomb-Anderson failure mechanism or by slip on pre-existing faults can account for earthquakes on faults of other orientations.

The documented active deformation on the northwest-trending faults of the central Mojave accounts for ~14% of the 50 mm/yr of relative motion between the North American

and Pacific plates. With some of the relative plate motion occurring to the east of the San Andreas fault, less slip is needed west of the San Andreas fault to account for the total predicted plate motion.

TABLE 1. Rate and Orientation of Maximum Right-Lateral Shear Strain, Mojave Network, 1934-1982

	Western Region	Eastern Region
No.of Angles	64	59
$\dot{\gamma}_1$, μrad/yr	0 .16 ± 0.03	0.02 ± 0.04
$\dot{\gamma}_2$, μrad/yr	-0.02 ± 0.03	0 .04 ± 0.03
$\dot{\gamma}$, μrad/yr	0.16 ± 0.03	0.05 ± 0.03
ψ	N41°W ± 5°	unresolvable

TABLE 2. Crustal Model for the Central Mojave Desert

Depth, km	P-wave velocity, km/sec
0-5	5.3
5-10	6.1
10-25	6.3
25-30	6.7
>30	7.8

[*Fuis*,1980]

TABLE 3. Source Parameters of Earthquakes in the Central Mojave Desert

							Preferred Nodal Plane			
									Slip Vector	
Event	Date	Time, UT	Latitude, °N	Longitude, °W	Depth (±1σ), km	M_L	Strike	Dip	Azimuth	Plunge
1	June 1, 1975†	0138	34.52	116.49	2.0 ± 1.0	5.2	M20°W	70°SW	N20°W	0°
2	Nov. 16, 1975†	0743	34.29	116.33	5.5 ± 0.6	3.0	N06°W	50°W	N38°W	32°
3	Dec. 14, 1975†	1816	34.29	116.32	2.1 ± 1.0	4.7	N30°W	90°	N30°W	0°
4	May 10, 1976	1024	34.47	116.88	1.8 ± 6.0	3.6	N18°E	54°W	N46°W	50°
4*							N44°E	90°	N44°W	0°
5	June 10, 1978	2258	34.54	116.82	5.6 ± 1.5	2.7	N19°W	90°	N19°W	0°
6	April 9, 1979	1732	34.42	116.46	3.9 ± 0.8	3.5	N-S	80°W	N-S	8°
7	Jan. 16, 1983	2007	34.42	116.01	6.7 ± 0.9	3.0	N14°W	90°	N14°W	0°
8	Jan. 18, 1984	0825	34.53	116.82	1.8 ± 0.8	2.5	N38°W	80°E	S42°E	20°
8	Jan. 18, 1984	0835	34.53	116.82	1.5 ± 0.8	2.7	N36°W	80°E	S38°E	20°

* Strike-slip solution.

† *Kanamori and Fuis* [1976] and G. Fuis (personal communication, 1985).

Figure Captions

Figure 1. Major Quaternary faults in California and Nevada shown on an oblique Mercator projection about the *Minster and Jordan* [1978] RM2 rotation pole for the Pacific and North American plates (modified from *Minster and Jordan* [1984]). G, Garlock fault; M, Mojave Desert block; SA, San Andreas fault; WT, western Transverse Ranges.

Figure 2. Quaternary faults of southern California (modified from *Lienkaemper* [1985]). AM, Avawatz Mountain; DV, Death Valley fault; ETR, eastern Transverse Ranges; FC, Furnace Creek fault; G, Garlock fault; PM, Pinto Mountain fault; PV, Panamint Valley fault; SA, San Andreas fault; SN, Sierra Nevada fault zone; TM, Tehachapi Mountains. The Barstow trilateration network [*King*, 1985] and the outline of the central Mojave network are shown for reference.

Figure 3. Triangulation/trilateration network in the central Mojave Desert. Quaternary faults for the central Mojave Desert are from *Bishop* [1963] and *Rodgers* [1967]. The location of the city of Barstow is indicated by the "*B."

Figure 4. Earthquakes in the study region with $M_L \geq 3.0$ between January 1932 and June 1984. The outline of the central Mojave geodetic network and Quaternary faults from Figure 3 are shown for reference.

Figure 5. Focal mechanism solutions and P wave first motions for earthquakes 4-9 in Table 3. Solid circles indicate compressional first motions, and open circles dilatations, on equal-area projections of the lower focal hemisphere. The dashed nodal planes for events 4, 5, and 7 represent alternate solutions. Since the two mechanisms depicted for event 4 are completely different, both solutions are considered in the analysis; the strike-slip solution is referred to as event 4* in Table 3.

Figure 6. Earthquake focal mechanisms (Table 3) in the Mojave Desert region. Compressional quadrants are shaded. Faults are from Figure 3.

Figure 7a. P and T axes for the events given in Table 3. The P axes are given by solid circles and the T axes by open circles. The orientation of the most compressive principal strain direction ($N4°E \pm 5°$) indicated by the geodetic measurements is given for reference.

Figure 7b. P_f axes (see text) and the region common to the dilatational quadrants for all events. The dashed line is the upper boundary of the region if the normal faulting mechanism instead of the strike-slip solution is adopted for event 4.

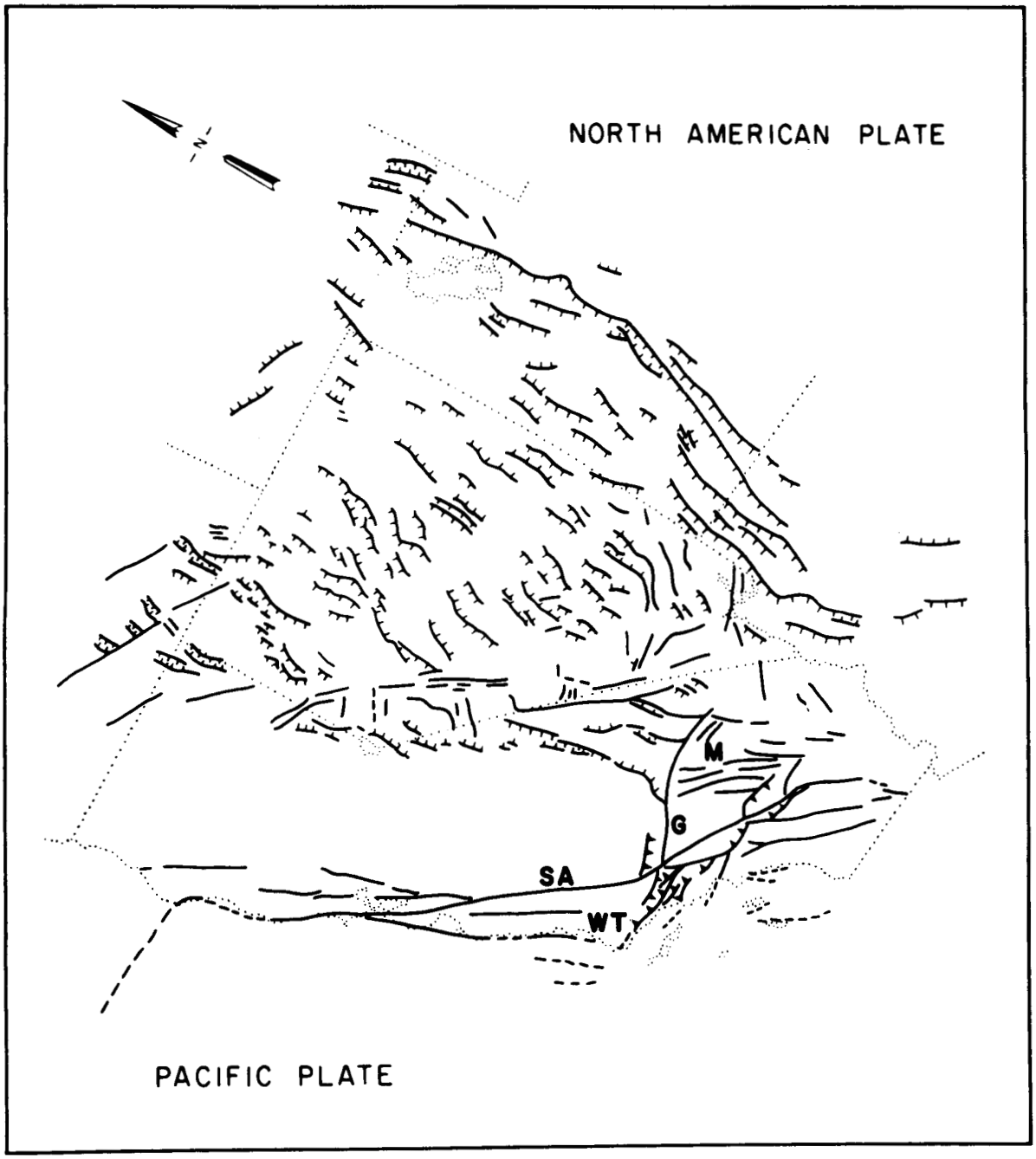

Figure 1. Major Quaternary faults in California and Nevada shown on an oblique Mercator projection about the *Minster and Jordan* [1978] RM2 rotation pole for the Pacific and North American plates (modified from *Minster and Jordan* [1984]). G, Garlock fault; M, Mojave Desert block; SA, San Andreas fault; WT, western Transverse Ranges.

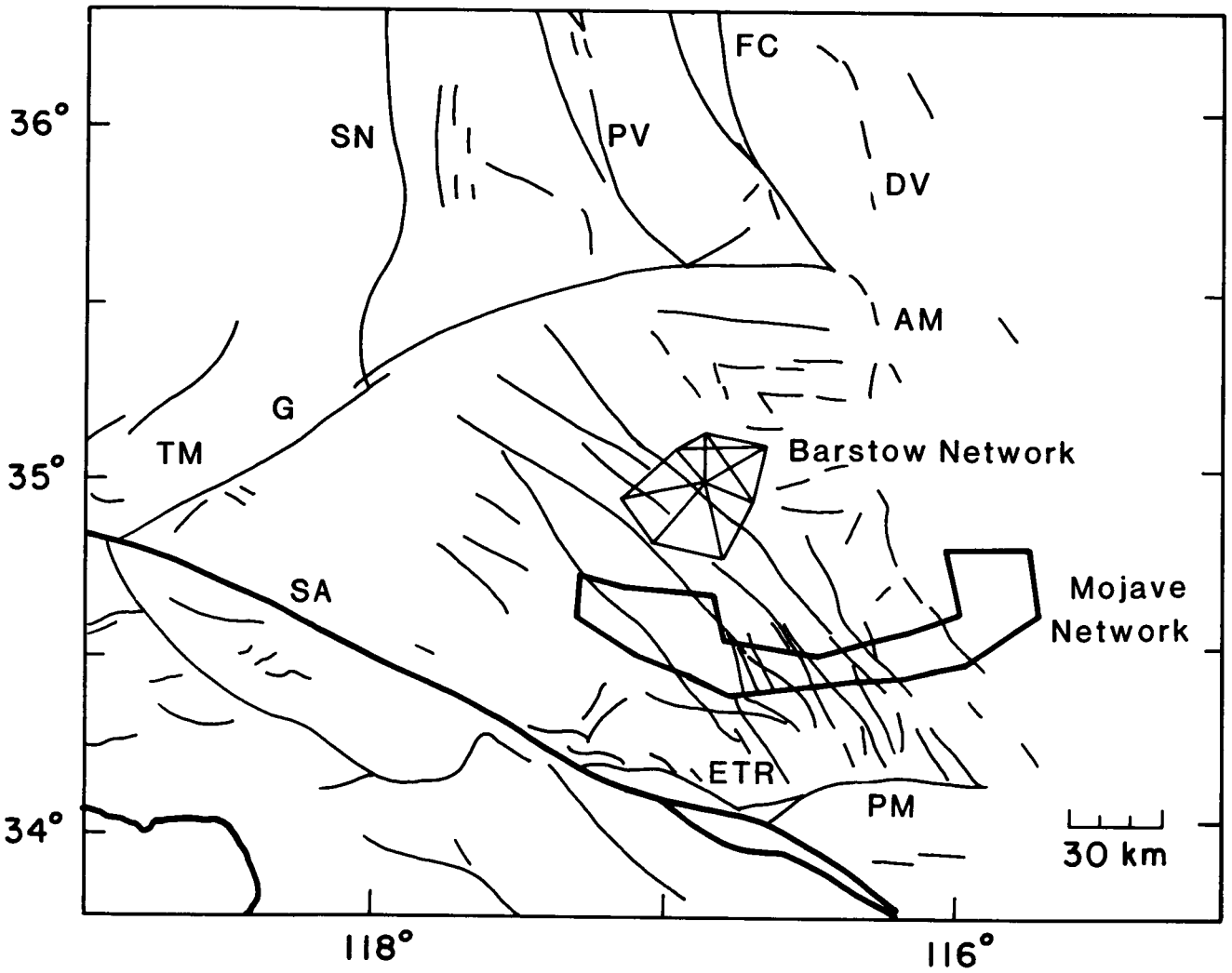

Figure 2. Quaternary faults of southern California (modified from *Lienkaemper* [1985]). AM, Avawatz Mountain; DV, Death Valley fault; ETR, eastern Transverse Ranges; FC, Furnace Creek fault; G, Garlock fault; PM, Pinto Mountain fault; PV, Panamint Valley fault; SA, San Andreas fault; SN, Sierra Nevada fault zone; TM, Tehachapi Mountains. The Barstow trilateration network [*King*, 1985] and the outline of the central Mojave network are shown for reference.

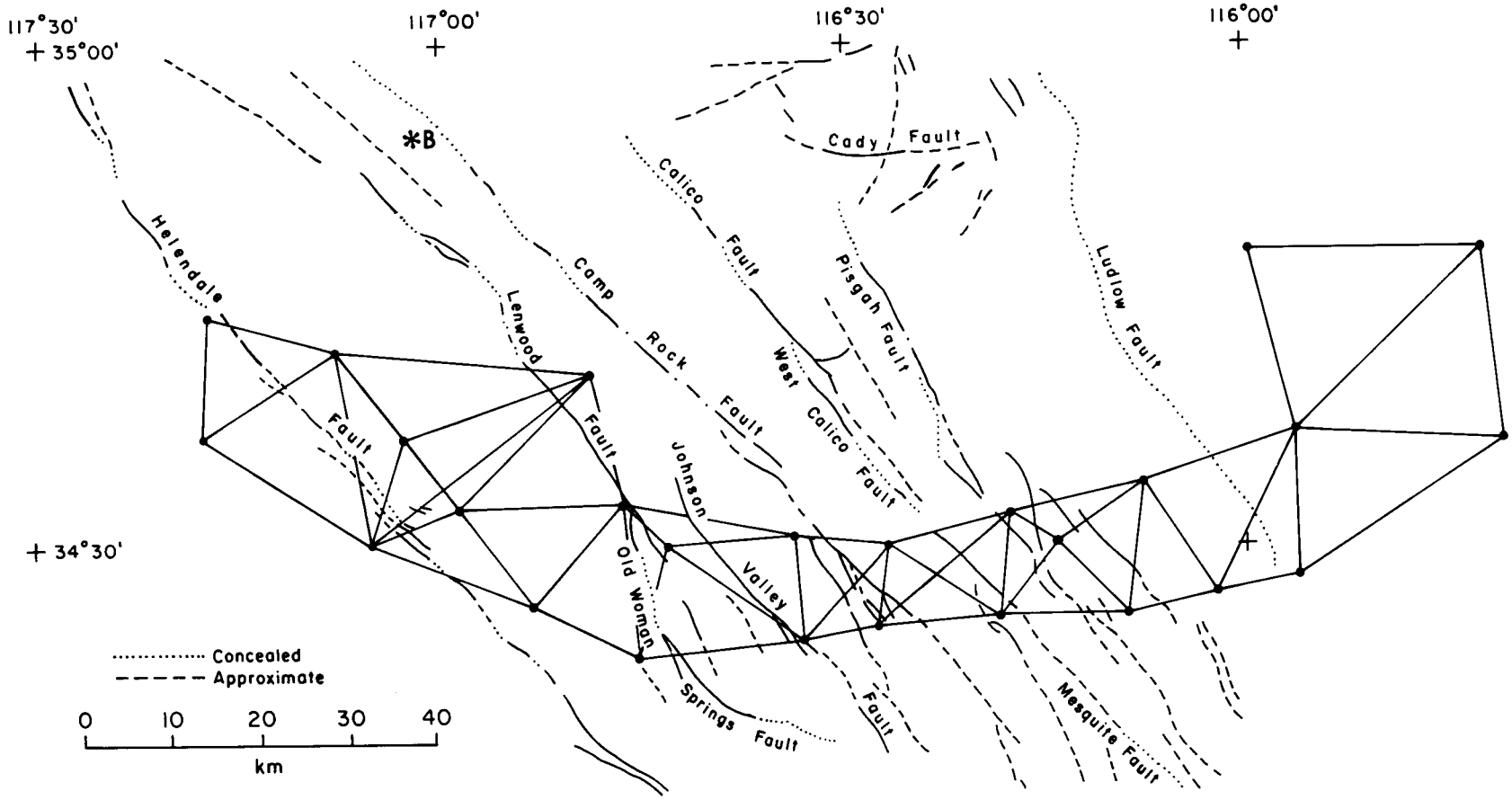

Figure 3. Triangulation/trilateration network in the central Mojave Desert. Quaternary faults for the central Mojave Desert are from *Bishop* [1963] and *Rodgers* [1967]. The location of the city of Barstow is indicated by the "*B."

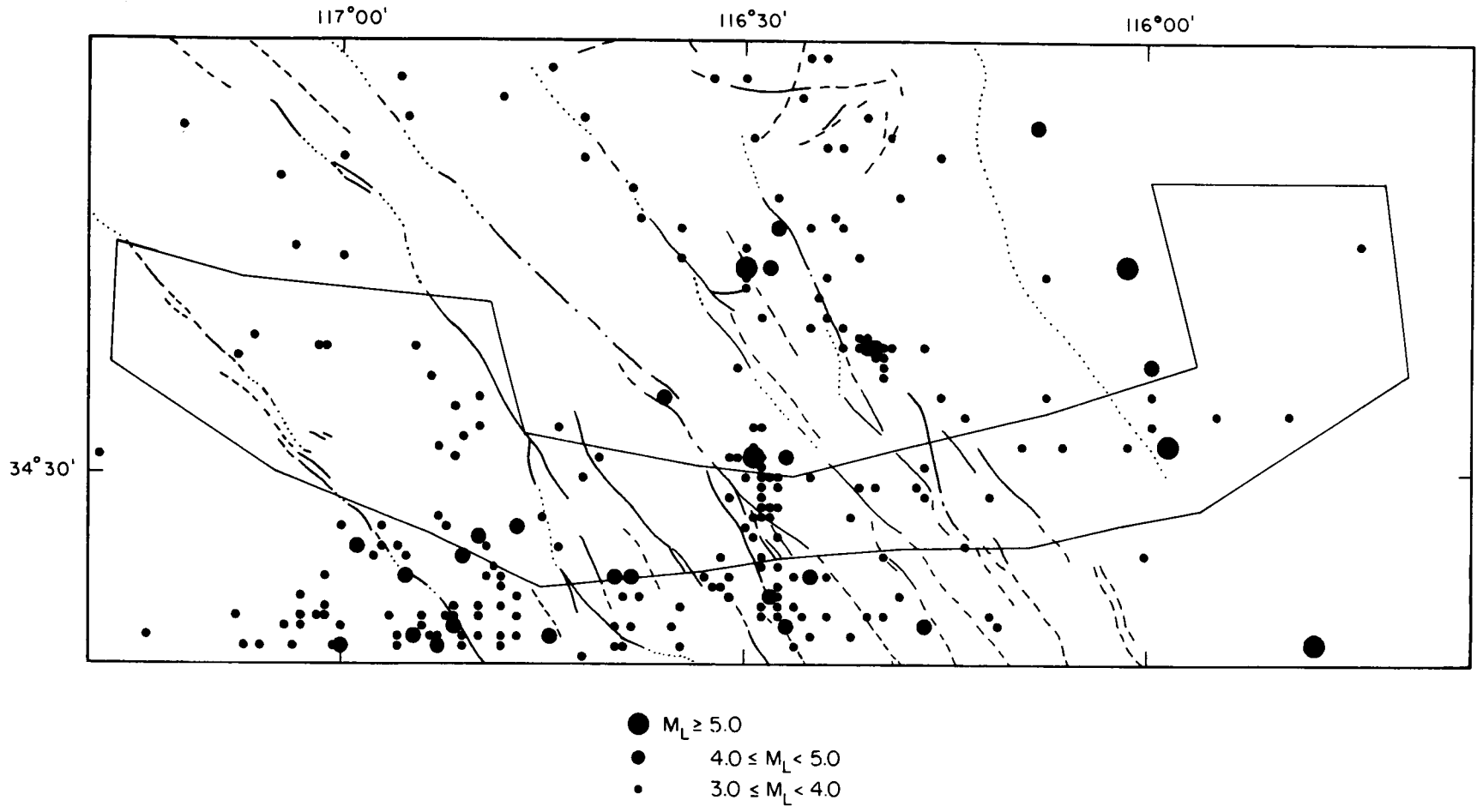

Figure 4. Earthquakes in the study region with $M_L \geq 3.0$ between January 1932 and June 1984. The outline of the central Mojave geodetic network and Quaternary faults from Figure 3 are shown for reference.

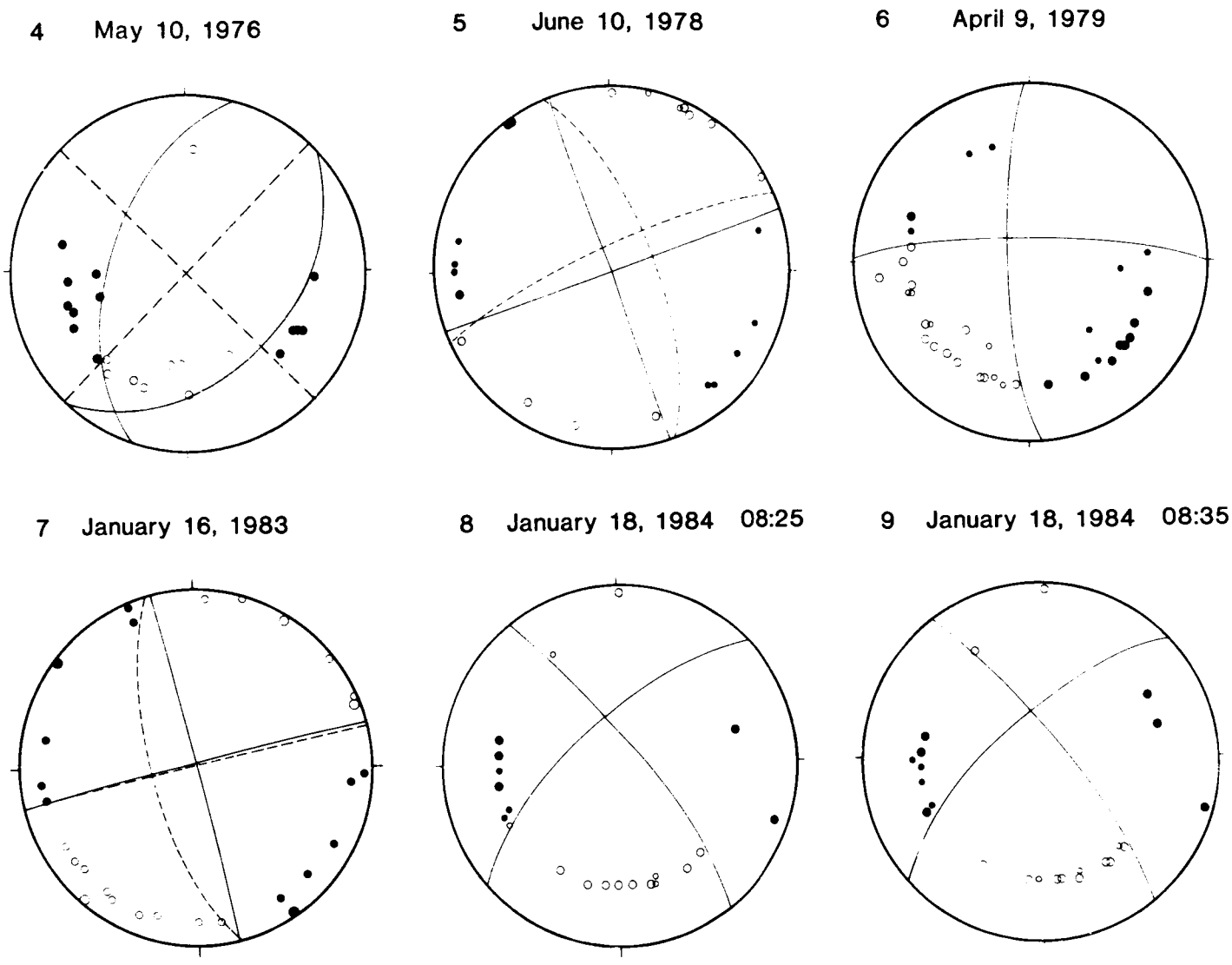

Figure 5. Focal mechanism solutions and P wave first motions for earthquakes 4-9 in Table 3. Solid circles indicate compressional first motions, and open circles dilatations, on equal-area projections of the lower focal hemisphere. The dashed nodal planes for events 4, 5, and 7 represent alternate solutions. Since the two mechanisms depicted for event 4 are completely different, both solutions are considered in the analysis; the strike-slip solution is referred to as event 4* in Table 3.

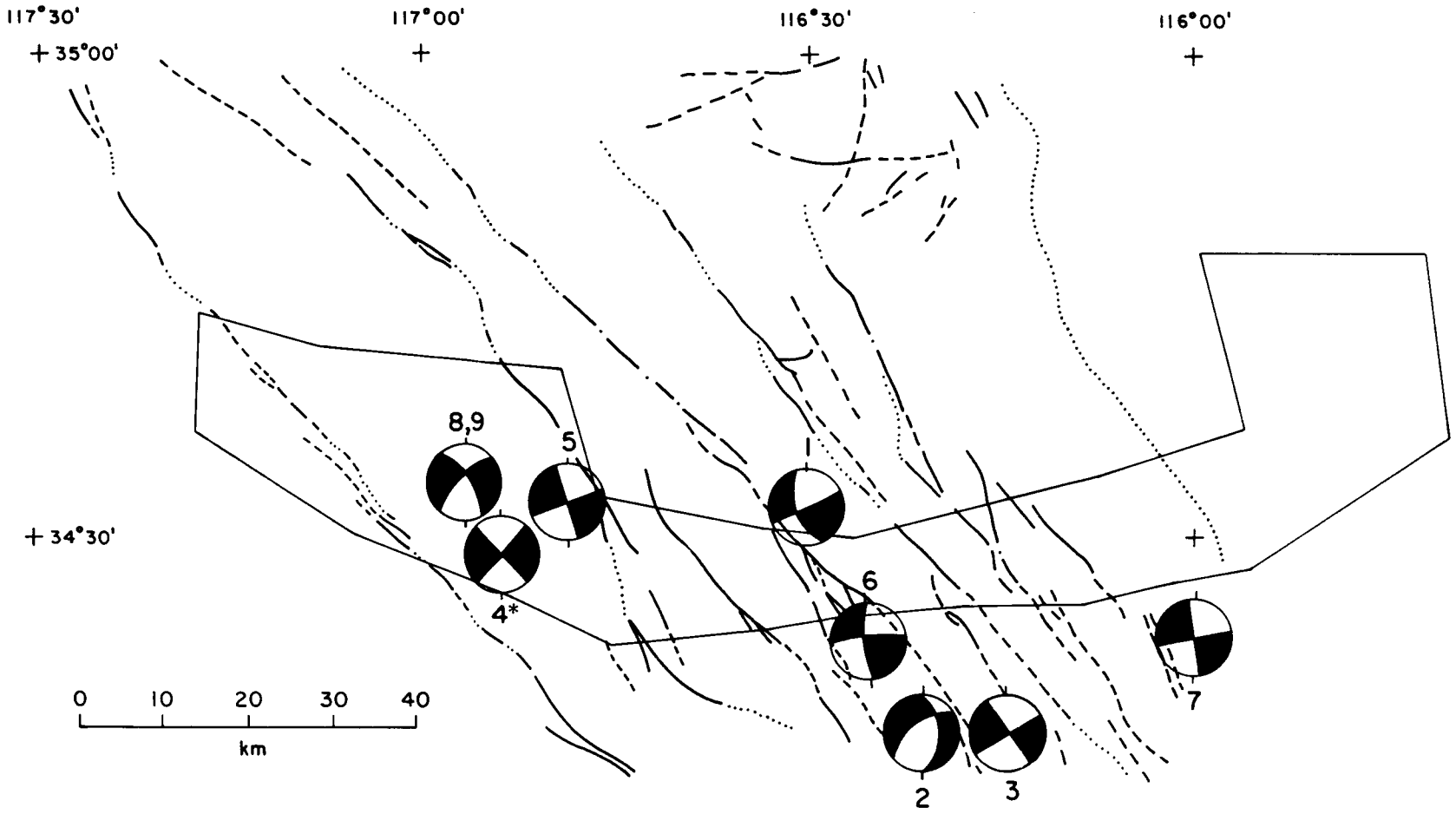

Figure 6. Earthquake focal mechanisms (Table 3) in the Mojave Desert region. Compressional quadrants are shaded. Faults are from Figure 3.

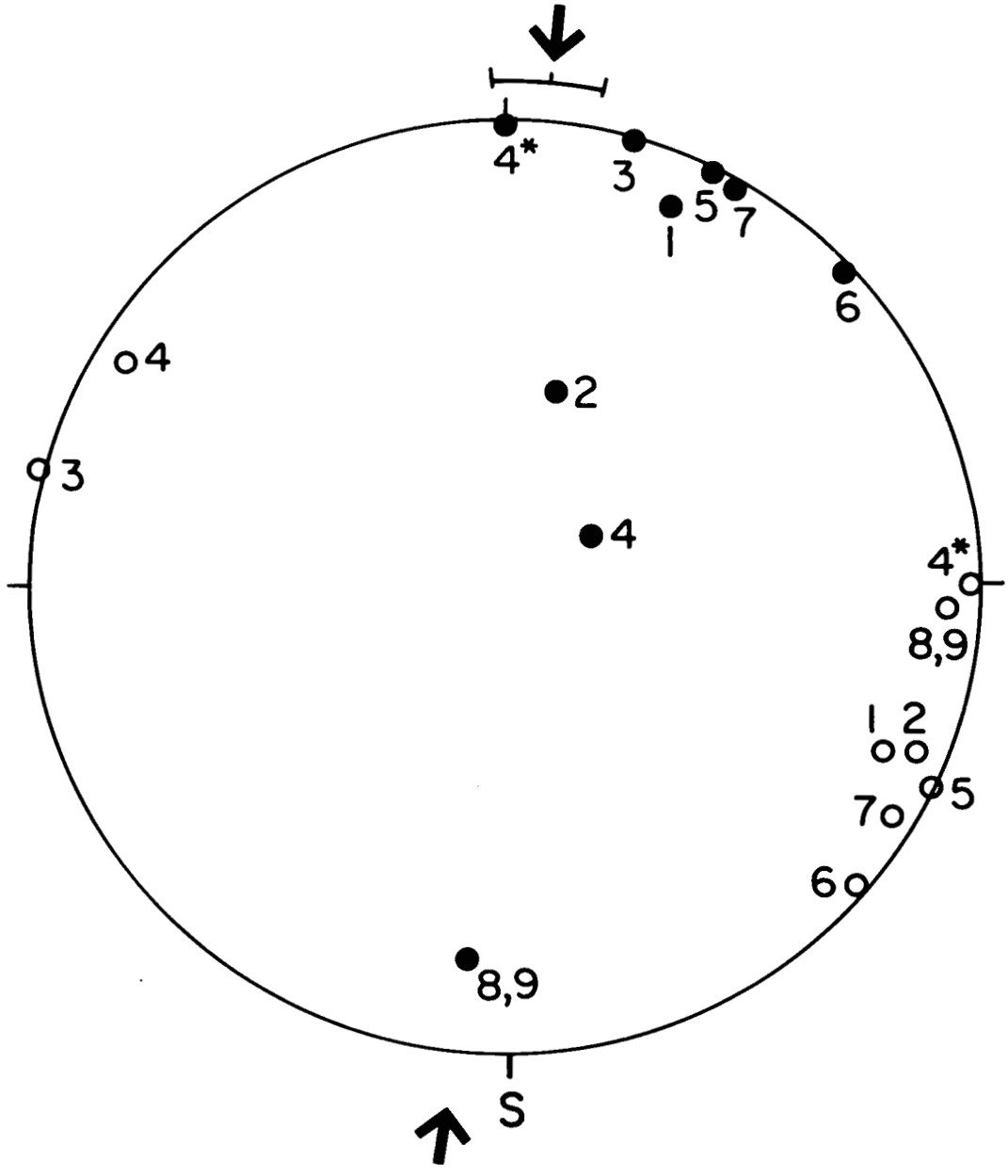

Figure 7a. P and T axes for the events given in Table 3. The P axes are given by solid circles and the T axes by open circles. The orientation of the most compressive principal strain direction (N4°E ± 5°) indicated by the geodetic measurements is given for reference.

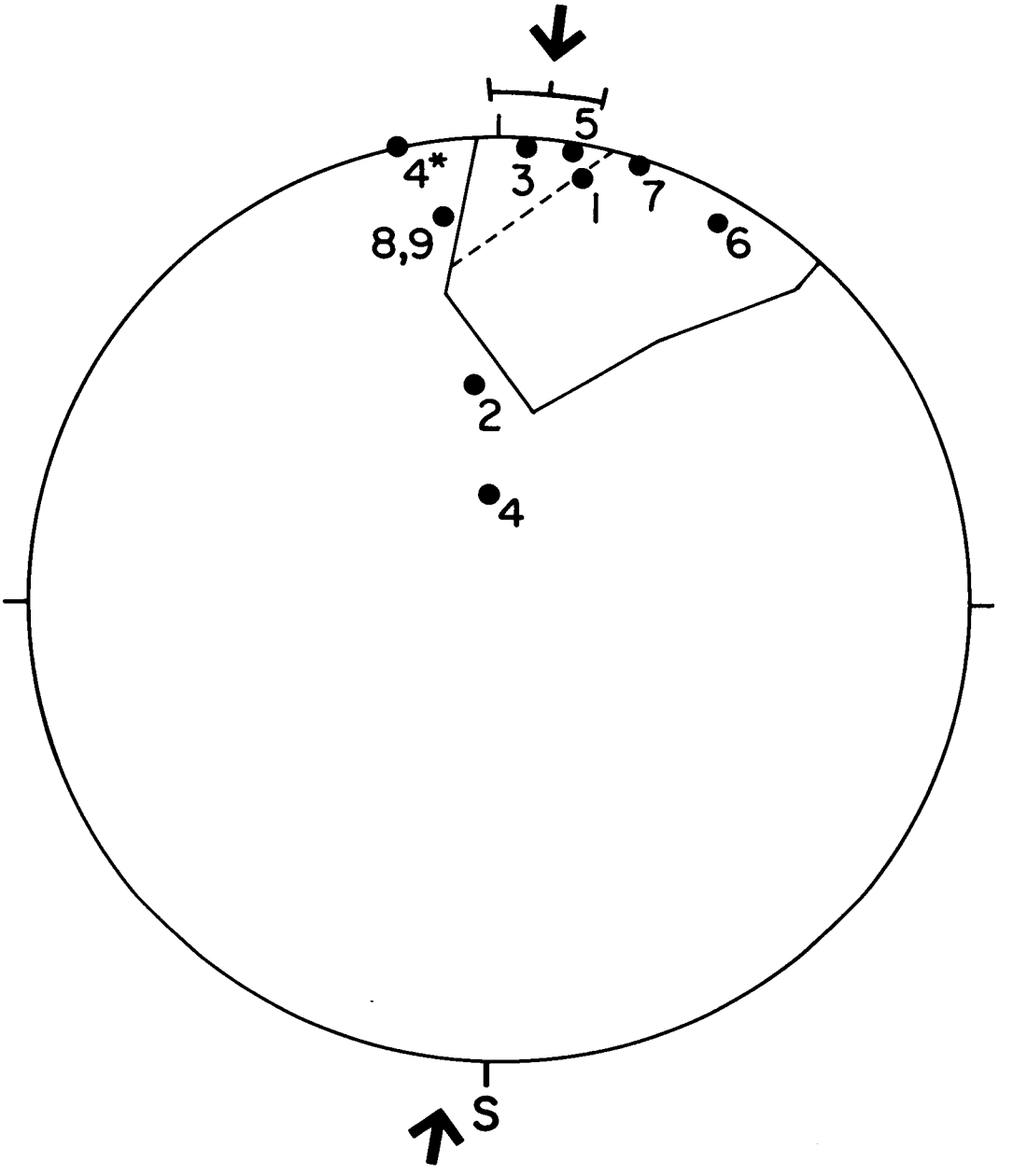

Figure 7b. P_f axes (see text) and the region common to the dilatational quadrants for all events. The dashed line is the upper boundary of the region if the normal faulting mechanism instead of the strike-slip solution is adopted for event 4.

Chapter 3. Geodetic Measurement of Deformation East of the San Andreas Fault in Central California

Introduction

Although most of the relative motion between the Pacific and North American plates in central California is accommodated by slip along the San Andreas fault, distributed compressive and right-lateral strike-slip motion also occurs on faults with surface traces subparallel to the San Andreas fault located between the continental escarpment and the Great Valley [*Gawthrop*, 1977; *Page*, 1981; *Crouch et al.*, 1984; *Eaton*, 1984; *Minster and Jordan*, 1984, 1987; *Namson and Davis,* 1988]. The axis of greatest compression across this region, the southern Coast Ranges subprovince [*Page*, 1981], is thought to be oriented nearly perpendicular to the trend of the San Andreas fault, a result attributed to a combination of slightly convergent relative motion between the Pacific and North American plates and low shear strength along the fault zone [*Mount and Suppe*, 1987; *Zoback et al.*, 1987]. While most recent earthquakes in central California are located on the San Andreas fault (Figure 1), scattered diffuse activity also occurs between the San Andreas fault and the Great Valley. The May 1983 Coalinga earthquake (M_L=6.7), which involved slip on a thrust or reverse fault beneath a young surface fold [*Stein and King*, 1984; *Stein*, 1985], has focused attention on the importance of understanding the state of stress and the rates of deformation to the east of the San Andreas fault in this region and their relation to the overall deformation in the Coast Ranges. In this chapter I determine rates of crustal strain in the Diablo Range north of Coalinga from a triangulation and trilateration network and from line-length changes determined by means of trilateration measurements within 10 km of the San Andreas fault. These geodetic results are then compared with other geological and geophysical data to characterize the nature of deformation across the southern Coast Ranges.

Tectonic Setting

The principal strike-slip faults in central California have been well characterized by geologic and geodetic studies. The branched system of subparallel faults near Hollister coalesces southward into a single shear zone, the San Andreas fault, south of Hepsedam (Figure 2). The Calaveras fault is the primary active fault to the northeast of the San Andreas fault near Hollister, while to the southeast of Hollister several faults comprise the southern end of the Calaveras fault zone, among which the Paicines fault is most prominent. Horizontal deformation across the San Andreas and Calaveras-Paicines faults in central California has been measured with near-fault alinement arrays, creepmeters, and trilateration at short and intermediate distances [*Savage and Burford*, 1973; *Thatcher*, 1979a; *Burford and Harsh*, 1980; *Lisowski and Prescott*, 1981]. Between Hollister and Hepsedam (Figure 2), the rate of steady surface slip (creep) across the San Andreas fault increases from ~ 13 to 32 mm/yr and surface slip on the Calaveras-Paicines fault decreases from ~17 to 0 mm/yr. Between Hepsedam and the latitude of Coalinga (Figure 2) near-fault and intermediate-scale geodetic measurements of right-lateral slip are in good agreement and indicate creep at a rate of approximately 32 mm/yr. The rate of slip on this segment of the San Andreas fault estimated from Holocene geological data is 34 ± 3 mm/yr [*Sieh and Jahns*, 1984] at an azimuth of N41°W $\pm$ 2° [*Minster and Jordan*, 1984; *Mount and Suppe*, 1987]. Southward of the latitude of Coalinga shallow slip on the San Andreas fault decreases and the width of the zone of deformation increases over the transition to a locked segment of the San Andreas fault in the Carrizo Plain (the southern aseismic portion of the San Andreas in Figure 1).

The major structural features in the region of this study are shown in Figures 2 and 3. Within 5-10 km to the east of the San Andreas fault the primary geologic structures are related to dextral shear on the San Andreas and Calaveras-Paicines faults (Figure 2). The Diablo Range to the east of this region is a broad antiform which trends approximately

N65°W [*Page*, 1985] and encompasses subsidiary fold structures such as the Vallecitos syncline (Figure 3). North of Coalinga the range is pierced by the New Idria diapir (Figure 3) of serpentine and Franciscan rocks. Along the northeast boundary of the study area is the Ortigalita fault (Figure 2), a high-angle fault along or near the contact of Franciscan rocks and the Great Valley sequence to the east [*Raymond*, 1973]. Trenching of the Ortigalita fault zone shows exposed offsets of late Pleistocene and Holocene soils, with possibly as much as 5 km of Quaternary right-slip displacement [*Hart et al.*, 1986].

Multiple phases of deformation in the Diablo Range have been documented by structural analysis [*Namson and Davis*, 1988]. *Harding* [1976] pointed out that there are folds of middle to late Miocene age which are synchronous with the initiation of displacement on the San Andreas fault. The most recent uplift of the Diablo Range began in Pliocene time and most likely accelerated in the Pleistocene [*Page*, 1981; *Page and Engebretson*, 1984]. The Quaternary (< 2.2 Ma) folding is more widely distributed and of much greater structural relief than the Miocene folds [*Namson and Davis*, 1988].

Focal mechanisms of earthquakes in the Diablo Range [*Eaton*, 1985] show a mixture of thrust, reverse, and strike-slip faulting. The locations of three of the larger earthquakes with well-determined focal mechanisms, the October 1982 Idria event (M_L=5.5), the May 1983 Coalinga event (M_L=6.7), and the August 1985 North Kettleman Hills event (M_L=5.5), are given in Figure 1. The focal mechanism determined for the Idria earthquake indicates thrust faulting on a plane oriented N72°E or reverse slip on a plane oriented N64°W [*Eaton*, 1985]. The Coalinga and Kettleman Hills events have similar focal mechanisms with slip occurring on fault planes oriented at about N53°W as either thrusting on a plane dipping shallowly to the southwest or reverse slip on a plane steeply dipping to the northeast [*Eaton*, 1985; J.P. Eaton, personal communication, 1987]. A preliminary focal mechanism determined for an earthquake which occurred on the Ortigalita fault on January 6, 1988 (M_L=3.7), indicates right-lateral slip on a fault plane oriented ~N25°W or

left-lateral slip on a plane oriented N65°E (P.A. Reasenberg, personal communication, 1988). The earthquake focal mechanisms and geological structures in the area suggest two primary modes of deformation to the northeast of the San Andreas fault: compression normal to the major fold structures of the region and right-lateral strike-slip motion on faults such as the Calaveras-Paicines and the Ortigalita.

By way of comparison, in the Coast Ranges to the west of the San Andreas fault focal mechanisms [*Gawthrop*, 1977; *Eaton*, 1984; *Dehlinger and Bolt,* 1987] and extensive geological mapping [summarized in *Crouch et al.*, 1984; *Slemmons*, 1987] suggest variable modes of deformation. Between the San Andreas and the Rinconada faults (Figure 1) is the seismically quiescent Salinian block. The upper crust is composed of high-strength granite which is only weakly folded and sparsely faulted [*Dehlinger and Bolt,* 1987; *Slemmons*, 1987]. Focal mechanisms from the Rinconada fault show a mixture of right-lateral strike-slip faulting on northwest striking planes, oblique slip, and reverse faulting [*Gawthrop*, 1977; *Dehlinger and Bolt,* 1987]. From field mapping of recent offsets, D.B. Slemmons (personal communication, 1987) and E.W. Hart (personal communication, 1988) suggest that right-lateral strike-slip faulting dominates the displacement along the Rinconada fault. Between the Rinconada and the San Gregorio-Hosgri faults (Figure 1) the upper crust consists of the very heterogeneous Franciscan complex. Focal mechanisms from this region indicate dominantly oblique reverse faulting along northwest-trending, northeast dipping planes, with P axes oriented N20°-50°E or S20°-50°W [*Dehlinger and Bolt,* 1987]. Significant late-Quaternary right-lateral strike-slip offsets have been measured on the San Gregorio fault [*Clark et al.*, 1984]. South of Monterey Bay this fault branches into several splays, with some branches showing primarily right-lateral strike-slip displacement and others showing east-up reverse faulting [*Hamilton*, 1987]. Focal mechanisms from the San Gregorio-Hosgri fault also indicate

right-lateral strike-slip faulting and oblique reverse faulting with a right-lateral component on a northeast dipping plane [*Gawthrop*, 1977; *Eaton*, 1984; *Dehlinger and Bolt*, 1987].

Geodetic Strain Rates

We make use of two geodetic networks to estimate current rates of deformation to the east of the San Andreas fault in central California. The San Benito triangulation and trilateration network spans the Paicines fault zone just east of the San Andreas fault, extends eastward to the western margin of the Great Valley, and is 50 km in extent in the southeast-northwest direction across the Diablo Range (Figure 3). To examine more localized deformation within the zone 10 km to the east of the San Andreas fault, short and intermediate range lines from the U.S. Geological Survey (USGS) Coalinga trilateration network were utilized. The geodetic results derived from the Coalinga trilateration data provide an update to the slip rates estimated for the Calaveras and Paicines faults by *Lisowski and Prescott* [1981].

To distinguish between engineering and tensor shear strain, we denote the former by γ and give in units of μrad, whereas the latter is denoted by ε and is given in units of μstrain [*Savage*, 1983]. Uncertainties, where not otherwise stated, are one standard deviation (σ).

San Benito Network

A triangulation survey of the San Benito network was conducted in 1962 by the National Geodetic Survey, and in 1982 a trilateration survey of the San Benito network was performed by the USGS. For interstation visibility, triangulation and trilateration stations are situated on the highest points in a region; thus, many of the stations in the San Benito network are located near anticlinal peaks (Figure 2). To determine the rates of deformation from the San Benito data the observations were processed utilizing two

independent procedures: an extended version of Frank's method [*Prescott*, 1976] and the DYNAP method [*Snay*, 1986; *Drew and Snay*, 1988]. In the Appendix we discuss the accuracy of the triangulation and trilateration measurements utilized in this study, the assumptions made in our estimation of the horizontal shear parameters, the considerations involved in combining triangulation and trilateration data to determine the rate of shear strain utilizing the Prescott and DYNAP methods, the corrections applied to reduce the triangulation and trilateration observations to a common reference system, and the methods used to estimate the deflection of the vertical and the geoid - reference ellipsoid separation needed to make the reduction corrections.

Utilizing both methods we calculate the horizontal shear strain rate components $\dot{\gamma}_1$ and $\dot{\gamma}_2$. In terms of elements of the strain tensor ε_{ij}, $\gamma_1 = \varepsilon_{11} - \varepsilon_{22}$ and $\gamma_2 = \varepsilon_{12} + \varepsilon_{21}$, where the strain tensor is referred to a geographic coordinate system in which the 1-axis is directed east and the the 2-axis is directed north. The strain component γ_2 is equal to the decrease induced by strain in the right angle between northward- and eastward-directed lines, whereas γ_1 is equal to the increase in the angle between lines directed northwest and northeast. Results are generally given in terms of the maximum shear strain rate $\dot{\gamma}$, where $\dot{\gamma}^2 = \dot{\gamma}_1^2 + \dot{\gamma}_2^2$, and the orientation ψ of the vertical plane with maximum rate of right-lateral shear [*Frank*, 1966; *Prescott*, 1976]. For comparison with the trends of fold structures of the Diablo Range, the orientation β of the maximum rate of compressive strain is sometimes given instead of the orientation of maximum rate of right-lateral shear.

Results with Prescott's method. The observations used to estimate $\dot{\gamma}_1$ and $\dot{\gamma}_2$ in the extended version of Frank's method [*Prescott*, 1976] are changes in angles. In this study we determined angle changes from two different data types, reflecting the different types of surveys made in 1962 and 1982. Further, we compared angles measured on the Earth's surface to angles determined from a network adjustment on a reference ellipsoid. In using

data derived from different measurement techniques it is preferable to reduce the data to a common reference surface. The required reduction corrections are discussed in the Appendix. In employing Prescott's procedure to determine the strain parameters we did not make these corrections. In our use of the alternative DYNAP method these corrections are performed, and we compare the results from the two techniques to illustrate in part the utility of making these corrections.

The angle changes associated with the stations Bitter, Hepsedam, and Panoche were significantly larger than angle changes from other portions of the network and were, therefore, examined separately. Bitter and Hepsedam are located near the Paicines fault zone. Using only the 11 angle measurements that include one of the stations Bitter or Hepsedam gives $\dot{\gamma} = 0.56 \pm 0.16$ μrad/yr and Ψ = N28°W ± 11° The shear strain rate across the approximately 10- km-wide zone to the northeast of stations Bitter and Hepsedam, assuming right-lateral motion on the Paicines fault, implies a rate of slip of 5 ± 2 mm/yr. Additional geodetic data from the Coalinga trilateration network relating to deformation across the San Andreas and Calaveras-Paicines faults is discussed in the next section.

The relatively large angle changes around station Panoche are not so easily explained. Using only the seven angle changes that include Panoche gives $\dot{\gamma} = 0.76 \pm 0.27$ μrad/yr and ψ = N58°W ± 9°, or β = N13°W ± 9°. These results are not consistent with either shear strain across the Ortigalita fault zone or contraction across the major fold structures of the region.

The strain rate parameters estimated on the basis of 25 angle changes in the central portion of the San Benito network, excluding angles to Bitter, Hepsedam, or Panoche, were $\dot{\gamma} = 0.15 \pm 0.08$ μrad/yr and β = N16°E ± 14°, or ψ = N29°W ± 14°. The standard deviations reflect both misfit and data uncertainties due to measurement imprecision.

To search for significant strain inhomogeneity, the shear strain parameters were estimated from spatial subsets of these data, again excluding the Bitter, Hepsedam, and Panoche stations (Table 1). There is a trade-off between improving the precision of the strain estimate by using a larger number of angles and averaging spatial variations as the size of the sampled region is increased. The data were first broken into two distinct groups, one set closer to the Great Valley ("east") and one set closer to the San Andreas fault ("west"). If the measured rates of shear strain were due to strain accumulation on the adjacent San Andreas fault, the rate of shear strain would be higher in the western subnet. Alternatively, if the rate of compressive strain was higher across the folds near the Great Valley, the eastern subnet might show a higher shear strain rate. There is no suggestion of a significant rate difference, however, between the strain rates determined from the eastern and western data subgroups. The set of 25 angles were also divided into "north" and "south" sets to look for any change which might be associated with along-strike variations on the San Andreas and Calaveras-Paicines faults. Although the strain rate results differ in the subnets, particularly in the orientation of maximum rate of compression, the magnitudes and orientations of strain rate in the various subregions are not significantly different from the average values determined from the complete set of 25 angles.

Results with the DYNAP method. In a second approach, the directions observed in 1962 and the distances measured in 1982 were employed to solve simultaneously for crustal motion parameters and the horizontal positional coordinates of the geodetic stations using the DYNAP method [*Snay*, 1986; *Drew and Snay*, 1988]. With DYNAP we are able to make single epoch adjustments to search for any observational errors during the individual surveys, and we are able to evaluate the effect of making reduction corrections to the distance and direction observations.

We first performed separate network adjustments for 1962 and 1982. A particular solution was determined by holding the minimum number of free parameters fixed. For the two-dimensional adjustment of 1962 triangulation data, these free parameters are two components of translation, a network rotation, and scale. For the two-dimensional adjustment of the 1982 trilateration data, scale is not a free parameter. Examination of the largest standardized residuals (given by the difference between observed and calculated values divided by the standard deviation of the observation) indicates that the 1962 direction observations to the station Panoche have large residuals. This may account for the anomalously large angle changes associated with Panoche discussed earlier. Large residuals are not systematically associated with any one station in the 1982 adjustment.

From the analysis utilizing the Prescott method we obtained the result that the angle changes associated with the stations Bitter and Hepsedam were consistent with right-lateral slip at the approximate orientation of the Paicines fault. To test this result we solved for strain parameters and horizontal coordinates for a small subnetwork consisting of Bitter, Hepsedam, Smoker, and Ley (Figure 2) using DYNAP. The rate of shear strain was estimated to be 0.53 ± 0.35 μrad/yr with $\psi = \text{N40°W} \pm 19°$, similar to the orientation of the San Andreas and Paicines faults.

The shear strain rate parameters $\dot{\gamma}_1$ and $\dot{\gamma}_2$ were estimated by the DYNAP method using data from the central portion of the network (excluding measurements to Panoche, Bitter and Hepsedam). Without taking into account corrections the rate of shear strain $\dot{\gamma} = 0.15 \pm 0.09$ μrad/yr and $\beta = \text{N17°E} \pm 16°$, similar to the result obtained utilizing Prescott's method. The rate of shear strain determined using the corrected data is $\dot{\gamma} = 0.19 \pm 0.09$ μrad/yr, with $\beta = \text{N16°E} \pm 13°$ (Figure 4).

As shown in Figure 4, at the 95% confidence level $\dot{\gamma}$ is not significantly greater than zero and β is not significantly different from the orientation predicted for shear strain associated with slip on the San Andreas fault (N4°E). The orientation β, however, is

similar to the direction of maximum compressive strain indicated by the orientation of major fold structures in this region. If we assume that the strain represents uniform horizontal contraction across a 30-km-wide region in the direction N16°E and that there is no extension in the orthogonal direction, this average strain rate corresponds to 5.7 ± 2.7 mm/yr of shortening.

The error in the estimate of shear strain rate determined in this study is dominated by the less accurate triangulation survey (see Appendix). It is instructive to estimate the accuracy that could be achieved with an additional trilateration or GPS survey of this network. An additional trilateration survey of all the stations in the San Benito network in 1992, for instance, would provide ~0.02 μstrain/yr accuracy in the principal strains, and all of the horizontal components of the tensor rate of strain ($\dot{\varepsilon}_{ij}$) could be estimated. At this level of accuracy we could better constrain the rate of crustal deformation across the Diablo Range as well as discern spatial variations in the deformation field.

Coalinga Trilateration Network

We have employed short and intermediate-length lines from the Coalinga trilateration network (Figure 2) to update previous estimates [*Lisowski and Prescott,* 1981] of the slip rates on the Calaveras and Paicines faults. Since 1972 trilateration measurements have been made periodically by the USGS in central California on a regional scale spanning a 20-km-wide zone centered on the San Andreas fault and including several distinct faults, as well as on smaller (1-2 km) aperture networks that span a single fault (Pionne, Dry Lake and Tully nets). The estimated accuracy in the line lengths determined from the short-range measurements is 4 mm [*Lisowski and Prescott,* 1981]. The estimates of line-length change made by *Lisowski and Prescott* [1981] also included earlier data collected by the California Division of Mines and Geology, but we have utilized only the more homogeneous set of USGS data.

For the region within 10 km to the east of the San Andreas fault we assume that the predominant mode of crustal deformation is right-lateral fault slip on the Calaveras-Paicines fault system. This is equivalent to the assumption that the measured deformation in this region is due neither to elastic strain accumulation that will be released episodically in earthquakes on the adjacent San Andreas fault nor to crustal shortening normal to the San Andreas fault. Several lines of reasoning support this assumption. As discussed above, on the segment of the San Andreas fault adjacent to the San Benito network, fault slip occurs primarily by steady creep, and we expect little right-lateral shear strain accumulation associated with the San Andreas fault to be measured on off-fault geodetic lines. In addition, elastic strain accumulation associated with the San Andreas fault would be measurable geodetically on both sides of the fault, yet to the west of the San Andreas fault the maximum right-lateral shear strain within the Salinian block, estimated from triangulation data measured during the time interval 1944-1963, is poorly resolved and is not oriented parallel to the San Andreas fault [*Thatcher*, 1979a]. An alternative mode of deformation adjacent to the San Andreas is compression across structures such as the Paicines syncline (Figure 3). Strike-slip motion across this region would shorten north-south lines and extend east-west lines, whereas contraction would shorten northeast-southwest lines. Line length changes in the Pionne short-range network and the lines from Bitter to Hepsedam and Browns to Cross are consistent with the hypothesis of right-lateral slip on the Calaveras-Paicines fault system. As discussed above, results from the San Benito geodetic subnetwork that includes measurements to Bitter and Hepsedam are most consistent with right-lateral shear at the orientation of the San Andreas and Paicines fault.

If the deformation in this region occurs as rigid block motion along the Calaveras-Paicines fault system, the observed length changes can be converted into a fault-parallel displacement rate from the slope of the least-squares linear fit to the interstation length data [*Prescott and Lisowski,* 1983]. The slip rates determined from lines crossing the fault at a

low angle are given in Table 2 for the Calaveras-Paicines region just south of Hollister and for the Paicines fault zone between Bitter and Coalinga. The sum of the slip rate determined from the station pairs that cross only the San Andreas fault (Cross-Chalone and Chalone-Bitter lines) and the slip rate from pairs that are completely east of the San Andreas fault (Browns-Cross and Bitter-Hepsedam) are approximately equal to the slip rate from station pairs that span both fault zones (Browns-Chalone and Chalone-Hepsedam lines). The line length changes across the Calaveras-Paicines fault zone are consistent with ~10 mm/yr of right-lateral slip. The rate of slip estimated for the Paicines fault south of the city of San Benito is 4 ± 1 mm/yr.

The Bitter to Hepsedam line showed a significant change in slope beginning in mid-1978. This change corresponded to an increase in the rate of slip on the Calaveras-Paicines system and a decrease in slip rate on the San Andreas fault. A similar change after 1979 in the slip rates for the Calaveras and San Andreas faults has been inferred from geodetic measurements of the USGS Hollister trilateration network [G. Gu and J. C. Savage, personal communication, 1986; *Matsu'ura et al.*, 1986]. The increase in slip on the Calaveras Paicines fault approximately coincided with the occurrence of the 1979 Coyote Lake earthquake (M_L=5.7) on the northern Calaveras fault. The rate of line length change, $\dot{L}$, between Bitter and Hepsedam for the 1973-1978 time period was 1 ± 1 mm/yr [*Lisowski and Prescott*, 1981]. The higher rate of slip given in Table 2 thus is largely due to the increased rate during 1978-1984.

The average fault slip indicated by the three short-range networks (Figure 2), again assuming simple block motion, is given in Table 3. The rate of slip on the Pionne net, 12 $\pm$ 2 mm/yr, is similar to the rate estimated from the line between Cross and Browns which crosses the Calaveras-Paicines fault zone (10 ± 1 mm/yr). Between the Dry Lake and Tully networks the rate of creep on the San Andreas fault increases from 27 ± 2 to 32 ± 1 mm/yr. South of the Tully network the rate of slip determined from near-fault data on the San

Andreas fault is the same as the rate estimated from the Chalone to Hepsedam line [*Prescott and Lisowski,* 1981].

The short and intermediate-range trilateration measurements document a transfer of slip associated with the Calaveras-Paicines fault zone to the San Andreas fault. The narrowing of the region that accommodates the ~32 mm/yr slip rate also corresponds to a transition from a complex multi-stranded portion of the fault system with locked segments that break in periodic moderate-to-large earthquakes to a geometrically simpler segment that accommodates slip through creep.

Comparison with Other Geodetic and Geologic Observations

As noted above, the strain rate parameters estimated on the basis of angle changes in the central portion of the San Benito network are $\dot{\gamma} = 0.19 \pm 0.09$ μrad/yr and $\beta = \text{N16°E} \pm 13°$, or $\psi = \text{N29°W} \pm 13°$. Interpreted in terms of uniform horizontal contraction in the direction given by the angle β, the rate of shortening is 5.7 ± 2.7 mm/yr. Although there is no significant strain at the 95% confidence limit, the orientation of the principal strain directions are consistent with the geological structures of the region (Figure 3). The azimuth of the least compressive strain (N74°W ± 13°) is close to the trend of the major fold structures of the region (N65°W). The direction of maximum rate of right-lateral shear is also close to the trend of the major strike-slip faults of the region.

From a geological reconstruction of the structures between the Great Valley and the San Andreas fault at the approximate latitude of Coalinga, *Namson and Davis* [1988] inferred that 11 km of late Cenozoic shortening has occurred perpendicular to the San Andreas fault. If active folding commenced 5 m.y. ago, the average rate of shortening has been 2.2 mm/yr. If folding began as recently as 2 m.y. ago an average rate of shortening of 5.5 mm/yr is implied. These figures are comparable to the geodetically inferred rate.

The rate of slip obtained in this study for the Calaveras-Paicines fault zone south of Hollister is 10 ± 1 mm/yr (Browns to Cross, Table 2) and 12 ± 2 mm/yr (Pionne net, Table 3). These slip rates may be compared to other estimates of slip rate derived from geological and geodetic observations. *Harms et al.* [1987] inferred a late Quaternary slip rate on the Paicines fault of 3.5 - 13 mm/yr from an offset terrace riser and an offset hill ~10 km south of Hollister. Between 1973 and 1986 the average rate of slip obtained from offset of the USGS Thomas Road alinement array, which spans the Paicines fault near its intersection with the Browns-Cross line, is approximately 6 mm/yr [*Harsh and Pavoni,* 1978; S. Burford, personal communication, 1988]. From trilateration measurements made between the stations Browns and Cross during an interval earlier than but overlapping that of our study (69.8-78.4), *Prescott and Lisowski* [1981] determined a slip rate of 8 ± 1 mm/yr. *Prescott and Lisowski* [1981] also calculated the rate of the slip from short-range trilateration measurements of the Pionne net to be 10 ± 3 mm/yr for approximately the same period. These estimates are not significantly different from the results reported here. Utilizing data from the (USGS) Hollister trilateration network, located north of our study region, *Matsu'ura et al.* [1986] inverted for fault displacement rate versus depth on the San Andreas, Calaveras, and Sargent faults. They estimated the rate of slip on the Calaveras-Paicines fault between 1971 and 1983 and between latitudes 36.70° and 36.87°N to be 18 ± 4 mm/yr, with no significant surface creep. Their result is higher than the rate of surface slip documented from the Thomas Road alinement array as well as with that obtained in this study. The inconsistency of the *Matsu'ura et al.* [1986] rate with other results from the region may be due to the fact that the Hollister network does not span the southern portion of the Calaveras fault; in particular, the 18 mm/yr value may reflect an average rate over a region where slip on the Calaveras fault is decreasing to the southeast.

The rate of slip obtained in this study for the Paicines fault south of the city of San Benito is 4 ± 1 mm/yr (Bitter to Hepsedam, Table 2). While geological mapping indicates

that recent right-lateral slip has occurred on the Paicines fault as far south as the city of San Benito, no active fault trace has been mapped further south (J. Perkins, personal communication, 1988). Sedimentation rates are high in this region, however, so a low rate of slip on the fault may be masked by alluvium. From a study of earthquake focal mechanisms and seismicity of this region, *Ellsworth* [1975] suggested that slip on the San Andreas fault is transferred to the faults northeast of the San Andreas between Bitter and Cross (Figure 2). The rate of slip estimated from the change in the Bitter-to-Hepsedam line length, 3-4 mm/yr, however, suggests that some slip may be occurring on an extension of the Paicines fault south of San Benito. As discussed above, the slip rate inferred for this line is higher than the rate of slip of 1 ± 1 mm/yr estimated by *Lisowski and Prescott* [1981] for an earlier period and may indicate a temporal variation in the rate of deformation in this region.

Principal Directions of Strain and Stress

The principal directions determined geodetically for rate of strain within the San Benito network may be compared with the orientation of the maximum principal stress (σ_1) estimated from wellbore breakouts and the azimuths of P axes determined from earthquake focal mechanisms for the region east of the San Andreas fault. As noted earlier, the orientations of principal stress directions determined from breakout orientations, earthquake fault plane solutions, and the azimuths of major fold structures in central California have been used to distinguish between models relating the formation of fold structures in the southern Coast Ranges to motion along the San Andreas fault and to infer the state of stress on and near the San Andreas fault [*Zoback et al.*, 1987; *Mount and Suppe*, 1987; *Namson and Davis*, 1988]

Due to extensive drilling for oil to the east of the San Andreas fault, a large number of wells have been available for measurement of stress-induced wellbore breakout

orientations. Borehole breakouts are caused by unequal stress concentrations around a borehole wall and create elongations of the hole in directions perpendicular to the orientation of the maximum horizontal stress [*Springer*, 1987]. Breakouts are generally oriented northwest-southeast, indicating a northeast-southwest orientation for the greatest compressive stress, a direction perpendicular to the axes of major folds near the Great Valley and at a 70°-90° angle to the San Andreas fault [*Springer*, 1987; *Zoback et al.*, 1987; *Mount and Suppe*, 1987]. To the east of the San Andreas fault the majority of breakout measurements have been made in wells near the western edge of the Great Valley (Figure 5); comparatively few wellbore breakout orientations have been obtained closer to the San Andreas fault within the area of the geodetic measurements reported in this paper.

The orientation of maximum principal stress may also be inferred from well-determined fault plane mechanisms, notably from the 1982 Idria, the 1983 Coalinga, and the 1985 North Kettleman Hills earthquakes (Figure 5). For the Coalinga and the North Kettleman Hills events the P-axis orientation is ~N37°E [*Eaton*, 1985; J.P. Eaton, personal communication, 1987], similar to the directions of σ_1 inferred from breakout orientations in the same region. The azimuth of the P axis for the Idria event is N12°E [*Eaton*, 1985].

As may be seen in Figure 5, the breakout orientations and the P-axis directions are very similar to the orientation of maximum compressive strain implied by the trend of local fold structures and by the inferred direction of horizontal shortening across the San Benito network. Along the western edge of the Great Valley and near Coalinga, the direction of σ_1 inferred from the breakout orientations and two earthquake focal mechanisms and the orientation of maximum compressive strain inferred from the fold trends is N30-50°E. To the northwest of Coalinga, including the region spanned by the San Benito network, the direction of maximum compressive strain predicted from the azimuth of the local fold structures, the σ_1 direction inferred from one wellbore breakout orientation, and the P-axis orientation of the Idria earthquake are N12-35°E. While *Mount and Suppe* [1987] have

suggested that the folds in this area have been inactive since the Miocene, the rate of deformation determined for the region spanned by the San Benito network suggests that ongoing compressive strain is being accommodated across these folds. The recency of folding in this region is further supported by the geological observation that the folds deform Quaternary deposits [*Namson and Davis,* 1988].

As summarized by *Mount and Suppe* [1987] and *Namson and Davis* [1988] the occurrence of folding in the Coast Ranges has been variously attributed to distributed right-lateral shear associated with the San Andreas fault or to oblique displacement across the region. On the basis of experimental simulations of simple shear and field studies of wrench faulting, en echelon fold structures are predicted to occur adjacent to a strike-slip fault due to distributed shear [*Wilcox et al.*, 1973]. Fold axes are expected to be oriented perpendicular to σ_1 in the early stages of wrench faulting; the folds may subsequently rotate into parallelism with the strike-slip fault through distributed shear [*Mount and Suppe,* 1987]. In central California, the axes of early-forming en echelon folds would be at an angle of 30° ± 15° to the trend of the San Andreas fault (~N41°W) in a counterclockwise direction, or N71°W ± 15° (β = N19°E ± 15°).

In an alternative model deformation is due to oblique displacement, sometimes termed "transpression"[*Harland,* 1971], across the southern Coast Ranges. This deformation is thought to be decoupled into a low-shear-stress, strike-slip component and a high-deviatoric-stress, thrust component [*Mount and Suppe*, 1987; *Zoback et al.*, 1987]. In this model the strike-slip component is accommodated within a narrow (< 3-10 km wide) zone and the compressive component is accommodated over a wider zone (10-100 km). The compression is held to be at least partly the result of a small (~ 6°) difference between the orientation of the San Andreas fault in central California and the local direction of Pacific-North American relative plate motion [*DeMets et al.*, 1987]. The precise orientation of σ_1 adjacent to the San Andreas fault, according to this model, depends on the relative strength

of the fault zone and the surrounding lithosphere [*Mount and Suppe*, 1987; *Zoback et al.*, 1987]; for a substantially weaker fault zone σ_1 may be nearly normal to the fault zone ($\beta \sim$ N49°E).

The direction of maximum compressive strain indicated by orientations of the local fold structures in the San Benito region is N25°E, close to the orientation of maximum incremental compressive strain estimated from the geodetic data (β = N16°E $\pm$ 13°). These orientations are in apparent agreement with the wrench faulting model. The significant difference between the trend of the fold axes in the San Benito region and in the San Emigdo Mountains [*Davis*, 1986] and the strike of the San Andreas fault is in contrast, however, to the situation throughout most of the Coast Ranges in central California, where fold axes have orientations approximately parallel to the San Andreas [*Mount and Suppe*, 1987]. In these two regions the fold orientations are thought to be controlled by reactivation of older structures (T.L. Davis, personal communication, 1988); in the San Benito area these older structures may be related to a late Miocene deformation event [*Namson and Davis*, 1988]. Given such structural control, the geodetic data reported here are also consistent with the oblique displacement, or transpression, model for deformation of the Coast Ranges.

As discussed earlier there are two observations which argue against models in which right-lateral shear strain is distributed across a zone significantly greater than 10 km in width. Because slip on the adjacent San Andreas fault occurs primarily by steady creep, little of the right-lateral shear strain accumulation associated with fault should be measurable on off-fault geodetic lines. Additionally, distributed shear strain associated with the San Andreas fault would be observable on both sides of the fault, yet there is no geodetic or geologic evidence of deformation within the Salinian block [*Thatcher*, 1979a].

There are several factors which may complicate the interpretation of measurements used to distinguish between models relating the formation of fold structures in the Coast

Ranges to motion along the San Andreas fault . First, there may be processes that act on different length scales which might explain the change in the σ_1 direction and the trend of fold structures at different distances from the San Andreas fault. Within a narrow zone centered on the San Andreas fault, local geological structures and focal mechanisms may be the result of geometrical complexities in the fault trace [*Segall and Pollard*, 1980] or the rheological structure of the fault zone [*Horns et al.*, 1985]. Between the San Andreas fault and the Paicines fault, for example, the focal mechanisms determined by *Ellsworth* [1975] may be due to interaction between the two faults. As seen in the San Benito region, fold orientations may also vary due to reactivation of older structures or material heterogeneity. Finally, as will be discussed in the next section, there is the additional complexity that deformation in the southern Coast Ranges is related, in a kinematic sense, to the overall deformation across the Pacific-North American plate boundary.

Relation of Deformation East of the San Andreas Fault to the Accommodation of Plate Motion

The results of the geodetic measurements presented in this chapter are relevant to deformation in other subregions of the Coast Ranges and to the question of how Pacific-North American plate motion is accommodated across California.

Global plate motion models, which yield the relative motion between the North American and Pacific plates, have been used as kinematic boundary conditions on the integrated deformation across the plate boundary zone in the western United States [*Minster and Jordan*, 1984, 1987; *Bird and Rosenstock*, 1984; *Weldon and Humphreys*, 1986]. If the San Andreas fault functioned as a simple boundary that accommodated the full motion between two rigid plates, the rate of slip in central California predicted by the NUVEL-1 global plate motion model would be about 49 mm/yr at N35°W [*DeMets et al.*, 1987]. Deformation across the Pacific-North American boundary is instead thought to be

distributed across a broad zone between the continental escarpment and the eastern front of the Basin and Range province. As summarized above, the rate of slip on the San Andreas fault in central California oriented at N41°W ± 2° is constrained from Holocene geological data and ground-based geodetic measurements to be 34 ± 3 mm/yr. The vector difference between the plate motion and the San Andreas rate is about 16 mm/yr in the direction N21°W. The integrated rate of extensional deformation to the east of the San Andreas fault across the Basin and Range has been estimated from geological observations averaged over the Holocene and from very long baseline interferometry (VLBI) to be 9.7 ± 2.1 mm/yr at N56°W ± 10° [*Minster and Jordan*, 1987]. The vector difference derived using the above rates of motion for the San Andreas fault and Basin and Range, referred to as the discrepancy vector by *Minster and Jordan* [1987], is about 10 mm/yr in the direction N14°E, or 5 mm/yr of slip parallel to the San Andreas fault and 8 mm/yr of convergence normal to the fault. On the basis of the estimates of *Minster and Jordan* [1987], the uncertainties in the discrepancy vector are approximately ± 5 mm/yr for the rate of slip and ± 15° for the direction. Although some minor internal deformation within the Sierra Nevada block [*Lockwood and Moore*, 1979] or across the Great Valley syncline may occur, most of the deformation represented by the discrepancy vector is thought to occur within the Coast Ranges. *Weldon and Humphreys* [1987] and *Saucier and Humphreys* [1988] have constructed a self-consistent description of deformation in southern and central California from geodetic data and Quaternary geologic slip rates. From their model they predict that the Pacific-North American relative plate motion vector is 9° more westerly than that given by NUVEL-1. They estimate ~ 5 mm/yr of convergence normal to the San Andreas fault in central California.

A compilatation of estimated and measured rates of deformation in the Coast Ranges, separated into right-lateral strike-slip motion on specific faults and distributed compression, is given in Table 4. In general the geological data are most useful for indicating long-term

modes of deformation and for placing upper and lower bounds on rates. The large range in most geologically determined rates is due to uncertainties in dating rock units and in the timing of geological reconstructions.

A comparison of incremental strain rates determined over a geologically short interval to long-term slip rates is meaningful only if the deformation process accumulates strain in a temporally uniform manner. On short-time scales (10^0 - 10^2 yrs) there are a number of mechanisms associated with temporal variations in strain rate. An increase in the rate of shear strain has been documented to occur after large earthquakes in a region adjacent to the rupture zone [*Thatcher*, 1986]. There is no evidence, however, for a change in the rate of slip on the San Andreas fault in central California for the time interval that spans the occurrence of the great 1906 earthquake on the northern locked segment of the San Andreas fault [*Thatcher*, 1979a]. As discussed above, there is a suggestion that the rate of slip on the Paicines and Calaveras faults changed at about the time of the 1979 Coyote Lake earthquake.

Within a fold and thrust belt such as the southern Coast Ranges the short-term temporal variations in the rate of deformation are poorly constrained. The pattern of moderate size earthquakes ($M_L > 5.0$) between 1932-1982 in the southern Coast Ranges [*Engdahl and Rinehart*, 1988] is similar to the seismicity pattern given in Figure 1; there is some additional seismicity in the region between the Rinconada fault (Figure 1) and the continental escarpment. This result suggests that over the past ~50 years the pattern of release of stress and strain by earthquakes has been approximately time-stationary. Comparison with geological data is further complicated by the observation that the plate boundary zone undergoes evolution on geological times scales. Field geological evidence from the Coalinga region indicates that the most recent episode of uplift began only 2-3 m.y. ago, well after slip commenced on the San Andreas fault [*Namson and Davis*, 1988]. A fold and thrust belt typically undergoes an evolution such that the locus of deformation

changes. In the initial stages of deformation the locus of activity is controlled by such factors as the nature and position of the driving and resisting forces, pre-existing zones of weakness, and rock properties such as the elastic moduli, effective viscosity, and stratification of the deforming medium [*Biot*, 1961; *Harland*, 1971]. At some point beyond this initial stage less work may be required to break new faults or build new folds, and the folding and faulting may commence elsewhere.

To explore the implications of the constraints provided by the San Andreas discrepancy vector we compare the predicted rate of ~5 mm/yr of fault-parallel and ~8 mm/yr of fault-normal deformation to the values given in Table 4. The rates of right-lateral slip on the Rinconada and San Gregorio faults estimated from geological observations are 0-2 and 6-9 mm/yr, respectively [*Clark et al.*, 1984]. These values compare with geodetically measured rates of 2 ± 1 mm/yr (Table 4) and 0 ± 8 mm/yr [*Prescott and Yu*, 1986], respectively. These results for the rate of slip on the San Gregorio fault are significantly smaller than some earlier estimates [*Minster and Jordan*, 1984; *Weldon and Humphreys*, 1986] but are more consistent with recent kinematic models [e.g, Model D, *Minster and Jordan*, 1987].

Geological and seismicity data suggest that northeast-southwest compression across the southern Coast Ranges may be localized to two regions, the 30-km-wide zone spanned by the San Benito network and a second zone to the west of the Rinconada fault [*Eaton*, 1984; *Dehlinger and Bolt*, 1987]. If shortening across the Coast Ranges is divided equally between these two regions, approximately 4 mm/yr of shortening should be occurring within the Diablo Range. If, in contrast, the predicted 8 mm/yr [*Minster and Jordan*, 1987] is distributed uniformly across the 170-km-wide zone between the continental escarpment and the Great Valley, the shortening across the region spanned by the San Benito network would be approximately 1.4 mm/yr. The rate of deformation estimated from the San

Benito study is most consistent with the first hypothesis, but the uncertainties in our calculated values do not allow the latter possibility to be ruled out.

Results from ongoing geodetic studies with stations in central California should provide additional constraints on the rate and distribution of slip within the Coast Ranges. The rate of slip estimated from VLBI measurements made at Vandenberg, Fort Ord, Presidio, and Point Reyes (Figure 6) could potentially be used to constrain the rate of deformation across the Coast Ranges. To distinguish between different models will require that uncertainties in the rate of slip, relative to a fixed reference, be 2-3 mm/yr or less. Our preliminary analysis of VLBI data, based on measurements between October 1982 and March 1987, indicate that only the rate of slip at the station Vandenberg meets this requirement [*Sauber et al.*, 1987; see also *Clark et al.*, 1987]. Additional measurements at all of the VLBI stations in central California have been made within the last year, and an analysis of these measurements will be the subject of the next chapter. The rate of deformation estimated from measurements to the Farallon Islands (Figure 6) will be updated following a trilateration survey of the network by the USGS in 1988; such information should provide a better constraint on the rate of slip on the San Gregorio fault.

Summary

Triangulation and trilateration data from two geodetic networks located between the San Andreas fault and the Great Valley have been used to calculate shear strain rates in the Diablo Range and to estimate the slip rate along the Calaveras and Paicines faults in central California. The shear strain rates, $\dot{\gamma}_1$ and $\dot{\gamma}_2$, were estimated independently from angle changes using Prescott's method and from the simultaneous reduction for station position and strain parameters using the DYNAP method. On the basis of Prescott method, the average shear strain rate for the time period between 1962 and 1982 is 0.15 ± 0.08 μrad/yr, with the orientation of the most compressive strain (β) at N16°E ± 14°. Utilizing the

DYNAP method with corrections for the deflection of the vertical and the geoid - reference ellipsoid separation computed on the basis of local gravity observations, $\dot{\gamma} = 0.19 \pm 0.09$ μrad/yr and β = N16°E ± 13°. At the 95% confidence level $\dot{\gamma}$ is not significantly greater than zero. The orientation β, however, is similar to the direction of maximum compressive strain indicated by the orientations of major fold structures in the region (N25°E). We infer that the measured strain is due to compression across the folds of this area; the average shear straining corresponds to a relative shortening rate of 5.7 ± 2.7 mm/yr.

The orientations of maximum principal stress inferred from wellbore breakouts and the azimuths of P axes determined from earthquake focal mechanisms within the Diablo Range and near the western edge of the Great Valley are similar to the orientation of maximum compressive strain implied by the trend of local fold structures. In contrast to the situation throughout most of the Coast Ranges in central California where fold axes have orientations approximately parallel to the San Andreas fault, within the Diablo Ranges between Hollister and Coalinga the trend of the fold axes are different and are thought to be controlled by reactivation of older structures. Given such structural control, the geodetic data reported here are consistent with transpression across the Coast Ranges.

For a zone within 10 km of the San Andreas fault, trilateration measurements on off-fault lines east of the San Andreas fault as well as lines that cross the San Andreas fault have been used to estimate the rate of slip along the Calaveras-Paicines fault and to document the gradual southward transition in the width of the zone accommodating right-lateral fault slip. South of Hollister the inferred rate of slip on the Calaveras-Paicines fault was found to be 10-12 mm/yr. The rate of slip on the Paicines fault near Bitter is ~4 mm/yr. Further to the south all of the right-lateral slip (at least across the 20-km-wide zone of measurements) occurs on the San Andreas fault.

To distinguish between different models that describe the distribution of strike-slip and compressive displacements within the Coast Ranges we examined data from regional

geologic and geodetic studies and global plate models. Geological and seismicity data [*Eaton,* 1984; *Dehlinger and Bolt,* 1987], as well as our geodetic results, suggest that northeast-southwest compression across the southern Coast Ranges may be localized to two regions, although uniform compression across the 170-km-wide zone between the continental escarpment and the Great Valley cannot be ruled out.

Appendix. Details of Data Reduction for the San Benito Network

Accuracy of the Triangulation and Trilateration Measurements

Triangulation is a measurement system consisting of joined or overlapping triangles of angular observations. During a single session observations of direction are made from a particular mark to several other marks that are located within a few tens of kilometers from the mark occupied. An angle observation is determined by differencing two direction measurements. Seventy of the 72 directions utilized in this study were second-order observations, with *a priori* uncertainty estimated to be $\sigma_d = 3.4$ μrad [*Federal Geodetic Control Committee,* 1984], and two were third-order observations ($\sigma_d = 5.8$ μrad). The expected uncertainty in a second-order angle measurement (σ_a) is $\sqrt{2}\ \sigma_d$, or about 4.8 μrad. The order of the triangulation denotes the measurement precision, which is determined by survey procedures and is reflected in the degree to which internal checks of the data are satisfied [*Thatcher,* 1979b]. The principal internal check is the triangle closure requirement that the angles within each triangle sum to 180° plus the known excess due to the Earth's sphericity. Triangle closures for these data indicate that the standard deviation of a single angle is approximately 5.3 μrad, very close to the expected value.

As practiced by the USGS, trilateration consists of distance measurements among a network of stations. The distances between geodetic monuments were measured in this study with a Geodolite, a precise electro-optical distance-measuring instrument. Regional

trilateration measurements made by the USGS on line lengths of 10-40 km have a precision of approximately 0.2-0.3 ppm [*Savage and Prescott,* 1973]. After corrections for refractivity and instrument and reflector height, a line length corresponds to the distance between two geodetic monuments.

Assumptions Made in the Estimation of Horizontal Shear Parameters

The full three-dimensional strain tensor includes horizontal and vertical shear components, dilatation, and vector rotation. Since height changes were not directly measured in either the 1962 or 1982 survey, we can estimate only the horizontal components of the strain tensor. Here we assume that vertical changes in station height are negligible. Since no large earthquakes occurred within the region spanned by the San Benito network between 1932-1982 [*Engdahl and Rinehart,* 1988], the estimated rate of uplift on the folds of the Diablo Range is only 1-3 mm/yr [*Zepeda et al.*, 1987], or 2-6 cm over the 20-year time period of this study. A 6-cm change in the height of Tum (Figure 2) between 1962 and 1982, for example, will cause a 0.1 ppm change in the 20-km-length line between Tum and Bonito (calculated from equation 1.72 of *Bomford* [1980]). Because of ground-water-induced subsidence, larger vertical changes may have occurred at the stations Stubble, located in the Great Valley, and Panoche, located in Panoche Valley. Further, astronomic azimuth measurements are made only at Hepsedam. Without a reliable external or conventionally adopted internal reference direction, we cannot estimate rotation of the network about a vertical axis. Additionally, since length measurements were made only in the 1982 survey, surface dilatation can not be estimated. We are thus able to estimate only the rate of change of horizontal shear components ($\dot{\gamma}_1$ and $\dot{\gamma}_2$). If the fold structures of the region are deforming as the result of simple uniaxial compression, block rotation is not expected and dilatation is assumed to be uniform.

The two modes of deformation suggested from the geological structures of the region (see text) can be used to interpret the $\dot{\gamma}_1$ and $\dot{\gamma}_2$ values. Right-lateral strike-slip motion at the orientation of the San Andreas fault (N41°W) would be seen primarily as $\dot{\gamma}_1 > 0$. North-south compression is also consistent with $\dot{\gamma}_1 > 0$. If the orientation of compressional strain is northeast-southwest, as is predicted from the orientation of the folds within the southern Coast Ranges, then $\dot{\gamma}_2 < 0$.

Prescott's Method

Angle changes are the observations used to estimate $\dot{\gamma}_1$ and $\dot{\gamma}_2$ in the extended version of Frank's method [*Prescott*, 1976]. The fundamental equation of the technique,

$$\Delta\Phi_i = (t_i - t_o)\,(A_i^1 \dot{\gamma}_1 + A_i^2 \dot{\gamma}_2) \qquad (A.1)$$

where

$$A_i^1 = [(\sin\theta_{i2} - \sin\theta_{i1})\,\dot{\gamma}_1\,] / 2$$

$$A_i^2 = [(\cos\theta_{i2} - \cos\theta_{i1})\,\dot{\gamma}_2\,] / 2$$

relates an observed angular change $\Delta\Phi_i$ for the time interval $t_i - t_o$ to the parameters $\dot{\gamma}_1$ and $\dot{\gamma}_2$. Here θ_{i1} and θ_{i2} represent the azimuths (clockwise from north) of the initial and terminal sides of the angle. To derive angles the 1982 data were used to adjust for station position. Rather than making an adjustment on a three-dimensional surface, the distances were projected onto the Clark 1866 reference ellipsoid (NAD27 geodetic system, *Defense Mapping Agency* [1987]), and an adjustment was made employing a variation of coordinates method [*Anderson*, 1969]. Azimuths for each station-to-station pair were then determined for comparison to the 1962 observations. In this approach we are comparing angles measured on the Earth's surface to angles determined from a network adjustment on

the reference ellipsoid. The classical solution to the adjustment of geodetic data derived from different measurement techniques has involved making corrections to the direction and distance observations such that the measurements are then given on a common reference ellipsoid [*Bomford*, 1980; *Vanicek and Krakiwsky*, 1986]. In employing the DYNAP method an alternative approach is used.

DYNAP Method

In the DYNAP (DYNamic Adjustment Program) technique the directions measured in 1962 and the distances measured in 1982 are used simultaneously to solve for both crustal motion parameters and positional coordinates of the geodetic marks for a specified reference time via weighted least squares [*Snay*, 1986; *Drew and Snay*, 1988]. A two-dimensional adjustment was carried out by holding the station elevations fixed. In this approach the direction observations are corrected for the deflection of the vertical, and the separation of the geoid and a reference ellipsoid are used to correct the distance observations. This technique is based on the assumption that the velocity field is linear in space and constant over the time interval of interest. The time dependent station positions can be written as

$$x(t_i) = x(t_o) + (t_i - t_o)\,\mathbf{L}\,x\,(t_o) \qquad (A.2)$$

where $x(t_i)$ are the two dimensional station coordinates at time t_i and t_o is the reference time. The four components of the 2 x 2 tensor **L** parameterize the velocity field v by its gradient [*Malvern*, 1969]:

$$L_{ij} = \frac{\delta v_i}{\delta x_j} \qquad (A.3)$$

In equation (A.2) the origin is arbitrary. In practice one station is chosen as an origin and is held fixed for all epochs. **L** can be decomposed into a sum of a symmetric tensor **D**, called the rate of deformation tensor, and a skew-symmetric tensor **W**, called the spin tensor [*Malvern*, 1969]

$$\mathbf{L} = \mathbf{D} + \mathbf{W} \tag{A.4}$$

For the case where all of the components of rate of deformation are zero, the instantaneous motion is then a rigid-body rotation. When displacements and displacement gradients are small **D** is approximately equal to $\dot{\varepsilon}_{ij}$.

Corrections to Reduce the Observations to a Common Reference System

When a direction measurement is made the theodolite is leveled; thus the measurement is made normal to the geoid, not normal to a reference surface. A correction for the deflection of the vertical is therefore required [*Bomford*, 1980; *Vanicek and Krakiwsky*, 1986]. The deflection of the vertical is the spatial angle between the vector normal to the geoid and the vector normal to an ellipsoidal surface. The correction $\Delta\alpha_{ij}$ to a direction of azimuth α_{ij} and elevation angle ν_{ij} [*Bomford*, 1980, p. 106] is

$$\Delta\alpha_{ij} = -[\, \xi_i \sin \alpha_{ij} - \eta_i \cos \alpha_{ij}] \tan \nu_{ij} \tag{A.5}$$

where ξ_i and η_i are the meridian and prime vertical components of the deflection of the vertical at the observing, or *i* th, station. Deflections of the vertical are usually estimated from astronomical azimuth observations or from computed values based on local gravity observations [*Coleman and Lambeck*, 1983]. Alternatively, the deflections can be computed from the long-wavelength part of the geopotential together with necessary transformation parameters between the geoid and the ellipsoid reference system.

In this study the initial latitude and longitude of the station are positions given in the NAD83 reference system [*Defense Mapping Agency,* 1987]. The initial heights are orthometric heights, the height above the geoid estimated primarily from spirit leveling. For the station coordinates to be in a common reference frame, the heights need to be converted to heights above the GRS 80 reference ellipsoid [*Defense Mapping Agency,* 1987]. To make this calculation the separation of the geoid and the reference ellipsoid needs to be estimated. Since astronomical azimuths are not available, the deflection of the vertical and the geoid -ellipsoid separation are initially estimated from the long-wavelength part of the geopotential.

The global gravity field representation given by the WGS 84 Earth Gravitational Model (EGM) [*Defense Mapping Agency,* 1987] was used to calculate the deflection of the vertical and geoid height at each station using the Defense Mapping Agency program CLENQUENT [*Gleason,* 1985]. The form of the WGS 84 EGM is a spherical harmonic expansion of the gravitational potential; we used an expansion to degree and order 360. The gravitational coefficients are from *Rapp and Cruz* [1986] and R. Rapp (personal communication, 1988). The reference ellipsoid used to calculate the deflections of the vertical and the geoid - ellipsoid height separation was GRS 80 [*Defense Mapping Agency,* 1987], which is used in both the WGS 84 and NAD83 reference systems. The deflections of the vertical vary in the network from 1.14"S to 0.14"N for ξ and from 1.40"E to 3.60"E for η. Utilizing the geoid - reference ellipsoid height separation and deflections of the vertical calculated from the long-wavelength part of the geopotential, the strain rate parameters were estimated using the DYNAP method, yielding $\dot{\gamma} = 0.12 \pm 0.09$ μstrain/yr and β = N17°E $\pm$ 21° and an increase in the variance of unit weight by 2%. The strain rate results are similar to those obtained without corrections ($\dot{\gamma} = 0.15 \pm 0.09$ μrad/yr and β = N17°E $\pm$ 16°.) The surface topography as well as the density distribution within the crust

of the San Benito region is irregular, so the geoid representation used represents poorly the higher order features of the gravity field.

Because we expect significant short wavelength variations in the geoid, we have obtained from the Defense Mapping Agency geoid - reference ellipsoid separations and deflections of the vertical computed for network station positions from local gravity observations. The deflections of the vertical vary in the network from 6.00"S to 7.38"N for ξ and from 12.47"E to 6.38"W for η. The strain rate parameters utilizing these corrections are $\dot{\gamma}$= 0.19 ± 0.09 μstrain/yr and β = N16°E ± 13°. The variance of unit weight decreases by 8%. This decrease is due to a lower misfit for the direction observations; the corrections do not change the rms misfit for distance observations. These results suggest that while it is desirable to correct for deflection of the vertical and for the separation between the geoid and the reference ellipsoid, these corrections are valuable only when based on local observations.

TABLE 1. Strain Rate Parameters for Spatial Subsets of the San Benito Network

Subnet	Number of Angles	$\dot{\gamma}_1$, μrad/yr	$\dot{\gamma}_2$, μrad/yr	$\dot{\gamma}$, μrad/yr	β	ψ
East	14	0.18 ± 0.11	0.01 ± 0.12	0.18 ± 0.10	N 1°W ± 20°	N46°W ± 20°
West	9	0.07 ± 0.14	-0.18 ± 0.13	0.19 ± 0.13	N34°E ± 22°	N11°W ± 22°
North	13	0.04 ± 0.10	-0.12 ± 0.10	0.16 ± 0.11	N37°E ± 20°	N 8°W ± 20°
South	7	0.22 ± 0.16	-0.13 ± 0.22	0.25 ± 0.20	N10°E ± 20°	N35°W ± 20°
All stations except BIT, HEP, and PAN	25	0.13 ± 0.08	-0.08 ± 0.08	0.15 ± 0.08*	N16°E ± 14°*	N29°W ± 14°*

* These strain parameters have been scaled by the *a posteriori* variance factor [*Vanicek and Krakiwsky*, 1986].

TABLE 2. Fault-Slip Rates Inferred from Length Changes on Fault-Crossing Lines

Calaveras - Paicines Fault Zone

Station 1	Station 2	No. of Obs.	Period	$\dot{L}$, mm/yr	Azimuth, deg	Slip Rate, mm/yr
BRN	CRS	7	72.7-83.9	-8.7 ± 0.8	168	9.9 ± 0.9
CRS	CHL	9	72.1-83.9	-18.5 ± 0.4	181	24.9 ± 0.5
BRN	CHL	8	72.1-83.9	27.4 ± 0.4	175	33.8 ± 0.5

Paicines Fault Adjacent to the Central Creeping Portion of the San Andreas Fault

Station 1	Station 2	No. of Obs.	Period	$\dot{L}$, mm/yr	Azimuth, deg	Slip Rate, mm/yr
BIT	HEP	6	73.1-83.9	3.7 ± 0.5	129	3.8 ± 0.5
CHL	BIT	8	72.1-83.9	19.8 ± 0.7	280	25.8 ± 0.9
CHL	HEP	7	72.7-83.9	27.4 ± 0.6	113	30.7 ± 0.6

The quantity $\dot{L}$ is the rate of change of line length determined by least-squares, shown together with one standard deviation. Azimuth is measured clockwise from north. The slip rate is that appropriate to the strike-slip fault crossed by the indicated line. The time intervals of observations are given in decimal fractions of years.

TABLE 3. Fault Slip Rates Indicated by Short-Range Trilateration Networks

Network	No. of Observations	Period	Slip Rate, mm/yr
Pionne	8	75.2-87.3	12 ± 2
Dry Lake	4	79.0-87.3	27 ± 2
Tully	8	74.9-87.3	32 ± 1

See Table 2 for explanation of notation.

TABLE 4. Summary of Deformation Rates within the central Coast Ranges

Fault	Orientation	Geological Slip Rate, mm/yr	Geodetic Slip Rate, mm/yr
Right-lateral strike-slip faults			
Ortigalita	N35°W	0-2[a]	
San Andreas	N41°W	31-37[b]	32 ± 3 [c]
Rinconada	N35°W	0-2[d]	2 ± 1[e]
San Simeon	N34°W	6-9[f]	
San Gregorio	N20°W	7-11[g]	0 ± 8[h]
Compression in the Coast Ranges			
East of San Andreas		2.2-5.5[i]	5.7 ± 2.7 [j]
West of San Andreas		4.4-11[i]	6.1 ± 1.7[k,l]

Notes For Table 4

a *Hart et al.* [1986].

b *Sieh and Jahns* [1984].

c *Savage and Burford* [1973]; *Thatcher* [1979a]; *Burford and Harsh* [1980]; *Lisowski and Prescott* [1981]; this study.

d *Hart et al.* [1986]; D. B. Slemmons, personal communication, 1987; E. W. Hart, personal communication, 1988.

e The line between Brush and Mulligan of the USGS Pajaro trilateration network has been measured five times between May 1978 and April 1983. If it is assumed that the average line length change is due to right-lateral slip on the King City fault, a northern extension of the Rinconada fault, then a slip rate of 2 ± 1 mm/yr is indicated.

f Rate of right-vertical oblique slip inferred from the offset of an ancient marine shoreline; a preferred slip rate of 6 mm/yr is given by *Clark et al.* [1984].

g Rate of right-lateral slip inferred from the offset of an ancient marine shoreline; a preferred slip rate of 7 mm/yr is given by *Clark et al.*, [1984].

h From trilateration measurements made to the Farallon Islands between mid-1979 and late 1985 [*Prescott and Yu,* 1986].

i *Namson and Davis* [1988] estimated that 11 km of late Cenozoic shortening has occurred between the San Andreas fault and the Great Valley. The 22 km of shortening to the west of the San Andreas fault was computed by *Namson and Davis* [1988] from a solution that satisfies the observed structural relief. The range in rate estimates were obtained by assuming that shortening commenced between 5 and 2 m.y. ago.

j This study. The direction of maximum contraction is N16°E ± 13°.

k *Segall and Harris* [1986]; *Harris and Segall* [1987]. Average rates of change of line length from the San Luis trilateration network were used to invert for slip rate at depth on the San Andreas fault. In order to fit the trilateration measurements from this network, it

was necessary to include a component of contraction normal to the trend of the San Andreas fault. The inversion results suggest a spatially uniform normal strain of -0.06 μstrain/yr. The net shortening rate across the network is 6.1 ± 1.7 mm/yr. This estimated compression, however, may be due to a systematic bias in the older trilateration data [J.C. Savage, personal communication, 1987] .

Two additional geodetic studies using historical triangulation data have been made west of the San Andreas fault. *Burford* [1967] analyzed triangulation data measured between 1930 and 1951 from two networks. One extends from Monterey Bay to the region where the San Andreas and Calaveras faults diverge (Figure 1), and one extends from Kettleman Hills near Parkfield west to San Luis Obisbo. Outside a zone close to the San Andreas fault, the direction of maximum shortening was estimated to be approximately N35°E. As part of a general study of the deformation in central California, *Thatcher* [1979a] examined triangulation data measured during the time interval 1944-1963 from the Salinias Valley network. Most of this network lies within the Salinian block located between the San Andreas and Rinconada faults. Examination of subregions suggest that the strains are poorly resolved, with the orientation of the inferred strain field not correlated with any known faults or tectonic trends. Because of the uncertainties in the results, neither of these studies were used for rate determinations.

Figure Captions

Figure 1. Epicenters of earthquakes ($M_L \geq 4.0$) in the Coast Ranges during 1962 - 1982 [*Engdahl and Rinehart,* 1988]. The locations of three earthquakes with well-determined focal mechanisms, the 1982 Idria, the 1983 Coalinga, and the 1985 North Kettleman Hills events, are indicated by stars. Fault traces are simplified from *Jennings* [1975]: HF = Hosgri fault, RF = Rinconada fault, SAF = San Andreas fault, SGF = San Gregorio fault, WTR =Western Transverse Ranges. An outline of the San Benito triangulation/trilateration network is given for reference. MB = Monterey Bay.

Figure 2. Location of stations in the San Benito triangulation/trilateration network (solid circles), the Coalinga trilateration network (open circles), and small aperture trilateration networks (triangles). Half-filled circles denote stations that were part of both the San Benito and Coalinga networks. Surface traces of Quaternary faults are indicated by solid lines where well located and by dashed lines where approximately located or inferred [*Jennings*, 1975]: CFZ= Calaveras fault zone, OFZ= Ortigalita fault zone, PF=Paicines fault, RF=Rinconada fault, SAF=San Andreas fault. Stations discussed in the text include BIT = Bitter, BON = Bonito, BRN = Browns, CHL = Chalone, CRS = Cross, HEP = Hepsedam, LEY = Ley, PAN = Panoche, SMO = Smoker and TUM = Tum. Also shown are the locations of Coalinga (C), Hollister (H), and San Benito (SB).

Figure 3. Major structural features of the Diablo Range between Hollister (H) and Coalinga (C), modified from *Dibblee* [1979]. The locations of stations in the San Benito triangulation/trilateration network are shown as circles for reference. Structures shown include: CA = Coalinga anticline, CFZ = Calaveras fault zone, NI = New Idria diapir, OFZ = Ortigalita fault zone, PF = Paicines fault, PS = Paicines syncline, and VS = Vallecitos syncline. Inward pointing double arrows indicate a syncline, outward pointing double arrows an anticline. Single arrows indicate the direction of plunge of a fold axis.

Figure 4. Strain rate inferred for the San Benito network by use of the DYNAP method, including corrections for deflection of the vertical and separation of the geoid and reference spheroid. (a) The orientation β of the axis of maximum compressive strain. The uncertainty in azimuth, at 95% confidence, is shown by an arc. (b) The shear strain rate parameters $\dot{\gamma}_1$ and $\dot{\gamma}_2$ together with a 95% confidence ellipse.

Figure 5. Fold structures and measured stress orientations in the region east of the San Andreas fault in central California [modified from *Mount and Suppe*, 1987]. Synclines are indicated by dashed lines, anticlines by dotted lines. Single arrows indicate the direction of plunge of a fold axis. Wellbore breakout measurements are given by a solid line with inward pointing arrows perpendicular to the direction of σ_1. The direction of σ_1 inferred from the azimuth of the P axes for three earthquakes are labeled by number: 1 = 1982 New Idria earthquake, 2 = 1983 Coalinga earthquake, and 3 = 1985 North Kettleman Hills earthquake. The axis of maximum compressive strain (b) determined from triangulation and trilateration data from the San Benito network is given along with its standard deviation.

Figure 6. Reference figure for the geodetic and geological studies cited in Table 4. Brush (B) and Mulligan (M) are two stations in the USGS Pajaro trilateration network. At sites f and g, rates of fault slip were estimated geologically [*Clark et al.*, 1984] for the San Gregorio and Hosgri faults. The line A-A' is that for which *Namson and Davis* [1988] constructed their geological cross section (see Table 4). Fault traces are as given in Figure 1. Geodetic networks include FIN = Farallon Islands network, SBN = San Benito network, and SLN = San Luis network. VLBI stations include FORT = Fort Ord, PRES = Presidio, PT. R = Point Reyes, and VNDN = Vandenberg.

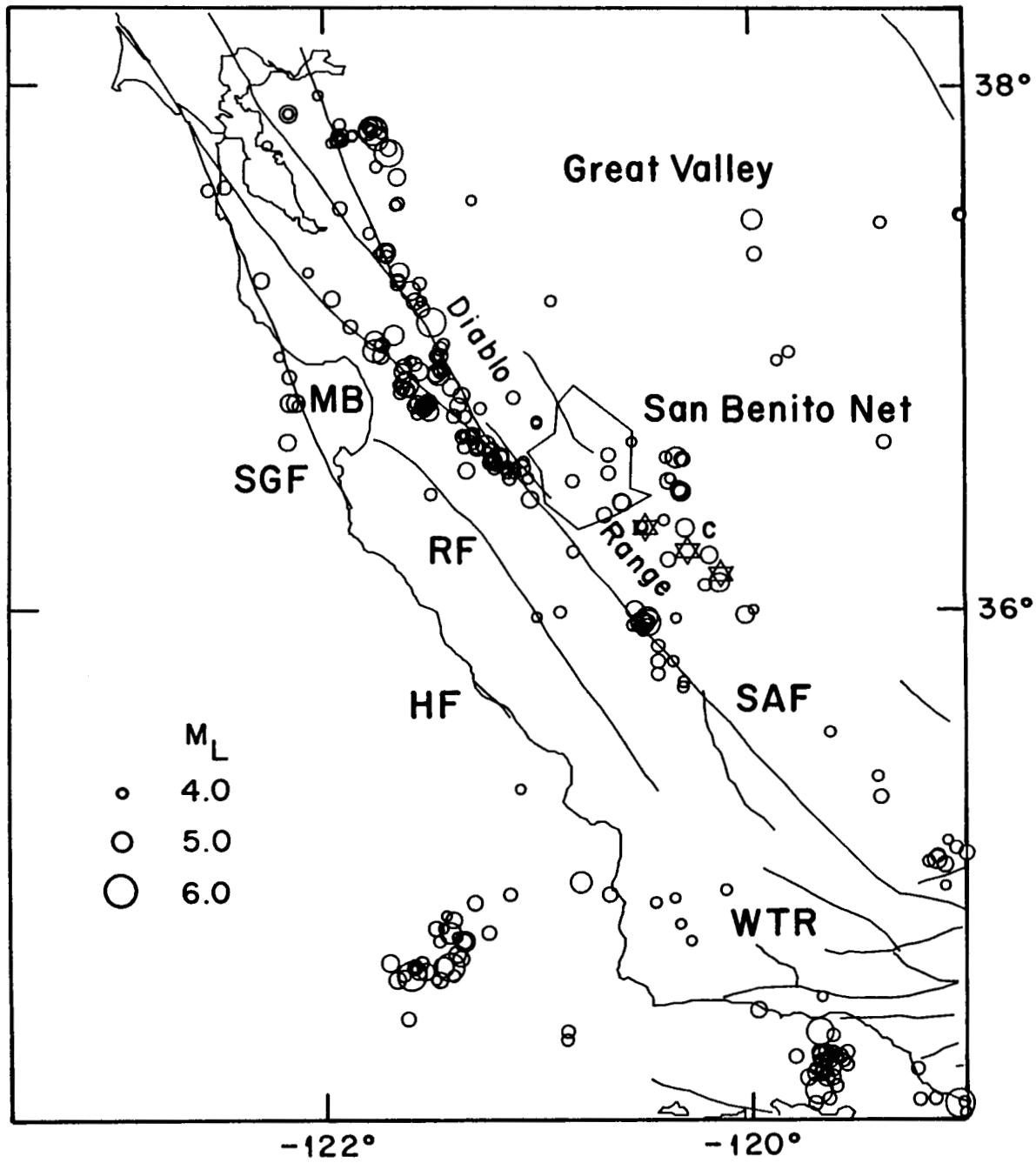

Figure 1. Epicenters of earthquakes ($M_L \geq 4.0$) in the Coast Ranges during 1962 - 1982 [*Engdahl and Rinehart,* 1988]. The locations of three earthquakes with well-determined focal mechanisms, the 1982 Idria, the 1983 Coalinga, and the 1985 North Kettleman Hills events, are indicated by stars. Fault traces are simplified from *Jennings* [1975]: HF = Hosgri fault, RF = Rinconada fault, SAF = San Andreas fault, SGF = San Gregorio fault, WTR =Western Transverse Ranges. An outline of the San Benito triangulation/trilateration network is given for reference. MB = Monterey Bay.

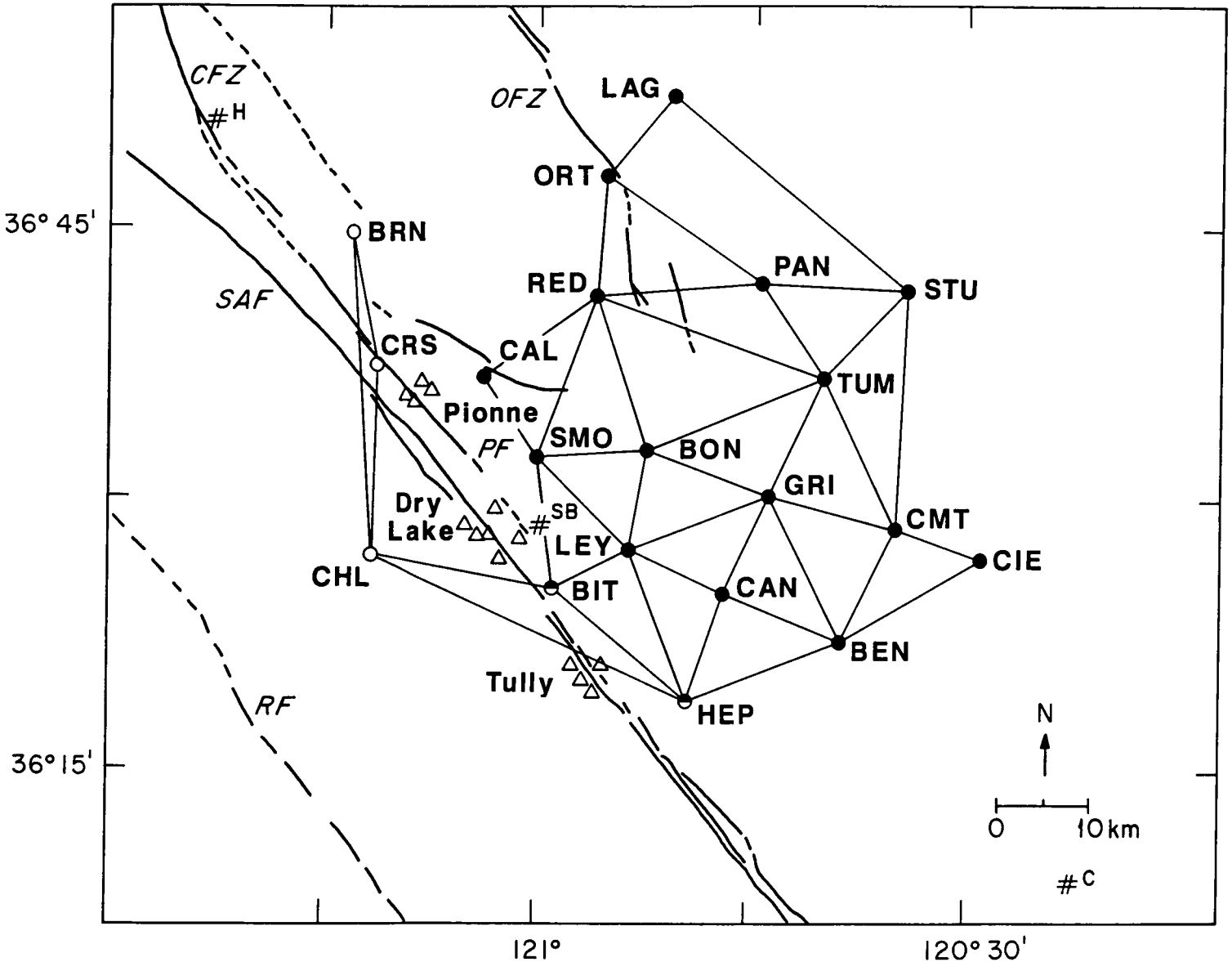

Figure 2. Location of stations in the San Benito triangulation/trilateration network (solid circles), the Coalinga trilateration network (open circles), and small aperture trilateration networks (triangles). Half-filled circles denote stations that were part of both the San Benito and Coalinga networks. Surface traces of Quaternary faults are indicated by solid lines where well located and by dashed lines where approximately located or inferred [*Jennings*, 1975]: CFZ= Calaveras fault zone, OFZ= Ortigalita fault zone, PF=Paicines fault, RF=Rinconada fault, SAF=San Andreas fault. Stations discussed in the text include BIT = Bitter, BON = Bonito, BRN = Browns, CHL = Chalone, CRS = Cross, HEP = Hepsedam, LEY = Ley, PAN = Panoche, SMO = Smoker and TUM = Tum. Also shown are the locations of Coalinga (C), Hollister (H), and San Benito (SB).

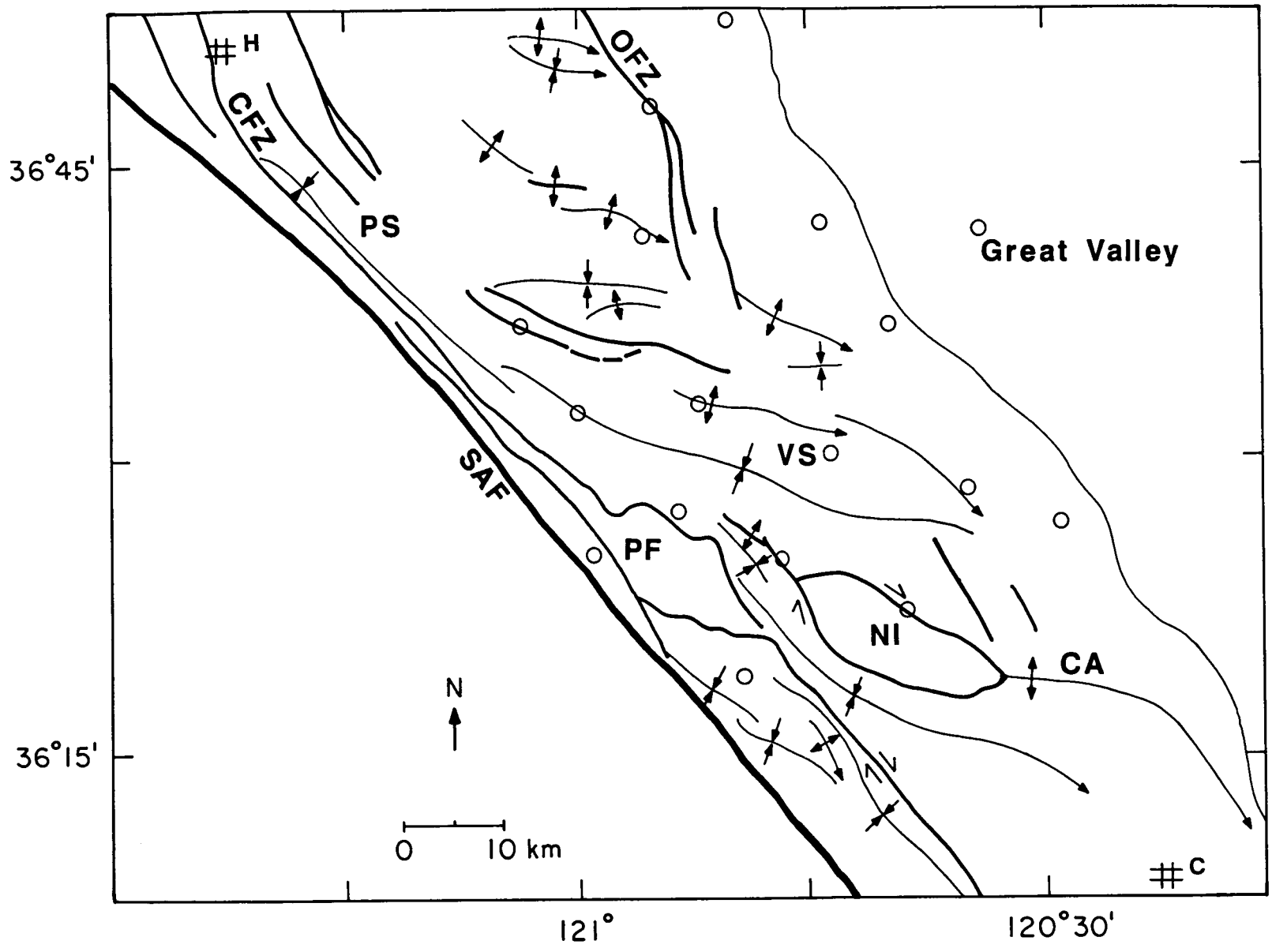

Figure 3. Major structural features of the Diablo Range between Hollister (H) and Coalinga (C), modified from *Dibblee* [1979]. The locations of stations in the San Benito triangulation/trilateration network are shown as circles for reference. Structures shown include: CA = Coalinga anticline, CFZ = Calaveras fault zone, NI = New Idria diapir, OFZ = Ortigalita fault zone, PF = Paicines fault, PS = Paicines syncline, and VS = Vallecitos syncline. Inward pointing double arrows indicate a syncline, outward pointing double arrows an anticline. Single arrows indicate the direction of plunge of a fold axis.

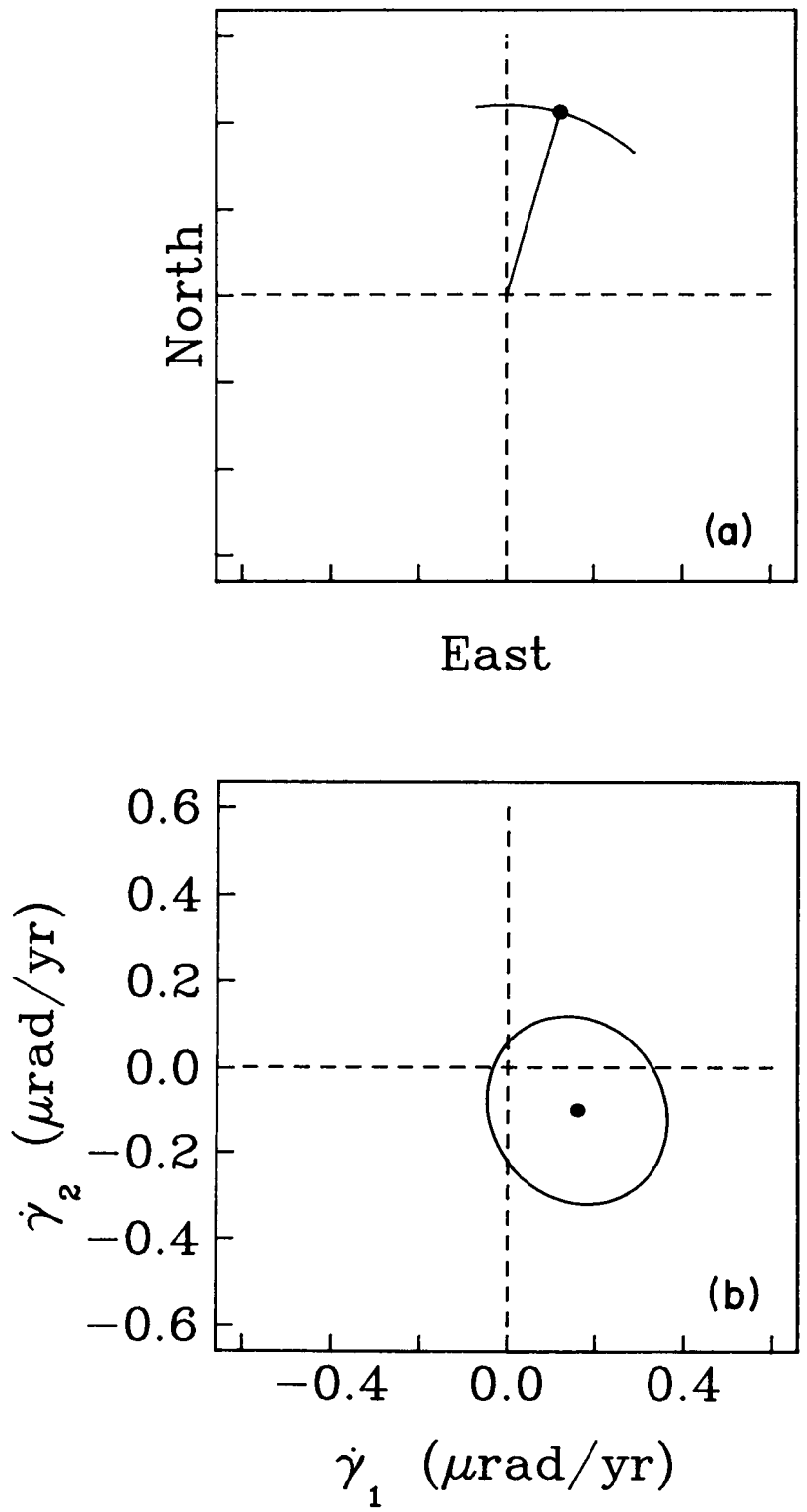

Figure 4. Strain rate inferred for the San Benito network by use of the DYNAP method, including corrections for deflection of the vertical and separation of the geoid and reference spheroid. (a) The orientation β of the axis of maximum compressive strain. The uncertainty in azimuth, at 95% confidence, is shown by an arc. (b) The shear strain rate parameters $\dot{\gamma}_1$ and $\dot{\gamma}_2$ together with a 95% confidence ellipse.

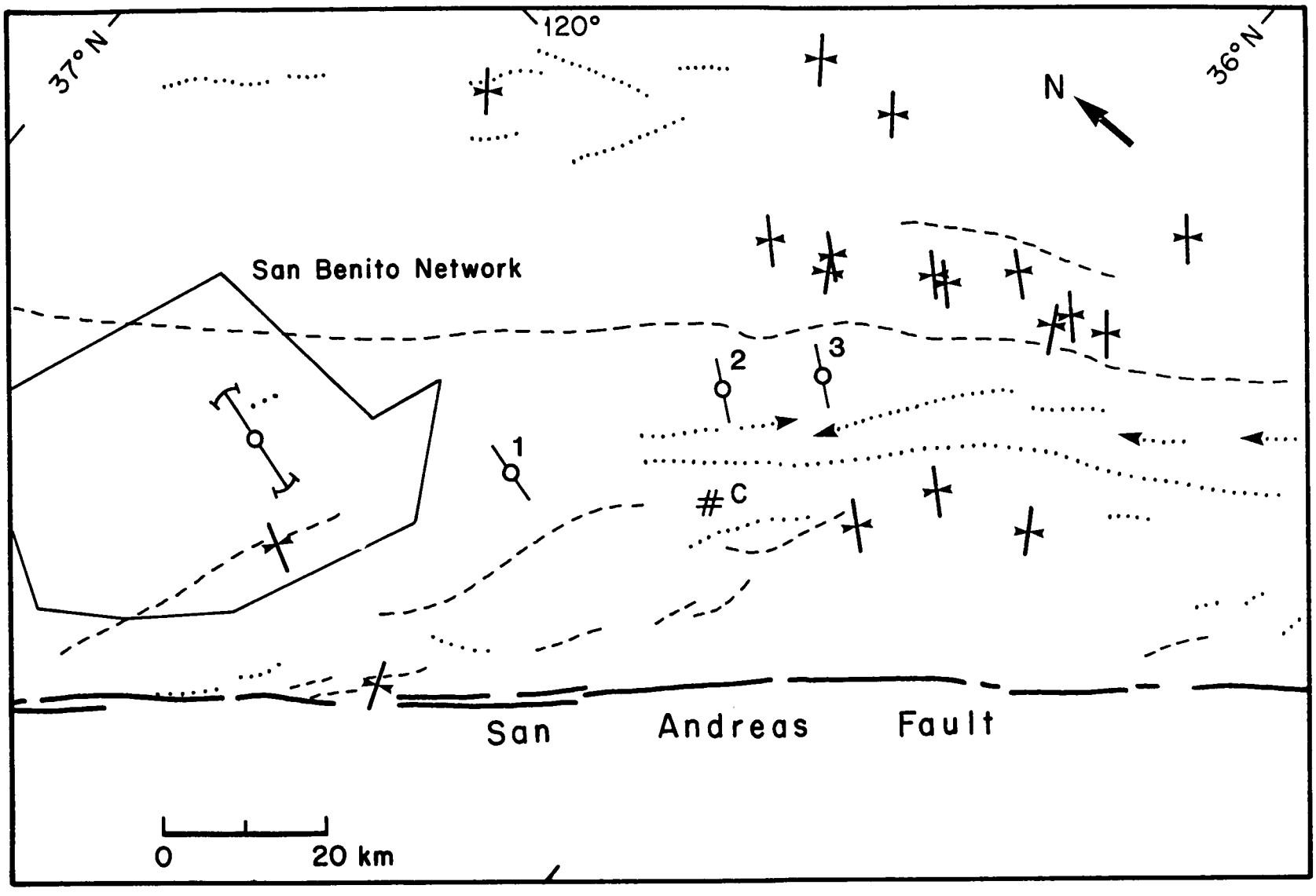

Figure 5. Fold structures and measured stress orientations in the region east of the San Andreas fault in central California [modified from *Mount and Suppe*, 1987]. Synclines are indicated by dashed lines, anticlines by dotted lines. Single arrows indicate the direction of plunge of a fold axis. Wellbore breakout measurements are given by a solid line with inward pointing arrows perpendicular to the direction of σ_1. The direction of σ_1 inferred from the azimuth of the P axes for three earthquakes are labeled by number: 1 = 1982 New Idria earthquake, 2 = 1983 Coalinga earthquake, and 3 = 1985 North Kettleman Hills earthquake. The axis of maximum compressive strain

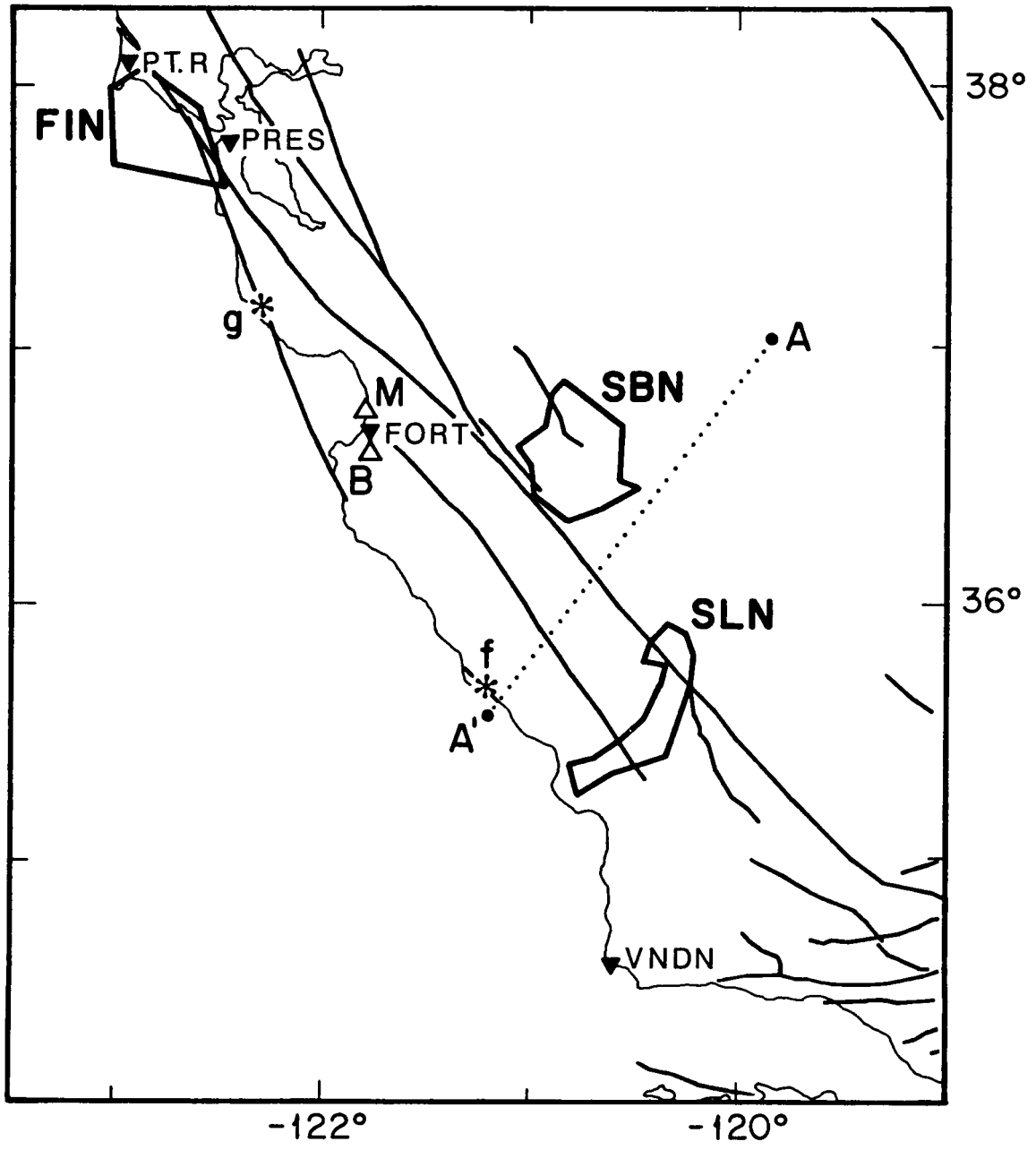

Figure 6. Reference figure for the geodetic and geological studies cited in Table 4. Brush (B) and Mulligan (M) are two stations in the USGS Pajaro trilateration network. At sites f and g, rates of fault slip were estimated geologically [*Clark et al.*, 1984] for the San Gregorio and Hosgri faults. The line A-A' is that for which *Namson and Davis* [1988] constructed their geological cross section (see Table 4). Fault traces are as given in Figure 1. Geodetic networks include FIN = Farallon Islands network, SBN = San Benito network, and SLN = San Luis network. VLBI stations include FORT = Fort Ord, PRES = Presidio, PT. R = Point Reyes, and VNDN = Vandenberg.

Chapter 4. Rates of Deformation in Southern and Central California from VLBI, Ground-based Geodetic, and Geologic Data

Introduction

Although rigid-plate models have been successfully used to describe global plate motions, the complexity in the spatial and temporal pattern of deformation at plate margins, particularly continental margins, are inadequately described by such simple interactions. The Pacific - North American plate boundary zone in the western U.S. has thus been a major focus of research on active tectonics. Although the San Andreas fault is usually identified as the major kinematic element at the plate boundary, significant deformation both east and west of the San Andreas has long been recognized by geologists [*Carey,* 1958; *Hamilton and Myers,* 1966; *Atwater,* 1970]. The distribution of deformation across different portions of this boundary document the transition from crustal spreading in the Gulf of California to right-lateral transcurrent motion along the San Andreas and extension in the Basin and Range province. How deformation is accommodated between different kinematic elements and the relation of this deformation to the overall accommodation of motion across the plate boundary on geodetic and geologic time scales is currently being examined. To address these questions previous workers have used the relative motion of the Pacific and North American plates determined from global plate motions and the rate of spreading in the Gulf of California, the rate and orientation of fault slip estimated from geological data, strain release patterns as seen in earthquakes, and the present-day rates of deformation estimated from data obtained from local and regional geodetic networks. Throughout much of the United States space-geodetic measurements are currently being made at intercontinental and regional spatial scales. In the last five years baselines that both span and are distributed within the Pacific - North American plate boundary zone have been measured with very long baseline interferometry (VLBI). In this study I use VLBI data to obtain estimates of the rate of change of tangential station position in a North-America-fixed reference frame. These data are used to constrain the integrated rate of deformation across portions of the continental plate boundary in California and to provide a tectonic framework

to interpret regional geodetic and geologic studies. For three regions, across southern California just north of the Imperial fault, in the 'big-bend' region, and in central California, I compare the rates of deformation derived from VLBI and ground-based geodetic data, and I examine the relationship between the rates of deformation determined from geological data and those estimated from geodetic data.

The rate of relative motion between the Pacific and North American plates obtained from global plate models such RM2 [*Minster and Jordan,* 1978] and NUVEL-1 [*DeMets et al.,* 1987] are based on magnetic anomalies averaged over the last several million years. Utilizing recently available marine magnetic data, the spreading rate in the southern Gulf of California has been estimated to be ~48 mm/yr [*DeMets et al.,* 1987]. To determine the present-day spreading rate across the Gulf of California satellite laser ranging (SLR) and global positioning system (GPS) measurements are currently being made [*Tralli et al.,* 1987]. The relative motion between the North American and Pacific plates determined from global plate models have been used as boundary conditions on kinematic models that describe the rate and distribution of deformation across the plate boundary in the western U. S. [*Minster and Jordan,* 1984, 1987; *Bird and Rosenstock,* 1984; *Weldon and Humphreys,* 1986].

In central California, the rate-of-slip vector of the San Andreas estimated from Holocene geological data [*Sieh and Jahns,* 1984] and ground-based geodesy [*Savage and Burford,* 1973; *Thatcher,* 1979a; *Lisowski and Prescott,* 1981; *Sauber et al.,* 1988] is 34 ± 3 mm/yr at N41°W ± 2° [*Minster and Jordan,* 1984; *Mount and Suppe,* 1987]. If the San Andreas fault functioned as a simple boundary that accommodated the full motion between two rigid plates, the rate of slip in central California predicted by global plates models would be 56 ± 3 mm/yr at N35°W ±2° [RM2, *Minster and Jordan,* 1978] or approximately 49 mm/yr at N35°W [NUVEL-1, *DeMets et al.,* 1987]. The discrepancy between the San Andreas fault and the global plate rate is represented by the integrated rate of deformation to

the east of the San Andreas in the Basin and Range province and across the Coast Ranges. The integrated rate of extensional deformation across the Basin and Range has been estimated from geological observations and from VLBI baselines that cross the region to be 9.7 ± 2.1 mm/yr at N56°W ± 10° [*Minster and Jordan,* 1984, 1987]. The vector difference derived using the above rate of motion for the San Andreas fault and Basin and Range, referred to as the discrepancy vector, is about 10 mm/yr in the direction N14°E, or 5 mm/yr of slip parallel to the San Andreas fault and 8 mm/yr of convergence normal to the fault [Model D, *Minster and Jordan,* 1987]. On the basis of the estimate made by *Minster and Jordan* [1987] the uncertainties in the discrepancy vector are approximately ± 5 mm/yr for the rate of slip and ± 15° for the direction. Although some minor internal deformation within the Sierra Nevada block [*Lockwood and Moore,* 1979] or across the Great Valley syncline may occur, most of the deformation represented by the discrepancy vector is thought to occur within the Coast Ranges. To distinguish between different models that describe the distribution of strike-slip and compressive displacements within the southern Coast Ranges in Chapter 3 we compared the findings of regional geologic and geodetic studies to the predictions represented by the discrepancy vector. These results support the view that the fault-parallel component of the discrepancy vector may be accommodated by strike-slip motion on the Rinconada as well as the San Gregorio fault. Geological and seismicity data, as well as our geodetic results, suggest that northeast-southwest compression in the Coast Ranges of central California may be localized to two regions, the 30-km-wide zone spanned by the San Benito triangulation and trilateration network [Chapter 3] and a second zone to the west of the Rinconada fault. The inferred shortening to the east of the San Andreas fault may represent a significant component of the fault-normal compression predicted by the discrepancy vector.

Utilizing geologic slip rates *Bird and Rosenstock* [1984] constructed a block model for the present horizontal velocity of the crust in southern California consistent with the

constraints of the RM2 Pacific - North American plate vector. On the basis of Quaternary slip rates derived from geological data *Weldon and Humphreys* [1986] proposed an alternative kinematic model for southern California which made very different predictions regarding the distribution of deformation. In southernmost California, Bird and Rosenstock estimated that approximately 57 mm/yr of right-lateral slip is distributed across the San Andreas, San Jacinto and Elsinore faults. In contrast, Weldon and Humphreys estimated only 37 mm/yr across the same faults, and they predicted that additional deformation occurs on the offshore faults in the California borderlands. Another major difference is seen in the rate of slip estimated for the northwest striking faults of the central Mojave Desert. Weldon and Humphreys assumed that the Mojave block is part of stable North America, whereas Bird and Rosenstock estimated 6.8 mm/yr of right-lateral strike-slip motion across the local faults. Both groups used a geological estimate of the cumulative displacement across the northwest trending faults [*Dokka,* 1983] to calculate the rate of slip for these faults. Unfortunately the time of initiation of fault slip is poorly constrained, and very different rates were thus assumed in the two models. *Sauber et al.* [1986], given in Chapter 2, used data from triangulation and trilateration surveys made during 1934 - 1982 to calculate shear strain rates in the central Mojave. If we assume that the rate of deformation measured across the network was due to right-lateral displacement across the local faults, the average shear straining corresponds to a relative displacement of 6.7 ± 1.3 mm/yr. Bird and Rosenstock predict that as a result of the ~ 7 mm/yr of relative motion across the central Mojave, either crustal shortening occurs on the western portion of the Garlock fault or crustal extension takes place on the eastern portion of this fault. We proposed that the distributed deformation on the northwest striking faults of the Mojave may instead be kinematically related to strike-slip motion on the right-lateral faults north of the Garlock fault that bound the region of extensional tectonics in the Great Basin.

In general the geological data are most useful for indicating long-term modes of deformation and for placing upper and lower bounds on rates. The differences in the kinematic models of southern California are due primarily to the uncertainties in the geologically determined rates associated with dating rock units and in the timing of geological reconstructions. The present-day rate of deformation can be estimated from geodetic measurements. Of course, the use of these rates of deformation, determined over a geologically short interval, to infer long-term deformation patterns is meaningful only if strain accumulates in a temporally uniform manner [Chapter 3].

Ground-based geodetic measurements from as early as 1880 have been used in crustal deformation studies in California. Historical surveys sample a long portion of the seismic cycle and have recorded coseismic and postseismic movements during and following earthquakes like the 1906 San Francisco and 1940 Imperial Valley earthquake [*Thatcher,* 1979b; *Thatcher,* 1986]. Combining historical triangulation and astronomic azimuth data with trilateration measurements, *Snay et al.* [1987] estimated the average rate of shear strain across most regions of California. From precise trilateration measurements made over the last 20 years on local and regional networks, the rates of horizontal deformation have been obtained for seismically active regions in the western U.S. [*Savage,* 1983]. Surface strain associated with an individual strike-slip fault occurs on distance scales that make it easy to measure with ground-based geodetic methods. In extensional and compressional regimes deformation, in contrast, may be distributed over a broad region, and it has therefore been difficult to obtain accurate estimates of the rate of such deformation. The northwest - southeast extension of the Basin and Range province could, in principle, be determined by repeated measurement of a network spanning the entire province. This would be a tedious and expensive operation, however, requiring the survey of many intermediate reference marks. Moreover, due to the propagation of errors across the network the estimated rate of extension would not be accurate enough for tectonic

modeling [*Minster and Jordan,* 1988]. Longer baselines can alternatively be measured using space-geodetic techniques. In this chapter, we utilize such data obtained from VLBI measurements made in the western U.S.

Determination of Rates of Deformation Utilizing VLBI

VLBI experiments have been conducted in the western U.S. since 1979 as part of the National Aeronautics and Space Administration (NASA) Crustal Dynamics Project. To supplement data available from large fixed radio antennae, mobile radio telescopes have been deployed at stations throughout the western U.S. The location of all the VLBI stations used in this study are shown in Figure 1. In Figure 2 the VLBI sites in California are shown along with Quaternary fault traces simplified from *Jennings* [1975]. The observational history of the 5 stations used in this study with permanent antennae, referred to as base stations, and the 17 sites which are periodically occupied by mobile VLBI units are given in Table 1. The station acronyms, full station names, approximate locations, and the geodetic latitudes and longitudes are given in *Clark et al.* [1987]. The antenna size of the base stations range from 9 to 40 m [*Clark et al.,* 1987]. The two mobile systems, MV 2 and MV 3, that are used for temporary occupation of sites in the western U.S. and Alaska have smaller antennae (3.7 m and 5.0 m, *Davidson and Trask,* 1985; *Clark et al.,* 1987). Data from frequent measurements to the base stations are available over an approximately five year time period (Table 1). Of the mobile sites in the western U.S., MON and JPL have been observed most frequently; DEAD, FLAG, MAMM, OCOT, and PVER have been observed less than 4 times.

Single-Epoch Processing

A VLBI experiment consists of two or more widely separated radio telescopes which simultaneously observe and record noise signals from extragalactic radio sources; these

recorded signals are later cross-correlated in pairs to determine the delay, with respect to local station clocks, between their arrival at the two antennae and the rate of change of this delay [*Shapiro*, 1983; *Clark et al.*, 1985a]. All the data utilized in this study have been acquired in a dual-band MARK III system VLBI geodesy experiment. In a Mark III experiment, observations are made at X-band (center frequency ~8.4 GHz) and S-band (center frequency ~2.2 GHz). During a typical 24-hour experiment, 10-15 sources are observed 5-15 times each.

After the cross-correlation process the delays and rates are used to estimate geodetic and nongeodetic parameters such as the station positions, the orientation of the Earth in inertial space, and the coordinates of the radio sources. From *a priori* site and source coordinates, theoretical delays and delay rates were computed by Goddard Space Flight Center (GSFC) using a VLBI model which includes the effects of precession, nutation, polar motion, sidereal rotation, UT1, Earth tides, and special and general relativity [*Clark et al.*, 1987]. Corrections for the ionosphere's dispersive effects were calculated from the differences in delay at the two frequencies. Tropospheric refraction corrections were estimated using meteorological data. The observations, their theoretical values, and the corrections mentioned above were combined to compute observation residuals which were used in a weighted least squares adjustment of the site locations and other parameters. These other parameters include low-order polynomial coefficients to describe relative clock and atmosphere behavior at each station and corrections to the *a priori* nutation model.

The principal sources of error in the determination of VLBI station positions are the troposphere and the Earth's orientation [*Shapiro*, 1983; *Davis et al.*, 1985; *Clark et al.*, 1987]. To minimize tropospheric errors the Saastamoinen zenith model, which utilizes surface measurements of pressure, temperature, and humidity, along with the CfA-2.2 mapping function [*Davis et al.*, 1985; C. Ma, personal communication, 1988] was utilized. To supplement this model one or more corrections to the tropospheric zenith path delay at

each site was made in a least squares estimation process. Variations in the rate of rotation of the Earth (UT1) and in the position of the axis of figure with respect to axis of rotation (polar motion) affect the directions of baseline vectors. To minimize orientation errors the GSFC group utilized an Earth orientation series based on primarily VLBI experiments [*Mallama and Ryan*, 1988]. Utilizing IRIS (International Radio Interferometric Surveying) experiments an Earth orientation series containing values of pole position and UT1 at 5-day intervals were compiled. The four station IRIS network, Westford, Fort Davis (FT.D), Richmond, and Wettzell in the Federal Republic of Germany became fully operational in January 1984. The predecessor to IRIS, the polar motion analysis by radio interferometric surveying (POLARIS) project, was a two-station network and could not simultaneously measure all components of Earth orientation. To supplement the POLARIS information, an Earth orientation series derived from SLR data was also used for the earlier time period. The standard deviation in the values derived utilizing IRIS experiments are approximately 0.002 arcsec for pole position and 0.0001 s for UT1.

Through the least squares adjustment process briefly described above (see also *Clark et al.*, 1987) *a priori* geocentric position vectors, denoted as $\mathbf{r}_i^o$ where i represents the station, were adjusted to obtain geocentric position vectors of N_{k-1} stations which were free to move in the k^{th} experiment, denoted by $\mathbf{X}_{i-1}^k$, relative to the position vector of the one station that is held fixed. For experiments in the western U.S. the number of stations N_k in an individual experiment k ranged from 3 to 7. For each experiment k the geocentric position vectors for the free stations, $\mathbf{X}_{i-1}^k$, are given with the corresponding covariance matrix $\mathbf{V}_d$.

The difference between the position vector at one site $\mathbf{X}_1^k$ and the position vector at a second site $\mathbf{X}_2^k$ is referred to as the baseline vector and is given by $\mathbf{B} = \mathbf{X}_2^k - \mathbf{X}_1^k$. The orthogonal vectors **L**, transverse **T**, and vertical **V** are defined in terms of the *a priori* station position vectors $\mathbf{r}_i^o$ as

$$\mathbf{L} = \mathbf{r}_2^o - \mathbf{r}_1^o$$

$$\mathbf{T} = \mathbf{L} \times \mathbf{r}_2^o$$

$$\mathbf{V} = \mathbf{T} \times \mathbf{L}$$

The length L, transverse T, and vertical V components of the measured baseline are defined as the projections of **B** on **L**, **T**, and **V**, respectively. The length component L of this vector is the magnitude of the baseline vector. The transverse component is positive when the azimuth of the baseline is rotated in the clockwise direction. The vertical component V is the adjustment from the *a priori* baseline perpendicular to the length and transverse components and is directed toward the local zenith at the midpoint of the baseline. The length L, transverse T, and vertical components V of the baseline vectors have been used in previous studies, and they provide a useful reference frame for the discussion of the effect of different observation errors.

The precision of baseline measurements in the western United States was estimated by *Clark et al.* [1987] from an examination of the weighted rms of the post-fit residuals of the least squares linear fits to each baseline component. The scatter in length L averages ~1 cm for a 500-km baseline and increases to 2 cm at 5000 km. For measurements made after 1984, the scatter in the transverse component T averages ~1 cm for a 500-km baseline and increases to ~2 cm at 5000 km. The scatter in the vertical component V was found to be much larger (~5 cm) and does not scale with baseline length.

The length component L of the baseline vector provides information similar to that obtained using trilateration. For trilateration measurements the basic observable is the round-trip travel time of a laser signal between two sites. From this observation the scalar length L between the sites can be calculated. Trilateration observations are made between stations in the area of interest and are not tied to an external reference frame. Since sites are

not simultaneously observed with trilateration the baseline length estimates from a network of stations are generally assumed to be uncorrelated. The stations in an individual VLBI experiment are, however, observed simultaneously and therefore the baselines are correlated.

With VLBI the delay or delay rate between the radio signal arrival at two stations is the basic observable. The theoretical delay or delay rates are calculated in the solar system barycentric coordinate system. Since geodesists are interested in motions in a terrestrial reference frame, e.g., geocentric coordinates, it is necessary to apply a series of transformations to change coordinate systems. Small errors in the determination of these transformations can map into rigid body motions of the geodetic network. These errors affect the *T* and *V* component; *L* is insensitive to rotations and translations of the entire network.

Multi-Epoch Processing for Determination of the Vector Motion of VLBI stations

Repeated geodetic observations can be used to infer information about movement of the crust of the Earth. The interesting parameters to be obtained from the data are the rate of change of the tangential station position, denoted by $\mathbf{v}_i$, in a well defined reference frame. The description of tangential velocity fields is natural for geological and geophysical studies across the Pacific - North American plate boundary zone. The rate of change of the local vertical component denoted by $\delta \mathbf{z}_i$ in a region undergoing uplift such as the Coast Ranges is expected to be only 1-3 mm/yr. As noted earlier, the local vertical component of site position is less well constrained than the horizontal components of position and it would be difficult to discern such small vertical changes over the five year interval of measurements.

A number of different approaches have been used to process repeated VLBI observations for crustal deformation studies. The rate of change of the length component,

denoted $\dot{L}$, can be estimated from the slope of the least-squares linear fit to the interstation length data. In the initial VLBI studies the rate of change of the length component $\dot{L}$ was utilized [*Clark* et al., 1985b; *Kroger et al.*, 1985; *Herring et al.*, 1986; *Minster and Jordan*, 1987]. This is partially due to the fact that the Earth orientation series was less accurate prior to 1984 when IRIS experiments commenced. $\dot{L}$ from individual baselines have been compared to rates of deformation determined from geological data. $\dot{L}$ from individual baselines in a network have been used to solve for the tangential rate of change in station position $\mathbf{v}_i$ relative to some reference frame. If only $\dot{L}$ data are used, the problems encountered are similar to those with trilateration data; i.e., the station velocities derived from observations are ambiguous; the addition of an arbitrary translation or rotation will have no effect on the residuals to the observations resulting from the adjustment [*Prescott*, 1981]. This datum defect can be removed in a number of different ways; for example, the rotational and translational ambiguity can be removed by fixing the position of one station and the azimuth to a second station. The velocities obtained depend on the azimuth of the fixed line and on the choice of the stations. In an alternative approach the indeterminate components of the displacement field are overcome by minimizing the difference between the computed displacements and those predicted by a geophysical model [*Prescott*, 1981; *Beroza et al.*, 1985; *Murray et al.*, 1985; *Segall and Matthews*, 1988]. *Prescott* [1981] has pointed out that in some tectonic environments, there is a reasonable expectation that displacements in one direction are more likely than in the orthogonal direction. In the vicinity of a strike-slip fault, for example, displacements parallel to the fault strike are expected to be larger than fault-normal displacements. An outer coordinate solution is defined as a solution that minimizes the displacement components in a particular direction.

Clark et al. [1987] utilized the average rates of change of length $\dot{L}$ and transverse $\dot{T}$ components to estimate the tangential station velocities $\mathbf{v}_i$ for stations distributed throughout the western U.S. Due to the large uncertainties in the earth orientation series

before IRIS experiments commenced, data from the transverse component was included only after 1984. The station velocities were estimated in two different reference frames, one in which MOJA and Westford, Massachusetts were held fixed and one in which ELY, FLAG, PLAT, FT.D, Westford and Fairbanks, Alaska were held fixed. In a reference frame in which the eastern stations were held fixed the horizontal velocity of MOJA was estimated to be 6.9 ± 0.8 mm/yr, N29°W [*Clark et al.* 1987; *Gordon and Sauber,* 1988]. This result accounts for the observation that in the reference frame in which MOJA was held fixed the stations ELY, FLAG, PLAT, and FT.D were all shown to have similar velocities to the south or southeast. In their solution the effects of possible correlations between baseline rates of change were neglected.

The data used in our study are the geocentric position vectors X_i^k of VLBI sites in the western U.S. In each experiment k the geocentric position vector for N_{k-1} stations were determined relative to the station position MOJA. The station position data are used to estimate the rate of change of tangential station position v_i utilizing an algorithm developed by *Beroza et al.,* [1986] (see also G.Beroza, unpublished manuscript, 1986). *Murray et al.* [1986] have applied the same techniques with slightly different model parameterizations to LAGEOS SLR data.

A problem common to most geodetic networks is that the distribution of sites surveyed varies considerably between epoches. In the VLBI data set utilized in this study, the number of stations participating in any one experiment ranged from three to seven; thus a given site is not included in all epoches. Such variable network geometry can introduce biases in the estimation of station positions. Additionally, analysis of a large geodetic network requires a more general procedure than analysis of small local networks. The outer coordinate solution or a homogeneous strain approximation are not appropriate for the large inter-station distances between VLBI sites, and a more flexible and general kinematic framework to relate the vector rate of change of station position to other tectonic

information is essential [*Beroza et al.*, 1986; G. Beroza, unpublished manuscript, 1986]. In the method utilized in this study we minimize the tangential displacement field with respect to an *a priori* geophysical model of deformation. We parameterize this model in terms of a tangential velocity of a station denoted by $\mathbf{v}_i^o$ in a North-America-fixed reference frame.

In the analysis of the VLBI position data we must discriminate between tectonic motions and apparent motions due to errors in Earth orientation parameters and errors in the vertical component due to the unmodeled tropospheric effects. It is desirable therefore to minimize the contribution that these parameters make to our estimate of the rate of change of tangential station position $\mathbf{v}_i$. Rigid body rotations of the network are given by $\mathbf{R\Omega}$, where R is an antisymmetric matrix of geocentric coordinates of the position vector $\mathbf{r}$ which operate on the angular rotation vector Ω:

$$\mathbf{R\Omega} = \Omega \times \mathbf{r}$$

Rigid-body rotations of the network $\mathbf{R\Omega}$ and changes in the local vertical component δz_j are considered to be what T.H. Jordan and coworkers have called "nuisance parameters".

Correlations between errors in site positions in each epoch should be fully accounted for when analyzing the data. In addition to the correlations for the data within a single epoch it would be desirable to account for the correlation between station positions made in different epoches. Errors in the data between epoches are, however, probably only weakly correlated through the assumed source positions and local site conditions (G. Beroza, unpublished manuscript, 1985). In this study we have assumed that errors in measurements made in different epoches are uncorrelated.

We assume that the parameters that map a station position from its initial position $\mathbf{r}_j^o$ to its position in the k^{th} experiment $\mathbf{X}_i^k$ are given by the relationship

$$\mathbf{X}_i^k = \mathbf{r}_i^o + (\mathbf{v}_i^o + \delta \mathbf{v}_i) \Delta t^k + \delta \mathbf{z}_i + \mathbf{R}_i \Omega^k + \mathbf{e}_i^k \qquad (1)$$

where $\delta \mathbf{v}_i$ is the tangential perturbation to the *a priori* reference velocity $\mathbf{v}_i^o$, Δt^k is the time interval between the first epoch measurement and the k^{th} experiment, and $\mathbf{e}_i^k$ is the error in the geocentric station position $\mathbf{X}_i^k$ of an individual station *i*. The estimate of the rate of change of tangential station position $\mathbf{v}_i$ is then given by:

$$\mathbf{v}_i = \mathbf{v}_i^o + \delta \mathbf{v}_i \qquad (2)$$

During an interseismic time period the rate of deformation may reasonably be assumed to be steady in time. There may, however, be changes at more local spatial scales that are non-tectonic in origin. Without other information we assume that $\mathbf{v}_i$ is constant.

In equation (1) the *a priori* reference velocity $\mathbf{v}_i^o$ and the *a priori* station position $\mathbf{r}_i^o$ are then known quantities that can be subtracted from both sides of equation (1). The change in local vertical $\delta \mathbf{z}_i$ and $\mathbf{R}_i \Omega^k$ are nuisance parameters. As we are interested in determining the tangential rate of change of station position we transform the geocentric position vectors to local position vectors, and the local vertical component $\mathbf{z}_i$ is removed. Rearranging terms, (1) is given by

$$\delta \mathbf{v}_i \, \Delta t^k + \mathbf{R}_i \Omega^k = \mathbf{X}_i^k - \mathbf{r}_i^o - \mathbf{v}_i^o \Delta t^k \qquad (3)$$

The model equation for multiple epoches can be written in the general form:

$$\mathbf{A}\,\mathbf{m} + \mathbf{B}\,\mathbf{n} = \mathbf{d} \qquad (4)$$

The first term in (4) represents the model vector **m** of station positons $\mathbf{X}^k$ which is operated on by the differencing matrix **A** to produce displacements due to $\delta\, v_i\, \Delta\, t^k$. The second term in (4) is the **B** operator which is composed of antisymmetric submatrices **R** of geocentric coordinates of the positon vector **r**, which operate on the vector **n**, of angular rotation vectors Ω to produce the rigid-body motions of the network between epochs. In equation (4) the effects of the model and nuisance parameters are equated with the left hand side of the equation given in (3).

In the first step the nuisance parameters **n** are determined using the data from non-fixed stations, referred to as free stations and denoted by the subscript *f*. For the free stations the error $\mathbf{e}_i^{\,k}$ is assumed to have zero mean and a variance given by $\mathbf{V}_d$. The correlations in site positions are accounted for by weighting the model equation with the inverse square root of the data covariance matrix denoted by $\mathbf{V}_d^{-1/2}$. The nuisance parameters **n** are later used to determine the motion of the fixed station, referred to as stationary and denoted by the subscript *s*. The model equation for the free stations for multiple epochs can be written in the general form

$$\mathbf{A}_f\, \mathbf{m}_f + \mathbf{B}_f\, \mathbf{n} = \mathbf{d}_f \qquad (5)$$

We seek to minimize the weighted L_2 norm [*Menke*, 1984] of the error vector.

$$\mathbf{e}^T\mathbf{e} = (\mathbf{d}_f - \mathbf{A}_f (\mathbf{m}_f - \mathbf{m}_f^o) - \mathbf{B}_f (\mathbf{n}))^T\, \mathbf{V}_d^{-1}\, (\mathbf{d}_f - \mathbf{A}_f (\mathbf{m}_f - \mathbf{m}_f^o) - \mathbf{B}_f (\mathbf{n})) \qquad (6)$$

This can be re-written in the simpler form

$$\hat{\mathbf{e}}^T\hat{\mathbf{e}} = (\hat{\mathbf{d}} - \hat{\mathbf{A}}\, \mathbf{m} - \hat{\mathbf{B}}\, \mathbf{n})^T\, (\hat{\mathbf{d}} - \hat{\mathbf{A}}\, \mathbf{m} - \hat{\mathbf{B}}\, \mathbf{n}) \qquad (7)$$

where we have made the substitutions:

$$\hat{\mathbf{d}} = \mathbf{V_d}^{-1/2} \, (\mathbf{d}_f - \mathbf{A}\mathbf{m}_f^o) \tag{8a}$$

$$\mathbf{m} = \mathbf{m}_f - \mathbf{m}_f^o \tag{8b}$$

$$\hat{\mathbf{B}} = \mathbf{V_d}^{-1/2} \, \mathbf{B}_f \tag{8c}$$

$$\hat{\mathbf{A}} = \mathbf{V_d}^{-1/2} \, \mathbf{A}_f \tag{8d}$$

The weighted normal equations to be solved for **m** and **n** are

$$(\hat{\mathbf{A}}^T \hat{\mathbf{A}}) \, \mathbf{m} = \hat{\mathbf{A}}^T \hat{\mathbf{d}} - \hat{\mathbf{A}}^T \hat{\mathbf{B}} \, \mathbf{n} \tag{9a}$$

$$(\hat{\mathbf{B}}^T \hat{\mathbf{B}}) \, \mathbf{n} = \hat{\mathbf{B}}^T \hat{\mathbf{d}} - \hat{\mathbf{B}}^T \hat{\mathbf{A}} \, \mathbf{m} \tag{9b}$$

Solving the second normal equation for the estimate of the nuisance vector **n** we obtain

$$\tilde{\mathbf{n}} = (\hat{\mathbf{B}}^T \hat{\mathbf{B}})^{-1} \, \hat{\mathbf{B}}^T \, (\hat{\mathbf{d}} - \hat{\mathbf{A}} \, \mathbf{m}) \tag{10}$$

Backsubstituting (10) into the normal equation for **m** (9a):

$$(\hat{\mathbf{A}}^T \hat{\mathbf{A}}) \, \mathbf{m} = \hat{\mathbf{A}}^T \hat{\mathbf{d}} - \hat{\mathbf{A}}^T \hat{\mathbf{B}} \, (\hat{\mathbf{B}}^T \hat{\mathbf{B}})^{-1} \, \hat{\mathbf{B}}^T \, (\hat{\mathbf{d}} - \hat{\mathbf{A}} \, \mathbf{m}) \tag{11}$$

Re-arranging and simplifying to get the model parameters on the left hand side:

$$\hat{\mathbf{A}}^T (\mathbf{I} - \hat{\mathbf{B}}\hat{\mathbf{B}}^\dagger) \, \hat{\mathbf{A}}\mathbf{m} = \hat{\mathbf{A}}^T (\mathbf{I} - \hat{\mathbf{B}}\hat{\mathbf{B}}^\dagger) \, \hat{\mathbf{d}} \tag{12}$$

where the dagger denotes the least-squares, minimum-norm generalized inverse. Solving for **m** we have

$$\tilde{\mathbf{m}} = [\hat{\mathbf{A}}^T \mathbf{Q}_{\hat{\mathbf{B}}} \hat{\mathbf{A}}]^{\dagger} \hat{\mathbf{A}}^T \mathbf{Q}_{\hat{\mathbf{B}}} \hat{\mathbf{d}} \tag{13}$$

where $\mathbf{Q}_{\mathbf{B}}$ is the symmetric, indempotent projection operator that annihilates **B n**, the effect of the nuisance parameters:

$$\mathbf{Q}_{\hat{\mathbf{B}}} = \mathbf{I} - \hat{\mathbf{B}}\hat{\mathbf{B}}^{\dagger} \tag{14}$$

Equation (13) is equivalent to:

$$\tilde{\mathbf{m}} = [\mathbf{Q}_{\hat{\mathbf{B}}} \hat{\mathbf{A}}]^{\dagger} \mathbf{Q}_{\hat{\mathbf{B}}} \hat{\mathbf{d}}. \tag{15}$$

Substituting in the relationships given in (8) into equation (15) :

$$\tilde{\mathbf{m}}_f = \mathbf{m}_f^o + [\mathbf{Q}_{\hat{\mathbf{B}}f} \hat{\mathbf{A}}_f]^{\dagger} \mathbf{Q}_{\hat{\mathbf{B}}f} \hat{\mathbf{d}}_f .$$

In the next step we seek to estimate the model parameters for the fixed station denoted $\mathbf{m}_s$. The estimate of **n** is then used in the equation for $\mathbf{m}_s$

$$\mathbf{A}_s \mathbf{m} + \mathbf{B}_s \mathbf{n} = \mathbf{d}_s \tag{16}$$

where

$$\mathbf{m} = \mathbf{m}_s - \mathbf{m}_s{}^o \tag{17}$$

to obtain

$$\mathbf{A}_s \mathbf{m} = \mathbf{d}_s - \mathbf{B}_s \mathbf{n} . \tag{18}$$

We assume the covariance for the right-hand side, the denuisanced data, is just the covariance propagated through the nuisance parameters **n**. That is, we assume that $\mathbf{V}_{ds} = \mathbf{B}_s{}^T \mathbf{V}_n \mathbf{B}_s$. Weighting and solving for **m** we obtain:

$$\tilde{\mathbf{m}}_s = \hat{\mathbf{A}}_s{}^\dagger (\hat{\mathbf{d}}_s - \hat{\mathbf{B}}_s \mathbf{n}) . \tag{19}$$

or substituting back in (17)

$$\tilde{\mathbf{m}}_s = \mathbf{m}_s{}^o + \hat{\mathbf{A}}_s{}^\dagger (\hat{\mathbf{d}}_s - \hat{\mathbf{B}}_s \hat{\mathbf{B}}_f{}^\dagger [\hat{\mathbf{d}}_f - \hat{\mathbf{A}}_f \tilde{\mathbf{m}}_f]) . \tag{20}$$

Thus, this algorithm provides an estimate of all the model parameters.

Data Analysis

A total of 81 experiments was used to estimate the rate of change of station position. Without rescaling the variance, the error in the rate of change of station position reflects only the uncertainty in the station position for a single epoch. An *a posteriori* variance was calculated from the condition that the χ^2 per degree of freedom of the postfit residuals be unity. The rescaling factor, denoted by $\sigma_o{}^2$, was estimated to be 4.2 for the set of 81 experiments. To look for data outliers the error residual was examined for each station. The error associated with one station was large for three of the experiments, and for one of

the experiments, April 12, 1984, the residuals were large at more than one station. T. Herring (personal communication, 1988) found a similar result and is currently examining problems with the phase calibrations made in the April 12, 1984, experiment. These four experiments were removed from the data set. In the remaining 77 experiments σ_0^2 was estimated to be 2.1.

As discussed above, a reference coordinate system can be obtained by minimizing the displacement field relative to an *a priori* geophysical model. Ideally, the rate of change of station positions within a network relative to one another will remain the same regardless of the *a priori* geophysical model used. However, because of biases due to the inhomogeneous distribution of stations in each experiment the results may be sensitive to the *a priori* model. A set of 50 experiments were analyzed with three different *a priori* models: (1) a model based on ground-based geodetic and geologic data (Table 2), (2) a model given by a uniformly distributed right-lateral shear strain over a 400-km-wide zone centered on the San Andreas fault, and (3) Model 2 with the addition of Basin and Range extension. The estimated station velocities for the three models do not differ by more than $\pm$ 4 mm/yr and are at orientations similar to within $\pm$ 5°. Using a larger set of data obtained from 77 experiments we tried using model 1 and model 2 and found results similar to that obtained for the set of 50 experiments. In the model given by distributed right-lateral shear distributed over a broad region centered on the San Andreas fault the rate of change of station positions for the sites YUMA, ELY, and FLAG all had southeast velocities, similar to result obtained by *Clark et al.* [1987] with MOJA held fixed. The results obtained using Model 1 represent our best estimate of the deformation field on the basis of ground-based geodetic and geologic data, and the results utilizing this *a priori* model are discussed below.

Results

In Table 2 are the calculated vector velocities with standard deviations, given as rates and orientations for all 23 stations. Uncertainties, where not otherwise stated, are one standard deviation (σ). Since OCOT, DEAD, MAMM, FLAG and PVER have been observed less than four times the vector velocities for these stations are not discussed in detail. In Figures 3 to 21 I show the estimated rates of change of station position for sites which have been measured at least four times and for a minimum of two years. The 95% confidence error ellipses given on each plot reflect the marginal uncertainty associated with the individual station velocities.

FT.D and PLAT are thought to be on cratonic North America, and ELY and FLAG are located within the Basin and Range province. The station velocities at FT.D (Figure 4), PLAT (Figure 5), and ELY (Figure 6) do not show a systematic trend, and the rate of change of station position is not significant at the 95% confidence level.

The station YUMA is located along the western boundary of the southern Basin and Range province. Although the station YUMA shows a rate of change of station position suggestive of Basin and Range extension (3.4 ± 2.7 mm/yr, N84°W ± 16°, Table 2) the value is not significant at the 95% confidence level (Figure 7).

BLKB and PINF are located near the southern segment of the San Andreas fault. The vector velocities of BLKB (Figure 8) and PINF (Figure 9) are 11.1 ± 3.3 mm/yr at N65°W ± 17° and 25.5 ± 3.7 mm/yr at N49°W ± 13° respectively. For comparison the azimuth of the San Andreas fault in this region is ~N45°W [*Jennings*, 1975].

The station MON is located approximately 15 km west of the Elsinore fault (Figure 2). Of the mobile VLBI sites MON was observed most frequently (21 times) and the vector velocity 40.1 ± 2.5 mm/yr at N44°W ± 6° (Figure 10) has a uncertainty comparable to the error for the vector velocity of the base station VNDN (45.7 ± 2.9 mm/yr at N41°W ± 6°).

The VLBI station MOJA is located just west of the domain of left-lateral faults in the northeast corner of the Mojave block (Figure 2, Chapter 2). The vector velocity of MOJA is 7.1 ± 0.9 mm/yr at N50°W ± 1° (Figure 11). The rate of change of station position of MOJA in a reference frame in which PLAT, ELY, FT.D, FLAG, Fairbanks and Westford are held fixed is 6.9 ± 0.8 mm/yr at N29°W [*Clark et al.*, 1987]. This result is similar to that obtained in a separate analysis by T. Herring [*Herring and Sauber*, 1988]. The rate of baseline length change $\dot{L}$ between MOJA and OVRO has shown no significant variation over the ~5 years that it has been measured [*Clark et al.*, 1987].

PBLO and JPL are located near the segment of the San Andreas fault referred to as the 'big-bend' region in which the azimuth of the San Andreas is ~N65°W [*Jennings*, 1975]. PBLO is located less than 5 km to the northeast of the San Andreas fault. Although these two stations are located on opposite sides of the San Andreas fault the vector velocity of JPL (34.0 ± 2.6 mm/yr at N44°W ± 6°, Figure 13) is not much higher than the vector velocity at PBLO (25.5 ± 2.7 mm/yr at N48°W ± 7°, Figure 12).

The station SANP is located in the Ventura Basin. Compression across this basin is thought to be oriented approximately north - south [*Yeats*, 1983; *Donnellan et al.*, 1988]. The vector velocity of SANP is 39.4 ± 4.5 mm/yr at N60°W ± 31°. This station has been measured only four times over a three and half year time period.

Of all VLBI sites in California VNDN is located at the greatest distance west of the San Andreas fault. The vector velocity of this station is 45.7 ± 2.9 mm/yr at N41°W ± 6°. Between the San Andreas fault and the VNDN site northeast - southwest compression is thought to occur across the Santa Maria Basin [*Feigl et al.*, 1988].

OVRO is located at the northern end of the Owens Valley graben between the Sierra Nevada Range to the west (Figure 2) and the Inyo Range and White Mountains to the east. Holocene offset on the Owens Valley fault is primarily right-lateral strike-slip with the azimuth of major segments of the fault zone varying from N5°W to N35°W [*Beanland and*

Clark, 1987]. The vector rate of change of the station OVRO is 10.3 ± 2.7 mm/yr at N37°W ± 4.5 (Figure 16). The orientation of the maximum right-lateral shear strain ($\dot{\epsilon}$) estimated from the Owens Valley trilateration network [*Savage and Lisowski,* 1980] is N20°W.

FORT is located just west of the Rinconada fault in central California. This station has been observed 7 times over a 4-year time period. The vector velocity of this station is 47.4 ± 2.8 mm/yr at N37°W ± 5° (Figure 17).

The HATC and QUIN sites are located west of the northern Basin and Range within a transition region between the Sierra Nevada and the Cascade Ranges (G. Beroza, unpublished manuscript, 1985). Both of these sites show significant motion, QUIN, 12.0 ± 3.1 mm/yr at N52°W ± 9° and HATC, 9.4 ± 2.6 mm/yr at N62°W ± 8°(Table 2, Figures 3, 18, and 19).

PRES and PT.R are located near the northern segment of the San Andreas fault which broke in the 1906 San Francisco earthquake. Although PRES is located east of the San Andreas fault the velocity of this station is quite high, 28± 7 mm/yr at N43°W ± 8° (Figure 20).

For the most western stations MON (Figure 10), SANP (Figure 14), VNDN (Figure 15), FORT (Figure 17) and PT.R (Figure 21) the NUVEL-1 Pacific - North American relative plate motion vector [*DeMets et al,* 1987] is shown for comparative purposes.

To examine the integrated rate of deformation between two VLBI sites it is desirable to calculate a differenced velocity vector for pairs of stations in regions of interest (Figures 22 through 29). The 95% confidence ellipse represents the scaled variance of the two stations as well as the station covariance.

Five difference vectors were determined for station pairs that are located on either side of the San Andreas fault (Table 3), MON - YUMA (Figure 22), MON - BLKB (Figure 23), JPL - MOJA (Figure 25), JPL - PBLO (Figure 26), and FORT - OVRO (Figure 28).

The difference vector for MON - YUMA is 37.6 ± 3.4 mm/yr at N40°W ± 8° and for MON - BLKB is 30.0 ± 4.5 mm/yr at N35°W ± 12°, consistent with right-lateral shear strain associated with the San Andreas, San Jacinito and Elsinore faults. The distance between the stations is ~110 km. For JPL - PBLO the difference vector is only 8.7 ± 3.7 at N34°W ± 6°; these two stations are located ~40 km apart. For JPL - MOJA the difference vector is 26.9 ± 2.6 mm/yr at N43°W ± 5°. The difference vector for OVRO and FORT is 37.1 ± 2.8 mm/yr at N37°W ± 5°; the distance normal to the San Andreas fault between these two stations is ~300 km.

The difference vector was also calculated between VNDN and three coastal stations, MON, SANP, and FORT. These results provide a constraint on the integrated rate of deformation along the coastal and offshore faults. Between VNDN and MON the difference vector is 5.6 ± 2.9 mm/yr, N23°W ±4°; consistent with primarily right-lateral strike-slip motion on northwest striking faults. The difference vector for VNDN - SANP indicate 15.2 ± 6.7 mm/yr of northeast-southwest compression (N15°E ±7°) between the two sites. The difference vector for VNDN - FORT is 3.8 ± 3.1 mm/yr at S25°W ± 4°.

Path Integral Formulation

The VLBI data provide discrete sampling of the temporal and spatial deformation field across a complex continental plate boundary. Individual stations are located within different tectonic domains. To interpret the VLBI-derived rates of deformation in terms of a regional tectonic framework requires integration with more densely sampled data. As is evident from Figure 30 and Figure 5 in Chapter 3 the VLBI, ground-based geodetic and geologic data are scattered throughout central and southern California. To provide a framework for discussion we construct three path integrals [*Minister and Jordan,* 1984; *Bird and Rosenstock;* 1984; *Weldon and Humphreys,* 1986]. For each path I consider two

different integrals, one in which geodetic data are used and one in which geological data are utilized.

For any given path connecting two points *a* and *b* the velocity of *b* relative to *a*, $\mathbf{v}(b)$, is given by

$$\mathbf{v}(b) = \mathbf{v}(a) + \int_a^b \hat{\mathbf{t}}(s)\, \nabla_s\, \mathbf{v}(r(s))dS \tag{21}$$

where $\mathbf{t}$ is the unit tangent vector to the path dr/ds, ∇_S is the surface gradient operator on S, $\mathbf{v}(r)$ is the tangential velocity field, and $\nabla_S\mathbf{v}(r)$ is the spatial gradient of velocity. Over the small distances (<100 km) between points we assume planar geometry; i.e., curvature of the Earth's surface is neglected.

On the assumption that a rate of change of station position determined from VLBI data represents the integrated rate of deformation between the VLBI site and stable North America this datum can be used as a fidicual point for the more densely sampled ground-based geodetic data. For example, when the VLBI stations are collocated with stations within the ground-based network $\mathbf{v}(a)$ can be taken as the velocity of the point on the southeastern edge of a network and $\mathbf{v}(b)$ the velocity on the northwestern edge of the network. For most regions of California VLBI stations are not collocated with ground-based networks and it is necessary to integrate the rate of deformation between sites.

For the sum of *p* independent determinations of the geological rate of slip on discrete faults equation (21) reduces to a simple sum of the relative slip across each fault between *a* and *b*:

$$\mathbf{v}(b) = \mathbf{v}(a) + \mathbf{v}_1 + \mathbf{v}_2 + \ldots\mathbf{v}_p \tag{22}$$

We assume the bounds on geological estimates of slip rate scale with the standard deviations so that if the estimates are independent their squares are additive and the standard deviation of $\mathbf{v}(a)$ is

$$\sigma_b = \sqrt{\sigma_a^2 + \sigma_1^2 + \sigma_2^2 + \ldots \sigma_p^2} \qquad (23)$$

[*Bomford,* 1985; p. 695]. Implicit in this formulation is that geological deformation occurs on discrete faults; these faults are assumed to be separated by rigid blocks. This approximation is most appropriate in a strike-slip environment where fault displacements can be measured most directly. In either extensional or compressional regimes deformation may be distributed over a broad region where slip on individual faults may be difficult to measure.

Comparison of Geodetic and Geologic Rates of Deformation in Southern and Central California

The rate of recent deformation estimated from geologic data in southern and central California is appropriate to time scales of approximately 10^2 - 10^6 yrs. The rate of deformation obtained with triangulation, trilateration, and VLBI data correspond to the last 10^0 - 10^2 yrs. In Tables 4 and 5 rates of deformation on the San Andreas system in southern California and east of the San Andreas fault are given for both types of estimates. Rates of deformation in central California estimated from geologic and geodetic data were presented in Chapter 3, Table 4. In this section I briefly consider how these rates of deformation are derived, and I present the results of the construction of path integrals based on these data.

The locations of the three path integrals are given in Figure 31. Along each path I plot the velocity of each appropriate station resolved into fault-normal and fault-parallel velocity components as a function of the distance from the San Andreas fault (Figures 32 through 37). I choose to plot these profiles perpendicular to the local orientation of the San Andreas fault for two reasons. As discussed in Chapter 3 if the shear stress parallel to the San Andreas fault is relieved through surface creep, as in central California, or during

periodic earthquakes, the maximum principal stress direction immediately adjacent to the San Andreas fault should be reoriented perpendicular to the San Andreas fault. Additionally, trilateration data from the Salton Sea and Eastern Transverse Ranges were processed employing the outer coordinate solution in which the fault-normal velocity component is minimized and the data are resolved into a fault-parallel and and fault-normal components.

Path 1 is located at the latitude of southernmost California (Figure 31). Deformation along this path includes possible extension in the southern Basin and Range and right-lateral slip along the the San Andreas, San Jacinto, Elsinore and possibly offshore faults (Table 4 and 5). The integrated rate of extension across the southern Basin and Range is given by the rate and orientation of slip at the station YUMA. For the region between the San Andreas and Elsinore faults we assume simple right-lateral slip at the orientation given by the fault-parallel component of velocity (N39°W). Due to the paucity of available geologic and geodetic data on the rate of offshore slip the path integral does not continue west of MON.

The second path crosses the 'big-bend' portion of the San Andreas fault. In this section the San Andreas fault locally changes its trend by 20°-30° along a 190-km-long segment between San Gorgonio Pass and Tejon Pass. Recent deformation is thought to occur as extension in the Basin and Range east of the Mojave Desert, right-lateral strike-slip motion on the faults of the central Mojave, right-lateral strike-slip on the San Andreas fault, and north-south to northeast-southwest compression across the western Transverse Ranges and the offshore faults in the Channel islands (Table 4 and 5; see also compilation given in *Bird and Rosenstock,* [1984] and*Weldon and Humphreys,* [1986]). N62°W is used as the fault-parallel orientation with N28°E for the fault normal component.

Although slip along the San Andreas fault is thought to occur primarily through surface creep within a narrow zone in central California, path 3 crosses numerous distinct

tectonic elements east and west of the San Andreas fault (Chapter 3; see also *Minster and Jordan,* [1984]). Relative to stable North America the first region where active deformation is thought to occur is across the Basin and Range through a combination of right-lateral strike-slip motion and extension on pull-apart basins. As discussed in Chapter 3 little deformation is thought to occur within the Sierra Nevada batholith or across the Great Valley. To the west of the Great Valley deformation across the Coast Ranges is separated into right-lateral slip on the San Andreas, Rinconada, and San Gregorio faults and distributed northeast-southwest compression across the Coast Ranges (Chapter 3). The geological and seismicity data suggest that northeast-southwest compression may be localized to two regions, one zone within the 30-km-wide zone spanned by the San Benito network (Chapter 3) and a second zone west of the Rinconada fault (Chapter 3). The fault-parallel orientation is taken as N41°W with a fault-normal component of N49°E.

Path Integrals Utilizing Geodetic Data

The rate of change of angles or baseline length are the basic observable used to estimate the rate of deformation with either triangulation or trilateration data. From these data either the rate of strain ($\dot{e}$ or $\dot{\gamma}$) or the rate of change of individual station positions are determined. In the central Mojave Desert (Chapter 2) and in the Diablo Range (Chapter 3) the rate of slip was estimated from the average rate of shear strain ($\dot{\gamma}$) determined from triangulation and trilateration data. In Chapter 3 we utilized the average rate of line length change on individual trilateration lines to estimate the rate of right-lateral slip on the San Andreas, Paicines, and Rinconada faults in central California. To estimate the displacement rate across the Salton Sea and Eastern Transverse Range networks repeated trilateration measurements have been utilized to calculate the average rate of change of tangential station positions [*Prescott et al.*, 1987]. Since all observations were made between stations in the area of interest rigid body translation and rotation of the network can not be estimated; the

ambiguity expresses itself as a rank defect of 3 in the coefficient matrix of the normal equations [*Prescott*, 1981]. This ambiguity is overcome by selecting the rigid-body translation such that the centroid of the network remains fixed and the rms velocity component normal to a preselected direction is a minimum. The preselected direction is taken as the strike of the vertical plane of maximum right-lateral shear as determined from a uniform-strain-rate approximation to the observed values of line length change. This direction was N39°W for the Salton Sea network and N58°W for the Eastern Transverse Range network (J. Savage and M. Lisowski, personal communication, 1988). The requirement that the centroid of the network be fixed only specifies the point relative to which all velocities were determined; it does not affect the pattern of velocities.

Path 1. In Figures 32 and 33 the fault parallel (N39°W) and fault normal component (N51°E) of the rate of change of position of geodetic stations along path 1 are given in a North America (NOAM) fixed reference frame. Although the station YUMA shows a rate of change of station position suggestive of Basin and Range extension (3.4 ± 2.7 mm/yr at N84°W $\pm$ 16°, Table 2) the value is not significant at the 95% confidence level (Figure 7). The Salton Sea network, located northwest of YUMA, spans the San Andreas, San Jacinto and Elsinore faults. In Figures 32 and 33 the velocity profile for the northwestern portion of this subnetwork is given. The station BLKB is located just east of the network, PINF to the north, and MON is collocated with the USGS trilateration station Monument Peak within the network. Since the rate of change of station position is well determined for MON the velocity of the USGS station is set equal to the vector rate of change of station position of the VLBI station MON (40.1 mm/yr at N44°W).

The fault parallel component of the velocity of PINF and BLKB and the trilateration data are in close agreement (Figure 32). Although the fault-normal component of velocity of the VLBI stations have larger values than the corresponding trilateration data these velocities are not significantly different than the trilateration results.

Path 2. In Figures 34 and 35 the fault parallel (N62°W) and fault normal component (N28°E) of the rate of change of position of geodetic stations along path 2 are given in a North America-fixed-reference frame. Since there are few ground-based geodetic networks across the broad region given by the Basin and Range province to the east of the Mojave Desert block, we are unable to estimate the geodetic rate of deformation. The station MOJA is, however, located north of the region traversed by our path and is included on the path 2 velocity profile. As discussed in Chapter 2, a geodetic estimate of 6.7 ± 1.3 mm/yr at N41°W of right-lateral slip has been estimated for the region between the Helendale and Camp Rock faults (Table 5, K) in the central Mojave Desert. The Eastern Transverse Ranges network (ETR) spans the San Andreas near Palmdale. There are two VLBI stations within the network, JPL in the south and PBLO in the northeast. Since more observations have been made to JPL the vector velocity of this station (34.0 mm/yr at N44°W) was used to fix the corresponding site velocity in the ETR network. One VLBI station, SANP, located northwest of JPL is also included in the profile.

The rate and orientation of slip on the central Mojave faults determined from triangulation and trilateration data are similar to those of the vector velocity estimated for MOJA (the MOJA velocity vector is more westerly by 10°). After fixing the velocity of one station in the trilateration network the velocity of the other VLBI station, PBLO, is similar to the trilateration data results from the ETR network. The N28°E or fault-normal component (Figure 35) appears to be erratic in both the trilateration and VLBI data.

Path 3. In Figures 36 and 37 the fault parallel (N41°W) and fault normal component (N49°E) of the rate of change of position of geodetic stations along path 3 are given in a North America fixed reference frame. The station OVRO is used as a starting point for the path integral utilizing geodetic data. Between OVRO and the next most western station along this path, FORT, there are several geodetic networks. These include the San Benito network that spans the Diablo Range east of the San Andreas fault, the Coalinga

trilateration network that spans the Paicines and San Andreas fault, and one line from the Pajaro network which spans the Rinconada fault. The FORT - OVRO difference vector is 37.1 ± 2.8 mm/yr at N37°W ± 5°. The integrated rate of deformation estimated from the ground-based geodetic networks is 36.5 mm/yr at N34°W.

Path Integral Utilizing Geological Data

Geologic estimates of the rate of deformation depend on two key elements: the age and amount of deformation of a given stratigraphic unit. The current techniques that are available for estimating the age of late Cenozoic deposits can be grouped into three categories: numerical methods such as the radiometric ^{14}C technique, correlation methods which tie the deformed sequence with the age of a stratigraphic unit that can be dated, and relative dating methods such as soil development [*Pierce*, 1986]. The radiometric techniques yield accurate ages, but suitable samples for dating are often difficult to find and the less precise correlation and relative dating methods are instead used. Some of the methods employed to estimate the amount of deformation in southern and central California are offset of distinctive stratigraphic units [*Dokka*, 1983] and land forms such as alluvial fans, stream channels [*Sieh and Jahns*, 1984], and marine terraces[*Clark et al.*, 1984], degradation of fault-scarp morphology, and palinspastic reconstructions [*Namson and Davis*, 1988]. As discussed in Chapter 3, the geological data are most useful for indicating the long-term modes of deformation and for placing upper and lower bounds on rates of deformation. Thus in Tables 4 and 5 the geological estimate of slip rate is given as an upper and lower bound; a best estimate of the long-term average fault slip rate is also indicated.

Path 1. Little recent deformation is thought to occur within the southern Basin and Range; the rate of deformation is, however, poorly constrained by geological data (Table 5, M). Along Path 1, geologic slip is documented on the San Andreas, San Jacinito and

possibly the Elsinore fault. In Figures 32 and 33 the integrated rate of deformation estimated from the geological data , resolved into a fault-normal and a fault-parallel component, is given for path 1. Since we assume simple right-lateral slip at the orientation given by the fault-parallel component of velocity (N39°W) for the region between the San Andreas and Elsinore faults, no geological data are included on the fault-normal plot. The geologic data as well as the the station velocities estimated from VLBI and ground-based geodetic data suggest a broad zone of right-lateral deformation (at least 150 km wide). The best estimates of right-lateral slip across the San Andreas (Table 4, B), San Jacinto (Table 4, H), and Elsinore (Table 4, I) faults is higher than the corresponding velocity determined from geodetic data.

Path 2. The integrated rate of deformation estimated from the geological data is given for path 2 in Figures 34 and 35. Within the Quaternary little or no deformation is thought to have occurred between the Colorado Plateau and eastern Mojave Desert block (Table 5, M). Although Quaternary slip has been documented across all the faults of the central Mojave, the rate of slip on the faults of central Mojave is poorly constrained from geological data. The geological estimates of the long-term rate of slip on the San Andreas fault range from 16 to 60 mm/yr (Table 4, E), with the best estimate 30 ± 5 mm/yr [USGS, 1988]. As with the result noted on the Path 1 profile, the best estimate of the N58°E component of velocity from geological data are higher than the velocities predicted from the strain data.

Path 3. The integrated rate of deformation estimated from the geological data is given for path 3 in Figures 36 and 37. From the geological data the best estimate of the rate and orientation of extension in the Basin and Range are 9 mm/yr and N60°W (Table 5, W). In contrast, the estimated vector velocity of OVRO is 10.3 ± 2.7 mm/yr at N37°W ± 4°. With the exception of these discrepant directions, the geologic and geodetic data for the

Diablo Range, San Andreas fault, and the Rinconada fault are in good agreement (Chapter 3, Table 4) for both the fault-normal and fault-parallel components (Figures 36 and 37).

Discussion

The VLBI, ground-based geodetic, and geologic data provide a basis to discuss the relation between deformation in the southern Basin and Range province, the Mojave Desert block, and the northern Basin and Range province, the relation between geologic and geodetic rates of deformation in central and southern California, and constraints on the rate of deformation west of the San Andreas fault.

The Rate of Deformation Across the Basin and Range Province

The Basin and Range province is a region of active crustal spreading characterized by high regional elevation, thin crust, and high heat flow [*Zoback and Zoback*, 1980]. On the basis of the uniformity of the stress field inferred from *in situ* stress measurements, seismicity and stress sensitive geological features *Zoback and Zoback* [1980] delineated the Basin and Range - Rio Grande rift stress province. This province extends from the Sierra Nevada eastward to the Colorado Plateau physiographic province and around the southern margin of the Colorado Plateau and northward into the Rio Grande rift in New Mexico. Although the northern and southern Basin and Range have similar stress field orientations little recent deformation is thought to occur in the southern Basin and Range. The rate of change of station position at the VLBI station YUMA is not greater than the 95% uncertainty in the determination (Table 2 and Figure 7). This station has been observed approximately the same number of times over a similar interval as the station QUIN located along the western edge of northern Basin and Range. The results for QUIN (Figure 18), however, show significant slip at a rate and orientation consistent with other estimates of

Basin and Range extension (Table 5, W). This result supports a lower rate of deformation across the southern Basin and Range.

Within the Basin and Range extension occurs in approximately the N60°W ± 20° direction (Table 5, W). To the north of the Garlock fault in the Basin and Range extension occurs as right-lateral strike-slip motion on northwest trending faults separated by pull-apart basins [*Zoback and Zoback*, 1980; *Burchfiel et al.*, 1987]. The vector rate of change of the station OVRO, 10.3 ± 2.7mm/yr at N37°W ± 4.5°, is closer to the local orientation of the Owens Valley fault than the assumed direction of extension in the Basin and Range. Within the northern Basin and Range purely dip-slip motion is observed on north-northeast striking faults. The vector velocities for HATC are 9.4 ± 2.6 mm/yr at N62°W ± 8°, and for QUIN, 12.0 ± 3.1 mm/yr at N52°W ± 9°. Within the uncertainties in estimated vector velocities, the stations north of the Garlock are consistent with the rate and orientation of deformation derived from local geodetic and geological data.

The VLBI station MOJA is located in the northeast corner of the Mojave Desert block. The vector velocity of MOJA is 7.1 ± 0.9 mm/yr at N50°W ± 1°, similar the rate of change of station position determined for OVRO (Table 2). The velocity of the Mojave Desert site is puzzling because the rate of extension in the southern region of the Basin and Range province is not thought to be greater than 1 - 3 mm/yr [*Herring and Sauber*, 1988]. As discussed in Chapter 2, the left-lateral slip observed on the Garlock fault has been hypothesized to occur due to the difference in motion between extension in the Basin and Range and a more stable Mojave block. Within the Mojave block there are two domains of transcurrent faults that show Quaternary movement, right-lateral faults in the central Mojave Desert and left-lateral faults in the northeast corner of the block (Figure 2, Chapter 2). In Chapter 2 we proposed the hypothesis that the deformation on the northwest striking faults of the central Mojave may be kinematically related to strike-slip motion on the right-lateral faults that bound the region of extensional tectonics in the Great Basin. By this view, the

MOJA station as well as the Garlock fault are within a deforming region connecting slip in the central Mojave to deformation north of the Garlock fault.

The maximum shear rate on the eastern segment of the Garlock fault was determined to be 0.18 ± 0.01 μrad/yr, oriented N59°E ± 2° if left-lateral or N31°W ± 2° if right-lateral (Table 5, P). The strain data along the Garlock fault are thus consistent with the rate and orientation of strain estimated from the central Mojave region and north of the Garlock fault. The accommodation of this strain along faults of the region is geometrically complex. The orientation of the surface trace of the Garlock fault is approximately east-west, significantly different from the orientation of the rate of maximum shear strain. The geometry of the Garlock fault is suggestive of clockwise rotation. This interpretation is further supported by the presence of left-lateral faults in the northeast corner of the Mojave block.

An alternative hypothesis is that the slip in the central Mojave Desert, including the rate of change of the station MOJA, is due to elastic shear strain accumulation associated with the 'big-bend' portion of the San Andreas fault. The last large earthquake along this segment occurred in 1857 [*USGS*, 1988]. In Chapter 2 we argued against the hypothesis that strain in the central Mojave was associated with elastic strain which would be released in a large San Andreas earthquake on the basis of the orientation of the measured shear strain (N41°W versus ~N65°W for the San Andreas fault) and the 40-90 km distance of the central Mojave deformation from the San Andreas fault. MOJA is located approximately 125 km from the San Andreas fault. The relation of deformation in tectonic domains adjacent to the San Andreas to slip on the San Andreas fault is discussed further below.

Geologic Strain versus Incremental Strain

Although we have parameterized the strain results in terms of a velocity vector relative to North America, the rate of change of an individual station may be due to elastic strain

accumulation which may be relieved in a large earthquake. Extensive modeling of geodetic data has been used to examine the parameters thought to influence the rate and pattern of surface deformation throughout the seismic cycle [*Reid,* 1910; *Savage and Burford,* 1973; *Yang and Toksoz,* 1981; *Thatcher,* 1983; *Cohen and Kramer*, 1984; *Li and Rice*, 1987]. *Reid* [1910] assumed that a major earthquake would not recur until all strain released by the preceding even had reaccumulated. Implicit in this assumption is that all crustal deformation is elastic and recoverable [*Thatcher,* 1986]. The contribution viscous relaxation makes to the rate and pattern of deformation following a large earthquake just south of profile 1 in the Imperial Valley (the 1940 El Centro earthquake, $M_S = 7.1$) was examined for several rheological models [*Sauber et al.*, 1984; J. Sauber unpublished manuscript, 1984]. The effect of post-seismic relaxation on both horizontal and vertical displacements was estimated utilizing a three dimensional finite element method with a viscoelastic earth model [*Yang and Toksoz,* 1981]. Externally applied displacements corresponding to coseismic slip associated with the 1940 earthquake were prescribed, and the time-dependent displacements were calculated. Similar to the results reported by *Yang and Toksoz* [1981] and *Cohen and Kramer* [1983] the temporal and spatial patterns of surface deformation were found to be most sensitive to the geometry and rheological properties of the material that lies below the slip plane in a volume whose extent is a few times the seismogenic fault depth. Although horizontal displacements are much larger than vertical displacements for a strike-slip earthquake, the time dependent behavior of vertical displacements were found to be particularly sensitive to lateral changes in viscosity distribution. Post-seismic vertical movements were most closely matched with an Earth model with an elevated low viscosity zone near the fault; viscous relaxation accounted for approximately 25% of the post-seismic deformation measured adjacent to the Imperial fault between 1941 and 1954.

A large earthquake has not occurred on the southern segment of the San Andreas fault within the last ~400 years [*Sieh,* 1986], and the last large earthquake to occur in the 'big-bend' region was in 1857 [*USGS,* 1988]. In central California slip along the San Andreas fault is thought to occur primarily through surface creep. For the interseismic period, a simple model that approximates the postulated behavior of strain along a strike-slip boundary is a screw dislocation in an elastic half-space [*Savage and Burford,* 1973]. The rate of slip in the elastic half-space is assumed to be zero down to a depth given by D but equal to b below that depth. The strike-slip velocity, denoted by υ, on the free surface is then given by

$$\upsilon / b = \pi^{-1} \arctan (x / D)$$

where x is the distance perpendicular to the fault. In California, the depth of the seismogenic zone along the San Andreas fault is approximately 10 km; it is assumed that in the upper 10 km most slip is accommodated by stick-slip at the time of infrequent large earthquakes [*Sibson,* 1982]. The velocity b controls the overall range of υ, and D specifies the breadth of the zone of deformation. In such a model 50% of the relative slip is accommodated in the interval $-D < x < D$; to include 90% of the relative slip one must span $-6.3\ D < x < 6.3\ D$ [*Savage and Lisowski,* 1988]. This simple relationship is used to approximate the width over which elastic strain which may be relieved in a large earthquake on the San Andreas fault in southern California or the 'big-bend' region of the California.

The velocities estimated from geodetic data represent the average of the rate of deformation over only a small portion of a plate boundary seismic cycle. The geological estimates of rates of deformation, as indicated by the upper and lower bounds on the profiles, are subject to large uncertainties. Given these limitations we discuss the results obtained by comparing geologic and geodetic data.

The best estimate of the geologically derived value for the integrated rate of slip across the southern Basin and Range and the San Andreas, San Jacinto, and Elsinore faults, if correct, is close to the relative plate motion vector predicted by NUVEL-1 (46.5 mm/yr at N39°W); little deformation is then predicted to occur offshore. The geological estimate of 30 mm/yr (Table 4, B) for the southern San Andreas fault is higher than other estimates of the slip rate on this segment [*Weldon and Humphreys*, 1986] and is higher than the rate of slip on the San Andreas fault in Cajon Pass [Table 4, D]. If the long term slip rate on the San Andreas is instead 25 mm/yr, the geologically derived values for the integrated rate of slip are in Figure 32 is shifted down 5 mm/yr and the geological and geodetic estimates of velocity are similar near the San Jacinito and Elsinore faults. If strain along this segment of the San Andreas were being relieved through surface creep, as in central California, we would expect the velocity profile to have an abrupt step across the fault. Between BLKB, located ~25 km east of the San Andreas fault, and MON located ~85 km southwest of the San Andreas fault, the differenced velocity vector is 30.0 ± 4.5 mm/yr at N35°W ± 2°. Between YUMA, located ~105 km east of the San Andreas fault, and MON the differenced velocity vector is 37.6 ± 3.4 mm/yr at N40°W ± 8°. If the MON - YUMA differenced velocity vector represents the rate of slip that will be accommodated by geological slip on the San Andreas, San Jacinto, and Elsinore faults, then additional deformation, as suggested by *Weldon and Humphreys* [1986], is predicted on the offshore faults in the California borderlands.

Along Path 2, the geologically estimated velocity is also higher than the rate of slip given by the geodetic data. If the rate of slip on the San Andreas fault is as low as 25 mm/yr as suggested by the Cajon result, the geologic and geodetic results are closer. The rate of deformation between the station pairs JPL - PBLO and JPL - MOJA can be used to look at deformation associated with the 'big-bend' portion of the San Andreas fault. Between PBLO, located ~5 km northeast of the San Andreas fault, and JPL located ~ 40

km southwest of the San Andreas fault, the differenced velocity vector is 8.7 ± 3.7 mm/yr at N34°W ± 6°. Between MOJA, located ~125 km east of the San Andreas fault, and JPL the differenced velocity vector is 26.9 ± 2.6 mm/yr at N43°W ± 5°. Over the broad region between MOJ and JPL the rate of deformation given by differenced velocity vector is quite low. This result suggests that the long term rate of slip on this segment may be only 25 mm/yr.

Slip on Offshore Faults

Within the central and southern Gulf of California the plate boundary may be traced along a series of well-defined en echelon transform fault zones, each trending approximately along the mean direction of plate motion [*Goff et al.*, 1987]. In the northern Gulf of California, plate motion appears to be taken up over a wider zone of deformation that includes faults in northern Baja California, such as the Agua Blanca and San Miguel faults, as well as the principal continental transform fault, the Cierro Prieto fault. Both the Agua Blanca and San Miguel faults are currently active on the basis of recent seismicity, large historic earthquakes and Quaternary stream offsets [*Allen et al., 1960; Lomnitz et al.*, 1970]. Slip on the Agua Blanca and San Miguel faults are thought to transfer motion onto the offshore faults of the southern California borderland [*Weldon and Humphyreys*, 1986; *Goff et al.* 1987]. *Schug et al.* [1987] report a lower mid-Pleistocene to present rate of ~4 mm/yr along the western reach of the Agua Blanca fault and a slip rate of 2 to 5 mm/yr for the Agua Blanca 50 km inland from the Pacific Ocean.

The relative motion between the North American and Pacific plates in southern California is predicted to be 46.5 mm/yr at N39°W (NUVEL-1, *DeMets et al.*, 1987). West of MON an additional ~6 mm/yr of primarily right-lateral northwest slip is predicted to occur on the basis of the VLBI results. This rate is consistent with the recent estimates slip along the Agua Blanca and San Miguel faults. Further north, the rate of slip at the

station VNDN suggest that most the Pacific - North American relative plate motion is accommodated east of this site (Figures 3 and 15). The velocity of VNDN relative to MON, SANP, and FORT could ideally be used to constrain the amount of deformation occurring between the site pairs in southern California, the western Transverse Ranges, and in central California. Between VNDN and MON the difference vector is 5.6 ± 2.9 mm/yr at N23°W ±4°, consistent with primarily right-lateral strike-slip motion on northwest striking faults. The difference vector for VNDN - SANP indicates that 15.2 ± 6.7 mm/yr of northeast-southwest compression (N15°E ± 7°) between the two sites may be occurring. The difference vector for VNDN - FORT, 3.8 ± 3.1 at S25°W ± 4°, is not consistent with other geologic and geodetic from the region (Chapter 3).

Summary

The geocentric position vectors from a set of 77 experiments beginning in October 1982 have been used to estimate the tangential rate of change of station position of VLBI sites in the western U.S. These data were processed utilizing a procedure developed to remove from apparent tectonic motion the contamination due to errors in Earth-orientation parameters and non-uniform station geometry; this procedure accounts fully for the position covariance between stations. In this method the tangential displacement field is minimized with respect to an *a priori* geophysical model of deformation. This model is parameterized in terms of a tangential velocity of a station in a North-America-fixed-reference frame. The vector velocities estimated for the stations in the western U.S. provide discrete sampling of the temporal and spatial deformation field.

To interpret the VLBI derived rates of deformation an examination of geologic and more densely sampled ground-based geodetic data. For three regions I compared the rates of deformation derived from VLBI and ground-based geodetic data, and I examined the relationship between the rates of deformation determined from geological data and those estimated from the geodetic data.

Deformation across southernmost California is fairly well described by simple right-lateral shear on the San Andreas, San Jacinto, Elsinore, and possibly the offshore faults of the California borderlands. An estimate of the integrated rate of deformation across the southern region of the Basin and Range province is given by the station YUMA (3.4 ± 2.7 mm/yr at N84°W $\pm$ 16°). A large earthquake has not occurred on the southern segment of the San Andreas fault within the last ~400 years [*Sieh*, 1986], and strain accumulation is observed over a broad region. Within the Salton Sea region there are three VLBI sites, BLKB, PINF, and MON, and with denser spatial coverage the Salton Sea trilateration network. MON is collocated with a trilateration station, and the velocity of the trilateration station is set equal to the MON vector velocity. The fault-parallel components of velocity

of PINF and BLKB are in close agreement with the velocity profile given by the trilateration data. If the vector velocity given by the MON - YUMA difference vector (37.6 ± 3.4 mm/yr at N40°W ± 8°) is approximately equal to the accumulated rate of long-term slip across the San Andreas, San Jacinto, and Elsinore faults, additional deformation is predicted to occur offshore in the California borderlands. This rate of deformation is similar to that given by *Weldon and Humphreys* [1986]. The velocity difference vector between VNDN and MON is 5.9 ± 2.9 mm/yr at N23°W ± 4°.

In the 'big-bend' region of the San Andreas fault recent deformation has been measured across the right-lateral strike-slip faults of the central Mojave, along the San Andreas fault, and as northeast-southwest compression across the western Transverse Ranges and the offshore faults in the Channel Islands. The vector velocity of MOJA is 7.1 ± 0.9 mm/yr at N50°W ± 1°. MOJA is located in the northeast corner of the the Mojave Desert block. This result, along with ground-based geodetic and geologic data from the Mojave Desert, the Garlock fault, and the Great Basin suggest that the estimated rate of deformation on the northwest striking faults of the central Mojave (6.7 ± 1.3 mm/yr at N41°W ± 2°, Chapter 2) may be kinematically related to deformation north of the Garlock. The station MOJA as well as the western Garlock fault are then within a deforming region connecting slip in the central Mojave to deformation north of the Garlock. The alternative hypothesis that the MOJA and central Mojave strain results are due to elastic strain accumulation which will be relieved in the next large earthquake on the San Andreas fault is rejected on the basis of several arguments; the most convincing argument is that recent slip has been documented along the faults of the central Mojave [*Dokka* , 1983; E. Hart, personal communication, 1987] .

Two VLBI stations, JPL and PBLO, are located within the Eastern Transverse Ranges trilateration network. After fixing the site velocity of JPL to be the same in both networks the fault-parallel component of PBLO closely resembles the velocity profile given

by the trilateration results. Over the broad region between MOJA and JPL the rate of deformation given by the differenced velocity vector is quite low (26.9 ± 2.6 mm/yr at N43°W ± 5°) and suggests that the long term rate of slip on this segment may be ~25 mm/yr. The velocity difference vector for VNDN - SANP suggest 15.2 ± 6.7 mm/yr of northeast-southwest compression (N15°E ± 7°) between the two sites. The SANP station, which is located in the Ventura Basin, however, has been measured only 4 times.

In central California slip along the San Andreas fault is thought to occur primarily through surface creep. Recent deformation has also been measured on tectonic elements east and west of the San Andreas. These include extension across the Basin and Range, right-lateral strike-slip motion on the Rinconada and San Gregorio faults and northeast-southwest compression within the Coast Ranges. The vector rate of change of the station position for OVRO, 10.3 ± 2.7 mm/yr at N37°W ± 4.5°, is closer to the local orientation of the Owens Valley fault than the assumed direction of extension in the Basin and Range (N60°W). The integrated rate of extensional deformation across the Basin and Range estimated from geological observations and VLBI baseline that cross the region is given by *Minster and Jordan* [1984, 1987] to be 9.7 ± 2.1 mm/yr at N56°W ± 10°. The difference velocity vector between FORT and OVRO, 37.1 ± 2.8 mm/yr at N37°W ± 5°, is similar to the integrated rate of deformation estimated from ground-based geodetic networks (36.5 mm/yr at N34°W) and from geological data (35.2 mm/yr at N34°W). The rate of shortening to the east of the San Andreas [Chapter 3] estimated from ground-based geodetic data may represent a significant component of the fault-normal compression.

TABLE 1. VLBI Station Observation History

Station	No. of Experiments	Period
CDP Base Stations		
FT.D	38	82.79 - 87.82
HATC	30	83.48 - 87.81
MOJA	75	83.48 - 87.82
OVRO	43	82.79 - 87.82
VNDN	63	83.64 - 87.82
Mobile VLBI Sites		
BLKB	10	83.85 - 87.81
DEAD	3	84.16 - 87.24
ELY	4	84.31 - 87.36
FLAG	3	84.29 - 86.23
FORT	7	83.64 - 87.79
JPL	15	82.79 - 87.79
MAMM	2	84.81 - 86.81
MON	21	82.79 - 87.82
OCOT	3	84.17 - 85.17
PBLO	8	83.14 - 87.79
PINF	15	83.84 - 87.23
PLAT	7	84.29 - 86.25
PRES	9	83.65 - 87.81
PT R	6	84.16 - 87.81
PVER	3	83.86 - 87.23
QUIN	6	83.49 - 87.82
SANP	4	83.66 - 87.24
YUMA	16	83.84 - 87.81

The time interval of observations are given in decimal fractions of years.

TABLE 2. VLBI Station Velocities

Station	*A Priori* Velocity, mm/yr	*A Priori* Orientation	*A Posteriori* Velocity, mm/yr	*A Posteriori* Orientation
BLKB	21.0	N39°W	11.1 ± 3.3	N65°W ± 17°
DEAD	7.0	N41°W	14.8 ± 6.7	N72°W ± 7°
ELY	1.0	N58°W	3.9 ± 4.0	S72°W ± 28°
FLAG	0.5	N58°W	6.1 ± 7.2	S51°W ± 46°
FORT	40.0	N41°W	47.4 ± 2.8	N37°W ± 5°
FT.D	0.0		5.7 ± 3.9	N12°W ± 4°
HATC	7.0	N50°W	9.4 ± 2.6	N62°W ± 8°
JPL	35.0	N65°W	34.0 ± 2.6	N44°W ± 6°
MAMM	0.0		11.5 ± 9.4	N65°W ± > 90°
MON	40.0	N45°W	40.1 ± 2.5	N44°W ± 6°
OCOT	28.7	N40°W	18.9 ± 28.5	S64°W ± > 90°
OVRO	9.0	N60°W	10.3 ± 2.7	N37°W ± 4°
PBLO	25.0	N65°W	25.5 ± 2.7	N48°W ± 7°
PINF	30.0	N45°W	25.5 ± 3.7	N49°W ± 13°
PLAT	0.0		3.8 ± 4.5	N77°W ± 37°
PRES	30.0	N41°W	28.7 ± 3.3	N43°W ± 8°
PT R	35.0	N41°W	38.8 ± 3.8	N36°W ± 8°
PVER	35.9	N38°W	42.4 ± 5.4	N39°W ± 17°
QUIN	9.0	N60°W	12.0 ± 3.1	N52°W ± 9°
SANP	35.0	N65°W	39.4 ± 4.5	N60°W ± 31°
VNDN	48.0	N36°W	45.7 ± 2.9	N41°W ± 6°
YUMA	2.0	N60°W	3.4 ± 2.7	N84°W ± 16°
MOJA	7.0	N41°W	7.1 ± 0.9	N50°W ± 1°

TABLE 3. Difference Vectors

Stations	Rate, mm/yr	Orientation
Southern California		
MON - YUMA	37.6 ± 3.4	N40°W ± 8°
MON - BLKB	30.0 ± 4.5	N35°W ± 12°
VNDN - MON	5.9 ± 2.9	N23°W ± 4°
'Big-Bend' Region		
JPL - MOJA	26.9 ± 2.6	N43°W ± 5°
JPL - PBLO	8.7 ± 3.7	N34°W ± 6°
VNDN - SANP	15.2 ± 6.7	N15°E ± 7°
Central California		
FORT - OVRO	37.1 ± 2.8	N37°W ± 5°
VNDN - FORT	3.8 ± 3.1	S25°W ± 4°

TABLE 4. Summary of Deformation Rates along the San Andreas system in southern California

Fault Segment	Orientation	Geological Slip Rate mm/yr	Geodetic Slip Rate, mm/yr
Imperial fault	N38°W	35 ± 5[A]	
San Andreas fault			
Coachella Valley	N45°W	20-40[B]	34.5 ± 1.3[C]
Cajon Pass	N45 - 66°W	21-29[D]	
Mojave	N65°W	25-35[E]	18.3 ± 1.2[F]
Cholame-Carrizo	N40°W	31-37[G]	
San Jacinto fault	N45°W	8-14[H]	34.5 ± 1.3[C]
Elsinore fault	N45°W	1-7[I]	1.4 ± 0.6[J]

All fault orientations are approximate azimuths determined from fault map of *Jennings* [1975]. Lettered notes follow on the next page.

Notes for Table 4

A. Triangulation and trilateration surveys have been performed by the National Geodetic Survey to monitor horizontal crustal movement in the Imperial Valley since 1934. Six surveys were carried out between 1934 and 1980. These geodetic observations include co-seismic deformation from the 1940 El Centro (M_S = 7.1) and 1979 Imperial Valley (M_S = 6.8) earthquakes. The rate of slip determined from the triangulation and trilateration data for the interseismic interval, 1941-1978, was 35 ± 5 mm/yr; however, due to the uncertain effect of the 1940 earthquake a value of 30 ± 5 mm/yr has been estimated for the long term slip rate [*USGS*, 1988]. Slip on the Imperial fault is thought to be transferred to the San Andreas and San Jacinto faults to the north.

B. Excavations at one site along the southern 200 km of the San Andreas fault (B, Figure 30) provide evidence of at least four large slip events and a slip rate of over 30 mm/yr during the time period 1000-1700 [*Sieh*, 1986]. The rate of slip on this segment of the San Andreas fault is poorly constrained by geologic data [*USGS*, 1988]; a slip rate of 30 mm/yr is used as the best estimate.

C. From trilateration measurements made on the USGS Salton Sea Network between 1972 and 1981 the total differential velocity across the network was estimated to be 34.5 ± 1.3 mm/yr [*Prescott et al.*, 1987].

D. From four independent determinations of the slip rate at Cajon Creek (D, Figure 30) on the San Andreas fault spanning different intervals of time from 5900 to 14,400 yr *Weldon and Sieh* [1985] estimated an average slip rate of 24.5 ± 3.5 mm/yr.

E. The estimated slip rate ranges from 16 to 60 mm/yr. *Salyards et al.* [1987] used dated offsets for the last three slip events at Pallet Creek (E, Figure 30) to obtain an averaged slip rate, corrected for non-brittle warping across the fault, of 22 mm/yr over the past ~500 yr. Eight kilometers northwest of Pallet Creek *Schwartz and Weldon* [1987] estimated a

minimum slip rate of 16 to 19 mm/yr and a maximum rate of 38 mm/yr from the offset of a stream channel. From an examination of displacements across a 10-km wide zone along a 26 km-long portion of the San Andreas *Rust* [1986] found that the total fault-zone slip rate was 46-60 mm/yr. The best estimate of the geological slip rate is 30 ± 5 mm/yr [*USGS*, 1988].

F. From trilateration measurements made between 1972 and 1981 the total differential velocity across a profile perpendicular to the San Andreas fault (N58°W) near Palmdale is 18.3 ± 1.2 mm/yr [*Prescott et al.*, 1987].

G. The offset history of Wallace Creek (G, Figure 30) requires that the average rate of slip along the San Andreas fault has been 33.9 ± 2.9 mm/yr for the past 3,700 yr [*Sieh and Jahns*, 1984]. This slip rate is similar to the rate determined for the central creeping portion of the San Andreas fault [Chapter 3, Tables 2, 4, and 5].

H. The estimated slip rate on the Clark fault, a strand of the San Jacinto fault near Anza, is 12-17 mm/yr for the last 30,000 yr [*Merifield et al.*, 1987]. An earlier estimate by *Sharp* [1981] gave a long-term minimum rate of 8 to 12 mm/yr for the past 730,000 yr. Further to the northwest, *Wesnousky et al.* [1987] and *Prentice et al.* [1988] suggest a minimum slip rate of 5.4 ± 1 mm/yr for the past 2000 years. Because of structural complexities of this part of the fault zone and the proximity of the San Andreas fault, it is unclear how slip is partitioned on the different structural elements; additionally the rate of slip could be decreasing toward the northern end of the fault. The best estimate of the geological slip rate is 11 ± 3 mm/yr [*USGS*, 1988].

I. *Rockwell et al.* [1985], Glen Ivy north stand. The rate of slip on the Elsinore fault is poorly constrained by geologic data; a rate of 2 mm/yr is used as a best estimate [*Weldon and Humphreys,* 1986].

J. The USGS Anza Trilateration network, which spans the Elsinore and San Jacinto faults near Palm Springs, has been surveyed seven times between late 1973 and December 1981.

On a subnetwork (~20 km in width) which spans only the Elsinore fault the rate of fault-parallel shear is ~0.07 ± 0.03 μrad/yr [*King and Savage*, 1983, Figure 2]. If we assume that the measured deformation is due to right-lateral slip across the Elsinore, this average shear strain corresponds to net displacement rate of 1.4 ± 0.6 mm/yr.

TABLE 5. Summary of Deformation Rates East of the San Andreas fault

Fault or region	Orientation	Geological Slip Rate mm/yr	Geodetic Slip Rate, mm/yr
Central Mojave (RL)	N41°W	2-13[K]	6.7±1.3[L]
Basin and Range east of Mojave Desert (E)	N60°W	0-3[M]	<1[N] (Rio Grande Rift only)
E. Garlock fault (LL)	E-W	0.7-1.1[O]	7.9 ± 1.1[P]
W. Garlock fault (LL)	N63°W	5->20[Q] 1-3[R] 5-8[S]	
Owens Valley (RL)	N25°W	0.7-2.2[T]	3.2 ± 1.2[U]
Hunter Mountain fault (RL)	N55°W	2.0-3.2[V]	
N. Basin and Range (E)	N60°W	1-12[W]	

RL = right-lateral slip, LL = left-lateral slip, E = extension. Lettered notes follow on the next page.

Notes for Table 5

K. *Dokka* [1983] has estimated that 27-38 km of cumulative slip has occurred across the northwest trending faults from detailed mapping and the location of a distinctive Miocene detachment terrain. *Dokka* [1983] has suggested that strike slip faulting may have started as late as Pliocene or Quaternary. If slip initiated 2 m.y ago the average rate of slip would correspond to 13-19 mm/yr. If slip initiated 20 m.y ago the slip rate could be as low as 1-2 mm/yr. A best estimate of the slip rate of 6.5 mm/yr is determined by assuming slip initiated 5 m.y. ago.

L. From triangulation and trilateration surveys made during 1934-1982 an average shear strain rate of 0.16 ± 0.03 μrad/yr at N41°W ± 5° was determined for the region between the Helendale and Camp Rock faults [Chapter 2, Figure 3, *Sauber et al.*, 1986]. If we assume that this deformation is due to right-lateral motion across the northwest tending local faults the average shear straining corresponds to a relative displacement rate of 6.7 ± 1.3 mm/yr. The Barstow trilateration network has been surveyed four times between 1979 and 1984 [*King*, 1985]. The maximum shear strain rate ($\dot{\gamma}$) was determined to be 0.08 ± 0.05 μrad/yr, with $\dot{\gamma}$ = N21°W ± 17°. This network spans only two of the northwest striking faults of the central Mojave and falls within the transition region between active deformation to the west and low strain rates to the east observed on the central Mojave network [*Sauber et al.*, 1986].

M. Within the Quaternary, little or no deformation is thought to occur between the eastern Mojave Desert block and the Colorado Plateau. This assessment is based on mapping of young fault scarps [*Howard et al.*, 1978], geologic field mapping [I. Lucchitta, personal communication, 1988; J. Knapp, personal communication, 1988] and recent seismicity [*Engdahl and Rinehart*, 1988]. The estimated range in the rate of extension across the southern Basin and Range is 0-3 mm/yr [R. Weldon, personal communication 1987]; the midpoint value of 1.5 mm/yr is used as a best estimate.

N. *Savage et al.* [1980]. The Socorro trilateration network spans the Rio Grande rift at the eastern end of the southern Basin and Range province. The trilateration measurements place an upper bound of about 1 mm/yr on the average east-west spreading across the 60-km-wide rift during the time interval 1972-1979.

O. *Clark et al.* [1984].

P. The Garlock trilateration network has been surveyed nine times between 1972 and 1984 [*King and Lisowski* 1985; N. King and M. Lisowski, unpublished data, 1988]. In addition to spanning the eastern 150 km of the Garlock fault, the network spans the Panamint Valley fault (right-lateral slip at N55°W) and the Owl Lake fault (left-lateral slip at N57°E). The maximum shear strain rate ($\dot{\gamma}$) is 0.18 ± 0.01 μrad/yr, oriented N59°E ± 2° if left-lateral or N31°W ± 2° if right-lateral. The rate of slip was estimated from dislocation modeling; the locking depth was taken from the depths of earthquakes, with 7.5 km being the typical depth and 15 km the lower limit. The slip rate on the eastern east-west trending fault segment was found to be insignificant at any depth. The slip rate on the central portion of the western fault striking N63°E scales with depth. The best fitting slip rate for a locking depth of 7.5 km was estimated to be 7.3 ± 1.1 mm/yr.

Q. *Clark et al.* [1984]. Slip estimate from Goler Gulch.

R. *Clark et al.* [1984]. Slip estimate from Oak Creek.

S. *Clark et al.* [1984]. Slip estimate from Koehn Lake.

T. The azimuth of major segments of the fault zone vary from 325° to 355° [*Beanland and Clark,* 1987]. The slip rate of 0.7-2.2 mm/yr on the Owens Valley fault was estimated from combining the average horizontal slip rates on the Owens Valley fault and the Lone Pine fault, a secondary fault [*Zoback and Beanland,* 1986; *Beanland and Clark,* 1987]. Holocene offset on the Owens Valley fault is primarily right-lateral strike-slip slip, with an estimated ratio of lateral to vertical offset for the 1872 (M_0 ~7.6) event averaging 6:1 and

possibly as great as 10:1. Late Pleistocene slip on the subparallel Sierra frontal fault, located 5 to 20 km west of the Owens Valley fault, is primarily vertical.

U. Trilateration surveys in 1974 and 1979 of a network spanning Owens Valley indicate that right-lateral tensor shear ($\dot{\varepsilon}$) is accumulating on the Owens Valley fault at a rate of about 0.08 ± 0.03 μstrain/yr at N20°W [*Savage and Lisowski,* 1980]. Neither the measured extension (0.01 ± 0.03 μstrain/yr) perpendicular to the Owens Valley fault nor the contraction (0.01 ± 0.03 μstrain/yr) parallel to it is significant. The rate of shear strain estimated from two triangulation surveys in 1934 and 1956 plus the 1974 trilateration is consistent with the 1974-1979 rate. If we assume that the measured deformation is due to right-lateral motion across the Owens Valley fault and that $\dot{\varepsilon}$ represents an average strain across a 20-km-wide zone, the average shear rate corresponds to a net displacement rate of 3.2 ± 1.2 mm/yr.

V. The formation of the northern Panamint Valley and Saline Valley has been attributed to the development of a late Pliocene to recent extensional system that consists of paired pull-apart basins connected by the Hunter Mountain transfer fault [*Burchfiel et al.*, 1987; *Sternlof*, 1988]. Assuming 3.0 Ma for the age of inception of the Hunter Mountain fault zone, a minimum average slip rate on the fault is 2-3.2 mm/yr. Palinspastic reconstructions of the Saline Range faults yield 4.5 ± 0.6 km of extension since 1.4 Ma, giving an average displacement rate of 2.8 to 3.6 mm/yr.

W. The orientation of Basin and Range extension of N60°W is the median azimuthal value from the *Zoback and Zoback* [1980] data set, and the ± 20° range corresponds to the standard deviation of a single observation [*Minster and Jordan*, 1984, 1987]. The rate of extension within the Basin and Range of 1-12 mm/yr was estimated by *Minster and Jordan* [1984] from geologic strain, heat flow, paleoseismicity and recent seismicity. *Eddington et al.* [1987] estimated a rate of 8-10 mm/yr from a detailed analysis of historical earthquakes. A value of 9 mm/yr is used for a best estimate of the geologic slip rate.

Figure Captions

Figure 1. Location of the VLBI sites, given by solid circles, utilized in this study. An orthometric projection of the western United States and Mexico about the pole 30°N, 130°W is given. The nominal Pacific-North American plate boundary is indicated in central California by the San Andreas fault (SA). The eastern extent of the Basin and Range province is delineated by the Wasatch front (WF). G of C = Gulf of California.

Figure 2. VLBI sites (triangles) in California, Nevada, and western Arizona in mercator projection. Quaternary faults traces are simplified from *Jennings* [1975]: E=Elsinore fault, IF = Imperial fault, G = Garlock fault, OV = Owens Valley fault, R = Rinconada fault, SA = San Andreas fault, SF = Sierra Frontal fault, SJ = San Jacinito fault.

Figure 3. The vector rate of change of station positions relative to fixed North America given on an oblique mercator projection of the western United States about the NUVEL-1 Pacific - North American pole of rotation [*DeMets et al.*, 1987]. The stations velocities are given for sites in California with at least four observations spanning at least 2 years. The 95% confidence error ellipses reflect the marginal uncertainty associated with the individual station velocities. In this projection, station velocities parallel to the bottom of the page are at the orientation predicted by NUVEL-1; the PCFC-NOAM relative motion vector is given at the bottom center for reference.

Figure 4. Vector rate of change of position of station FT.D.

Figure 5. Vector rate of change of position of station PLAT.

Figure 6. Vector rate of change of position of station ELY.

Figure 7. Vector rate of change of position of station YUMA.

Figure 8. Vector rate of change of position of station BLKB.

Figure 9. Vector rate of change of position of station PINF.

Figure 10. Vector rate of change of position of station MON. The Pacific-North American plate motion vector predicted by NUVEL-1 is given by the dashed line.

Figure 11. Vector rate of change of position of station MOJA.

Figure 12. Vector rate of change of position of station PBLO.

Figure 13. Vector rate of change of position of station JPL.

Figure 14. Vector rate of change of position of station SANP. The Pacific-North American plate motion vector predicted by NUVEL-1 is given by the dashed line.

Figure 15. Vector rate of change of position of station VNDN. The Pacific-North American plate motion vector predicted by NUVEL-1 is given by the dashed line.

Figure 16. Vector rate of change of position of station OVRO.

Figure 17. Vector rate of change of position of station FORT. The Pacific-North American plate motion vector predicted by NUVEL-1 is given by the dashed line.

Figure 18. Vector rate of change of position of station QUIN.

Figure 19. Vector rate of change of position of station HATC.

Figure 20. Vector rate of change of position of station PRES.

Figure 21. Vector rate of change of position of station PT.R. The Pacific-North American plate motion vector predicted by NUVEL-1 is given by the dashed line.

Figure 22. The velocity of MON relative to YUMA.

Figure 23. The velocity of MON relative to BLKB.

Figure 24. The velocity of VNDN relative to MON.

Figure 25. The velocity of JPL relative to MOJA.

Figure 26. The velocity of JPL relative to PBLO.

Figure 27. The velocity of VNDN relative to SANP.

Figure 28. The velocity of FORT relative to OVRO.

Figure 29. The velocity of VNDN relative to FORT.

Figure 30. Reference figure for the studies cited in Tables 4 and 5. At sites B, D, E, and G geologically estimated rates of fault slip were estimated geologically for the San Andreas fault; at sites O, Q, S and R for the Garlock fault; and at V for the Hunter Mountain fault. USGS ground-based geodetic networks include SSN = Salton Sea Network, ETR = Eastern Transverse Ranges Network, CMN = Central Mojave Network, BN = Barstow Network, OVN = Owens Valley Network. Also shown are the locations of the cities Anza and Palmdale (PL).

Figure 31. Reference figure for three path integrals. See Figure 30 for symbols and Figure 2 for fault names.

Figure 32. Fault-parallel component of velocity relative to North America (NOAM) along path 1 in southern California. The * indicates the best estimate of the geologically determined slip rate; the error bar indicates lower and upper bounds on these geological estimates. Solid circles indicate USGS trilateration data. Vertical error bars indicate the standard deviation relative to the network centroid (J. Savage and M. Lisowski, personal communication, 1988). Open triangles denote VLBI data with associated standard deviations shown by error bars.

Figure 33. Fault-normal component of velocity relative to North America along path 1 in southern California. Symbols are as in Figure 32.

Figure 34. Fault-parallel component of velocity relative to North America along path 2 in the 'big bend' region. The horizontal error bars indicate the region over which the measurement was made. Other symbols as given in Figure 32.

Figure 35. Fault-normal component of velocity relative to North America along path 2 in the 'big bend' region. Symbols as in Figures 32 and 34.

Figure 36. Fault-parallel component of velocity relative to North America along path 3 in central California. Symbols as in Figures 32 and Figure 34.

Figure 37. Fault-normal component of velocity relative to North America along path 3 in central California. Symbols as given in Figures 32 and Figure 34.

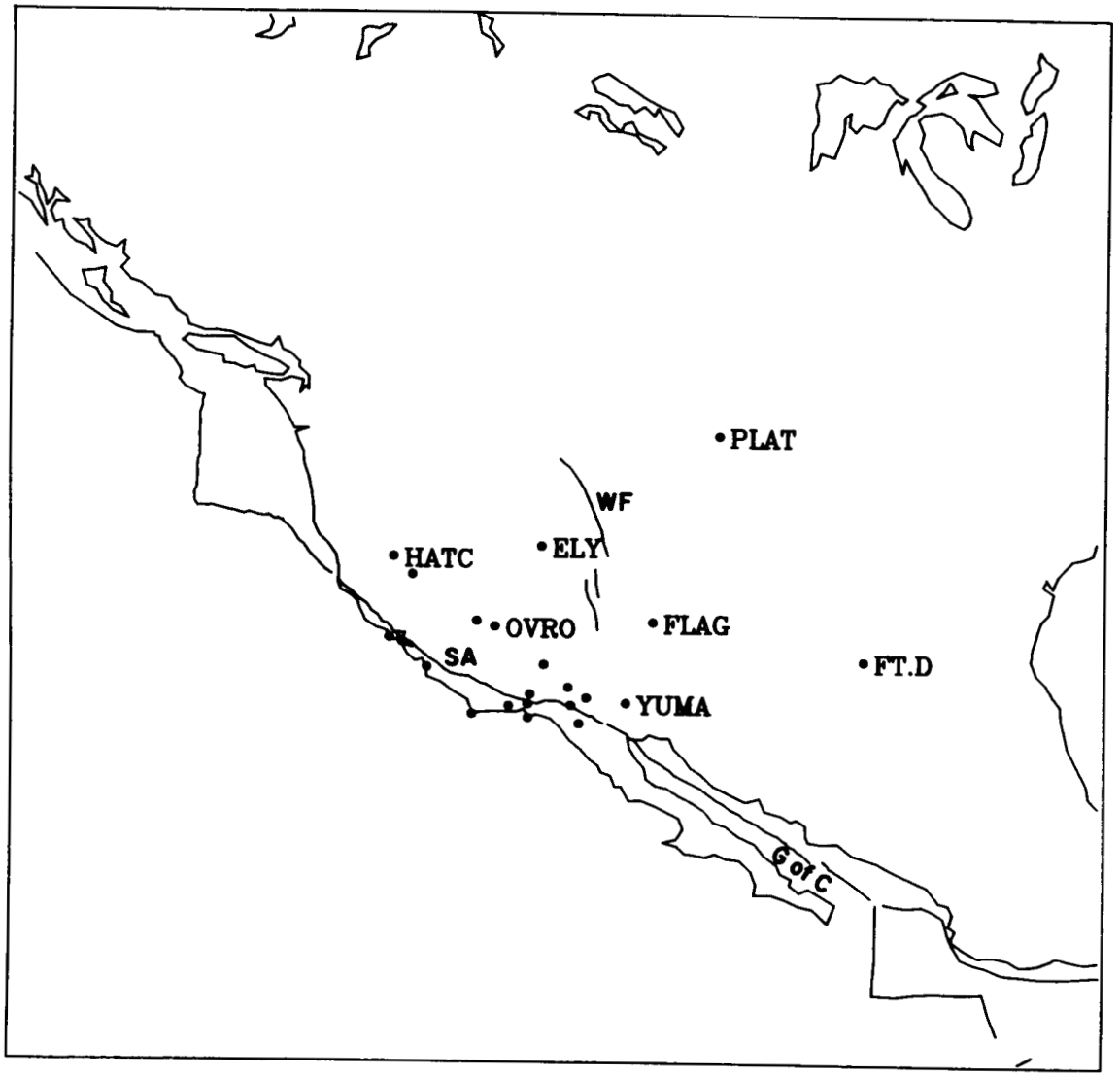

Figure 1. Location of the VLBI sites, given by solid circles, utilized in this study. An orthometric projection of the western United States and Mexico about the pole 30°N, 130°W is given. The nominal Pacific-North American plate boundary is indicated in central California by the San Andreas fault (SA). The eastern extent of the Basin and Range province is delineated by the Wasatch front (WF). G of C = Gulf of California.

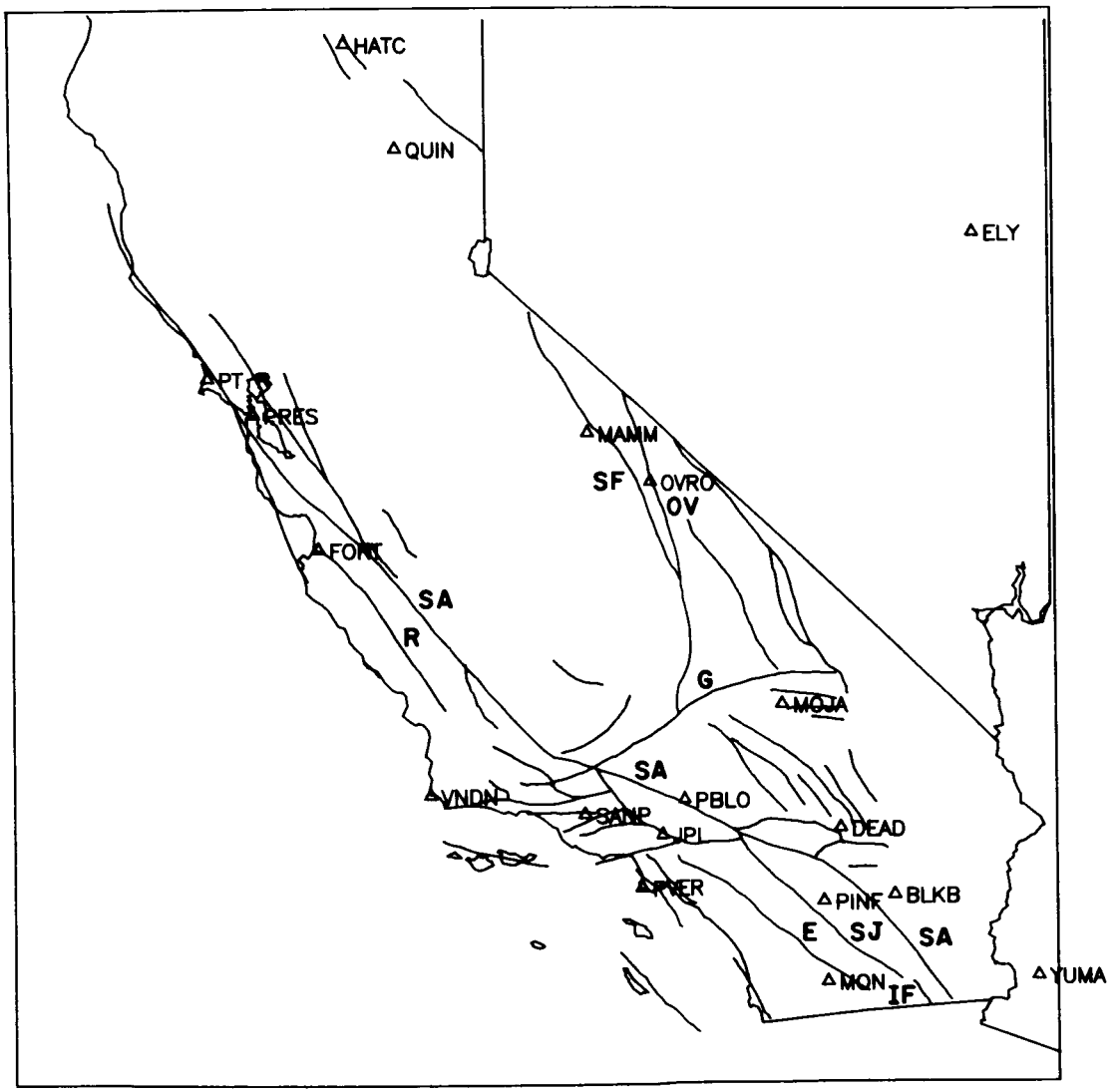

Figure 2. VLBI sites (triangles) in California, Nevada, and western Arizona in mercator projection. Quaternary faults traces are simplified from *Jennings* [1975]: E=Elsinore fault, IF = Imperial fault, G = Garlock fault, OV = Owens Valley fault, R = Rinconada fault, SA = San Andreas fault, SF = Sierra Frontal fault, SJ = San Jacinito fault.

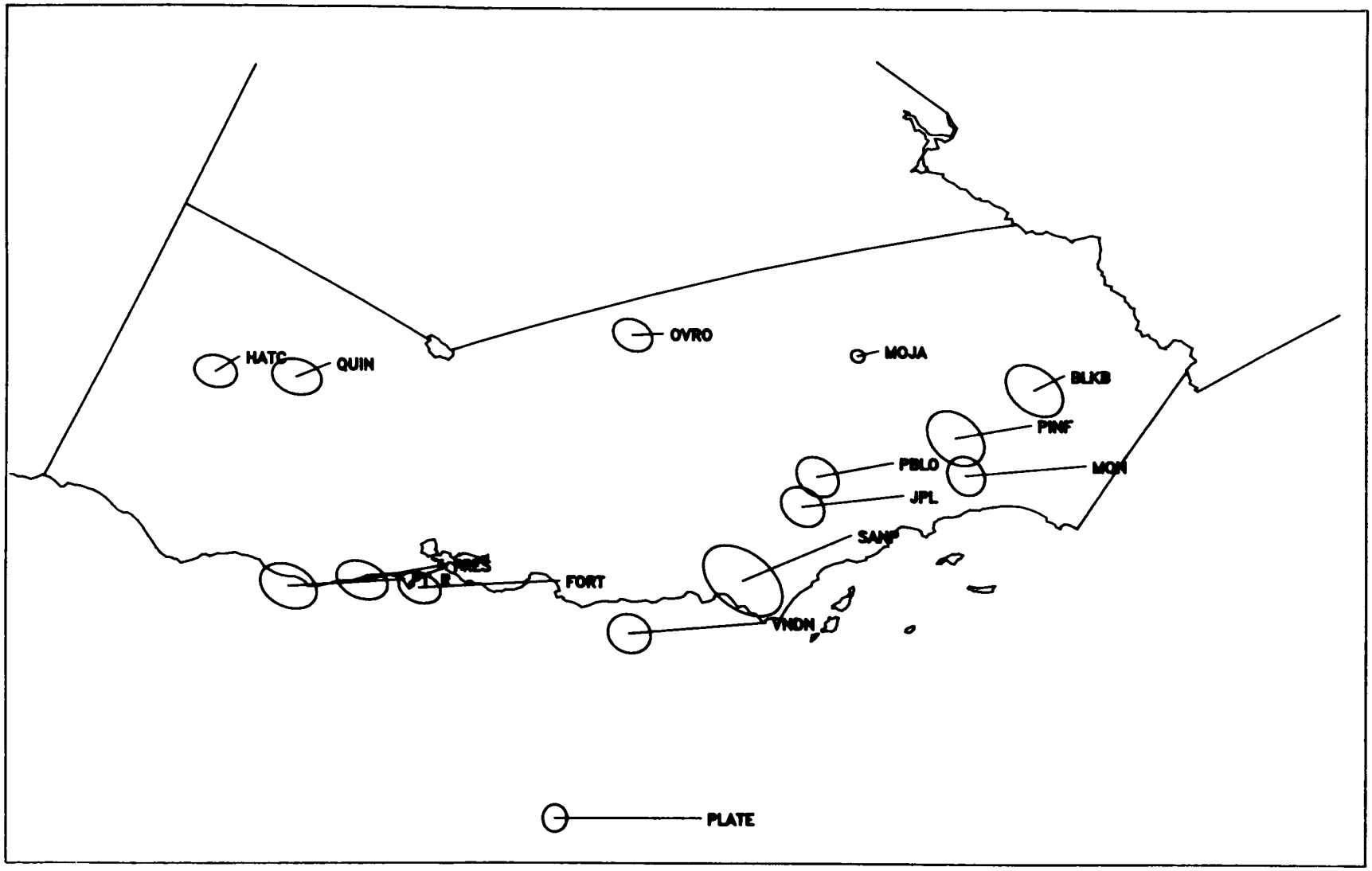

Figure 3. The vector rate of change of station positions relative to fixed North America given on an oblique mercator projection of the western United States about the NUVEL-1 Pacific - North American pole of rotation [*DeMets et al.*, 1987]. The stations velocities are given for sites in California with at least four observations spanning at least 2 years. The 95% confidence error ellipses reflect the marginal uncertainty associated with the individual station velocities. In this projection, station velocities parallel to the bottom of the page are at the orientation predicted by NUVEL-1; the PCFC-NOAM relative motion vector is given at the bottom center for reference.

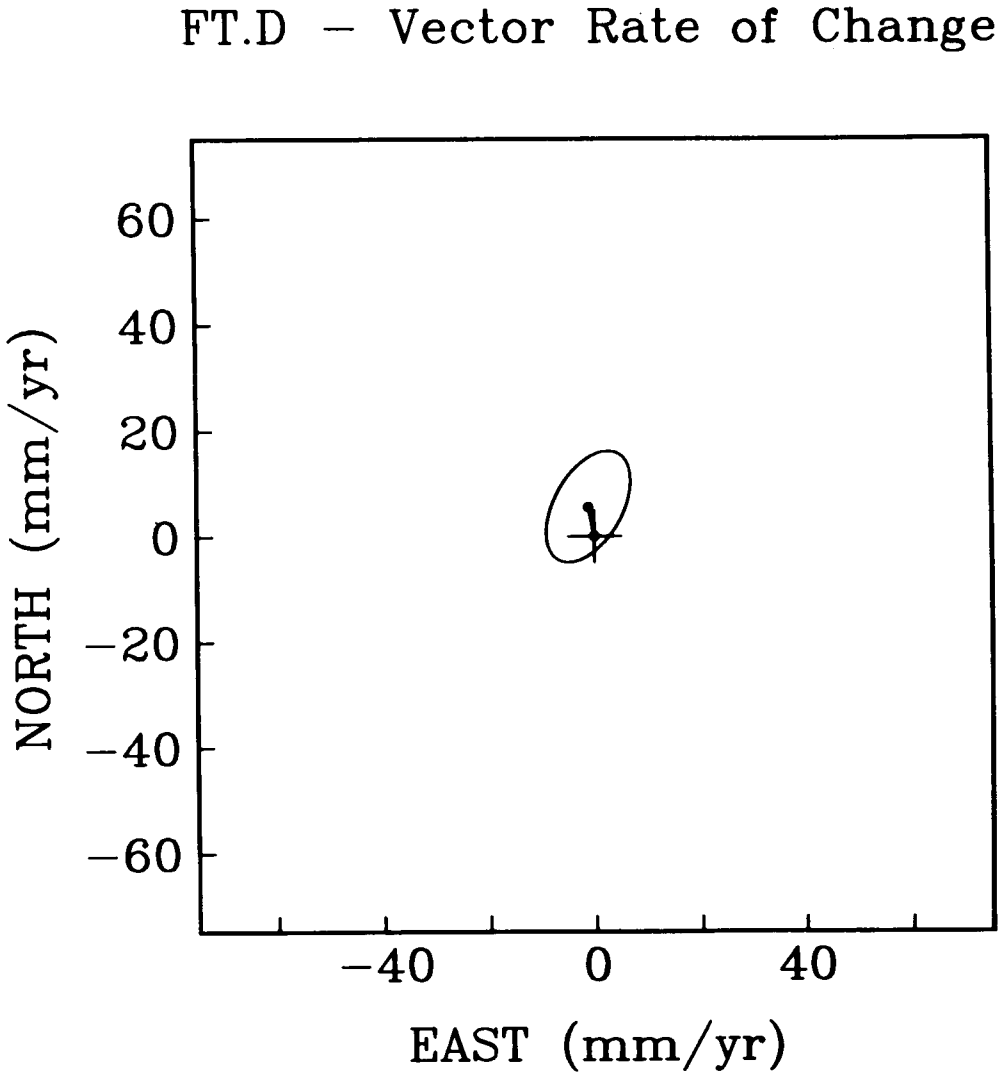

Figure 4. Vector rate of change of position of station FT.D.

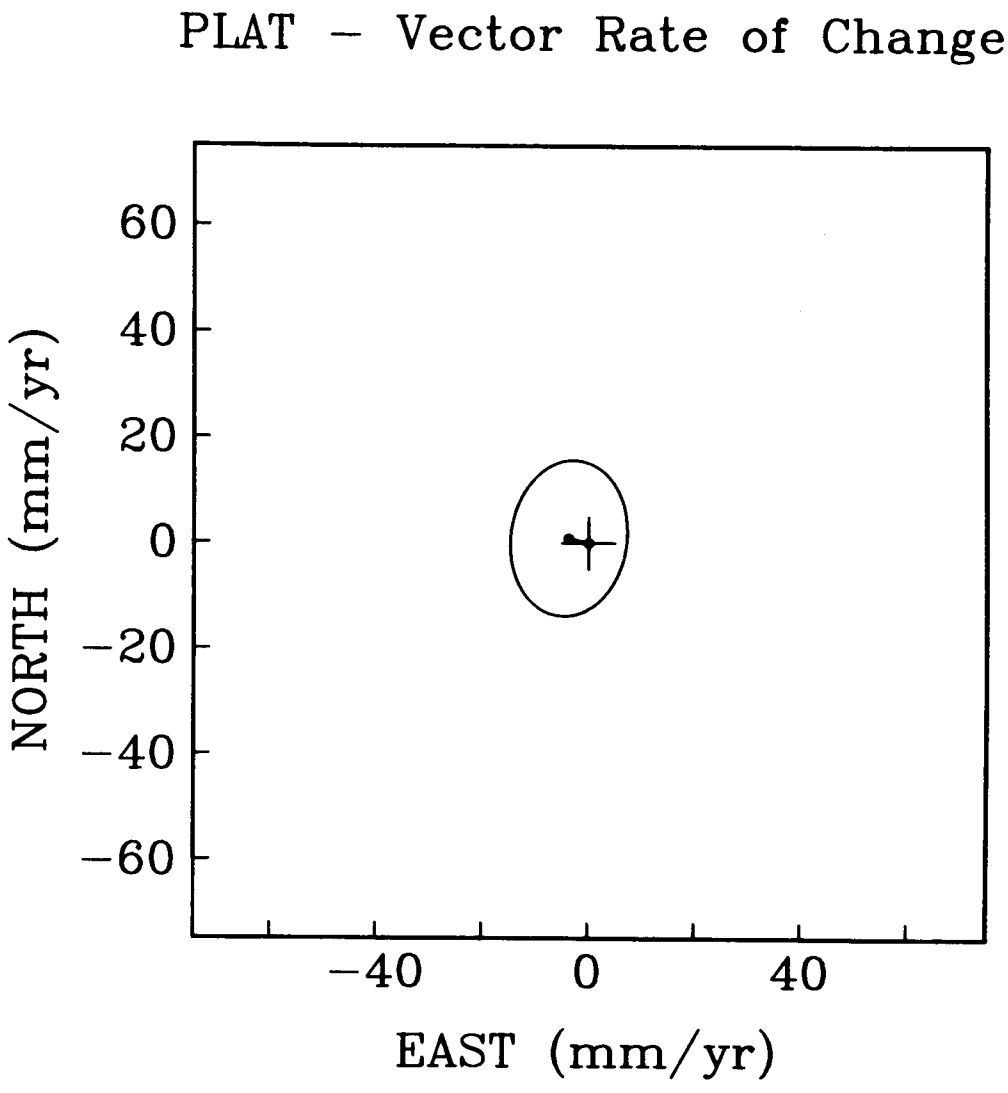

Figure 5. Vector rate of change of position of station PLAT.

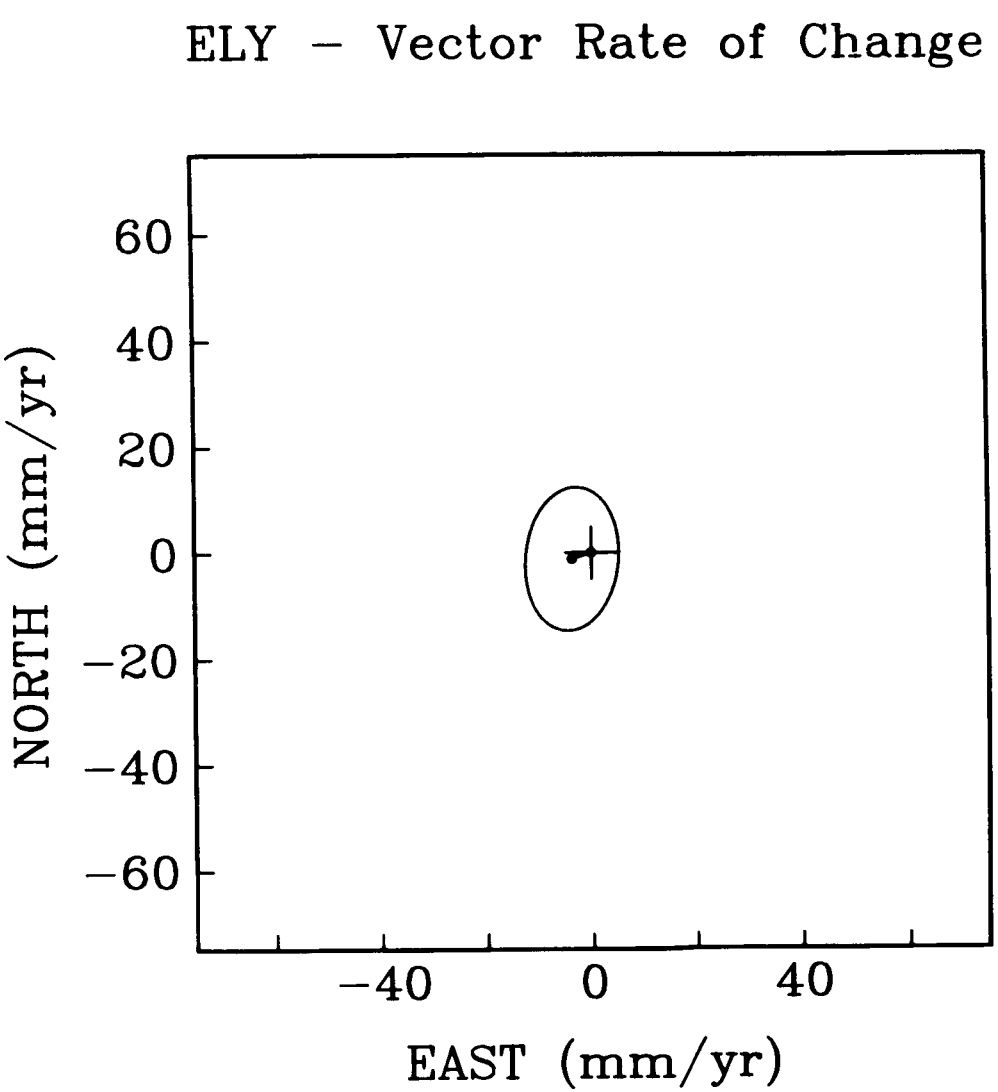

Figure 6. Vector rate of change of position of station ELY.

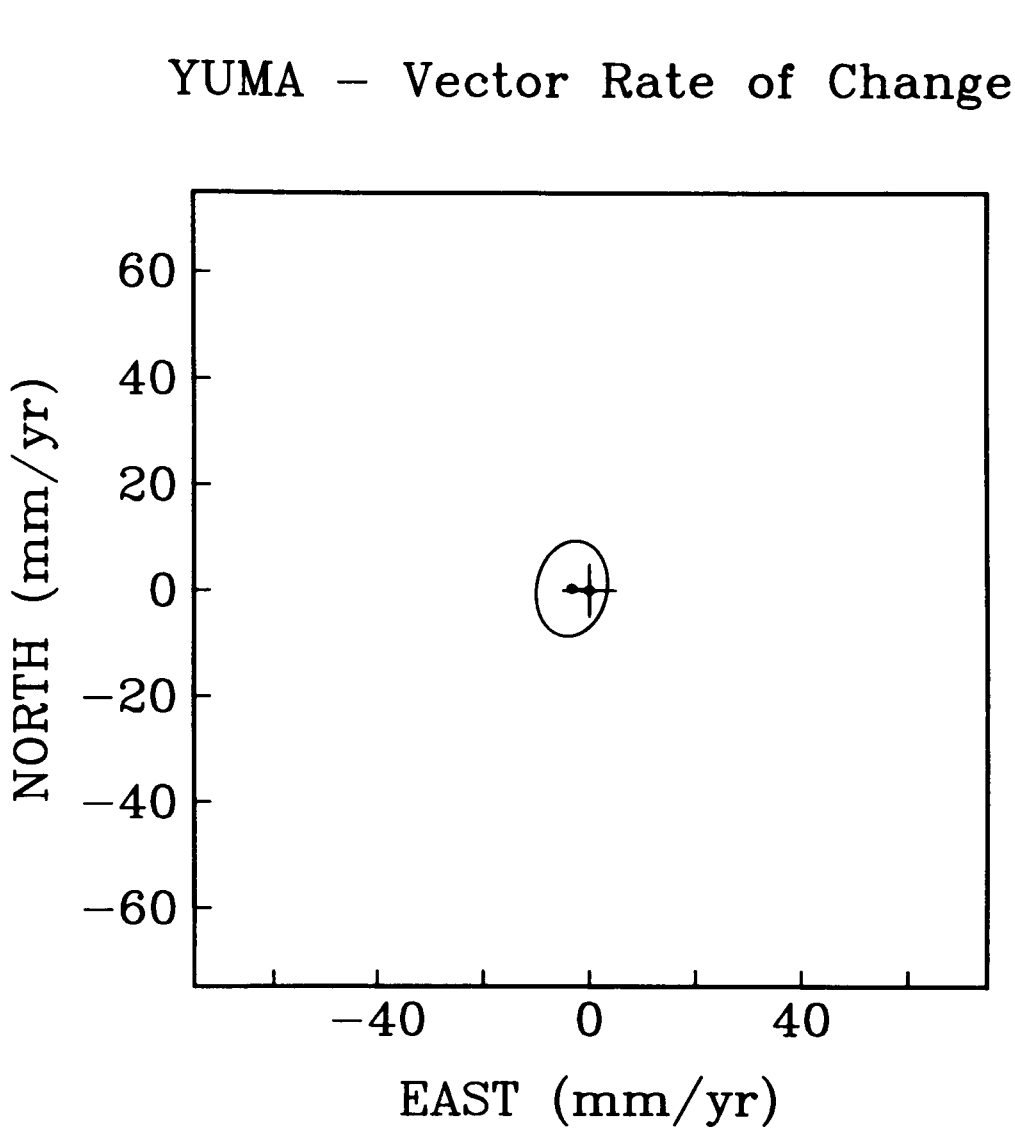

Figure 7. Vector rate of change of position of station YUMA.

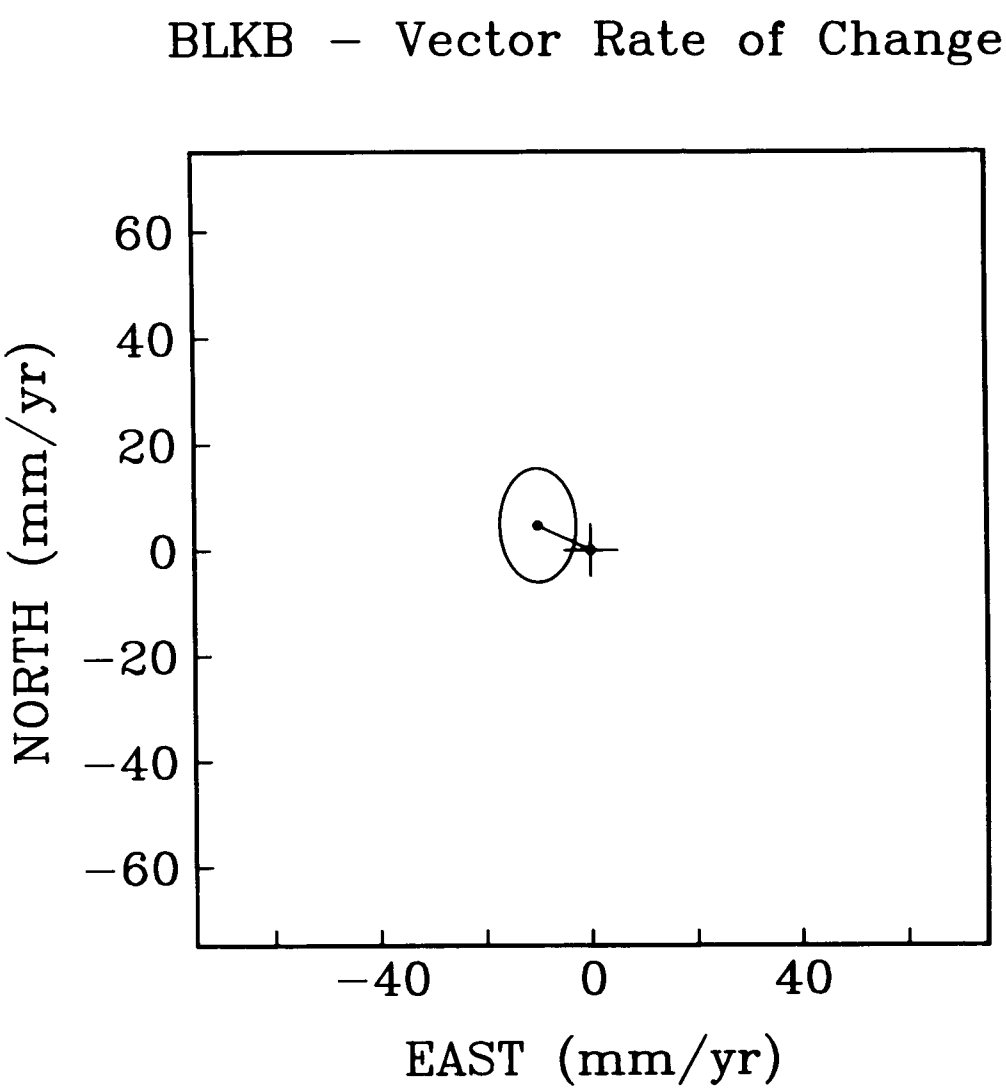

Figure 8. Vector rate of change of position of station BLKB.

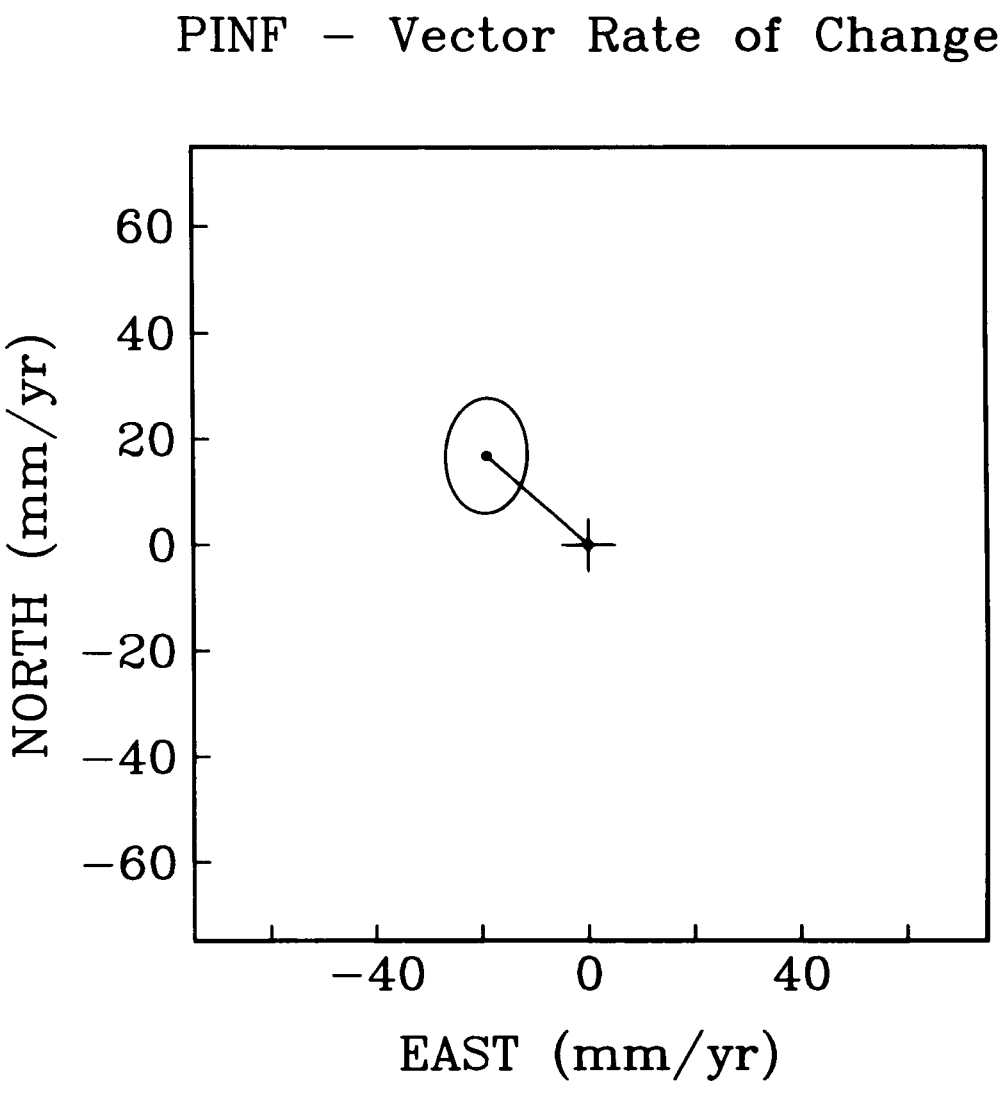

Figure 9. Vector rate of change of position of station PINF.

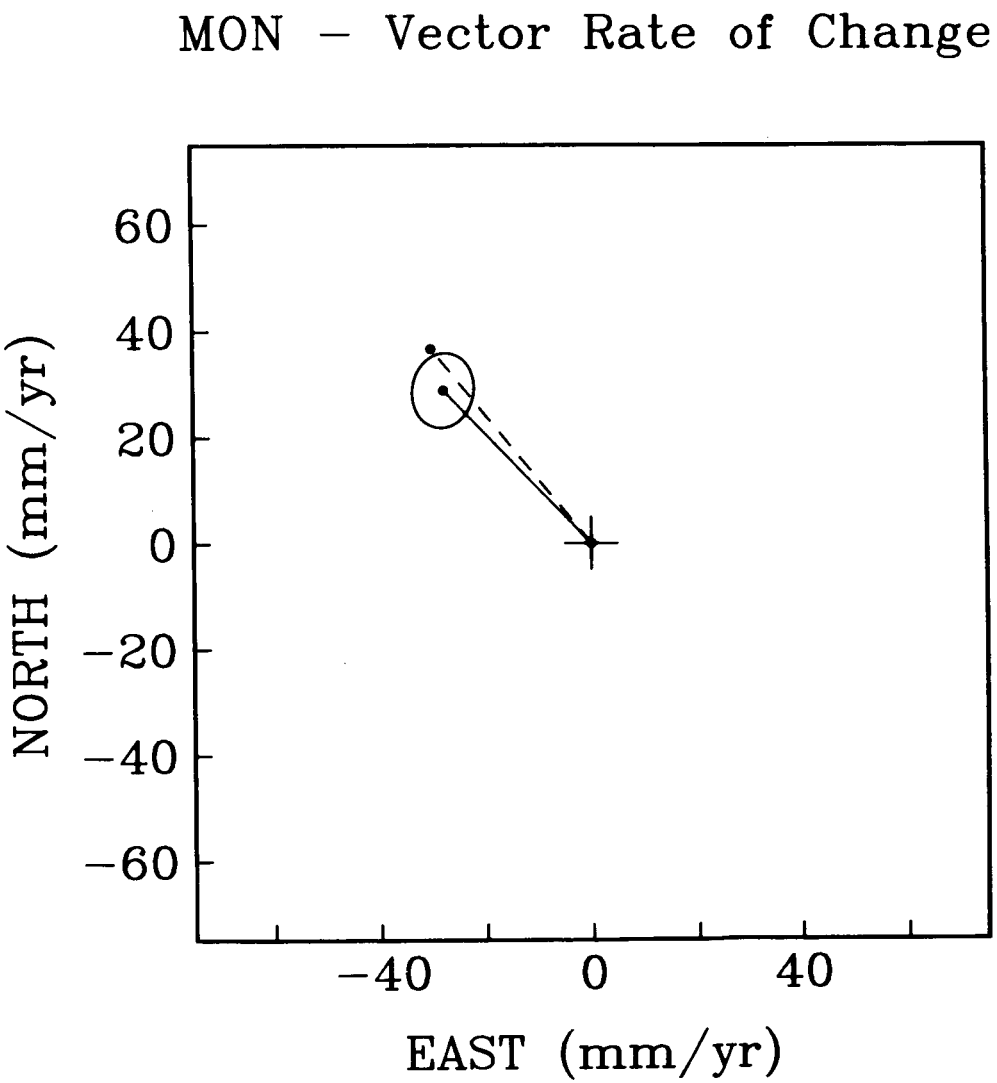

Figure 10. Vector rate of change of position of station MON. The Pacific-North American plate motion vector predicted by NUVEL-1 is given by the dashed line.

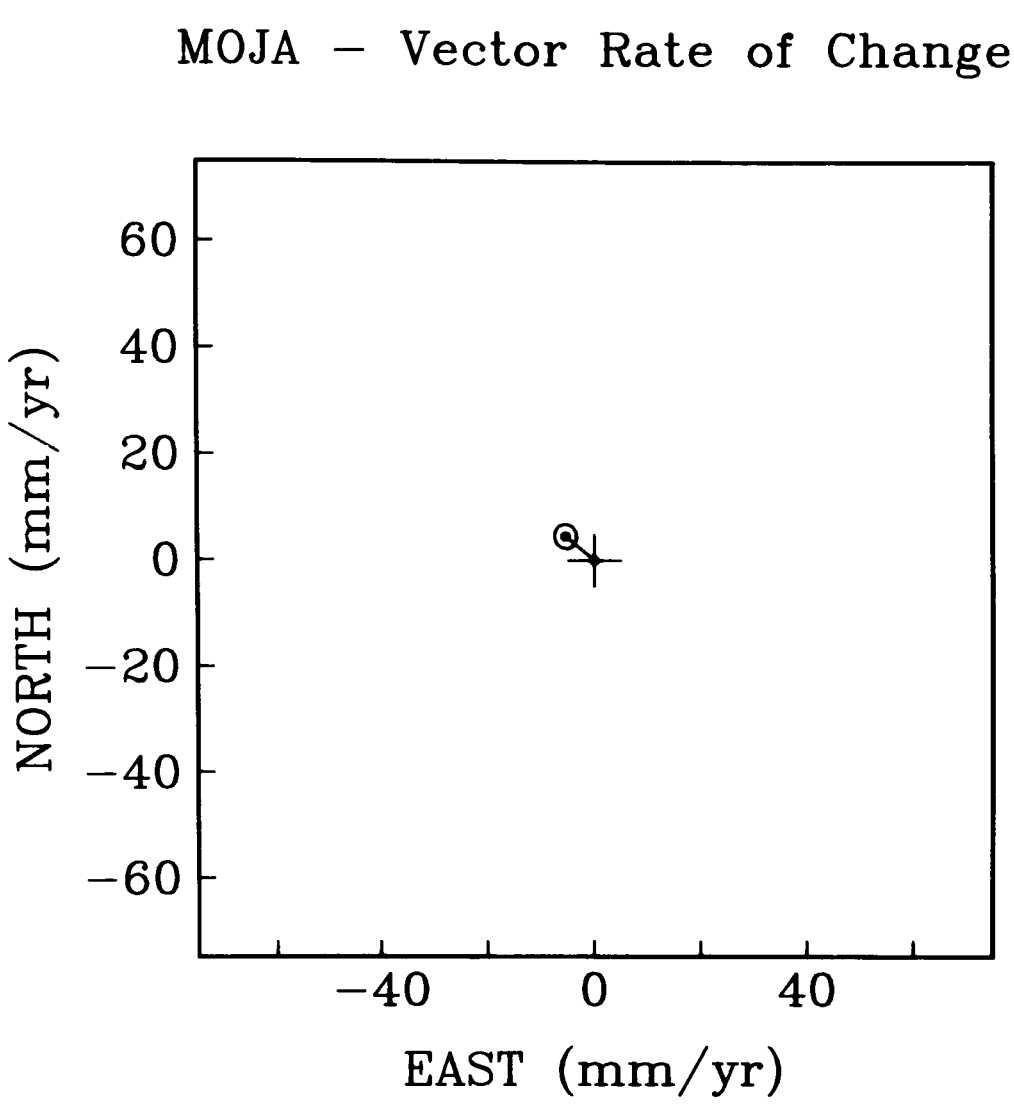

Figure 11. Vector rate of change of position of station MOJA.

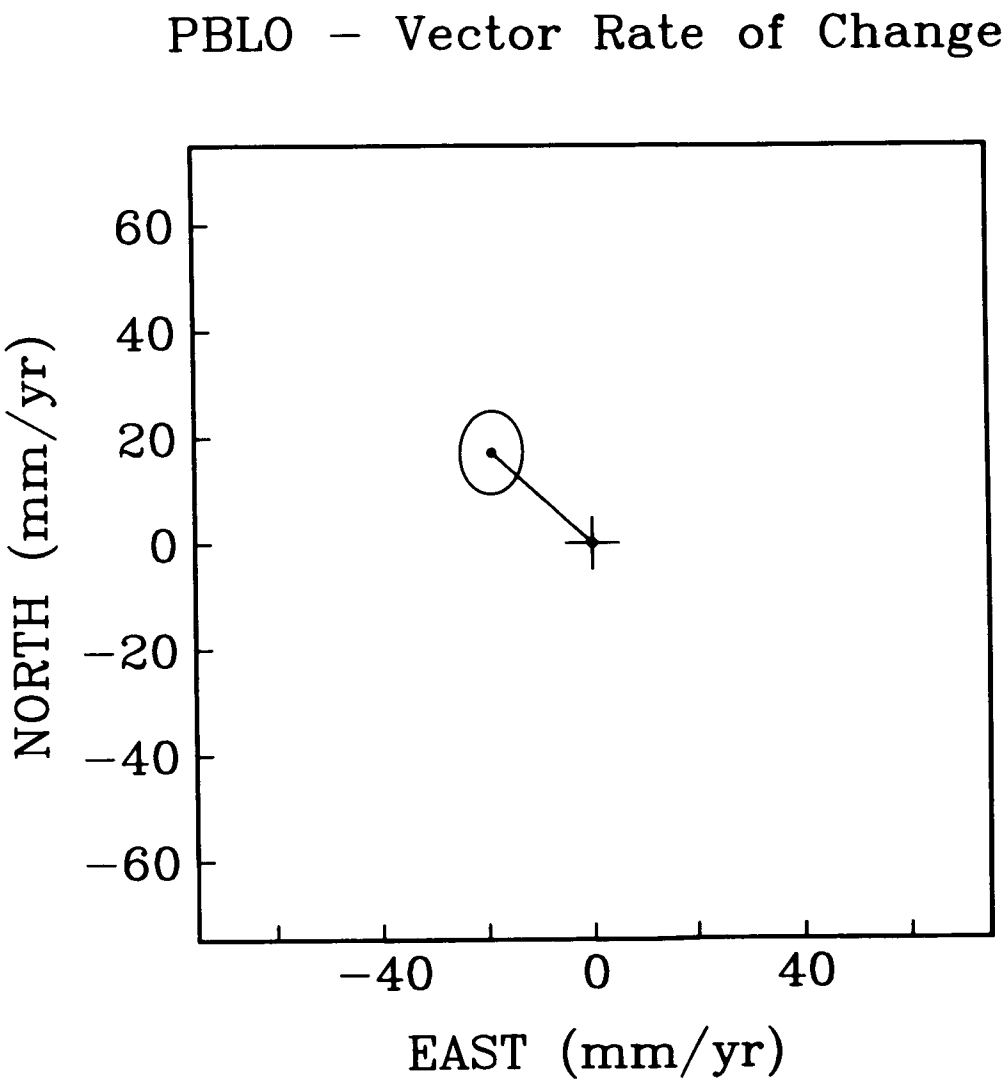

Figure 12. Vector rate of change of position of station PBLO.

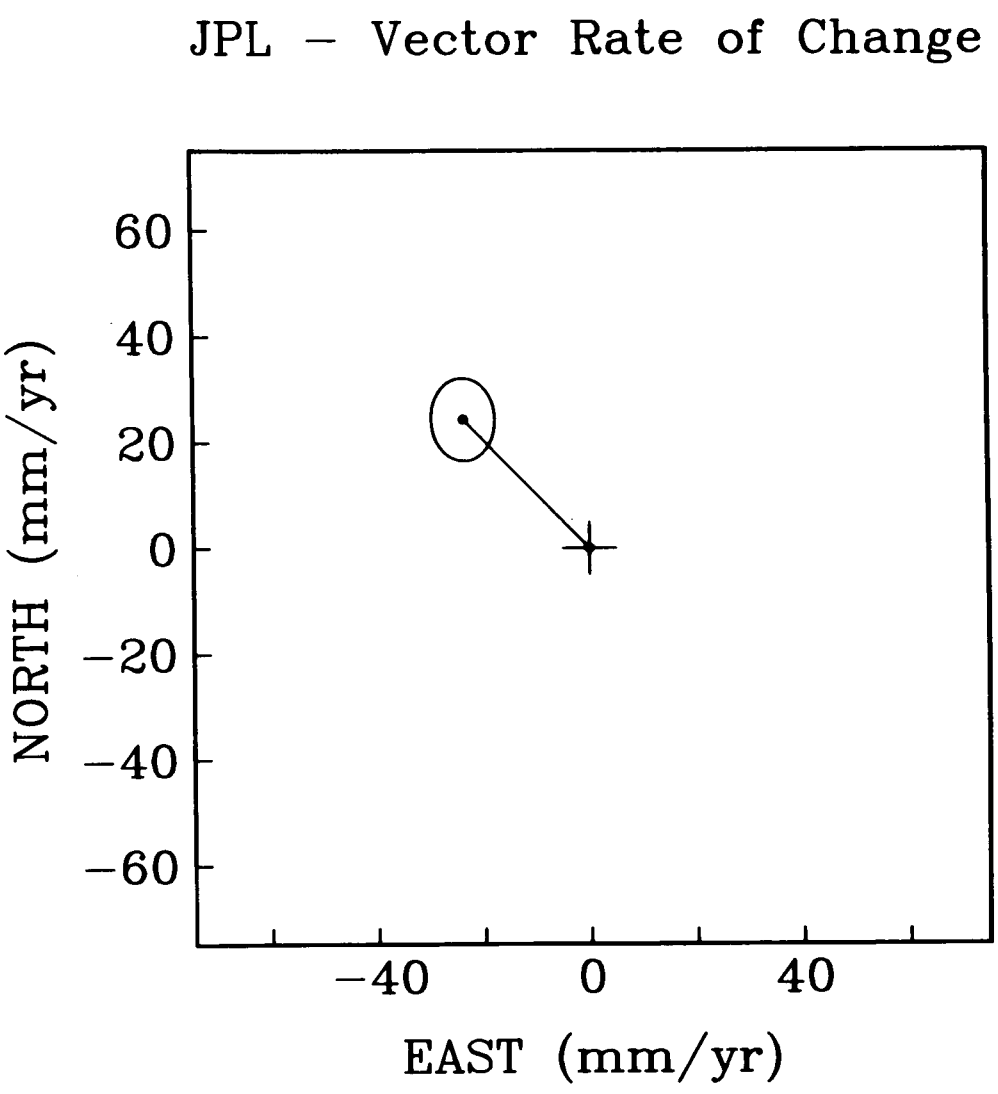

Figure 13. Vector rate of change of position of station JPL.

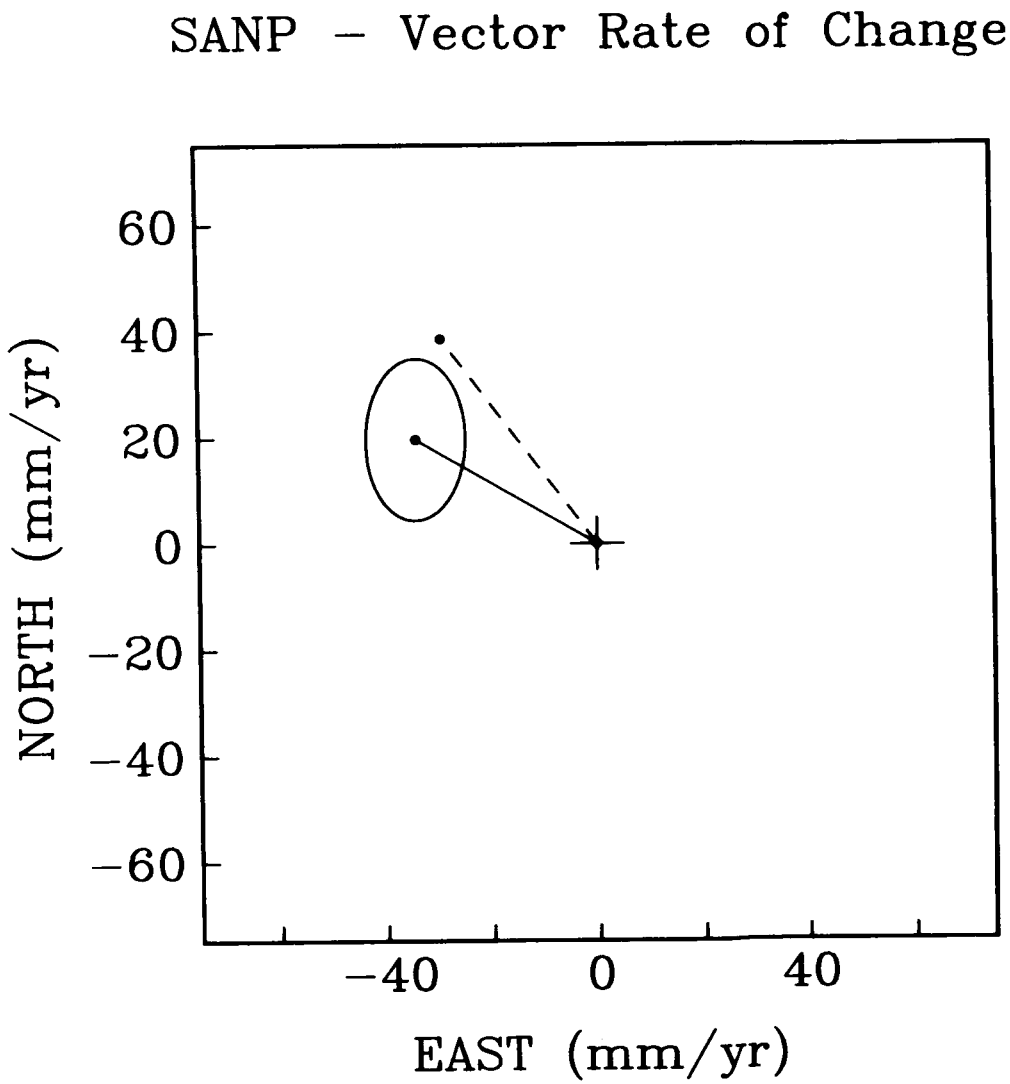

Figure 14. Vector rate of change of position of station SANP. The Pacific-North American plate motion vector predicted by NUVEL-1 is given by the dashed line.

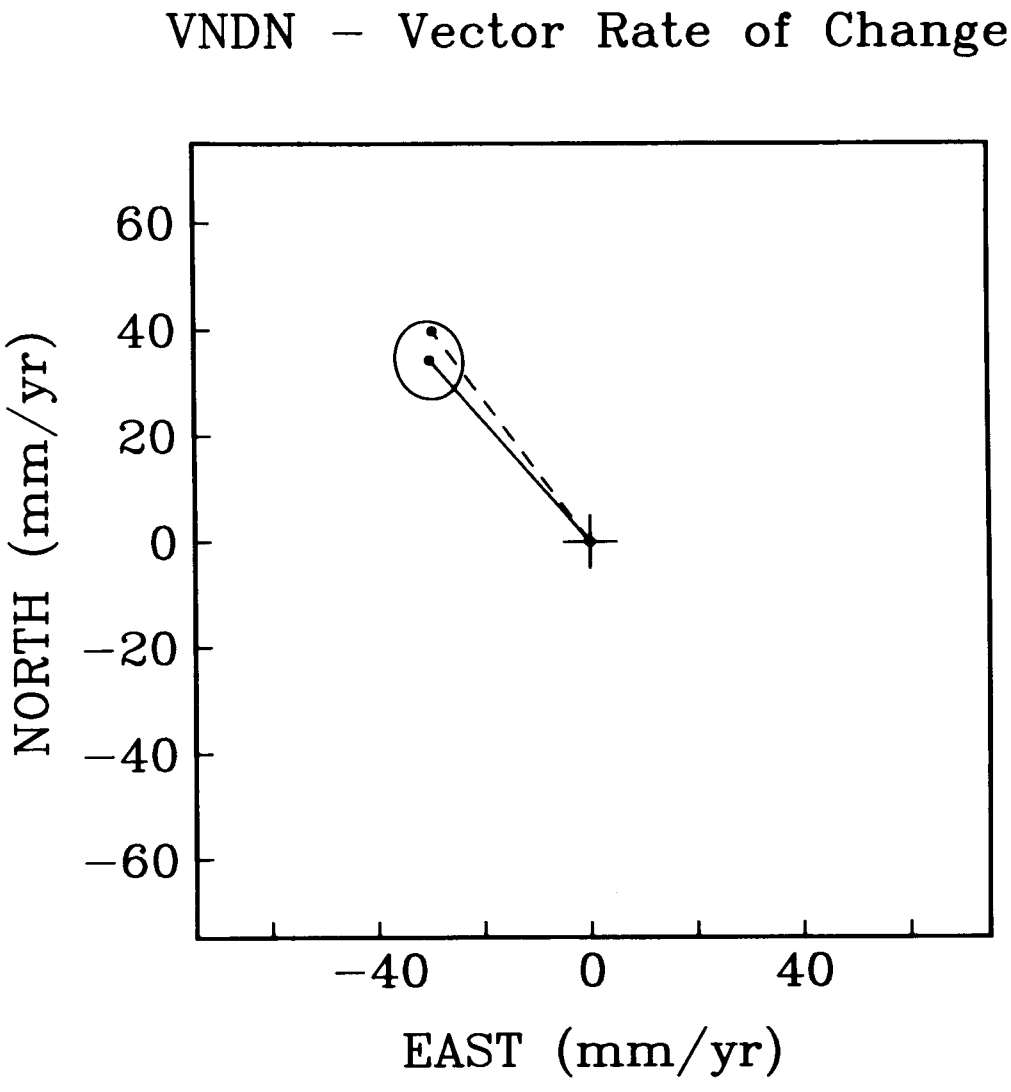

Figure 15. Vector rate of change of position of station VNDN. The Pacific-North American plate motion vector predicted by NUVEL-1 is given by the dashed line.

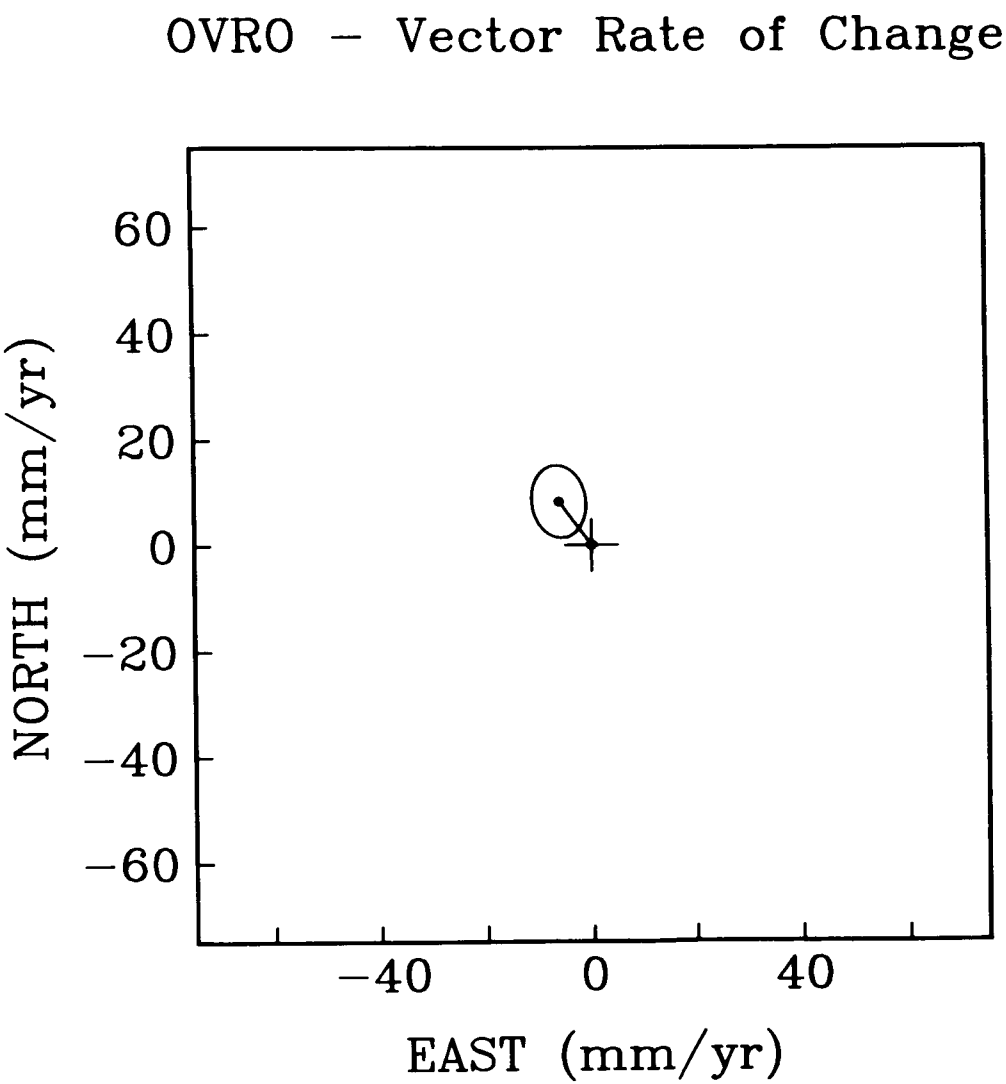

Figure 16. Vector rate of change of position of station OVRO.

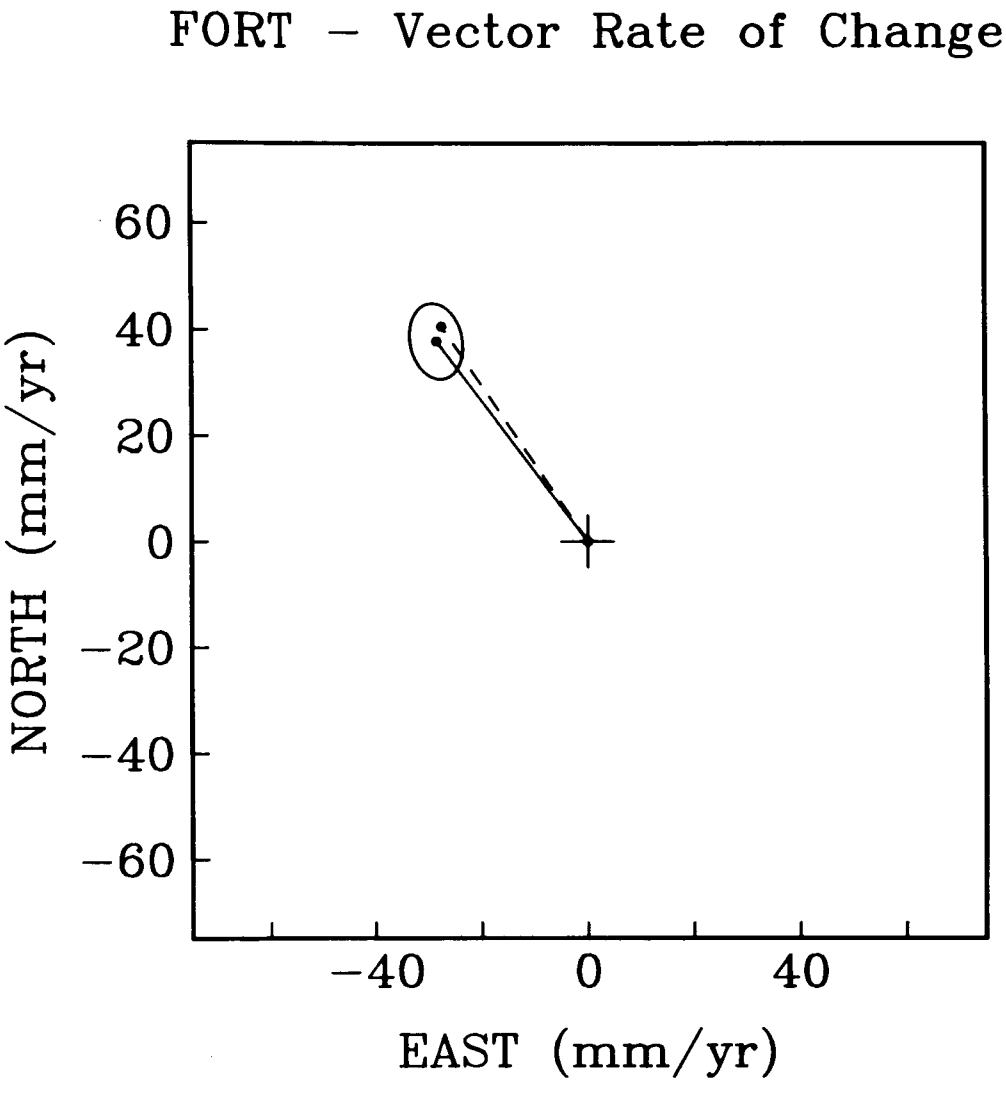

Figure 17. Vector rate of change of position of station FORT. The Pacific-North American plate motion vector predicted by NUVEL-1 is given by the dashed line.

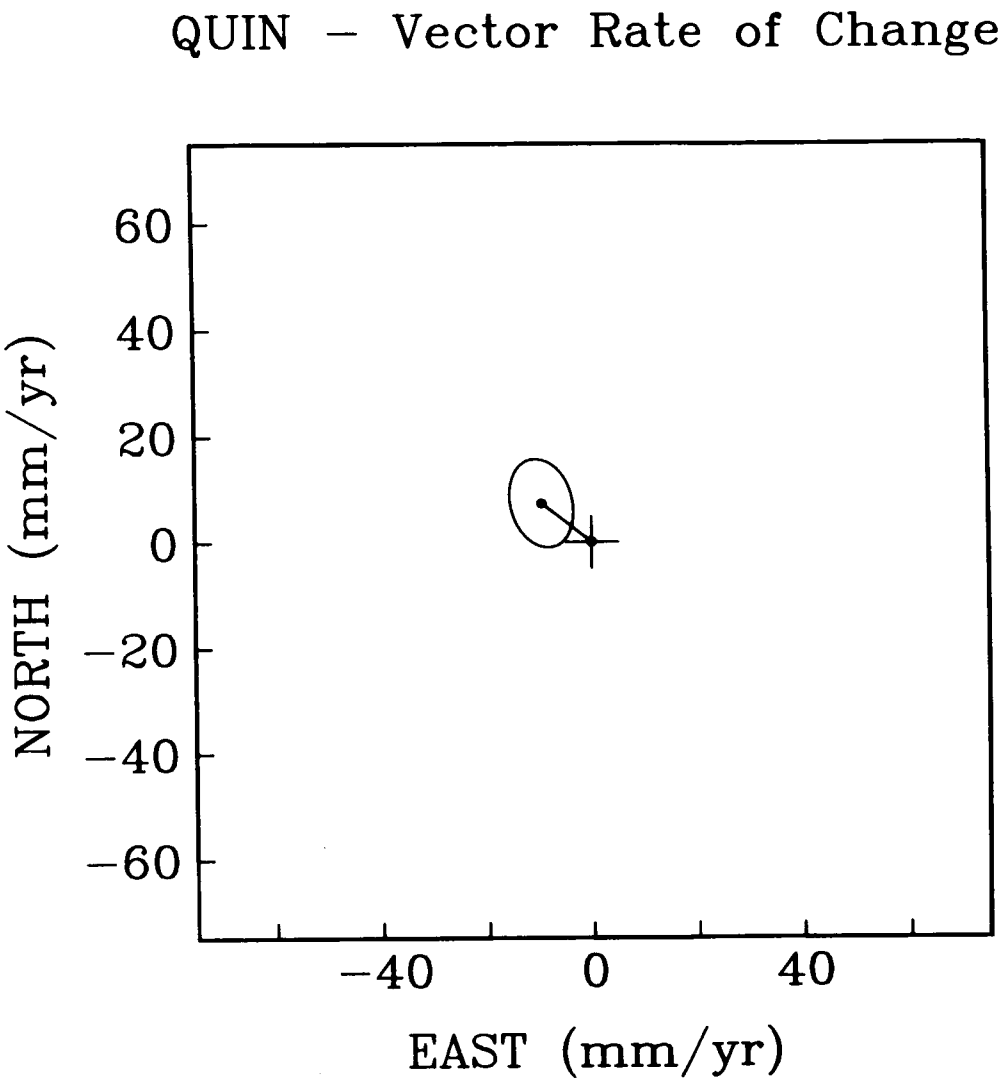

Figure 18. Vector rate of change of position of station QUIN.

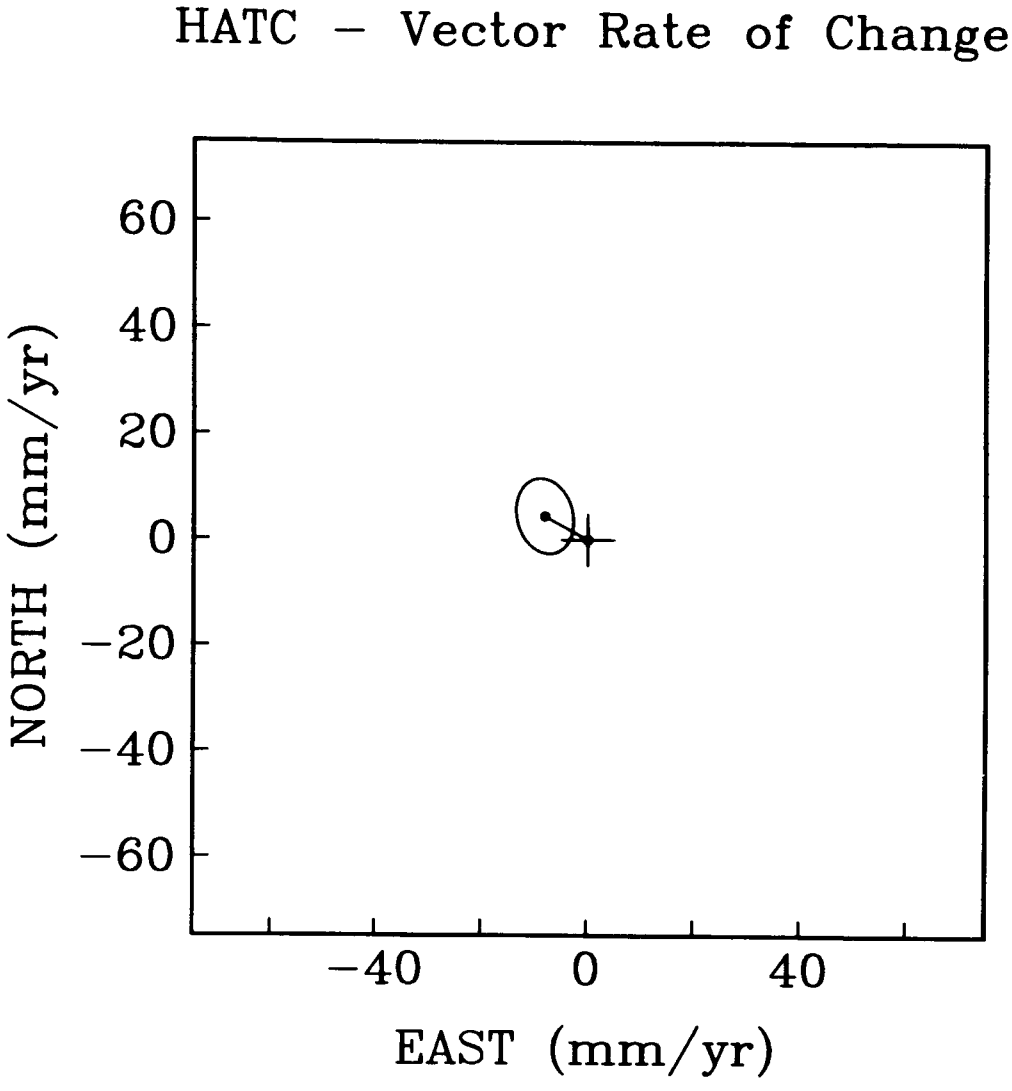

Figure 19. Vector rate of change of position of station HATC.

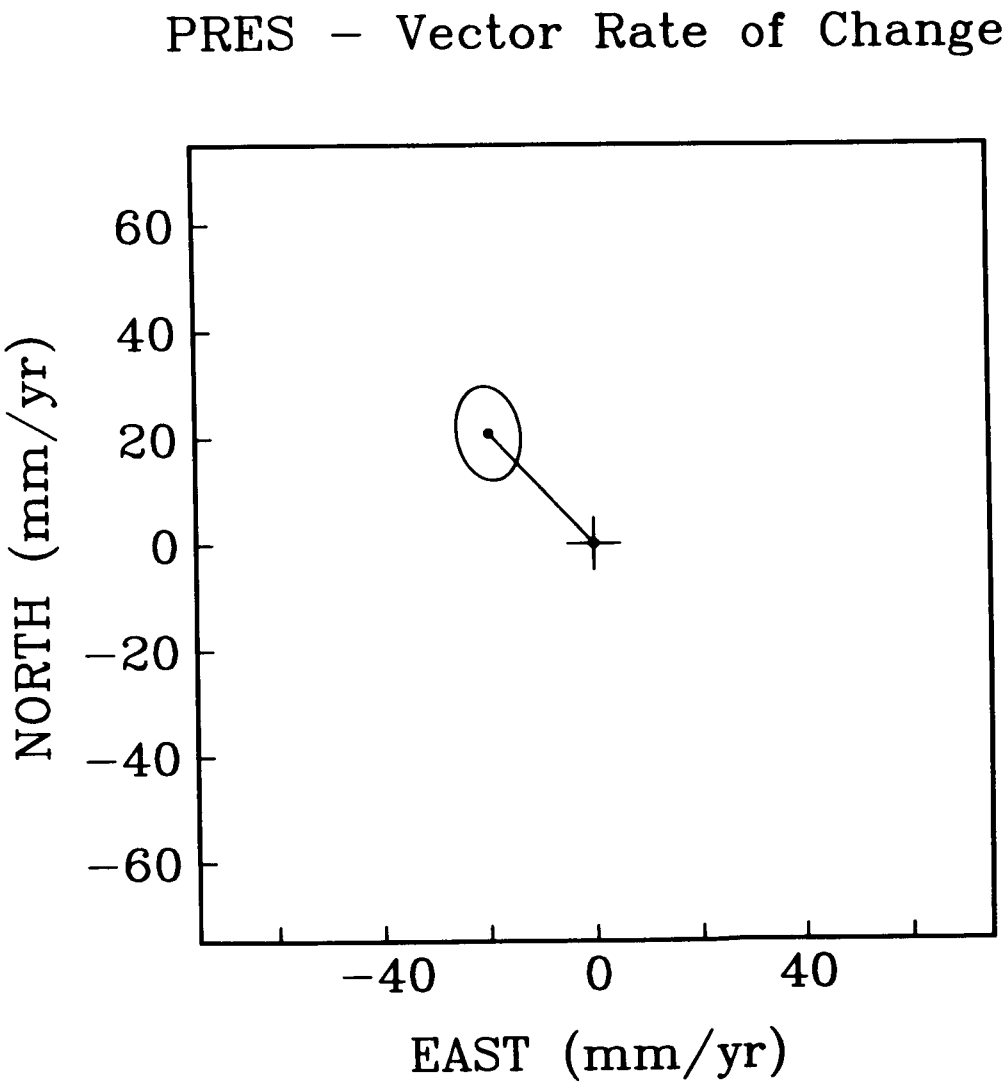

Figure 20. Vector rate of change of position of station PRES.

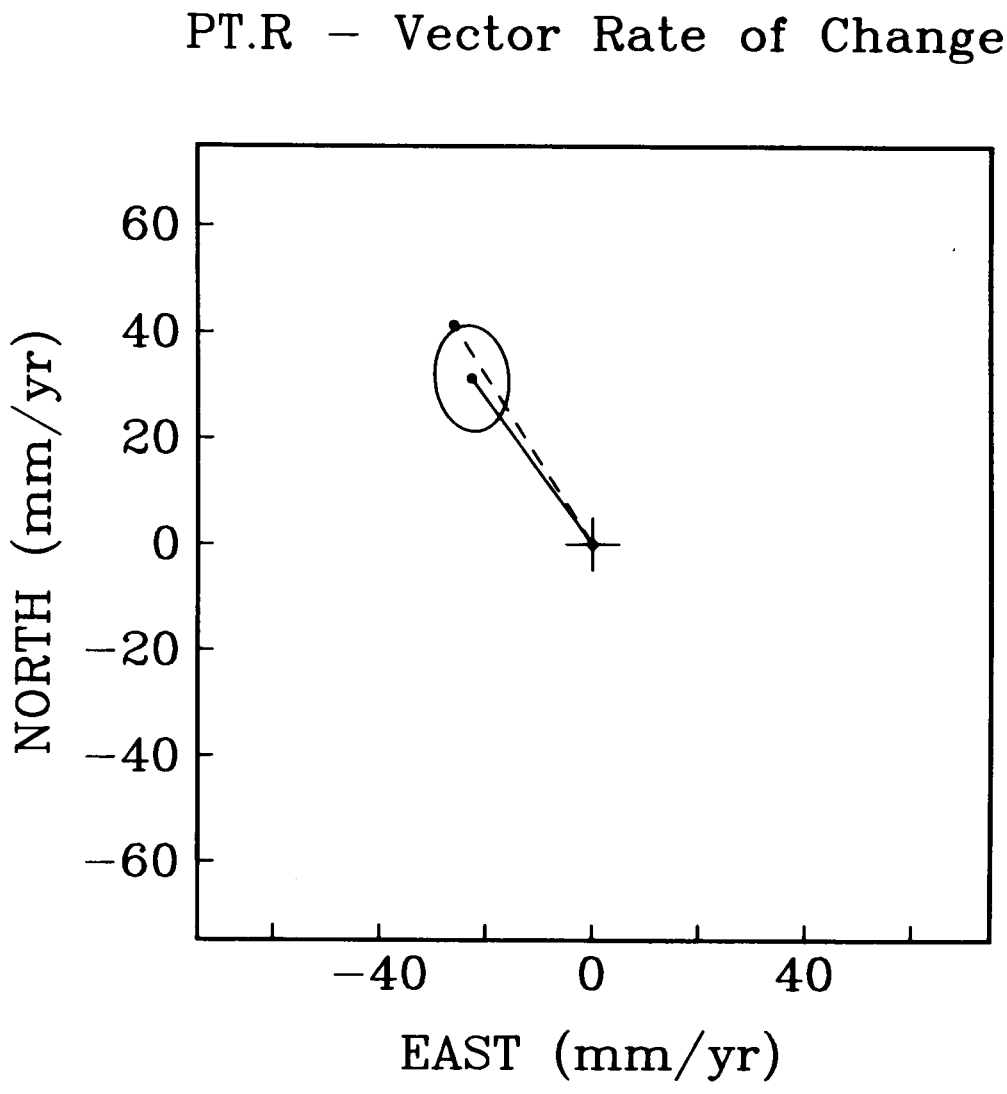

Figure 21. Vector rate of change of position of station PT.R. The Pacific-North American plate motion vector predicted by NUVEL-1 is given by the dashed line.

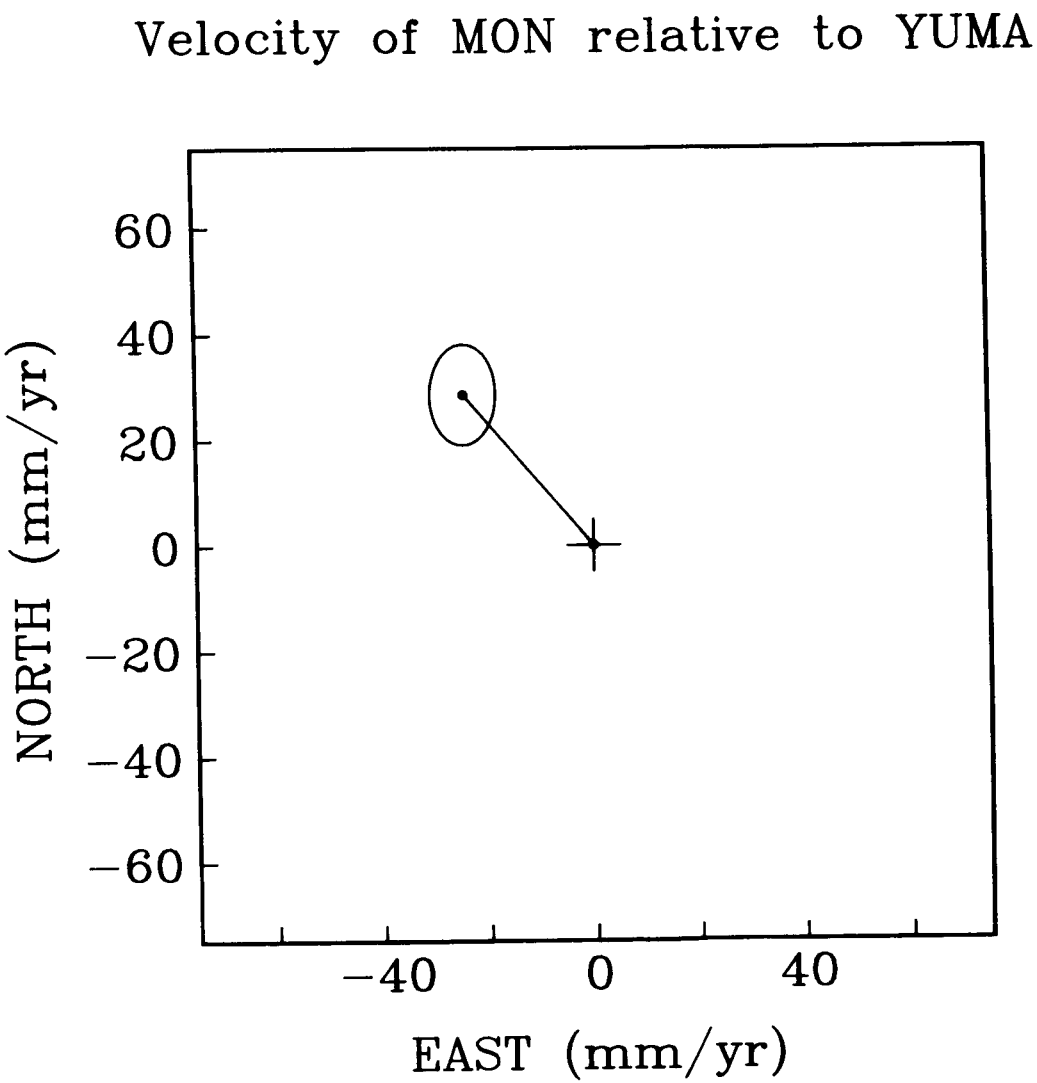

Figure 22. The velocity of MON relative to YUMA.

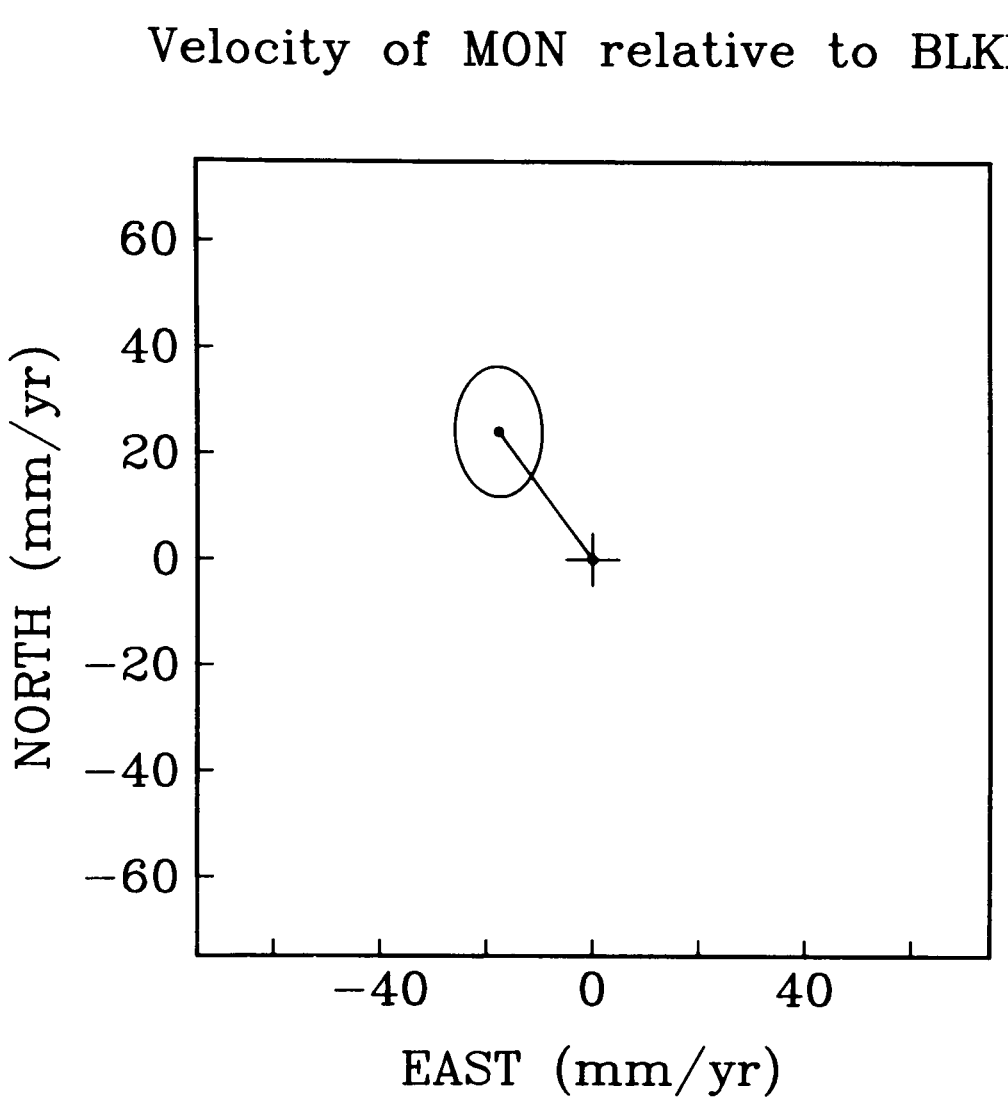

Figure 23. The velocity of MON relative to BLKB.

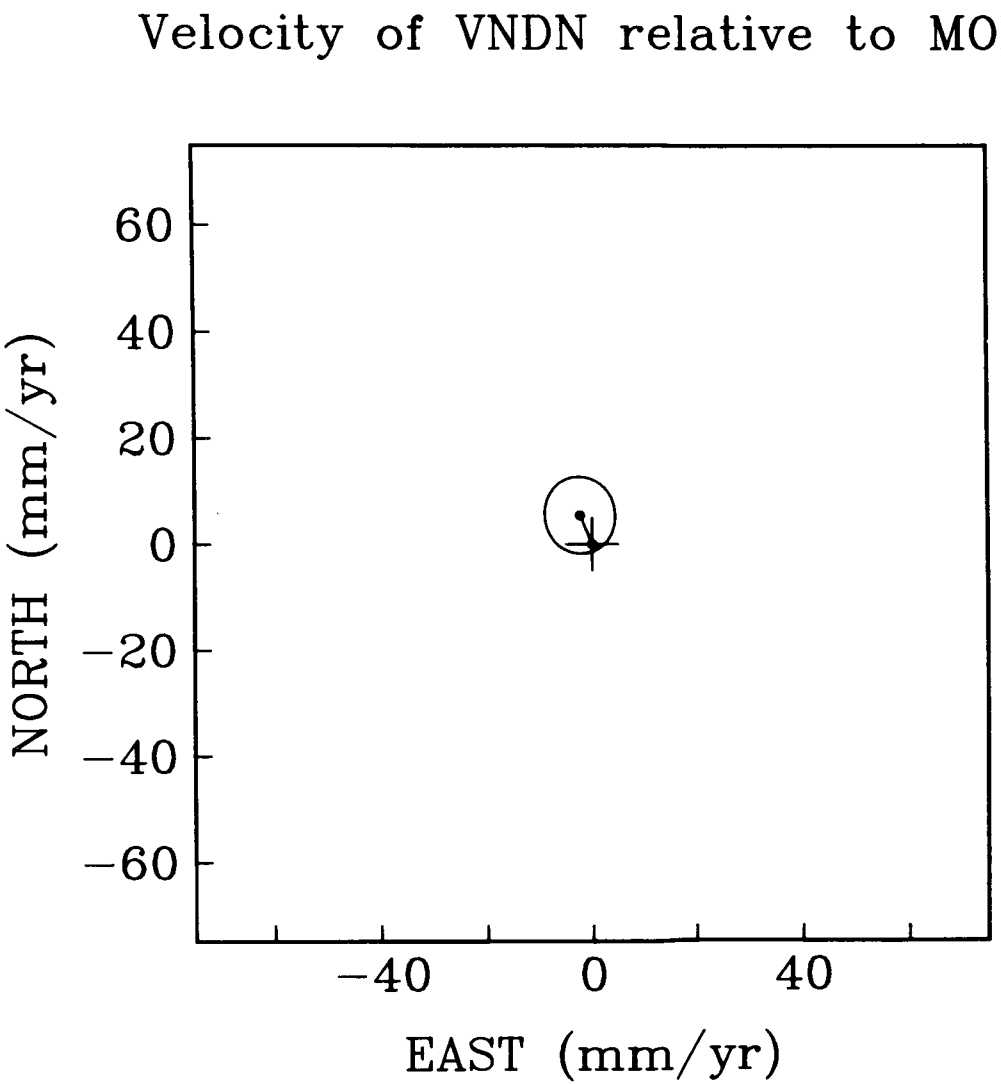

Figure 24. The velocity of VNDN relative to MON.

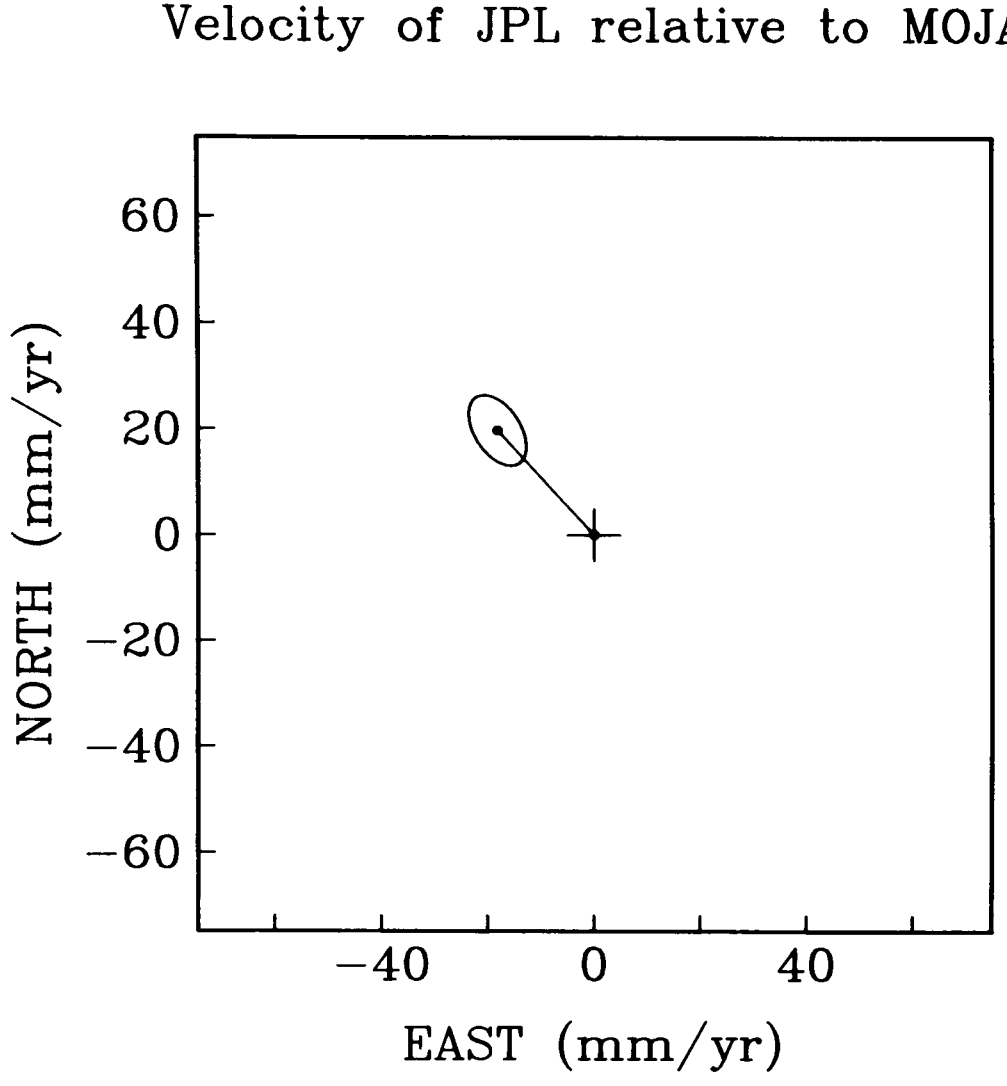

Figure 25. The velocity of JPL relative to MOJA.

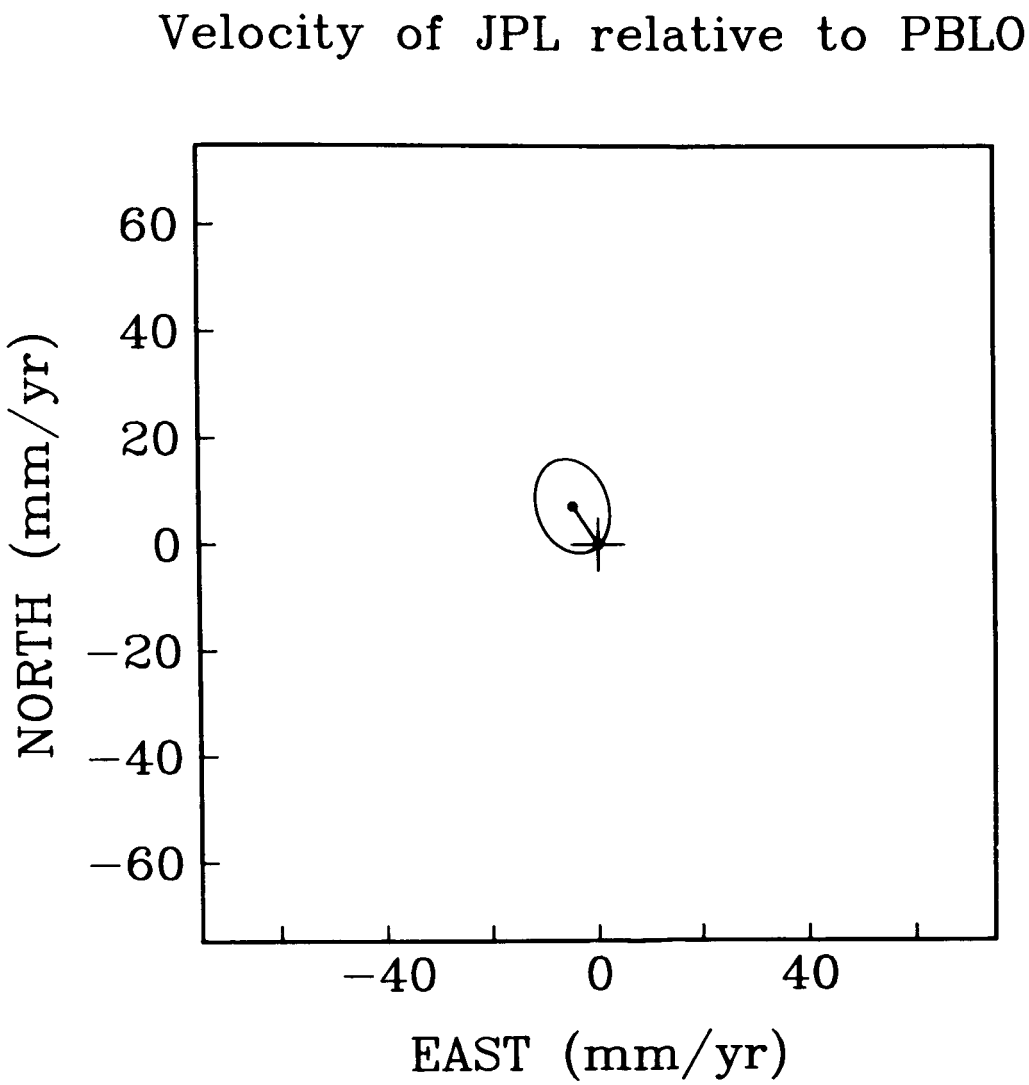

Figure 26. The velocity of JPL relative to PBLO.

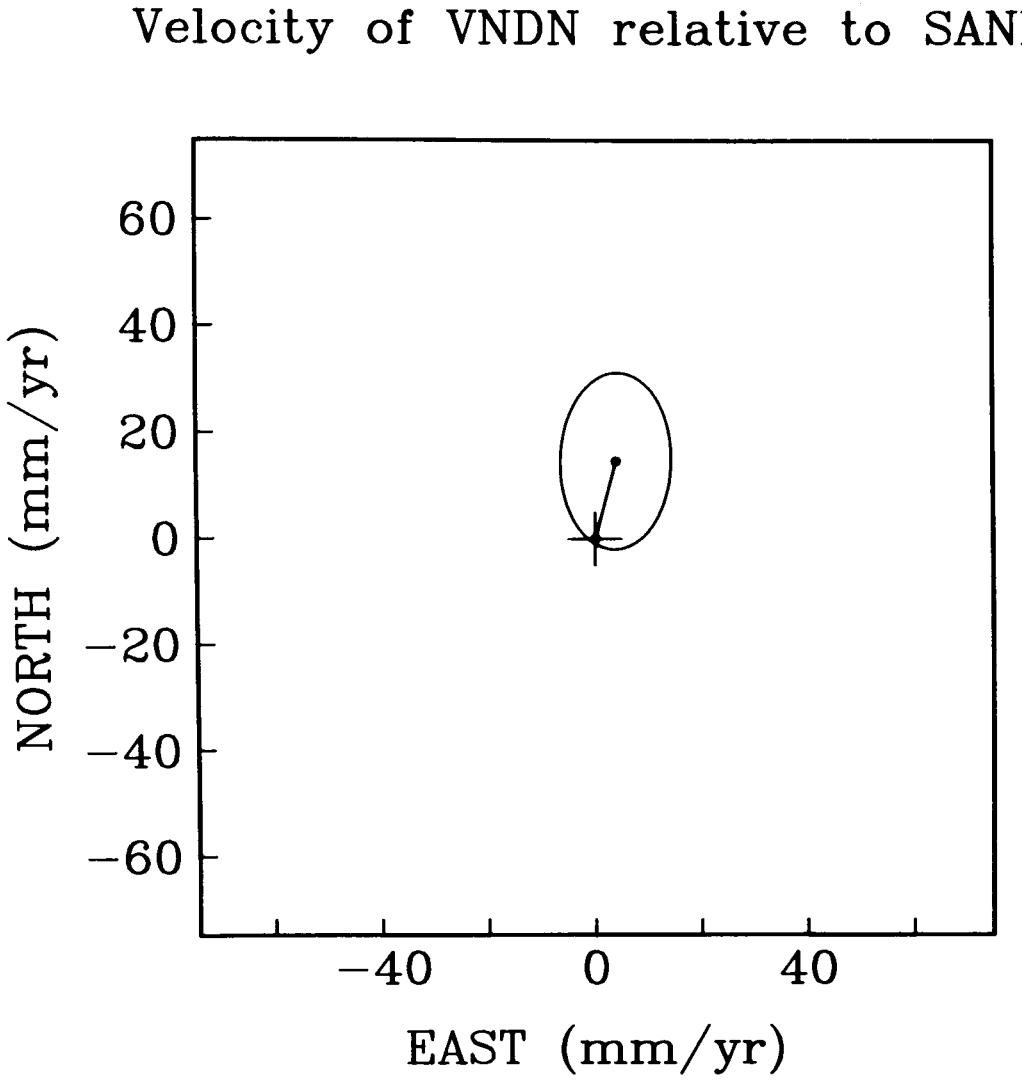

Figure 27. The velocity of VNDN relative to SANP.

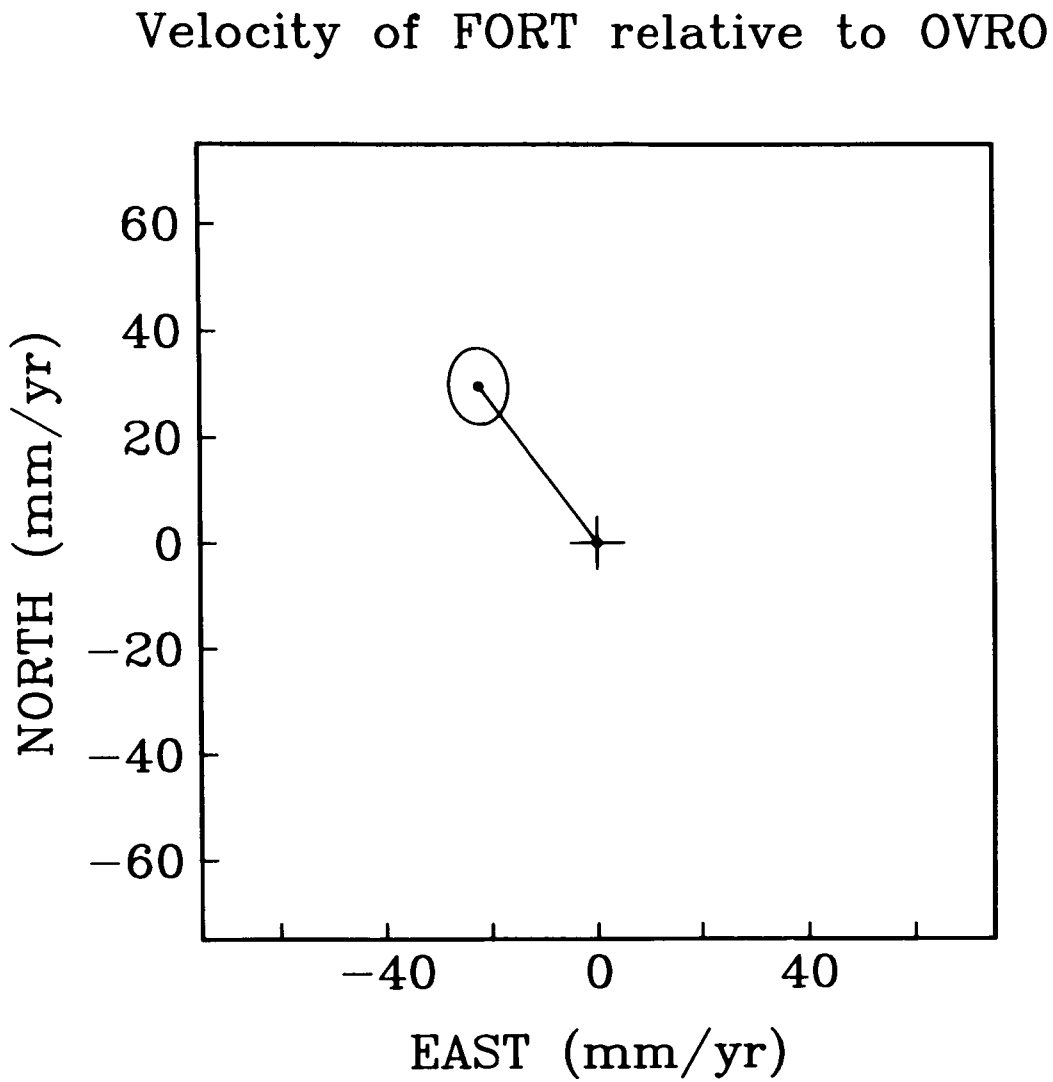

Figure 28. The velocity of FORT relative to OVRO.

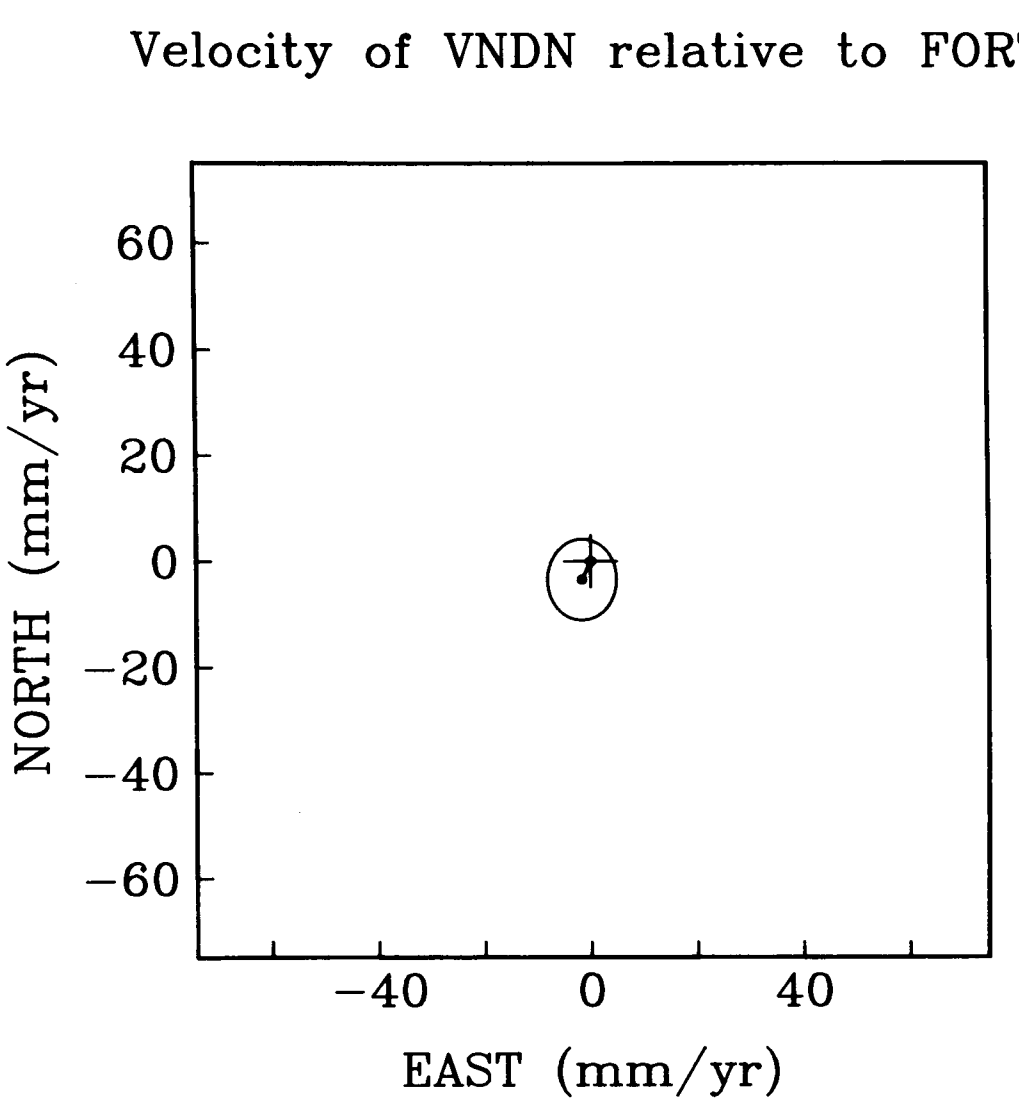

Figure 29. The velocity of VNDN relative to FORT.

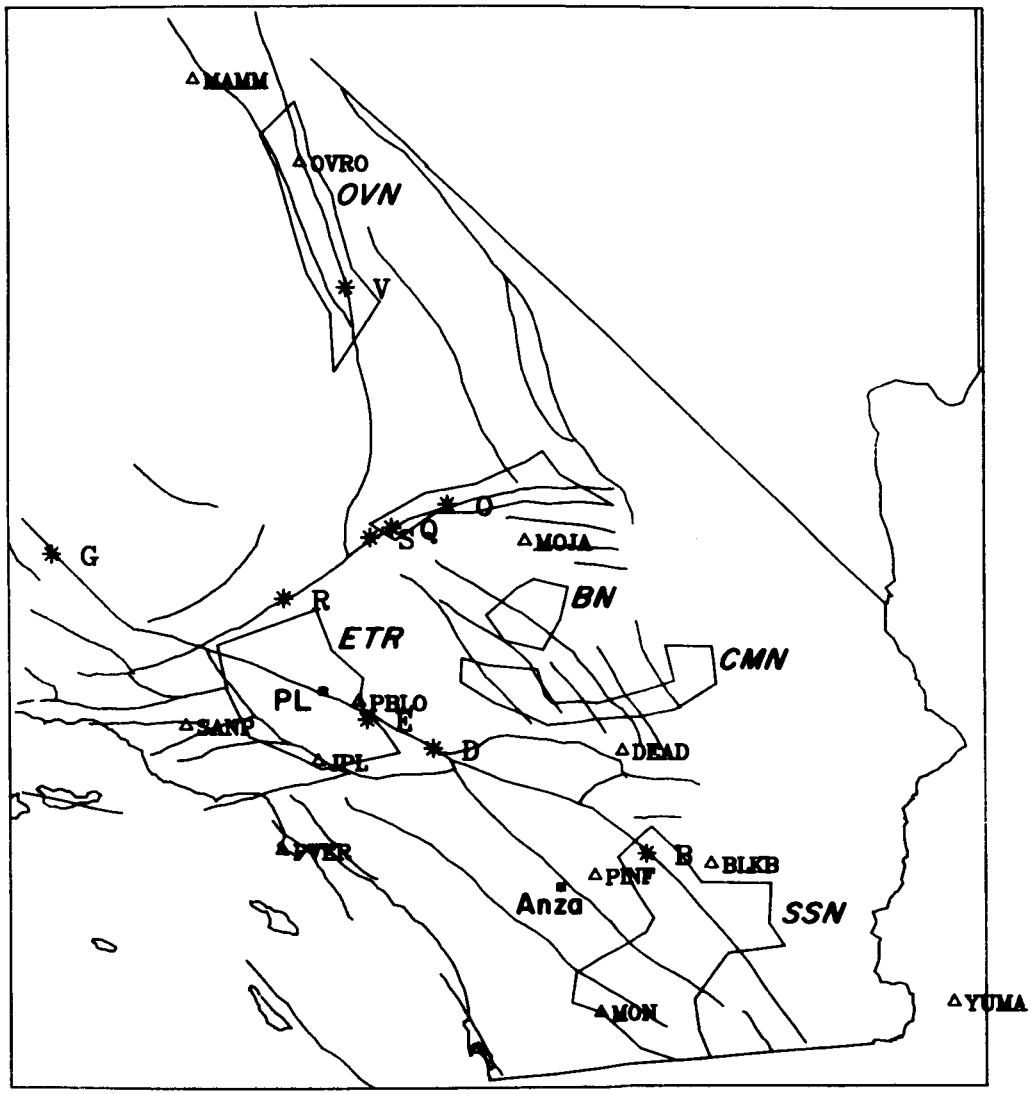

Figure 30. Reference figure for the studies cited in Tables 4 and 5. At sites B, D, E, and G geologically estimated rates of fault slip were estimated geologically for the San Andreas fault; at sites O, Q, S and R for the Garlock fault; and at V for the Hunter Mountain fault. USGS ground-based geodetic networks include SSN = Salton Sea Network, ETR = Eastern Transverse Ranges Network, CMN = Central Mojave Network, BN = Barstow Network, OVN = Owens Valley Network. Also shown are the locations of the cities Anza and Palmdale (PL).

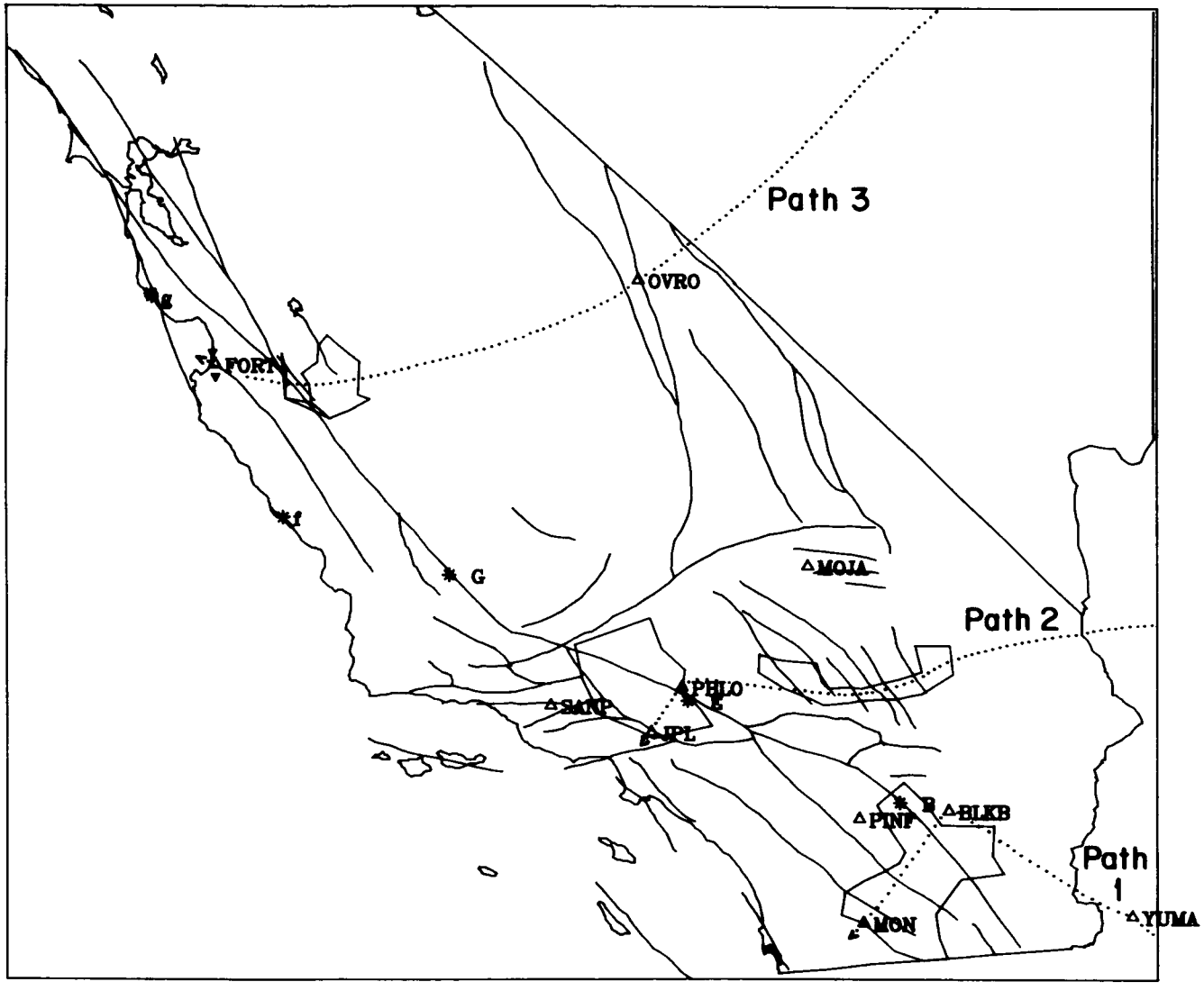

Figure 31. Reference figure for three path integrals. See Figure 30 for symbols and Figure 2 for fault names.

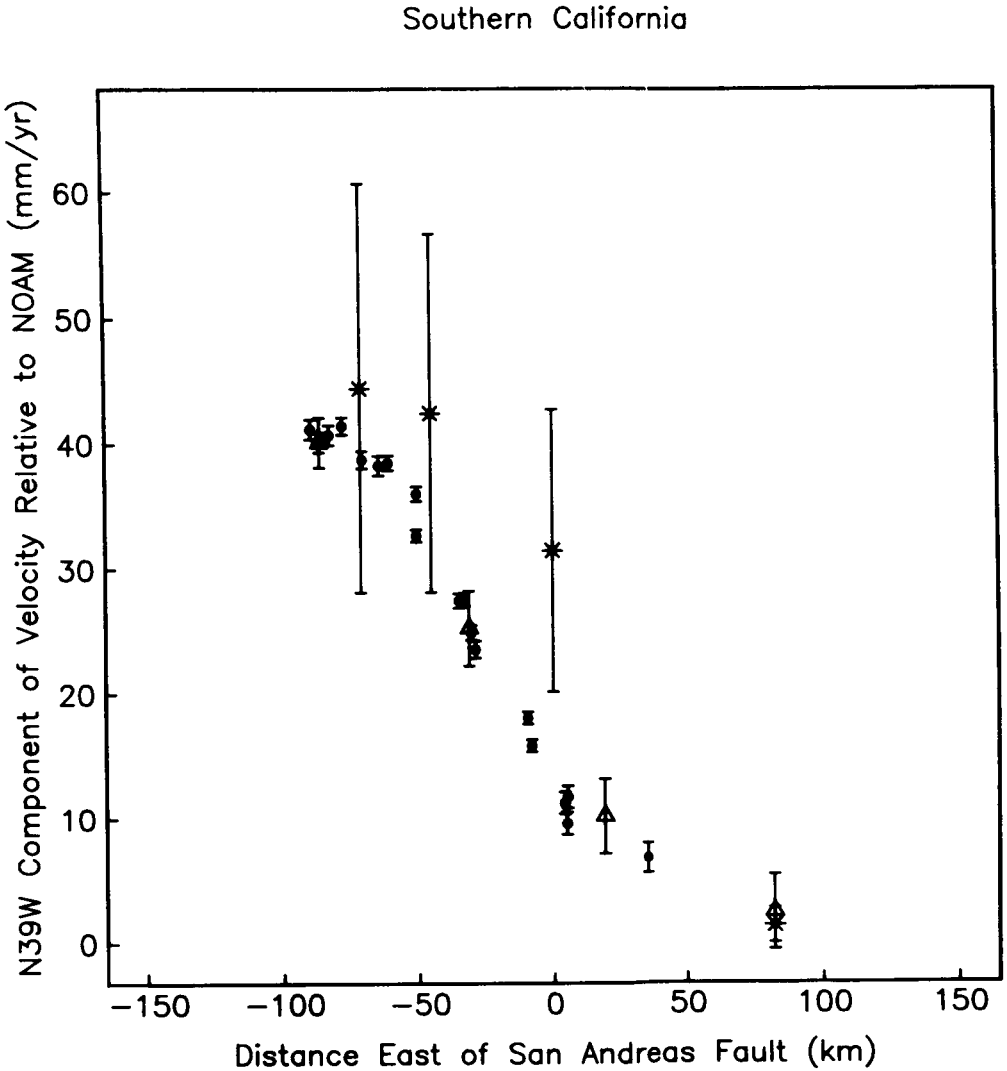

Figure 32. Fault-parallel component of velocity relative to North America (NOAM) along path 1 in southern California. The * indicates the best estimate of the geologically determined slip rate; the error bar indicates lower and upper bounds on these geological estimates. Solid circles indicate USGS trilateration data. Vertical error bars indicate the standard deviation relative to the network centroid (J. Savage and M. Lisowski, personal communication, 1988). Open triangles denote VLBI data with associated standard deviations shown by error bars.

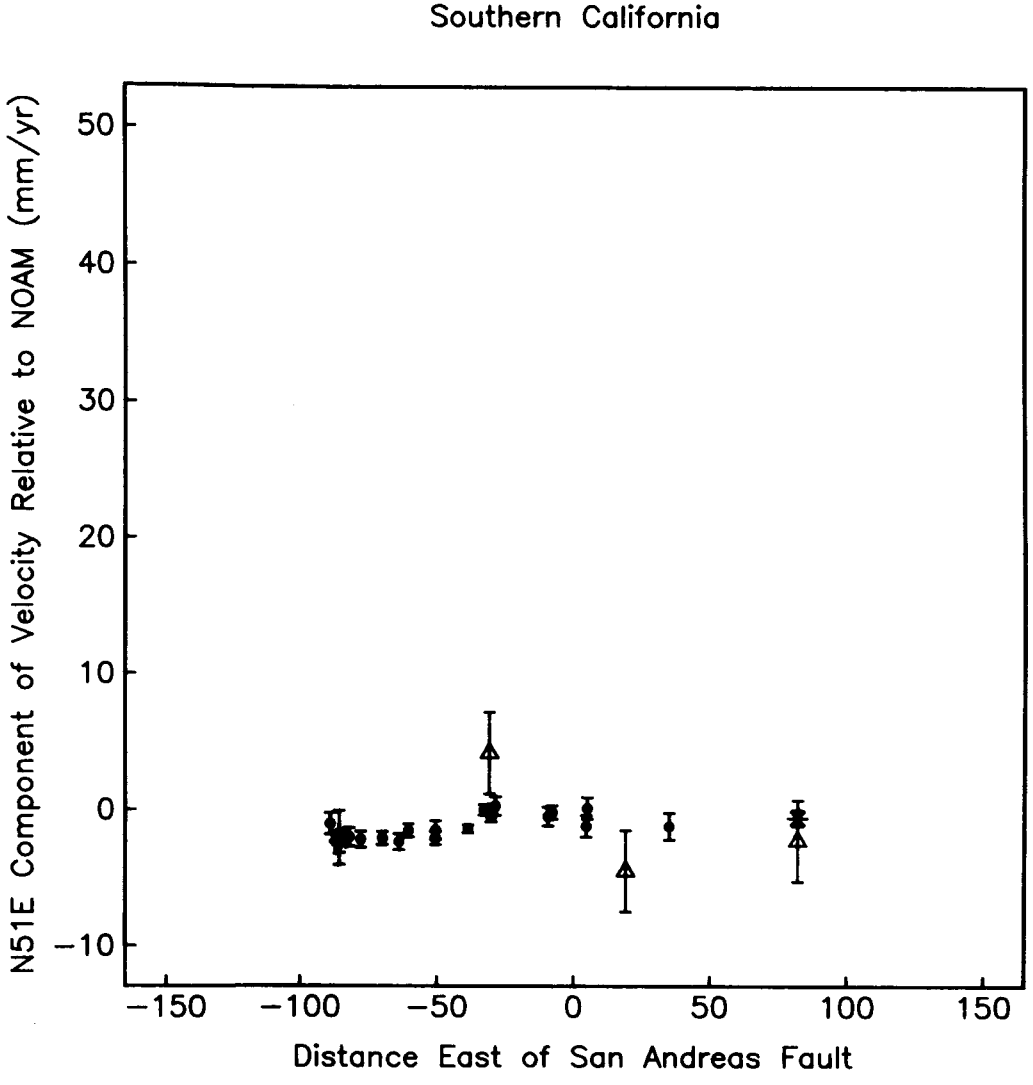

Figure 33. Fault-normal component of velocity relative to North America along path 1 in southern California. Symbols are as in Figure 32.

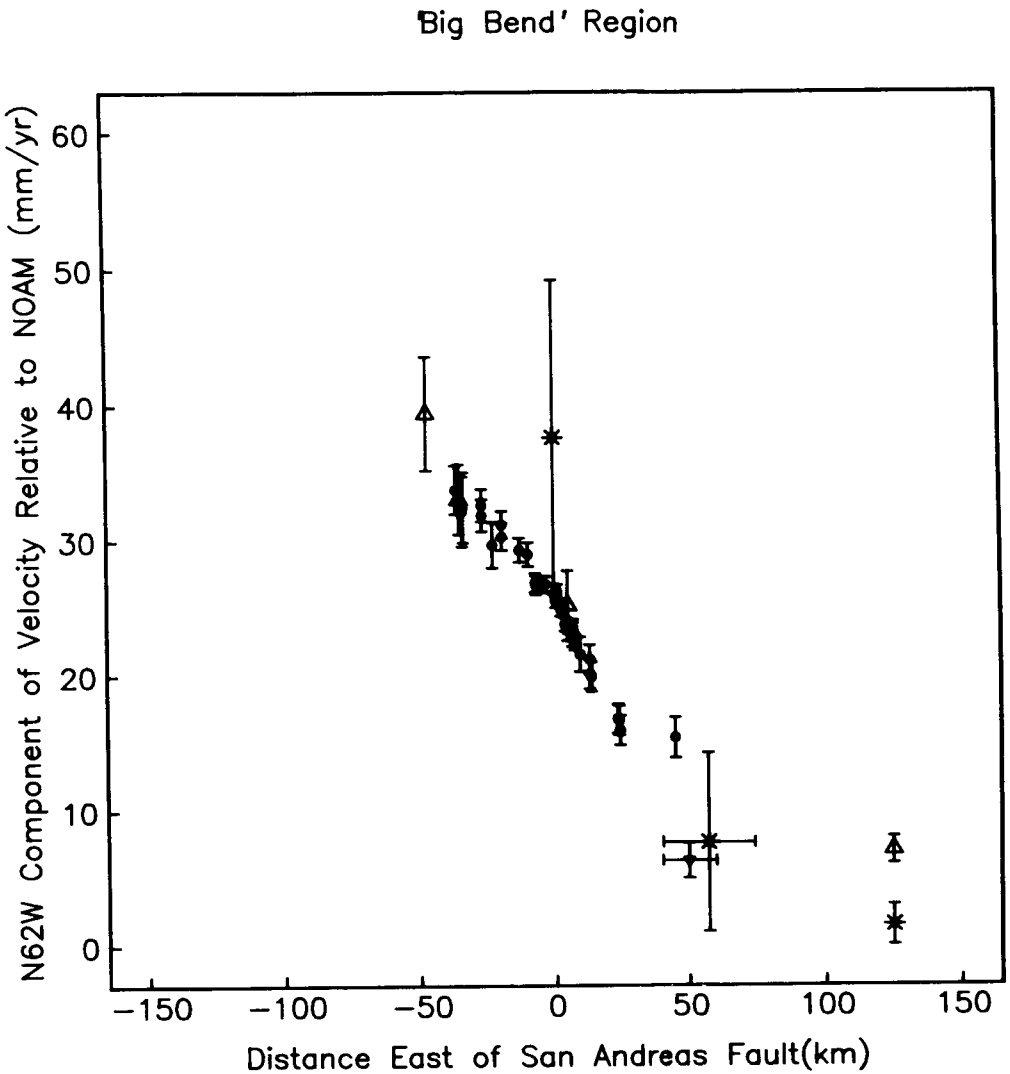

Figure 34. Fault-parallel component of velocity relative to North America along path 2 in the 'big bend' region. The horizontal error bars indicate the region over which the measurement was made. Other symbols as given in Figure 32.

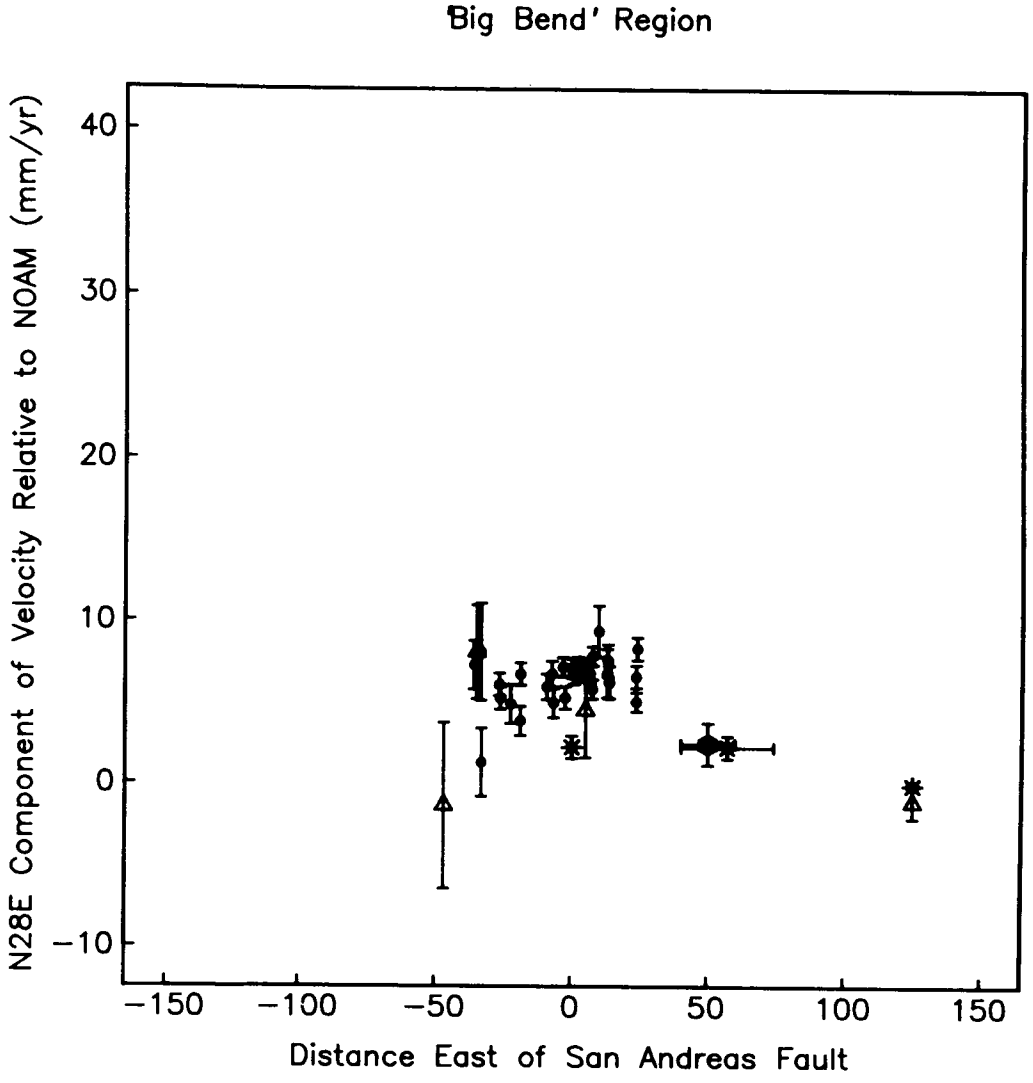

Figure 35. Fault-normal component of velocity relative to North America along path 2 in the 'big bend' region. Symbols as in Figures 32 and 34.

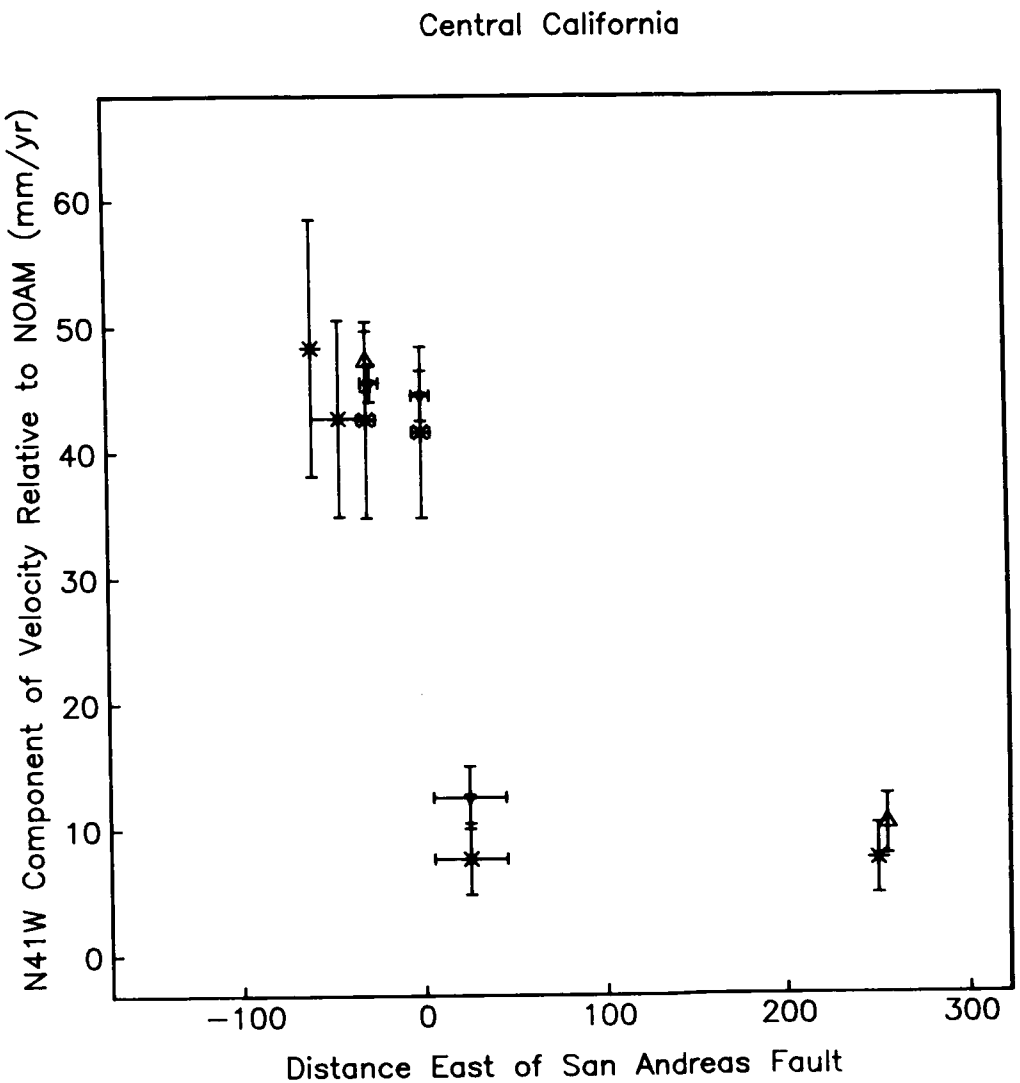

Figure 36. Fault-parallel component of velocity relative to North America along path 3 in central California. Symbols as in Figures 32 and Figure 34.

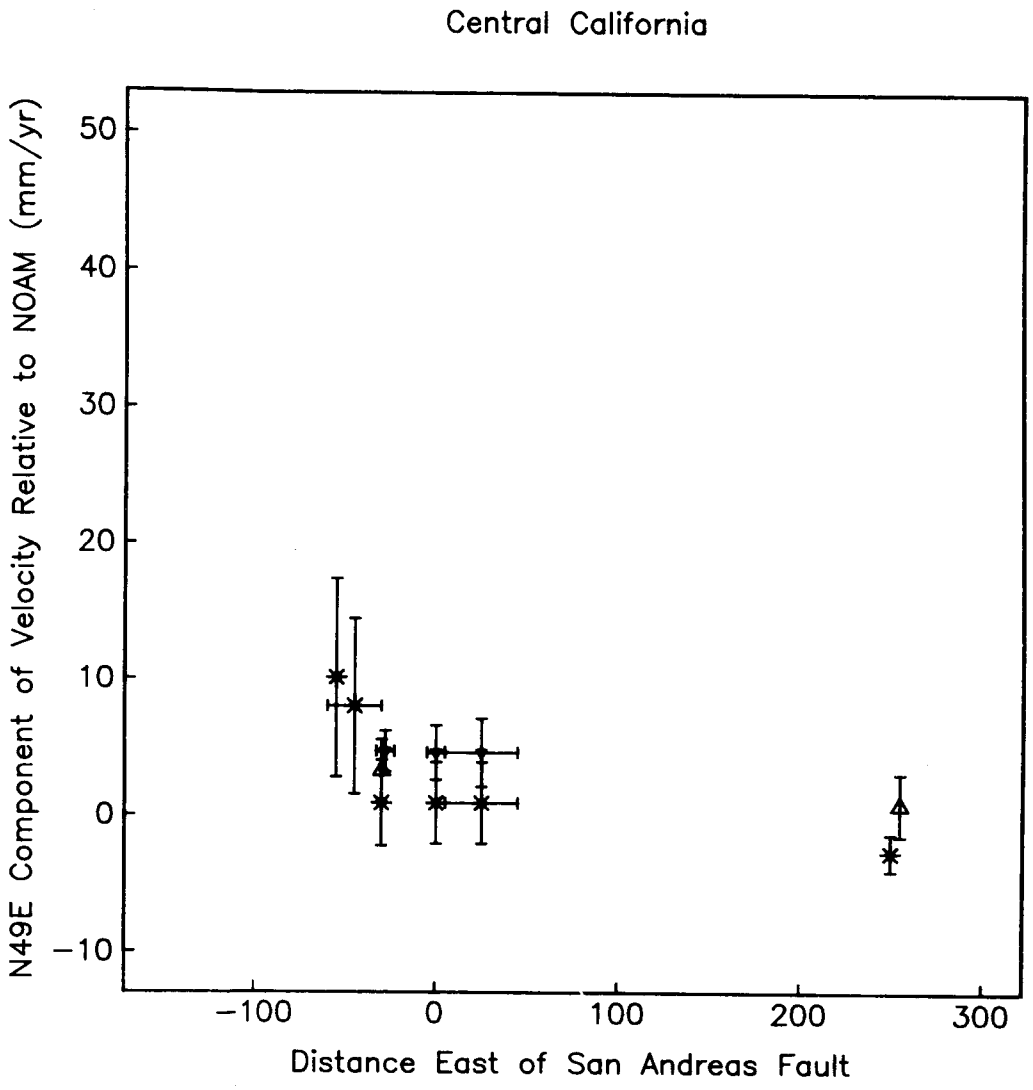

Figure 37. Fault-normal component of velocity relative to North America along path 3 in central California. Symbols as given in Figures 32 and Figure 34.

Chapter 5. Conclusions

In this thesis I estimated the rates of deformation across Pacific - North American plate boundary zone in California utilizing geodetic data. The rates of deformation in the central Mojave Desert and east of the central creeping portion of the San Andreas fault were estimated from triangulation and trilateration data. In these two studies the measured incremental strain was compared with the accommodation of strain seen in local geological structures, strain release in earthquakes, and principal stress directions inferred from *in situ* measurements. To address the question of the relation of deformation measured on local scales to the overall accommodation of deformation across the Pacific - North American plate boundary zone I utilized VLBI data. These data constrain the integrated rate of deformation across portions of the continental plate boundary in California and provide a tectonic framework to interpret regional geodetic and geologic studies.

The dominant active structural elements of the Mojave Desert block are right-lateral strike-slip faults trending approximately N35°W-N42°W. Data from triangulation and trilateration surveys made during 1932 - 1982 were used to calculate shear strain rates in the central Mojave Desert. The geodetic network extends ~110 km east - west and spans the area from west of the Helendale fault to east of the Ludlow fault. For the region between the Helendale and Camp Rock faults the shear strain rate was determined to be 0.16 ± 0.03 μrad/yr, with maximum right-lateral shear strain occurring on a plane oriented N41°W ± 5°. To search for strong spatial gradients in the strain field the rates of shear strain were determined for a number of different spatial subnets and the observed angle changes were compared with those predicted by least squares analysis assuming a uniform strain field. Because there are not enough stations located between potentially active faults, it is uncertain whether there is strain accumulation associated with the Helendale and Camp Rock faults or if all the observed strain is associated with the Lenwood and Johnson Valley faults. If we assume that the deformation measured between Helendale and Camp Rock

faults is due to right-lateral motion across the local faults, the average shear straining corresponds to a relative displacement of 6.7 ± 1.3 mm/yr across this portion of the network. From the Camp Rock fault eastward across the network there is a transition from significant to very low strain rates.

The spatial pattern and orientation of the observed strain field suggest a relation to the northwest trending faults of the central Mojave and argue against the observed strain being due to elastic strain accumulation that will be released in a large earthquake on the 'big-bend' portion of the San Andreas fault. The region of active deformation is measured on the central Mojave network at a distance of 40-90 km from the San Andreas. While the observations given by the trilateration and the VLBI data given in Chapter 4 and deformation models [*Thatcher, 1983*] suggest that interseismic elastic straining may be broadly distributed, neither the shear strain orientation nor the sharp decline in its magnitude across the Mojave network support the hypothesis that the observed strain will be released on the San Andreas during a large earthquake instead of on the local faults through fault creep or local earthquakes. The geological observation of Quaternary slip on the central Mojave faults [*Dokka,* 1983] further supports the view that the measured strain is associated with the local faults.

The measured strain could be due to one or more of several different mechanisms: (1) earthquakes, (2) fault creep, or (3) elastic and anelastic strain accumulation. On the basis of a calculation of strain due to earthquakes of $M_L \geq 3.0$ we concluded that slip due to earthquakes accounts for only an insignificant portion of the deformation measured in the region between Helendale and Camp Rock faults. Some combination of fault creep and elastic or anelastic deformation of the lithosphere must therefore be responsible for the measured strain.

The fault plane solutions for six earthquakes that occurred in the central Mojave Desert along with those of three events determined by others were used to compare the derived strain field with the directions of principal stress inferred from these focal mechanisms.

The strikes of the fault planes for some of these events were found to be similar to the orientation of the major faults in the area, a second group have preferred fault planes with strikes that are more northerly by 5° - 20°, and two events are normal faulting earthquakes that are thought to accommodate east-west extension. We concluded that the major faults of the region strike at the orientation of maximum strain accumulation and thus are the faults along which long term displacement will preferentially occur. Secondary faulting controlled by a Coulomb-Anderson type failure mechanism or by slip on preexisting faults can account for slip on faults of other orientations. Recent paleomagnetic evidence from the western Mojave suggest that the region may have rotated 10° - 20° counterclockwise since ~ 16 Ma [*McFadden et al.*, 1987; *Golombek and Brown*, 1988]. Such counterclockwise rotation of the Mojave block might eventually act to rotate the northwest striking faults out of an orientation favorable to accommodate relative plate motion.

Triangulation and trilateration data from two geodetic networks located between the San Andreas fault and the Great Valley have been used to calculate shear strain rates in the Diablo Range between Hollister and Coalinga and to estimate the slip rate along the Calaveras and Paicines faults in central California. The earthquake focal mechanisms and geological structures in the area suggest two primary modes of deformation to the northeast of the San Andreas fault: compression normal to the major fold structures of the region and right-lateral strike-slip motion on faults such as the Calaveras and the Paicines.

The Diablo Range in this region is a broad antiform which trends approximately N65°W and encompasses subsidiary fold structures such as the Vallecitos syncline. The shear strain rates, $\dot{\gamma}_1$ and $\dot{\gamma}_2$, were estimated independently from angle changes using Prescott's method and from the simultaneous reduction for station position and strain parameters using the DYNAP method with corrections to reduce the triangulation and trilateration data to a common reference surface. On the basis of Prescott's method, the average shear strain rate across the Diablo Range for the time period between 1962 and

1982 is 0.15 ± 0.08 μrad/yr, with the orientation of the most compressive strain (β) at N16°E ± 14°. Utilizing corrections for the deflection of the vertical and the geoid - reference ellipsoid separation computed on the basis of local gravity observations, $\dot{\gamma}$ = 0.19 ± 0.09 μrad/yr and β = N16°E ± 13°. Although $\dot{\gamma}$ is not significantly greater than zero at the 95% confidence level, the orientation of β is similar to the direction of maximum compressive strain indicated by the orientation of major fold structures in the region (N25°E). We infer that the measured strain is due to compression across the folds of this area; the average shear straining corresponds to a relative shortening of 5.7 ± 2.7 mm/yr. In contrast to the situation throughout most of the Coast Ranges, where fold axes have orientations approximately parallel to the San Andreas fault, within the Diablo Range between Hollister and Coalinga the trend of the fold axes are different and are thought to be controlled by reactivation of older structures. Given such structural control, the geodetic data reported here are also consistent with an oblique displacement, or transpression, model for deformation of the Coast Ranges. There are two observations which argue against models in which right-lateral shear strain is distributed across a zone significantly greater than 10 km in width. Because slip on the adjacent San Andreas fault occurs primarily by steady creep, little of the right-lateral shear strain accumulation associated with the fault should be measurable on off-fault geodetic lines. Additionally, distributed shear strain associated with the San Andreas fault should be observable on both sides of the fault, yet there is no geodetic or geologic evidence of deformation to the west of the San Andreas fault within the Salinian block in this region.

Within 5 - 10 km to the east of the San Andreas fault the primary geologic structures are related to dextral shear on the San Andreas and Calaveras - Paicines faults. Since 1972 trilateration measurements have been made by the USGS in central California on a regional scale spanning a 20-km-wide zone centered on the San Andreas fault and including several distinct faults, as well as on smaller (1 -2 km) aperture networks that span a single fault. A

slip rate of 10 - 12 mm/yr was calculated for the Calaveras - Paicines fault south of Hollister. The slip rate on the Paicines fault decreases to 4 mm/yr near Bitter.

The geocentric position vectors from a set of 77 VLBI experiments beginning in October 1982 were used to estimate the tangential rate of change of station positions in the western U.S. These data were processed utilizing a procedure developed to remove from apparent tectonic motion the contamination due to errors in earth-orientation parameters and non-uniform station geometry; this procedure accounts fully for the position covariance between stations. In this method the tangential displacement field is minimized with respect to an *a priori* geophysical model of deformation. This model is parameterized in terms of the tangential velocity of a station in a North-America-fixed reference frame.

The vector velocities estimated for the stations in the western U.S. provided discrete samples of the temporal and spatial deformation field. To interpret the VLBI-derived rates of deformation for three regions, across southern California just north of the Imperial fault, in the "big-bend" region, and in central California, I compared the rates of deformation derived from VLBI and ground-based geodetic data, and I examined the relationship between the rates of deformation determined from geological data and those estimated from the geodetic data.

Deformation across southernmost California is fairly well described by simple right-lateral shear on the San Andreas, San Jacinto, Elsinore, and possibly the offshore faults of the California borderlands. An estimate of the integrated rate of deformation across the southern region of the Basin and Range province is given by the station YUMA (3.4 ± 2.7 mm/yr at N84°W $\pm$ 16°) and is consistent with the low rate of deformation inferred from geologic data. Within the Salton Sea region there are three VLBI sites, BLKB, PINF, and MON, and with denser spatial coverage the Salton Sea trilateration network. MON is collocated with a trilateration station, and the velocity of the trilateration station is set equal to the MON vector velocity. The fault-parallel components of velocity of PINF and BLKB are in close agreement with the velocity profile given by the trilateration data. A large

earthquake has not occurred on the southern segment of the San Andreas fault within the last ~400 years [*Sieh*, 1986], and strain accumulation is observed over a broad region. If the vector velocity given by the MON - YUMA difference vector (37.6 ± 3.4 mm/yr at N40°W ± 8°) is approximately equal to the accumulated rate of long-term slip across the San Andreas, San Jacinto, and Elsinore faults, additional deformation is predicted to occur offshore in the California borderlands. This rate of deformation is similar to that given by *Weldon and Humphreys* [1986]. The velocity difference vector between VNDN and MON is 5.9 ± 2.9 mm/yr at N23°W ± 4° and further supports the hypothesis that additional deformation occurs on the offshore faults of the California borderlands.

In the big-bend region of the San Andreas fault recent deformation has been measured across the right-lateral strike-slip faults of the central Mojave, along the San Andreas fault, and as northeast-southwest compression across the western Transverse Ranges and the offshore faults in the Channel Islands. The VLBI station MOJA is located in the northeast corner of the the Mojave Desert block. The vector velocity of MOJA is 7.1 ± 0.9 mm/yr at N50°W ± 1°. This result, along with ground-based geodetic and geologic data from the Mojave Desert, the Garlock fault, and the Great Basin suggest that the estimated rate of deformation on the northwest striking faults of the central Mojave (6.7 ± 1.3 mm/yr at N41°W ± 2°, Chapter 2) may be kinematically related to deformation north of the Garlock. The station MOJA as well as the western Garlock fault are then within a deforming region connecting slip in the central Mojave to deformation north of the Garlock. The alternative hypothesis that the MOJA and the central Mojave strain results are due to elastic strain accumulation which will be relieved in the next large earthquake on the San Andreas fault is rejected on the basis of several arguments; the most convincing argument is that recent slip has been documented along the faults of the central Mojave [*Dokka* , 1983; E. Hart, personal communication, 1987] .

Two VLBI stations, JPL and PBLO, are located within the Eastern Transverse Ranges (ETR) trilateration network. The ETR network spans the big-bend segment of the

San Andreas near Palmdale. After fixing the site velocity of JPL to be the same in both networks the fault-parallel component of PBLO is similar to the velocity given by the trilateration data. Over the broad region between MOJA and JPL the rate of deformation given by the differenced velocity vector is quite low (26.9 ± 2.6 mm/yr at N43°W ± 5°) and suggests that the long term rate of slip on the big-bend segment of the San Andreas may be ~25 mm/yr. The velocity difference vector for VNDN - SANP suggest 15.2 ± 6.7 mm/yr of northeast-southwest compression (N15°E ± 7°) between the two sites. The SANP station, which is located in the Ventura Basin, however has been measured only 4 times. Extensive GPS measurements being made in the western Transverse Ranges and to the offshore Channel Islands will provide additional constraints on the rate of deformation in this region.

In central California slip along the San Andreas fault is thought to occur primarily through surface creep. Recent deformation has also been measured on tectonic elements east and west of the San Andreas; these include extension across the Basin and Range, right-lateral strike-slip motion on the Rinconada and San Gregorio faults and northeast-southwest compression within the Coast Ranges. The integrated rate of deformation given by the vector rate of change of the station position for OVRO is 10.3 ± 2.7 mm/yr at N37°W ± 4.5°; the azimuth is closer to the local orientation of the Owens Valley fault than the assumed direction of extension in the Great Basin (N60°W). The integrated rate of extensional deformation across the Basin and Range estimated from geological observations and VLBI baselines that cross the region is given by *Minster and Jordan* [1987] to be 9.7 ± 2.1 mm/yr at N56°W ± 10°. The difference velocity vector between FORT and OVRO, 37.1 ± 2.8 mm/yr at N37°W ± 5°, is similar to the integrated rate of deformation estimated from ground-based geodetic networks (36.5 mm/yr at N34°W) and from geological data (35.2 mm/yr at N34°W). The VLBI results thus are consistent with the conclusions obtained from an examination of regional geologic and geodetic studies from the Coast Ranges and global plate models; specifically, that the fault-parallel

component of the San Andreas discrepancy vector may be accommodated by strike-slip motion on the Rinconada as well as the San Gregorio fault and that the inferred shortening to the east of the San Andreas fault may represent a significant component of the fault-normal compression predicted by the discrepancy vector.

For the three regions where ground-based geodetic and VLBI results could be directly compared the results are similar and suggest that at least the differenced velocity vectors from VLBI may be used to estimate the integrated rate of deformation between sites. Although there is some uncertainty in interpreting the VLBI station velocities in terms of an absolute velocity in a North-America-fixed coordinate system, the VLBI data provide a framework to interpret the local and regional geodetic results.

The comparison of geodetic results to the long-term accommodation of deformation as seen in the local geological structures has been used to examine tectonic models of deformation. Additionally, the geodetic results may provide an improved estimate of the rate of deformation that can be used for comparison to geologic rates of slip. The geodetic results given in this thesis were determined by assuming steady-state deformation. The major challenge to using the measured incremental strain to infer the long-term rate of deformation is to understand temporal variations in the rate of strain accumulation. Five years ago I attempted to estimate the contribution viscous relaxation makes to the rate and pattern of deformation following a large earthquake in the Imperial Valley (Chapter 4); with the geodetic data available at that time I was unable to determine a unique model of post-seismic deformation. In the future I hope to use the findings of this thesis to tie the kinematic results to such dynamic models of deformation.

REFERENCES

Allen, C.R., L.T. Silver, and F.G. Stehli, Agua Blanca Fault - A major transverse structure in northern Baja California, Mexico, *Geol. Soc. Am. Bull., 71*, 457-482, 1960.

Anderson, W.L., Weighted triangulation adjustment, *U.S. Geol. Surv. Open File Rep.*, Computer Contribution Number 1, 52 pp., U.S. Geol. Surv. Computer Center Div., Washington, D.C., 1969.

Astiz, L., and C. R. Allen, Seismicity of the Garlock Fault, California, *Bull. Seismol. Soc. Am., 73*, 1721-1734, 1983.

Atwater, T., Implications of plate tectonics for the Cenozoic tectonic evolution of western North America, *Geol. Soc. Amer. Bull., 81*, 3513-3536, 1970.

Aydin, A., and B. M. Page, Diverse Pliocene-Quaternary tectonics in a transform environment, San Francisco Bay region, California, *Geol. Soc. Am. Bull., 95*, 1303-1317, 1984.

Beanland, S., and M.M. Clark, The Owens Valley fault zone, eastern California, surface rupture associated with the 1872 earthquake (abstract), *Seismol. Res. Lett., 58*, 32, 1987.

Beroza, G.C., T.H. Jordan, J.B. Minster, T.A. Clark, and J.W. Ryan, VLBI vector position data: Application to western U.S. deformation (abstract), *Eos Trans. AGU, 66*, 848, 1985.

Biot, M.A., Theory of folding of stratified viscoelastic media and its implications in tectonics and orogenesis, *Geol. Soc. Am. Bull., 72*, 1592-1620, 1961.

Bird, P., and R.W. Rosenstock, Kinematics of present crust and mantle flow in southern California, *Geol. Soc. Am. Bull., 95*, 946-957, 1984.

C - 3

Bishop, C., Geologic map of California Needles sheet, Olaf P. Jenkins edition, Calif. Div. of Mines and Geol., Sacramento, 1963.

Bomford, G., *Geodesy*, 855 pp., Clarendon Press, Oxford, 1980.

Burchfiel, B.C., K.V. Hodges, and L.H. Royden, Geology of Panamint Valley - Saline Valley pull-apart system, California: Palinspastic evidence for low-angle geometry of a neogene range-bounding fault, *J. Geophys. Res.*, 92, 10422-10426, 1987.

Burford, R.O., Strain analysis across the San Andreas fault and Coast Ranges of California, Ph.D. thesis, 74 pp., Stanford University, Stanford, California, 1967.

Burford, R.O., and P.W. Harsh, Slip on the San Andreas fault in central California from alinement array surveys, *Bull. Seismol. Soc. Am., 70*, 1233-1261, 1980.

Burke, D.B., J.W. Hillhouse, E.H. McKee, S.T. Miller, and J.L. Morton, Cenozoic rocks of the Barstow Basin area of southern California - Stratigraphic relations, radiometric ages, and paleomagnetism, *U. S. Geol. Surv. Bull., 1529-E,* 16 pp., 1982.

Carey, S.W., The tectonic approach to continental drift, in *Continental Drift, a Symposium,* edited by S.W. Carey, pp. 177-355, Univ. Tasmania, 1958.

Carter, B.A., Quaternary displacement on the Garlock fault, California, in *Geology and Mineral Wealth of the California Desert, Dibblee Volume,* edited by D.L. Fife and A.R. Brown, pp. 457-465, South Coast Geological Society, Santa Ana, California, 1980.

Celerier, B., and W. F. Brace, Principal stresses orientations from fault plane and slip vector: Theory (abstract), *Eos Trans. AGU, 65*, 1113, 1984.

Clark, M.M., K. Harms, J. Lienkaemper, D. Harwood, K. Lajoie, J. Matti, J. Perkins, M. Rymer, A. Sarna-Wojcicki, R. Sharp, J. Sims, J. Tinsley and J. Ziony, Preliminary slip-rate table and map of late Quaternary faults of California, *U.S. Geol. Surv. Open-File Rep., 84-106*, 12 pp., 1984.

Clark, T.A., B.E. Corey, J.L. Davis, G. Elgered, T.A. Herring, H.F. Hinteregger, C. Knight, J.I. Levine, G. Lundqvist, C. Ma, E. F. Nesman, R.B. Phillips, A.E.E. Rogers, B.O. Ronnang, J.W. Ryan, B.R. Schupler, D.B. Shaffer, I.I. Shapiro, N.R. Vandenberg, J.C. Webber, and A.R. Whitney, Precision geodesy using the Mark III very-long-baseline interferometer system, *IEEE Trans. Geosci. Remote Sens., GE-23*, 438-449, 1985a.

Clark, T.A., J.W. Ryan, and D. Gordon, Geodesy by radio interferometry: Recent measurements of North American to Pacific plate motions, *Eos Trans. AGU, 66,* 848, 1985b.

Clark, T.A., D. Gordon, W.E. Himwich, C. Ma, A. Mallama, and J.W. Ryan, Determination of relative site motions in the western United States using Mark III very long baseline interferometry, *J. Geophys. Res., 92*, 12741-12750, 1987.

Cohen, S.C., A multilayer model of time dependent deformation following an earthquake on a strike-slip fault, *J. Geophys. Res., 87,* 5409 - 5421, 1982.

Cohen, S.C., and M.J. Kramer, Crustal deformation, the earthquake cycle and models of viscoelastic flow in the asthenosphere, NASA Tech. Mem., 85117, 1983.

Coleman, R., and K. Lambeck, Crustal motion in southeastern Australia: Is there geodetic evidence for it?, *Aust. J. Geod. Photo. Surv., 39*, 1-26, 1983.

Corbett, E. J., and T. M. Hearn, The depth of the seismic zone in the Transverse Ranges of southern California (abstract), *Earthquake Notes, 55*, 23 ,1983.

Cox, D.R. and D.V. Hinkley, *Theoretical Statistics*, Chapman and Hall, London, 1974.

Crouch, J.K., S.B. Bachman, and J.T. Shay, Post-Miocene compressional tectonics along the central California margin, in *Tectonics and Sedimentation along the California Margin,* edited by J.K. Crouch and S.B. Bachman, Pac. Sect. Soc. Econ. Paleontol. Mineral., *38,* 37-54, 1984.

Davidson, J.M. and D.W. Trask, Utilization of mobile VLBI for geodetic measurements, *IEEE Trans. Geosci. Remote Sens., GE-23*, 360-368, 1985.

Davis, G.A., and B.C. Burchfiel, Garlock fault: An intracontinental transform structure, southern California, *Geol. Soc. Am. Bull., 84*, 1407-1422, 1973.

Davis, J.L., T.A. Herring, I.I. Shapiro, A.E.E. Rodgers, and G. Elgered, Geodesy by radio interferometry: Effects of atmospheric modeling on estimates of baseline length, *Radio Science, 20*, 1593-1607, 1985.

Davis, T.L., A structural outline of the San Emigdo Mountains, in *Geologic transect Across the Western Transverse Ranges,* edited by T.L. Davis and J. Namson, Pac. Sect. Soc. Econ. Paleontol. Mineral. Guidebook, pp. 23-32, 1986.

Defense Mapping Agency, Department of Defense World Geodetic System 1984: Its definition and relationships with local geodetic systems, *DMA Tech. Rep., 8350.2*, 120 pp., 1987.

Dehlinger, P. and B.A. Bolt, Earthquakes and associated tectonics in a part of coastal central California, *Bull. Seismol. Soc. Am, 77*, 2056-2073, 1987.

DeMets, C., R.G. Gordon, S. Stein, and D.F. Argus, A revised estimate of Pacific-North American motion and implications for western North America plate boundary zone tectonics, *Geophys. Res. Lett., 14*, 911-914, 1987.

Dibblee, T.W., Regional geology of the central Diablo Range between Hollister and New Idria, in *Field Trip Guidebook for the Geological Society of America Cordilleran Section Meeting*, edited by T.H. Nilsen and T.W. Dibblee, pp. 6-16, Geol. Soc. Am., Boulder, Colo., 1979.

Dokka, R. K., Displacements on late Cenozoic strike-slip faults of the central Mojave Desert, California, *Geology, 11*, 305-308, 1983.

Dokka, R.K., and A.K. Glazner, Late Cenozoic tectonic and magmatic evolution of the central Mojave Desert, California, in *Geologic Excursions in the California Desert,*

Field Trip Guidebook, pp. 1-30, Geol. Soc. Am., Cordilleran Section, Los Angeles, Calif., 1982.

Donnellan, A., B.H. Hager, and S. Larsen, Determination of convergence rates across the Ventura Basin, southern California, using GPS and historical triangulation (abstract), *Eos Trans. AGU, 69,* 326, 1988.

Drew, A., and R. Snay, DYNAP: Software for estimating crustal deformation from geodetic data (abstract), *Eos Trans. AGU, 69*, 325, 1988.

Eaton, J.P., Focal mechanisms of near-shore earthquakes between Santa Barbara and Monterey, California, *U.S. Geol. Surv. Open File Rep., 84-477*, 13 pp. 1984.

Eaton, J.P., Regional seismic background of the May 2, 1983 Coalinga earthquake, in *Proceedings of Workshop XXVII, Mechanics of the May 2, 1983 Coalinga Earthquake,* edited by M.J. Rymer and W.L. Ellsworth, *U.S. Geol. Surv. Open File Rep., 85-44*, pp. 44-60, 1985.

Eddington, P.K., R.B. Smith, and C. Renggli, Kinematics of Basin and Range intraplate extension, in *Continental Extensional Tectonics* edited by M.P. Coward, J.F. Dewey, and P.L. Hancock, , Geol. Soc. Lond. Special Pub. No. 28, pp. 371-392, 1987.

Ellsworth, W.L., Bear Valley, California, earthquake sequence of February-March 1972, *Bull. Seismol. Soc. Am., 65*, 483-506, 1975.

Engdahl, E.R., and W.A. Rinehart, Seismicity of North America, in *Neotectonics of North America,* edited by D.B. Slemmons, Geol. Soc. Am., Boulder, Colo., in press, 1988.

Federal Geodetic Control Committee, Standards and specifications for geodetic control networks, Nat. Ocean Atmos. Admin., U.S. Dept. Commerce, Rockville, Md., 1984.

Feigl, K.L., T.H. Jordan, and R.W. King, Geodetic measurement of tectonic deformation in the Santa Maria Basin, California (abstract), *Eos Trans. AGU, 69,* 1418, 1988.

Frank, F.C., Deduction of Earth strains from survey data, *Bull. Seismol. Soc. Am., 56*, 35-42, 1966.

Freund, R., Kinematics of transform and transcurrent faults, *Tectonophysics, 21*, 93-134, 1974.

Fuis, G.S., Crustal structure of the Mojave Desert, California, in *Tectonic Framework of the Mojave and Sonoran Deserts, California and Arizona, U.S. Geol. Surv. Open File Rep., 81-503*, 36-38, 1980.

Garfunkel, Z., Model for the late Cenozoic tectonic history of the Mojave Desert, California, *Geol. Soc. Am. Bull., 85*, 1931-1944, 1974.

Garfunkel, Z., and H. Ron, Block rotation and deformation by strike-slip faults, 2, The properties of a type of macroscopic discontinuous deformation, *J. Geophys. Res., 90,* 8589-8602, 1985.

Gawthrop, W.J., Seismicity and tectonics of the central California coastal region, M.S. thesis, University of Colorado, Boulder, 76 pp., 1977.

Gleason, D.M., Partial sum of Legendre series via Clenshaw summation, *Manuscripta Geodetica,* 10, 115-130, 1985.

Goff, J.A., E.A. Bergman, and S.C. Solomon, Earthquake source mechanisms and transform fault tectonics in the Gulf of California, *J. Geophys. Res., 92*, 10485-10510, 1987.

Golombek, M.P. and L.L. Brown, Clockwise rotation of the western Mojave Desert, *Geology*, 16, 126 - 130, 1988.

Gordon, D., and J. Sauber, Geodesy by radio interferometry: Determination and analysis of vector site motions in the southwestern United States, (abstract), *Eos Trans. AGU, 69,* 331, 1988.

Hamilton, D.H., Characterization of the San Gregorio-Hosgri fault system, coastal central California (abstract), *Geol. Soc. Am. Abstr. Programs, 19*, 385, 1987.

Hamilton, W., and Myers, W.B., Cenozoic tectonics of the western United States, *Rev. Geophys., 4*, 509-549, 1966.

Harding, T.P., Tectonic significance and hydrocarbon trapping consequences of sequential folding synchronous with San Andreas faulting, San Joaquin Valley, California, *Am. Assoc. Petro. Geol. Bull., 60*, 356-378, 1976.

Harland, W.B., Tectonic transpression in Caledonian Spitsbergen, *Geol. Mag., 108*, 27-42, 1971.

Harms, K.K., J.W. Harden, and M.M. Clark, Use of quantified soil development to determine slip rates on the Paicines fault, northern California (abstract), *Geol. Soc. Am. Abstr. Programs, 19*, 387, 1987.

Harris, R.A., and P. Segall, Detection of a locked zone at depth on the Parkfield, California, segment of the San Andreas fault, *J. Geophys. Res., 92*, 7945-7962, 1987.

Harsh, P.W., and N. Pavoni, Slip on the Paicines fault, *Bull. Seismol. Soc. Am., 68*, 1191-1193, 1978.

Hart, E.W., W.A. Bryant, M.W. Manson and J.E. Kahle, Summary report: Fault evaluation program 1984-1985, south Coast Ranges region and other areas, *Calif. Div. of Mines and Geol. Open File Rep. 86-3SF*, 1986.

Heiskanen, W.A., and H. Moritz, *Physical Geology*, 364 pp., Freeman, 1967.

Herring, T.A., I.I. Shapiro, T.A. Clark, C. Ma, J.W. Ryan, B.R. Schupler, C.A. Knight, G. Lundqvist, D.B. Shaffer, N.R. Vandenberg, B.E. Corey, H.F. Hinteregger, A.E.E. Rogers, J.C. Webber, A.R. Whitney, G. Elgered, B.O. Ronnang, and J.L. Davis, Geodesy by radio interferometry: evidence for contemporary plate motion, *J. Geophys. Res.*, 91, 8341-8347, 1986.

Herring, T.A., and J. Sauber, Geodetic studies of Mojave Desert and Basin and Range tectonics, (abstract), *Eos. Trans. AGU, 69*, 326, 1988.

Hileman, J.A., C.R. Allen, and J.M. Nordquist, Seismicity of the southern California region - 1 January 1932 to 31 December 1972, Seismol. Lab., Calif. Instit. of Tech., Pasadena, Calif., 1973.

Hill, R.L., and D.J. Beeby, Surface faulting associated with the 5.2 magnitude Galway Lake earthquake of May 31, 1975: Mojave Desert, San Bernardino County, California, *Geol. Soc. Am. Bull., 88*, 1378-1384, 1977.

Horns, D.M., C.Y. Wang, and Y.Shi, Investigation of the uplift along the San Andreas fault zone (abstract), *Eos Trans. AGU, 66*, 1093, 1985.

Jennings, C.W., Fault map of California, *Calif. Geol. Data Map Ser.*, map 1, Calif. Div. of Mines and Geol., Sacramento, 1975.

Kanamori, H., and G. Fuis, Variation of P-wave velocity before and after the Galway Lake earthquake (M_L=5.2) and the Goat Mountain earthquakes (M_L=4.7,4.7) in the Mojave Desert, California, *Bull. Seismol. Soc. Am., 66*, 2017-2037, 1976.

Keller, E.A., Investigation of active tectonics: Use of surficial earth processes, in *Active Tectonics*, edited by R.E. Wallace, pp. 137-147, National Academy Press, Washington, D.C., 1986.

King, N.E., Horizontal deformation in the Mojave Desert near Barstow, California, 1979-1983, *J. Geophys. Res., 90*, 4491-4494, 1985.

King, N.E., and M. Lisowski, Horizontal deformation across the eastern section of the Garlock fault, California (abstract), *Earthquake Notes, 55*, 31, 1985.

King, N.E. and J.C. Savage, Regional deformation near Palmdale, California, 1973-1983, *J. Geophys. Res., 89*, 2471-2477, 1984.

Kroger, P.M., J.M. Davidson, and S.A. Stephens, Mobile VLBI results in 1984 (abstract), *Eos Trans. AGU, 66*, 246, 1985.

Kroger, P.M., G.A. Lyzenga, K.S. Wallace and J.M. Davidson, Tectonic motion in the western United States inferred from very long baseline interferometry measurements, 1980-1986, *J. Geophys. Res., 92*, 14151-14163, 1987.

Lee, W.H.K., and J.C. Lahr, HYPO71(revised): A computer program for determining hypocenter magnitude and first motion pattern of local earthquakes, *U.S. Geol. Surv. Open File Rep., 75-311,* 35 pp., 1975.

Li, V.C., and J.R. Rice, Crustal deformation in great California earthquake cycles, *J. Geophys. Res., 92*, 11533-11551, 1987.

Lienkaemper, J.J., Quaternary faults of California, *U.S. Geol. Surv. Open File Rep. 85-2111*, 14 pp., 1985.

Lisowski, M., and W.H. Prescott, Short-range distance measurements along the San Andreas fault system in central California, 1975 to 1979, *Bull. Seismol. Soc. Am., 71*, 1607-1624, 1981.

Lockwood, J.P., and J.G. Moore, Regional deformation of the Sierra Nevada, California, on conjugate microfault sets, *J. Geophys. Res., 84,* 6041-6049, 1979.

Lomnitz, C., F. Mooser, C.R. Allen, J.N. Brune and W. Thatcher, Seismicity and tectonics of the northern Gulf of California, Mexico, Preliminary results, *Geofis. Inter., 10*, 37-48, 1970.

Lubetkin, L.K.C., and M.M. Clark, Late Quaternary activity along the Lone Pine fault, eastern California (abstract), *Seismol. Res. Lett, 58*, 32, 1987.

Luyendyk, B.P., M.J. Kamerling, and R. Terres, Geometric model for Neogene crustal rotations in southern California, *Geol. Soc. Am. Bull., 91,* 211-217, 1980.

Lyzenga, G.A., K.S. Wallace, J.L. Fanselow, A. Raefsky, and P.M. Groth, Tectonic motions in California inferred from VLBI observations, 1980-1984, *J. Geophys. Res., 91*, 9473-9487, 1986.

MacFadden, B.J., N.D. Opdyke, and M.O. Woodburne, Pelomagnetism of the middle Miocene Barstow formation, Mojave desert, southern California: magnetic polarity stratigraphy and tectonic rotation (abstract), *Eos Trans. AGU, 68*, 291, 1987.

Mallama, A., and J. Ryan, Comparison between six Earth orientation series (abstract), *Eos Trans. AGU, 69*, 327, 1988.

Malvern, L.E., *Introduction to the Mechanics of a Continuous Medium,* 713 pp., Prentice-Hall, Englewood Cliffs, N.J., 1969.

Matsu'ura, M., D.D. Jackson, and A. Cheng, Dislocation model for aseismic crustal deformation at Hollister, California, *J. Geophys. Res., 91*, 12661-12674, 1986.

McKenzie, D.P., The relation between fault plane solutions for earthquakes and the directions of the principal stresses, *Bull. Seismol. Soc. Am., 59*, 591-601, 1969.

Meisling, K.E., The north frontal fault system of the San Bernardino Mountains, Cajon Pass to Lucerne Valley, California (abstract), *Geol. Soc. Am. Abstr. Programs 16*, 592, 1984.

Menke, W., *Geophysical Data Analysis: Discrete Inverse Theory*, 260 pp., Academic Press, San Diego, Calif., 1984.

Merifield, P.M., T.K. Rockwell, and C.C. Loughman, Slip rate on the San Jacinto fault zone in the Anza seismic gap, southern California (abstract), *Geol. Soc. Am. Abstr. Programs, 19*, 431, 1987.

Minster, J.B., and T.H. Jordan, Present-day plate motions, *J. Geophys. Res., 83*, 5331-5354, 1978.

Minster, J.B., and T.H. Jordan, Vector constraints on Quaternary deformation of the western United States east and west of the San Andreas fault, in *Tectonics and Sedimentation along the California Margin*, edited by J.K. Crouch and S.B. Bachman, Soc. Econ. Paleont. Mineral., Pacific Section, *38*, 1-16, 1984.

Minster, J.B., and T.H. Jordan, Self-consistent modeling of western U.S.deformation (abstract), *Eos Trans., AGU, 66*, 849, 1985.

Minster, J.B., and T.H. Jordan, Vector constraints on western U.S. deformation from space geodesy, neotectonics, and plate motions, *J. Geophys. Res.*, *92*, 4798-4804, 1987.

Minster, J.B., and T.H. Jordan, Measuring crustal deformation in the American west, *Scientific American, 256,* 48-58, 1988.

Molnar, P., Average regional strain due to slip on numerous faults of different orientations, *J. Geophys. Res.*, *88*, 6430-6432, 1983.

Moore, D.G., and J.R. Curray, Geologic and tectonic history of the Gulf of California, *Initial Rep. Deep Sea Drill. Proj., 64,* 1279-1294, 1982.

Moths, B. L., and W. L. Ellsworth, The California earthquake of 1857 and the seismic cycle (abstract), *Eos Trans. AGU, 61*, 1030, 1980.

Mount, V.S., and J. Suppe, State of stress near the San Andreas fault: implications for wrench tectonics, *Geology*, *15*, 1143-1146, 1987.

Murray, M.H., T.H. Jordan, J.B. Minster, D.E. Smith and D.C. Christodoulidis, SLR vector position data: rate scaling of global plate tectonic models (abstract) *Eos Trans., AGU, 66,* 850, 1985.

Namson, J.S., and T.L. Davis, Seismically active fold and thrust belt in the San Joaquin Valley, central California, *Geol. Soc. Am. Bull.*, *100*, 257-273, 1988.

Page, B.M., The southern Coast Ranges, in *The Geotectonic Development of California*, edited by W. G. Ernst, pp. 329-417, Prentice Hall, Englewood Cliffs, N.J., 1981.

Page, B.M., Geologic background of the Coalinga earthquake of May 2, 1983, in *Proceedings of Workshop XXVII, Mechanics of the May 2, 1983 Coalinga Earthquake*, edited by M.J. Rymer and W.L. Ellsworth, *U.S. Geol. Surv. Open File Rep., 85-44*, pp. 4-9, 1985.

Page, B.M., and D.C. Engebretson, Correlation between the geologic record and computed plate motions for central California, *Tectonics, 3*, 133-156, 1984.

Penrose, R., A generalized inverse for matrices, *Proc. Camb. Phil. Soc., 51*, 406-413, 1955.

Pierce, K.L., Dating methods, in *Active Tectonics*, edited by R.E. Wallace, 195-214, National Academy Press, Washington, D.C., 1986.

Prentice, C.S., S.G. Wesnousky, and K.E. Sieh, A minimum Holocene slip rate on the northern San Jacinto fault, San Bernardino Valley, southern California (abstract), *Geol. Soc. Am. Abstr. Programs, 20*, 222, 1988.

Prescott, W.H., An extension of Frank's method for obtaining crustal shear strains from survey data, *Bull. Seismol. Soc. Am., 66*, 1847-1853, 1976.

Prescott, W.H., The determination of displacement fields from geodetic data along a strike-slip fault, *J. Geophys. Res., 86*, 6067-6072, 1981.

Prescott, W.H., and M. Lisowski, Strain accumulation along the San Andreas fault system east of San Francisco Bay, California, *Tectonophysics, 97*, 41-56, 1983.

Prescott, W.H., and S.Yu, Geodetic measurement of horizontal deformation in the northern San Francisco Bay region, California, *J. Geophys. Res.*, 91, 7475-7484, 1986.

Prescott, W.H., M. Lisowski, and J.C. Savage, Velocity field along the San Andreas fault in southern California (abstract), *Eos. Trans. AGU, 68*, 1506, 1987.

Prescott, W.H., J.C. Savage, and W.T. Kinoshita, Strain accumulation rates in the western United States between 1970-1978, *J. Geophys. Res., 84*, 5423-5435, 1979.

Prescott, W.H., J.C. Savage, and M. Lisowski, Earth-based measurements of plate-motion and deformation (abstract), *Eos Trans. AGU, 66*, 849, 1985.

Ramsay, J.G., *Folding and Facturing of Rocks*, 568 pp., McGraw-Hill, New York, 1967.

Rapp, R.H., and J.Y. Cruz, The representation of the Earth's gravitational potential in a spherical harmonic expansion to degree 250, *Air Force Geophys. Lab. Tech. Rep. 86-0191*, 64 pp., 1986.

Raymond, L.A., Tesla-Ortigalita fault, Coast Range thrust fault, and Franciscan metamorphism, northeastern Diablo Range, California, *Geol. Soc. Am. Bull.*, 84, 3547-3562, 1973.

Reid, H.F., Permanent displacements of the ground, in *The California Earthquake of April 18, 1906*, Report of the State Earthquake Investigation Commission, vol. 2, pp. 16 - 28 Carnegie Institution of Washington, Washington, D.C., 1910.

Rockwell, T.K., D.L. Lamar, R.S. McElwain, D.E. Millman, Late Holocene recurrent faulting on the Glen Ivy north strand of the Elsinore fault, southern California, (abstract), *Geol. Soc. Am. Abstr. Programs, 17,* 404, 1985.

Rodgers, T.H., Geologic map of California - San Bernadino sheet, Olaf P. Jenkins edition, Calif. Div. of Mines and Geol., Sacramento, 1967.

Rust, D.J., Neotectonic behavior of the San Andreas fault zone in the big bend (abstract), *Geol. Soc. Am. Abstr. Programs, 18*, 179 1986.

Salyards, S.L., K.E. Sieh, and J.L. Kirschvink, Paleomagnetic measurement of dextral warping during the past three large earthquakes at Pallet Creek, southern California, (abstract), *Geol. Soc. Am. Abstr. Programs, 19,* 828, 1987.

Sauber, J., K. McNally, J. Pechman, and H. Kanamori, Seismicity near Palmdale, California, and its relation to strain changes, *J. Geophys. Res., 88,* 2213-2219, 1983.

Sauber, J., R. Reilinger, and M.N. Toksoz, Post seismic viscoelastic relaxation associated with the 1940 Imperial Valley earthquake (abstract), *Eos. Trans. AGU, 65,* 190, 1984.

Sauber, J., W. Thatcher, and S. Solomon, Geodetic measurement of deformation in the central Mojave Desert, California, *J. Geophys. Res., 91,* 12683-12693, 1986.

Sauber, J., M. Lisowski, and S. Solomon, Geodetic measurement of deformation east of the San Andreas fault, central California, in *Slow deformation and transmission of stress in the Earth,* Geophys. Mon. Series, edited by S. Cohen and P. Vanicek, AGU, Washington, D.C., in press, 1988.

Sauber, J., T.H. Jordan, G.C. Beroza, T.A. Clark, and M. Lisowski, Constraints on North American-Pacific plate boundary deformation in central California from VLBI and ground-based geodetic data, (abstract) in *Programs and Abstracts, The Impact of VLBI on Astrophysics and Geophysics*, Inter. Astron. Un. Symp., No. 129, p.7.1, 1987.

Saucier, F., and E. Humphreys, Finite element kinematic model of southern California (abstract), *Eos Trans. AGU, 69,* 331, 1988.

Savage, J.C., Strain accumulation in western United States, *Ann. Rev. Earth Planet. Sci., 11,* 11-43, 1983.

Savage, J.C., and R.O. Burford, Geodetic determination of relative plate motion in central California, *J. Geophys. Res., 78,* 832-845, 1973.

Savage, J.C., and M. Lisowski, Deformation in Owens Valley, California, *Bull. Seis. Soc. Am., 70* , 1225-1232, 1980.

Savage, J.C., and W.H. Prescott, Precision of Geodolite distance measurements for determining fault movements, *J. Geophys. Res.*, *78*, 6001-6008, 1973.

Sbar, M.L., Delineation and interpretation of seismotectonic domains in western North America, *J. Geophys. Res.*, *87*, 3919-3928, 1982.

Schug, D.L., T.K. Rockwell, and M.E. Hatch, Slip rate estimates for the western reach of the Agua Blanca fault, Baja California, Mexico (abstract), *Geol. Soc. Am.. Abstr. Programs, 19,* 448, 1987.

Schwartz, D.P. and R.J. Weldon, San Andreas slip rates: preliminary results from the 96 St. site near Little Rock, CA. (abstract), *Geol. Soc. Am. Abstr. Programs, 19,* 448, 1987.

Segall, P., and R. Harris, Slip deficit on the San Andreas fault at Parkfield, California, as revealed by inversion of geodetic data, *Science, 233*, 1409-1413, 1986.

Segall, P., and M.V. Matthews, Displacement calculations from geodetic data and the testing of geophysical deformation models, *J. Geophys. Res.*, submitted, 1988.

Segall, P., and D.D. Pollard, The mechanics of discontinuous faults, *J. Geophys. Res.*, *85*, 4337-4350, 1980.

Shapiro, I.I., Use of space techniques for geodesy, in *Earthquakes: Observation, Theory, and Interpretation*, Proc. Int. Sch. Phys. Enrico Fermi, edited by H. Kanamori, pp. 530-568, North-Holland, Amsterdam, 1983.

Sharp, R.V., Variable rates of late Quaternary strike-slip on the San Jacinto fault zone, southern California, *J.Geophys. Res., 86,* 1754-1762, 1981.

Sibson, R.H., Fault zone models, heat flow, and the depth distribution of earthquakes in the continental crust of the United States, *Bull. Seism. Soc. Am., 72*, 151 - 163, 1982.

Sieh, K.E., Slip rate across the San Andreas fault and prehistoric earthquakes at Indio, California (abstract), Eos Trans. AGU, 67, 1200, 1986.

Sieh, K.E., and R. H. Jahns, Holocene activity of the San Andreas fault at Wallace Creek, California, *Geol. Soc. Am. Bull., 95*, 883-896, 1984.

Slemmons, D.B., Capable faults and tectonically active folds of the California central Coast Ranges (abstract), *Geol. Soc. Am. Abstr. Programs, 19,* 452, 1987.

Snay, R.A., Horizontal deformation in New York and Connecticut: Examining contradictory results from the geodetic evidence, *J. Geophys. Res., 91*, 12695-12702, 1986.

Snay, R.A., M.W. Cline, E.L. Timmerman, Project REDEAM: models for historical deformation, *NOAA Tech. Rep.*, NOS 125 NGS 42, 1987.

Springer, J.E., Stress orientations from wellbore breakouts in the Coalinga region, *Tectonics, 6*, 667-676, 1987.

Stein, R.S., Evidence for surface folding and subsurface fault slip from geodetic elevation changes associated with 1983 Coalinga, California earthquake, in *Proceedings of Workshop XXVII, Mechanics of the May 2, 1983 Coalinga Earthquake*, edited by M.J. Rymer and W.L. Ellsworth, *U.S. Geol. Surv. Open File Rep., 85-44*, pp. 225-253, 1985.

Stein, R.S., and G.C.P. King, Seismic potential revealed by surface folding: 1983 Coalinga, California, earthquake, *Science*, 224, 869-872, 1984.

Stein, R.S., and M. Lisowski, The 1979 Homestead Valley earthquake sequence, California: Control of aftershocks and postseismic deformation, *J. Geophys. Res., 88*, 6477-6490, 1983.

Sternlof, K.C., Structural style and kinematic history of the active Panamint - Saline extensional system, Inyo County, California, M.S. thesis, 32 pp., Mass. Inst. of Technol., Cambridge, 1985.

Tchalenko, J.S., Similarities between shear zones of different magnitudes, *Geol. Soc. Am. Bull.*, *81*, 1625-1640, 1970.

Tchalenko, J.S., and N.N. Ambraseys, Structural analysis of the Dasht-e-Bayaz (Iran) earthquake fractures, *Geol. Soc. Am. Bull.*, *81*, 41-60, 1970.

Thatcher, W., Systematic inversion of geodetic data in central California, *J. Geophys. Res.*, 84, 2283-2295, 1979a.

Thatcher, W., Horizontal crustal deformation from historic geodetic measurements in southern California, *J. Geophys. Res.*, *84*, 2351-2370, 1979b.

Thatcher, W., Non-linear strain buildup and the earthquake cycle on the San Andreas fault, *J. Geophys. Res.*, *88*, 5893-5902, 1983.

Thatcher, W., Geodetic measurement of active-tectonic processes, in *Active Tectonics*, edited by R.E. Wallace, pp. 155-163, National Academy Press, Washington, D.C., 1986.

Thatcher, W., and T.C. Hanks, Source parameters of southern California earthquakes, *J. Geophys. Res.*, *78*, 8547-8576, 1973.

Timmerman, E.L., R.A. Snay, and M.W. Cline, Regional deformation for the Barstow region, California, *Bull. Seism. Soc. Am.*, submitted, 1985.

Torge, W., *Geodesy*, 254 pp., Walter de Gruyter, New York, 1980.

Tralli, D.M., and T.H. Dixon, A few parts in 10^8 geodetic baseline repeatability in the Gulf of California using the global positioning system, *Geophys. Res. Lett.*, *15*, 353-356, 1988.

Tralli, D.M., T.H. Dixon, L.L. Skrumeda, S.A. Stephens, C. Vegos, J.M. Davidson, P. Dauphin, F. Suarez-Vidal, GPS baselines across the Gulf of California, *Eos Trans. AGU, 68,* 283, 1987.

United States Geological Survey, Probabilities of large earthquakes occurring in California on the San Andreas fault, *U.S. Geol. Surv. Open File Rep., 88-398*, 62 pp., 1988.

Vanicek, P., and E. Krakiwsky, *Geodesy: The Concepts,* 697 pp., Elsevier, New York, 1986.

Walker, J. D., Permo-Triassic paleogeography and tectonics of the southwestern United States, Ph.D. thesis, 224 pp., Mass. Inst. of Technol., Cambridge, 1985.

Wegener, A. *The Origin of Continents and Oceans*, 246 pp., Dover, New York, 1966 (translation of 4th German ed., F. Vieweg und Sohn, 1962).

Weldon, R., and E. Humphreys, A kinematic model of southern California, *Tectonics, 5*, 33-48, 1986.

Weldon, R. and E. Humphreys, Plate model constraints on the deformation of coastal southern California north of the Transverse Ranges (abstract), *Geol. Soc. Am. Abstr. Program, 19*, 462, 1987.

Weldon, R. J., and K.E. Sieh, Holocene rate of slip and tentative recurrence interval for large earthquakes on the San Andreas fault, Cajon Pass, southern California, *Geol. Soc. Am. Bull., 96*, 793-812, 1985.

Weldon, R. J., D.S. Winston, J.L. Kirschvink, and D.W. Burbank, Magnetic stratigraphy of the Crowder formation, Cajon Pass, southern California (abstract), *Geol. Soc. Am. Abstr. Programs, 16*, 689, 1984.

Wilcox, R.E., T.P. Harding, and D.R. Seely, Basic wrench tectonics, *Am. Assoc. Petrol. Geol. Bull., 57*, 74-96, 1973.

Winker, C.D., and S.M. Kidwell, Implications of fluvial paleocurrents for palinspastic reconstruction of the Neogene Colorado delta and early northern Gulf of California (abstract), *Geol. Soc. Am. Abstr. Programs, 17* , 752-753, 1985.

Yang, M. and M.N. Toksoz, Time-dependent deformation and stress relaxation after strike-slip earthquakes, *J. Geophys. Res., 86*, 2889-2901, 1981.

Yeats, R.S., Large scale Quaternary detachments in Ventura Basin, southern California, *Jour. Geophys. Res., 88,* 569-583, 1983.

Zepeda, R.L., E.A. Keller, and T.K. Rockwell, Soil chronosequence at Wheeler Ridge, southern San Joaquin Valley, California (abstract), *Geol. Soc. Am. Abstr. Programs, 19*, 466, 1987.

Zoback, M.L., and S. Beanland, Stress and tectonism along the Walker Lane belt, western Great Basin (abstract), *Eos Trans. AGU, 67*, 1225, 1986.

Zoback, M.L., and M. Zoback, State of stress in the conterminous United States, *J. Geophys. Res., 85*, 6113-6156,1980.

Zoback, M.D., M.L. Zoback, V.S. Mount, J. Suppe, J.P. Eaton, J.H. Healy, D. Oppenheimer, P. Reasenberg, L. Jones, C.B. Raleigh, I.G. Wong, O. Scotti, and C. Wentworth, New evidence on the state of stress of the San Andreas fault sytem, *Science, 238*, 1105-1111, 1987.

NASA
National Aeronautics and Space Administration

Report Documentation Page

1. Report No.	2. Government Accession No.	3. Recipient's Catalog No.
NASA TM-100732		

4. Title and Subtitle	5. Report Date
Geodetic Measurement of Deformation in California	April 1989
	6. Performing Organization Code: 621

7. Author(s)	8. Performing Organization Report No.
Jeanne Sauber	89B00124
	10. Work Unit No.: RTOP #692

9. Performing Organization Name and Address	11. Contract or Grant No.
Geodynamics Branch Goddard Space Flight Center Greenbelt, Maryland 20771	NAG5-814 NAG5-459
	13. Type of Report and Period Covered: Technical Memorandum
12. Sponsoring Agency Name and Address Goddard Space Flight Center National Aeronautics and Space Administration Washington, D.C. 20546-0001	14. Sponsoring Agency Code

15. Supplementary Notes
This report is essentially a copy of the Ph.D. thesis submitted by Jeanne Sauber to the Department of Earth, Atmospheric and Planetary Sciences at the Massachusetts Institute of Technology.

16. Abstract The very long baseline interferometry (VLBI) measurements made in the western U.S. since 1979 as part of the NASA Crustal Dynamics Project provide discrete samples of the temporal and spatial deformation field. The interpretation of the VLBI-derived rates of deformation requires an examination of geologic information and more densely sampled ground-based geodetic data. In the first two of three related studies embodying this report triangulation and trilateration data measured on two regional networks, one in the central Mojave Desert and one in the Coast Ranges east of the San Andreas fault have been processed. At the spatial scales spanned by these local geodetic networks, auxiliary geologic and geophysical data have been utilized to examine the relation between measured incremental strain and the accommodation of strain seen in local geological structures, strain release in earthquakes, and principal stress directions inferred from in situ measurements. In a third study, the geocentric position vectors from a set of 77 VLBI experiments beginning in October 1982 have been used to estimate the tangential rate of change of station positions in the western U.S. in a North-America-fixed reference frame. The VLBI data have been used to constrain the integrated rate of deformation across portions of the continental plate boundary in California and to provide a tectonic framework to interpret regional geodetic and geologic studies.

17. Key Words (Suggested by Author(s))	18. Distribution Statement
Crustal Deformation, Very Long Baseline Interferometry, VLBI Geodesy, Geodynamics	Unclassified - Unlimited Subject Category 46

19. Security Classif. (of this report)	20. Security Classif. (of this page)	21. No. of pages	22. Price
Unclassified	Unclassified		